

①

AD-A281 016

PL-TR-93-2227



**RMS Lg STUDIES OF UNDERGROUND NUCLEAR
EXPLOSIONS IN THE U.S.S.R. AND THE U.S.**

**P. G. Richards
W.-Y. Kim
G. Ekström**

**Lamont-Doherty Earth Observatory
of Columbia University
Route 9W
Palisades, NY 10964**

19 August 1993

**Final Report
August 22, 1990 - August 21, 1993**

**DTIC
ELECTE
JUL 06 1994
S G D**

Approved for public release; distribution unlimited.



**PHILLIPS LABORATORY
Directorate of Geophysics
AIR FORCE MATERIEL COMMAND
HANSCOM AIR FORCE BASE, MA 01731-3010**

94-20458




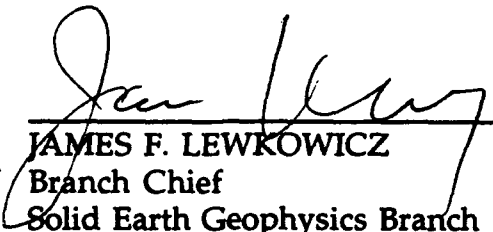
12386

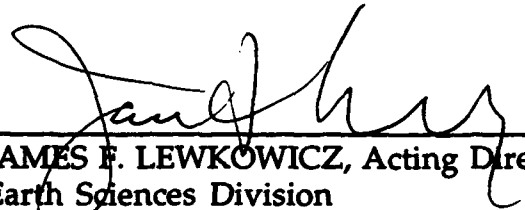
94 7 5 099

The views and conclusions contained in this document are those of the authors and should not be interpreted as representing the official policies, either express or implied, of the Air Force or the U.S. Government.

This technical report has been reviewed and is approved for publication.


DR. KATHARINE KADINSKY-CADE
Contract Manager
Solid Earth Geophysics Branch
Earth Sciences Division


JAMES F. LEWKOWICZ
Branch Chief
Solid Earth Geophysics Branch
Earth Sciences Division


JAMES F. LEWKOWICZ, Acting Director
Earth Sciences Division

This report has been reviewed by the ESC Public Affairs Office (PA) and is releasable to the National Technical Information Service (NTIS).

Qualified requestors may obtain additional copies from the Defense Technical Information Center. All others should apply to the National Technical Information Service.

If your address has changed, or if you wish to be removed from the mailing list, or if the addressee is no longer employed by your organization, please notify PL/TSI, 29 Randolph Road, Hanscom AFB, MA 01731-3010. This will assist us in maintaining a current mailing list.

Do not return copies of this report unless contractual obligations or notices on a specific document requires that it be returned.

REPORT DOCUMENTATION PAGE

Form Approved
OMB No. 0704-0188

Public reporting burden for this collection of information is estimated to average 1 hour per response, including the time for reviewing instructions, searching existing data sources, gathering and maintaining the data needed, and completing and reviewing the collection of information. Send comments regarding this burden estimate or any other aspect of this collection of information, including suggestions for reducing this burden, to Washington Headquarters Services, Directorate for Information Operations and Reports, 1215 Jefferson Davis Highway, Suite 1204, Arlington, VA 22202-4302, and to the Office of Management and Budget, Paperwork Reduction Project (0704-0188), Washington, DC 20503.

1. AGENCY USE ONLY (Leave blank)		2. REPORT DATE 19 August 1993	3. REPORT TYPE AND DATES COVERED Final (August 22, 1990 - Aug. 21, 1993)	
4. TITLE AND SUBTITLE RMS Lg Studies of Underground Nuclear Explosions in the U.S.S.R. and the U.S.			5. FUNDING NUMBERS F19628-90-K-0048 PE 62101F PR 7600 TA 09 WU AV	
6. AUTHOR(S) Paul G. Richards W.-Y. Kim G. Ekstrom				
7. PERFORMING ORGANIZATION NAME(S) AND ADDRESS(ES) Lamont-Doherty Earth Observatory of Columbia Univ. Route 9W Palisades, NY 10964			8. PERFORMING ORGANIZATION REPORT NUMBER	
9. SPONSORING/MONITORING AGENCY NAME(S) AND ADDRESS(ES) Phillips Laboratory 29 Randolph Road Hanscom AFB, MA 01731-3010 Contract Manager: Katharine Kadinsky-Cade/GPEH			10. SPONSORING/MONITORING AGENCY REPORT NUMBER PL-TR-93-2227	
11. SUPPLEMENTARY NOTES				
12a. DISTRIBUTION/AVAILABILITY STATEMENT Approved for Public Release: Distribution Unlimited			12b. DISTRIBUTION CODE	
13. ABSTRACT (Maximum 200 words) This final report is in six sections. Section one describes a new method for interpreting radiation patterns of surface waves from underground nuclear explosions at the Balapan Test Site, East Kazakhstan. We add information from body waves and RMS Lg, to conclude that strike directions of inferred faulting lie in the range 90° to 120°. This section has an Appendix. Section two describes a successful method, based on high-frequency P/Lg spectral ratios, of discriminating between small earthquakes and industrial explosions in the eastern U.S. Section three gives location estimates, derived from SPOT photographs, of 83 nuclear explosions at the Balapan Test Site. Section four describes the seismicity at the Nevada Test Site that is apparently induced by nuclear explosions. This study has relevance in the context of on-site inspections that might be associated with monitoring a comprehensive test ban. Section five describes analog data from China, used to obtain Lg magnitudes for two Soviet nuclear explosions, for which Lg data had not previously been available. Section six describes digital data from Borovoye station in Kazakhstan. RMS Lg for 12 Soviet nuclear explosions show scatter of only a 0.024 magnitude units against NORSAR $m_b(Lg)$.				
14. SUBJECT TERMS Regional seismic waves Yield Estimation Discrimination of earthquakes and explosions			15. NUMBER OF PAGES 126	
			16. PRICE CODE	
17. SECURITY CLASSIFICATION OF REPORT Unclassified	18. SECURITY CLASSIFICATION OF THIS PAGE Unclassified	19. SECURITY CLASSIFICATION OF ABSTRACT Unclassified	20. LIMITATION OF ABSTRACT Unclassified	

TABLE OF CONTENTS

Empirical Measurements of Tectonic Moment Release in Nuclear Explosions from Teleseismic Surface Waves and Body Waves	1
Discrimination of Earthquakes and Explosions in the Eastern United States using Regional High-Frequency Data	57
SPOT Picks of Nuclear Explosion Locations on the Balapan Test Site, near Semipalatinsk, Kazakhstan	67
Seismicity Induced by Nuclear Explosions	71
Lg Signals Recorded in China, for Certain Underground Nuclear Explosions in East Kazakhstan	85
RMS Lg Amplitude of Balapan Explosions using Regional Data from Borovoye, Kazakhstan	95

Accession For	
NTIS CRA&I	<input checked="" type="checkbox"/>
DTIC TAB	<input type="checkbox"/>
Unannounced	<input type="checkbox"/>
Justification	
By	
Distribution /	
Availability Codes	
Dist	Avail and/or Special
A-1	

DTIC QUALITY INSPECTED 3

Empirical measurements of tectonic moment release in nuclear
explosions from teleseismic surface waves and body waves

Göran Ekström

Department of Earth and Planetary Sciences

Harvard University

20 Oxford Street

Cambridge, MA 02138

Paul G. Richards

Lamont-Doherty Earth Observatory and Department of Geological Sciences

Columbia University

Palisades, NY 10964

SUMMARY

A method of source parameter estimation based principally on observations of teleseismic long-period surface waves is developed and applied to 71 underground nuclear explosions at the Balapan (Shagan River) test site in Kazakhstan. First, we quantify the observed radiation patterns of Love and Rayleigh waves, noting that such data place only three linear constraints on the five parameters of the standard point source model for each explosion. The three constraints are the strengths of the isotropic, $\sin 2\Phi$, and $\cos 2\Phi$ components of the observed pattern (where Φ is azimuth). The five source parameters are the isotropic moment M_I ; the double couple moment M_0 ; and the strike, dip, and rake angles, $(\Phi_S, \delta, \lambda)$. These last four parameters characterize the inferred faulting (tectonic release). Surface waves which propagate from different seismic events in a geographically tight cluster to a distant station are similar in shape, and for very shallow sources the propagation operator can be described by a single wave shape, a differential propagation delay, and a single amplitude factor containing the effects of attenuation, scattering, focusing, and geometrical spreading. The inverse problem is formulated which iteratively solves simultaneously for the path amplitude factors and the three radiation pattern parameters for all events using observed seismograms as the empirical wave shapes. We fit 1110 relative measurements of Rayleigh and Love wave amplitudes to determine path amplitude factors to 29 globally distributed stations and radiation pattern parameters for the 71 explosions.

Second, we present a new method for interpreting such radiation patterns. In previous studies, two of the five source parameters have typically been fixed by making the very restricted assumption of pure dip-slip faulting at 45° dip. The assumption leads to estimates of strike that are mostly in the northwest-southeast direction at Balapan, and to estimates of M_I that correlate very poorly with estimates based upon short-period signals (P , Lg). However, now that excellent yield estimates have become available, we can avoid the assumption of pure dip-slip faulting. Instead we can estimate M_I from P and Lg wave data, thus adding a fourth constraint to help in interpreting the teleseismic surface wave amplitudes. The outcome is a method for estimating the strike Φ_S of faulting associated with tectonic release for each explosion, and for estimating the two combinations $M_0 \sin \delta \cos \lambda$ and $\frac{1}{2} M_0 \sin 2\delta \sin \lambda$, which, respectively, are the strike-slip and dip-slip components of the tectonic release.

The strike directions of inferred faulting at Balapan are found to lie in the range 90° to 120° , which conforms better with limited geological information on faulting in the region than does the trend that has long been inferred from assuming pure dip-slip faulting. We find that without additional information about individual explosions, we are not able to provide a high precision isotropic moment or yield estimate from teleseismic surface waves.

Key words: surface waves, radiation patterns, nuclear explosions, tectonic release, Balapan

INTRODUCTION

For explosions and shallow earthquakes the largest teleseismic amplitudes on long-period seismograms usually correspond to the arrival of fundamental mode Rayleigh and Love waves. Because of their large amplitude and signal-to-noise ratio, these waves were recognized early on as ideal for the purpose of determining the sizes of seismic events over a wide range of magnitudes (Richter, 1935; Gutenberg, 1945). The surface wave magnitude M_S , calculated from amplitudes of surface waves with approximately 20 s period, is routinely reported in global seismicity bulletins for events as small as $M_S = 4.5$, reflecting the high level of observability of these waves at teleseismic distances.

Another characteristic of teleseismic surface waves is that their generation is largely insensitive to details of the time history of moment release with periods much shorter than the dominant period in the seismogram ($T \sim 15\text{--}25$ s). For seismic events with source durations less than 10 s (explosions and most moderate ($M_W < 6.0$) earthquakes) the surface wave amplitudes therefore reflect the total time-integrated moment release of the source. High frequency and broad band teleseismic P waves, on the other hand, are dominated by frequencies around the corner frequency of the event, and are for earthquakes often very complex. The similarity in how shallow earthquakes and explosions excite teleseismic surface waves, and the difference in how they generate P waves, lead to systematic differences in the corresponding magnitudes m_b and M_S , which are used as a robust discriminant (Marshall & Basham, 1972; Stevens & Day, 1985; Richards & Zavales, 1990).

Much is known about the generation and propagation of surface waves, and while M_S provides a useful measure of event size, it is an unsophisticated measure of these waves, since in its calculation the effects of source geometry and complex propagation paths are generally ignored. Also, the choice of where in a seismogram to make an M_S amplitude measurement is somewhat arbitrary, and no use is made of the complete wave shape or polarity. A natural improvement on the traditional M_S measurement technique would consist of using forward or inverse waveform modeling methods to quantify surface waves. There are, however, several serious obstacles to such an approach. First, for sources of a fixed moment, the amplitudes of surface waves depend strongly on the depth of the event and the elastic structure near the hypocenter, neither of which is necessarily well known. Second, the propagation of surface waves is well understood in simple media, but in realistic structures the waves are strongly affected by focusing and defocusing, reflection, refraction, attenuation, and scattering along the path from source to receiver. All of these processes can have large effects on the amplitudes, and to account for them correctly would require a more detailed knowledge of the elastic and anelastic structure of the crust and uppermost mantle than is available, as well as the use of elaborate computational techniques.

As an alternative to methods which rely on calculations of synthetic seismograms, we present an empirical approach based on measurements of relative surface wave amplitudes, to determine the explosive and tectonic release of seismic moment of a set of nuclear explosions in the Balapan (Shagan River) portion of the former Soviet Union's nuclear test site near Semipalatinsk, Kazakhstan. Our approach is based on the observation

that two events close to each other write very similar surface wave seismograms at distant stations. Figure 1 shows three-component seismograms for two explosions at the Balapan test site (August 4, 1979 and April 3, 1988) recorded at Matsushiro (MAJO), Japan, at an epicentral distance of 44° . The similarity in the shape of the surface waves is remarkable and the amplitude of surface wave generation for the second event can be measured very precisely with respect to the first event through cross-correlation of the waveforms. By this method the complex effects of propagation are accounted for and the correlation factor can be interpreted as reflecting differences between the two sources. In general, the cross-correlation between two surface wave trains will be a function of frequency when the two events have different source geometries or depths, but under certain circumstances the cross-correlation is accurately approximated by a frequency independent factor.

Observations confirm that each teleseismic station sees essentially the same waveform from all the large explosions at Balapan. However, for a set of explosions, the relative amplitudes of the waveforms are different for different stations, indicating that the radiation patterns are different for different explosions. For each explosion, we are able to estimate three linear combinations of the moment tensor components for each point source, not allowing yet for an overall scale factor relating absolute seismic motion to source moment. These three constraints on each source are essentially derived from measures of the relative strength of the isotropic, $\sin 2\Phi$ and $\cos 2\Phi$ components of the Love and Rayleigh wave radiation patterns, where Φ is azimuth to the station measured at the source. Our method of data analysis, which does not require surface wave propagation confined to great circle paths, can be extended and applied to the radiation pattern of earthquakes.

It has long been known that underground nuclear explosions generate seismic waves that cannot be explained by the explosion itself [for example Press & Archambeau (1962); Brune & Pomeroy (1962); Toksöz, Ben-Menahem & Harkrider (1965); Aki *et al.* (1969); Aki & Tsai (1972); North & Fitch (1982); Helle & Rygg (1984); Massé (1981); Given & Mellman (1986)]. The part of the seismic radiation that is not due to the explosive source is generally thought to be due to tectonic strain release, and different mechanisms for this release have been proposed. Archambeau (1972), for example, argued that the strain release occurs in the fractured rock around the explosion, while Aki and Tsai (1972) suggested that the strain is released through triggered motion on a preexisting fault. There are no significant differences in how these mechanisms affect the radiation of surface waves at 20 s or greater period. While there are observations that the tectonic release sometimes occurs within one or a few seconds after the explosion (Rygg, 1979; Goforth, Rafipour & Herrin, 1982; Day *et al.*, 1987), these time differences are small in comparison with the periods of teleseismic surface waves, and can be ignored for our purposes.

We adopt a standard five-parameter model for each source, using the isotropic moment M_I ; the double couple moment M_0 ; and the strike, dip and rake angles (Φ_S , δ , λ). We interpret the results of the data inversion by first exploring the inherent ambiguity in determining five source parameters subject only to three constraints. Second, we briefly explore the consequences of assuming dip-slip faulting for all the

events. Though our study uses about four times as much data as the previously most extensive analysis of surface waves from Balapan (Given & Mellman, 1986), we then find the same unsatisfactory conclusion reached by previous studies based upon the assumption of dip-slip faulting; namely that estimates of the isotropic moment based on surface waves agree very poorly with estimates based upon short-period signals such as P and Lg waves. This conclusion would imply that surface waves are a poor basis upon which to estimate explosion yield. Third, we show that a consistent interpretation of high-quality long-period (surface wave) and short-period signals is possible, if we drop the dip-slip assumption. To this end, we present a new method which combines the three constraints obtained from surface waves with an estimate of the isotropic moment obtained from P and Lg waves. The immediate result is a set of estimates of the strike directions of inferred faulting associated with Balapan explosions: the trend is quite consistently in the range 90° to 120° , in good agreement with available information on mapped faults, and with a radiation pattern derived for one explosion from local data, collected by seismic stations operated on and near the Balapan test site.

Our approach provides a new framework for evaluating the interplay between tectonic release and nuclear explosion yield estimates based upon surface waves. We believe this is the first study in which empirical Green functions exclusively have been used both to calibrate wave paths and to determine radiation patterns. This is also the first study to show how the amplitudes and radiation patterns of long-period (Love, Rayleigh) signals from nuclear explosions can be interpreted consistently with short-period (P , Lg) amplitudes.

THEORY

To develop the simple relationships that allow us to apply the empirical approach to the study of underground nuclear explosions, we need to consider how surface waves are generated by shallow seismic sources. Following Aki & Richards (1980), we can write, for a particular frequency ω , the vertical component of Rayleigh wave displacement, due to a moment tensor source M_{ij} acting at depth h , as

$$u^R(\omega) = \sum_n \frac{r_2(z)}{8cUI_1} \left(\frac{2}{\pi kr} \right)^{1/2} \exp[i(kr + \frac{\pi}{4})] \\ \times \left\{ kr_1(h) \left[\frac{1}{2}(\cos 2\Phi + 1)M_{xx} - \frac{1}{2}(\cos 2\Phi - 1)M_{yy} + \sin 2\Phi M_{xy} \right] \right. \\ \left. + \left(i \frac{dr_1}{dz} \Big|_h - ikr_2(h) \right) [\cos \Phi M_{xz} + \sin \Phi M_{yz}] + \frac{dr_2}{dz} \Big|_h M_{zz} \right\} \quad (1)$$

and similarly for the transverse component of Love wave displacement

$$u^L(\omega) = \sum_n \frac{l_1(z)}{8cUI_1} \left(\frac{2}{\pi kr} \right)^{1/2} \exp[i(kr + \frac{\pi}{4})] \\ \times \left\{ kl_1(h) [\sin 2\Phi M_{xx} - \sin 2\Phi M_{yy} - 2 \cos 2\Phi M_{xy}] + i \frac{dl_1}{dz} \Big|_h [\sin \Phi M_{xz} - \cos \Phi M_{yz}] \right\} \quad (2)$$

where r_1, r_2, l_1 are eigenfunctions, c and U are the phase and group velocity, I_1 is an energy integral of the particular wave type (Rayleigh or Love), and k is the wave number. All of these quantities depend on ω , and the mode branch. In the following we shall discuss only the fundamental mode surface waves, since for very shallow events these dominate the seismograms at teleseismic distances. The expressions above hold for a

laterally homogeneous medium, and we will make several assumptions and approximations when we apply them to real data which are affected by inhomogeneous and otherwise complex Earth structure.

First, we assume that the main surface wave arrival propagates along a single path between the source and the receiver. This allows us to use the simple angular dependence of the excitation given by equations (1) and (2). Real rays in the Earth will refract and scatter in the heterogeneous structure so that a wave which arrives at the station may have propagated along a path which leaves the source in a direction other than directly towards the receiver and arrives at the station from an azimuth different from the great circle back-azimuth. The effect of propagation off the great circle path primarily influences the source excitation, which depends on azimuth. The angle Φ in equations (1) and (2) should therefore be interpreted as the take-off azimuth, and not the great circle azimuth. We will consider the possibility that the true take-off azimuth Φ is perturbed from the great circle azimuth Φ^0 by an amount $\delta\Phi$, and attempt to estimate $\delta\Phi$ for different paths. There is no effect of propagation off the great circle at the receiver for the vertical component of Rayleigh wave motion. For the horizontal components of motion, the error in separating the transversely and longitudinally polarized wavefields using the great circle as opposed to the true back-azimuth is proportional to $(1 - \cos \delta\Phi_{\text{receiver}})$, which is small for realistic deviations. Moreover, for a particular source-receiver pair, this factor will be a constant which is independent of the source excitation. Cross contamination between Love and Rayleigh waves is not significant since these signals arrive in different time windows at teleseismic distances.

Second, we note that the surface wave excitation due to the vertical dip-slip components (M_{xx}, M_{yy}) of the moment tensor is small for shallow sources, since these correspond to shear stresses that must vanish at the Earth's surface. Given & Mellman (1986) have shown that for a vertical dip-slip source (M_{xx} or M_{yy}) at 1 km depth, the Rayleigh wave excitation at 20 s period is one tenth that of a similar size strike-slip (M_{xy} or $M_{xx} - M_{yy}$) source. For shallower sources and longer periods the ratio of excitation amplitudes becomes even smaller. We therefore assume that the contribution of these source components to the seismograms is insignificant. This assumption is valid provided the vertical dip-slip components do not dominate the source.

Third, we observe that for very shallow sources ($h \rightarrow 0$), since the normal stresses are then small, the excitation function for the M_{xx} component can be approximated by

$$\left. \frac{dr_2}{dz} \right|_h = -\frac{\alpha^2 - 2\beta^2}{\alpha^2} r_1(h)k \quad (3)$$

where α and β are the compressional and shear wave speeds averaged over the depth range of the emplacement shaft and the vicinity of the shot point (see Aki & Richards (1980), equation (7.26)). This approximation becomes better for longer periods and shallower source depths.

We can now rewrite equations (1) and (2) as

$$u^R(t) = G^R(t) \times \left[\frac{1}{2}(\cos 2\Phi^R + 1)M_{xx} - \frac{1}{2}(\cos 2\Phi^R - 1)M_{yy} + \sin 2\Phi^R M_{xy} - \frac{\alpha^2 - 2\beta^2}{\alpha^2} M_{zz} \right] \quad (4)$$

and

$$u^L(t) = G^L(t) \times \left[\frac{1}{2} \sin 2\Phi^L (M_{xx} - M_{yy}) - \cos 2\Phi^L M_{xy} \right] \quad (5)$$

in which we have included the possibility of perturbed take-off azimuths for the two wave types in $\Phi^R = \Phi^0 + \delta\Phi^R$ and $\Phi^L = \Phi^0 + \delta\Phi^L$, where Φ^0 is the unperturbed great circle azimuth. $G^R(t)$ and $G^L(t)$ represent Green functions giving the vertical Rayleigh wave motion and transverse Love wave motion due to a moment tensor source. These functions can in theory be estimated given a model of the elastic and anelastic structure at and between the source and the receiver, but here we shall use an empirical approach, noting that the shape of the Green function is the same for the different components of the moment tensor, and that this shape is therefore known from observed seismograms. What remains to be determined is a scale factor (sign and amplitude) of the seismogram for a particular source excitation.

We will be concerned here with studying surface wave arrivals from a set of N closely clustered seismic events observed on a global network of M stations. If the Green functions were known, we could directly reduce the observed seismogram $S_{lm}^n(t)$ to a source radiation amplitude through cross-correlation

$$C_{lm}^n = \frac{\int G_{lm}^n(t) S_{lm}^n(t) dt}{\int G_{lm}^n(t) G_{lm}^n(t) dt} \quad (6)$$

where the subscript l indicates a vertical Rayleigh wave ($l = 1$) or a transverse Love wave ($l = 2$) trace. The subscript m runs over the stations, and superscript n runs over the sources. If the N sources are close to each other, Green functions for different events will be similar, apart from a time shift, since dispersion due to differences in path length will have a very small effect if relatively short time windows (a few wave cycles) are correlated in equation (6). We can estimate the shape of an empirical Green function for the path between the cluster of events to the m th station by stacking several observed seismograms or by choosing one seismogram as a reference. We here use a reference seismogram $s_{lm}(t)$ scaled by an unknown factor F_{lm} as our empirical Green function. For each individual event observed at the m th station we can write $G_{lm}^n(t) = F_{lm} s_{lm}(t - \delta t_{lm}^n)$ where δt_{lm}^n is a time delay reflecting a small difference in path length. The product $c_{lm}^n = F_{lm} C_{lm}^n$ is estimated through cross correlation between the reference seismogram $s_{lm}(t)$ and the observed seismogram $S_{lm}^n(t)$. The time shift δt_{lm}^n is determined by maximizing c_{lm}^n within reasonable *a priori* bounds on δt_{lm}^n .

Combining equations (4), (5) and (6) gives a potentially overdetermined set of equations for the source parameters, scaling of the Green functions, and perturbations to the take-off azimuths.

$$F_{lm} \sum_{j=1}^3 A_{lmj} U_j^n = \frac{\int s_{lm}(t - \delta t_{lm}^n) S_{lm}^n(t) dt}{\int s_{lm}(t) s_{lm}(t) dt} + \epsilon_{lm}^n = c_{lm}^n + \epsilon_{lm}^n \quad (7)$$

where U_j^n represents combinations of moment tensor elements for the n th explosion

$$\begin{aligned} U_1^n &= \frac{1}{2}(M_{xx} + M_{yy}) - \left(\frac{\alpha^2 - 2\beta^2}{\alpha^2}\right) M_{zz} \\ U_2^n &= \frac{1}{2}(M_{xx} - M_{yy}) \\ U_3^n &= M_{xy}, \end{aligned} \quad (8)$$

the geometrical coefficients for Rayleigh waves at the m th station are

$$A_{1m1} = 1 \quad (9)$$

$$A_{1m2} = \cos 2(\Phi_m^0 + \delta\Phi_{1m})$$

$$A_{1m3} = \sin 2(\Phi_m^0 + \delta\Phi_{1m}),$$

and for Love waves at the m th station

$$A_{2m1} = 0 \quad (10)$$

$$A_{2m2} = \sin 2(\Phi_m^0 + \delta\Phi_{2m})$$

$$A_{2m3} = -\cos 2(\Phi_m^0 + \delta\Phi_{2m})$$

and ϵ_{lm}^n is the misfit between observation and model. Each event is recorded only by a subset of the M stations so the total number of equations is less than $2MN$.

We shall seek a solution to this set of equations which minimizes the summed squared weighted misfit between observed correlations and model predictions,

$$\Xi^2(F_{lm}, U_j^n, \delta\Phi_{lm}) = \sum_{l=1}^2 \sum_{m=1}^M \sum_{n=1}^N \frac{\epsilon_{lm}^n \epsilon_{lm}^n}{\sigma_{lm}^n \sigma_{lm}^n} \quad (11)$$

where σ_{lm}^n are the *a priori* error estimates of the individual data points. It is clear that, as stated, the problem is non-unique, since a constant factor can multiply all F_{lm} and divide all U_j^n . This results from having formulated the problem entirely in terms of relative measurements. We remove this ambiguity by fixing one F_{lm} to be unity. A scaling factor is therefore needed to relate our retrieved values of U_j^n (obtained under the assumption that one of the F_{lm} is unity) to physical quantities such as the right-hand side of equation (8). The scaling factor may be determined from additional information about one or more explosions, thereby calibrating the results. It can also be shown that if all sources have the same excitation ratios, that is if U_1^n/U_2^n , U_1^n/U_3^n , or U_2^n/U_3^n is constant for all N events, equation (7) will not have a unique solution. Our method succeeds because of significant differences between radiation patterns for different events.

For each event, we can estimate only 3 combinations of 6 moment tensor elements. This indeterminacy is a direct consequence of the appropriate approximations that we made for the shallow source depth and the frequency contents of our observations. In particular, there is no possibility of determining the isotropic component ($M_{xx} = M_{yy} = M_{zz}$) of the source independently from a vertically oriented compensated linear vector dipole source, ($M_{xx} = M_{yy} = -\frac{1}{2}M_{zz}$), since both of these combinations contribute only to U_1 . In order to interpret the U_j^n in terms of an isotropic and a deviatoric moment tensor, we therefore have to introduce additional assumptions. We will assume that the total moment tensor M is a sum of the explosion described by an isotropic source $M_I = \frac{1}{3}(M_{xx} + M_{yy} + M_{zz})$, and tectonic release described by a double couple source M_{DC} , corresponding to a shear dislocation with strike Φ_S , dip δ , rake λ , and moment M_0 . Using relationships given by Aki & Richards (1980, page 117) we find that

$$U_1 = \frac{1}{2}(M_{xx} + M_{yy}) - \frac{\alpha^2 - 2\beta^2}{\alpha^2} M_{zz} = \frac{2\beta^2}{\alpha^2} M_I - \frac{3\alpha^2 - 4\beta^2}{2\alpha^2} M_0 \sin 2\delta \sin \lambda \quad (12)$$

$$U_2 = -M_0(\sin \delta \cos \lambda \sin 2\Phi_S - \frac{1}{2} \sin 2\delta \sin \lambda \cos 2\Phi_S) \quad (13)$$

$$U_3 = M_0(\sin \delta \cos \lambda \cos 2\Phi_S + \frac{1}{2} \sin 2\delta \sin \lambda \sin 2\Phi_S). \quad (14)$$

It is clear from equation (12) that M_I is maximized assuming a fixed value of M_0 if $\sin 2\delta = \sin \lambda = 1$, that is for a pure thrust with $\delta = \pi/4$ and $\lambda = \pi/2$. There is no *a priori* reason why the maximum possible value of M_I consistent with U_1, U_2, U_3 should be consistent with a pure thrust, since all of $(\Phi_S, \delta, \lambda, M_0)$ may be varied. Nevertheless, the result is true, but the maximum M_I can also be derived from other combinations of δ and M_0 and the key variable affecting M_I is Φ_S . To see this, note that

$$U_2 \cos 2\Phi_S + U_3 \sin 2\Phi_S = \frac{1}{2} M_0 \sin 2\delta \sin \lambda \quad (15)$$

and

$$U_2 \sin 2\Phi_S - U_3 \cos 2\Phi_S = -M_0 \sin \delta \cos \lambda \quad (16)$$

which can be rewritten as

$$U_2 \cos 2\Phi_S + U_3 \sin 2\Phi_S = \sqrt{U_2^2 + U_3^2} \cos[2(\Phi_S - \Phi_U)] = \frac{1}{2} M_0 \sin 2\delta \sin \lambda \quad (17)$$

$$U_2 \sin 2\Phi_S - U_3 \cos 2\Phi_S = \sqrt{U_2^2 + U_3^2} \sin[2(\Phi_S - \Phi_U)] = -M_0 \sin \delta \cos \lambda \quad (18)$$

where the angle Φ_U is determined from the observations by $\tan 2\Phi_U = U_3/U_2$. It follows then that

$$M_I = \frac{\alpha^2}{2\beta^2} U_1 + \left(\frac{3\alpha^2}{2\beta^2} - 2 \right) \sqrt{U_2^2 + U_3^2} \cos[2(\Phi_S - \Phi_U)]. \quad (19)$$

To maximize M_I we must require $\Phi_S = \Phi_U$. Then, from (18) and (17), $\lambda = \pi/2$ and $M_0 \sin 2\delta = 2\sqrt{U_2^2 + U_3^2}$. These choices describe a pure thrust with fixed strike, but various combinations of M_0 and δ will satisfy the last equality, all leading to the same maximum value of M_I . Of these combinations, that with $\delta = \pi/4$ will be associated with the least M_0 .

DATA

We studied all seismic events in the Balapan portion of the Soviet nuclear test site in eastern Kazakhstan since 1977 listed in the ISC (1977–August 1987) and PDE (September 1987–1990) bulletins. Two hours of long-period data were collected for all stations and channels available for a particular event. The data were extracted from the Harvard Seismic Archive Facility which contains data from the GDSN, CDSN, RSTN, and IRIS/USGS GSN networks. In 1977 as few as five stations were providing data, while in the late 1980's more than 25 stations were operational. Seismograms from 78 events were collected.

As a first step, all seismograms were normalized to the same filter response, and rotated into vertical, longitudinal, and transverse components using the great circle back azimuth. The response chosen for the analysis consists of an 8-pole Butterworth lowpass filter with a corner at 18 s period and a 4-pole Bessel highpass filter with a corner at 60 s. A relatively sharp corner at the high end of the passband is needed to remain within the original passband of the SRO and ASRO instruments while at the same time benefiting

from the higher signal-to-noise ratio at around 20–25 s period. The details of the filtering do not significantly influence our results.

An initial viewing was made of all events recorded at a particular station. For each station, one vertical and one transverse component seismogram with high signal-to-noise ratio were selected as reference seismograms. A number of stations were discarded when the data were too noisy for analysis for all of the events. Vertical Rayleigh wave reference seismograms were selected for 29 stations and transverse Love wave reference seismograms for 18 stations (Figure 2).

The correlation coefficients (c_{lm}^n) were calculated by systematically processing all events recorded on the vertical or transverse component at a particular station. Figure 3 shows an example of the correlation procedure for one explosion. A time window was selected, approximately 100 s long, in which the correlation between the traces was calculated. The selection of this window is governed mostly by the arrival of the highest amplitude portion of the surface wave train. The correlation processing is interactive, allowing for modifications of the window when the data in the initial window are noisy or disrupted by glitches or other problems.

In order to estimate the uncertainty in our derived source parameters, we assign standard deviations σ_{lm}^n in (11) to each correlation data point c_{lm}^n . Our assumption is that the measurement error is due primarily to the specific choice of correlation window and that this error is proportional to the value of the measurement. That is, we have a contribution $^{(1)}\sigma_{lm}^n = f c_{lm}^n$, where f is a factor assigned by visually evaluating the quality of correlation of the two waveforms. We use four classes of quality of fit: 'A' indicates an estimated uncertainty f in c_{lm}^n of 10%, 'B' 20%, and 'C' 40%. Data points which are questionable due to a suspicion of some malfunction of the instrument (mostly polarity reversals and multiplexing errors) are retained but given a quality label 'S', and are not used in the inversion. Using only proportional errors $^{(1)}\sigma_{lm}^n$ would lead to an emphasis on fitting small amplitudes at nodal stations. While nodal observations are important for constraining the radiation pattern, they are also most affected by propagation off the great circle path and the possibility of multipathing. We attempt to compensate for this source of error by adding a second term $^{(2)}\sigma^n$ which is the average of $^{(1)}\sigma_{lm}^n$ for the particular event. The total *a priori* error in each data point is then $^{(1)}\sigma_{lm}^n + ^{(2)}\sigma^n$.

The time shift δt_{lm}^n is determined by calculating the correlation for different time shifts between the observed and reference waveforms. An expected timeshift is estimated by calculating the delay caused by the difference in epicentral distance between the reference event and a particular event. An optimal δt_{lm}^n is sought within 5 s of this predicted value.

RESULTS: ESTIMATION OF RADIATION PATTERN COEFFICIENTS

In minimizing equation (11) we are faced with a non-linear problem, so it is difficult to ensure that a solution has been found which corresponds to a global minimum. While we cannot prove that such a minimum has been found, we here describe the inversion method and tests that we have employed.

We used the downhill simplex method of Nelder & Mead (1965) to determine the set of F_{lm} and $\delta\Phi_{lm}$

which minimizes equation (11). This method does not require the calculation of derivatives, only of functional values at different points in parameter space. For each choice of a set of F_{lm} and $\delta\Phi_{lm}$, we estimate source parameters U_j^n for each event independently of all other events, and the misfits $(\epsilon_{lm}^n \epsilon_{lm}^n)/(\sigma_{lm}^n \sigma_{lm}^n)$ are summed to form $\Xi^2(F_{lm}, U_j^n, \delta\Phi_{lm})$. The downhill simplex method generates sets of F_{lm} and $\delta\Phi_{lm}$ with smaller and smaller Ξ^2 until a minimum is reached.

We initially inverted only the Rayleigh wave observations for F_{lm} and U_j^n in order to predict the approximate polarities of the Love waves. For explosions with low to moderate tectonic release, Rayleigh waves have the same polarity in all azimuths, while Love wave polarities follow a $\sin 2\Phi$ pattern. The signs of F_{2m} for the Love waves were thus initially unknown. Once the Rayleigh wave inversion had converged, we used the predicted signs of F_{2m} as a starting point in our inversion of the whole data set.

The total number of observations was 1110. We inverted the full data set for the 46 scaling parameters F_{lm} (one was held fixed at 1), in order to see how well the observations could be fit while still assuming propagation along great circle paths. For this inversion Ξ^2 is 794. When we add the take-off azimuths to the list of parameters that are allowed to vary (47 additional unknowns), Ξ^2 is 392. While the improvement in fit is substantial, it was clear that the additional degrees of freedom made the inversion unstable. For some stations $|\delta\Phi|$ drifted to values of 30° , which probably is unrealistic, without significantly affecting Ξ^2 . At the same time small perturbations in take-off azimuths, in particular for Love waves at nodal stations, have a large influence on Ξ^2 . In order to balance these two effects, we added a penalty term to the function to be minimized so that we now minimize

$$\Upsilon = \Xi^2 + v \sum_{l=1}^2 \sum_{m=1}^M \delta\Phi_{lm} \delta\Phi_{lm} \quad (20)$$

where v is a parameter that we have to choose. Choosing v large corresponds to not allowing rays to deviate from a great circle path; $v = 0$ is the unconstrained case which leads to unstable solutions. With other values of v we balance the expectation that most $\delta\Phi$ are close to 0° against the observations that some stations are much better fit if the take-off angles are adjusted by a few degrees, which is physically reasonable. With a choice of $v = 0.1$, for example, none of the $|\delta\Phi|$ is greater than 15° , only five are greater than 5° while Ξ^2 is reduced to 458. We chose this, somewhat arbitrarily, as our favored solution.

Fortunately, the choice of v has almost no effect on the derived source parameters. For events which are recorded by more than just a few stations, the changes in U_j^n in response to extreme variations in v are only a few percent. Also, the results from minimizing the L1 norm are very similar to minimization of L2, which also indicates that the path and source parameter retrieval is robust.

Seven events of the 78 had fewer than five observations, and we did not calculate source parameters for these. The result of the minimization is thus a set of path parameters and source parameters for 71 events. The source parameters at this stage are the radiation pattern coefficients of equation (7). Table 1 reports our estimates of the coefficients U_1^n , U_2^n , and U_3^n , and their standard uncertainties, as well as the resulting goodness of fit parameter $Q(\nu/2, \chi^2/2)$ where ν is the number of degrees of freedom (*number of stations*

- 3 source parameters) and χ^2 is the sum of squared errors normalized to unit variance. An appendix lists further details of our inversion results, including the list of stations and the values of F_{lm} and $\delta\Phi_{lm}$.

We can also evaluate the quality of our estimates of U_1^n , U_2^n , and U_3^n by comparing the radiation amplitudes $C_{lm}^n = c_{lm}^n/F_{lm}$ with the predicted radiation patterns $\sum_{j=1}^3 A_{lmj} U_j^n$. A central finding of this study is the high degree of agreement between observed and predicted radiation amplitudes obtained and shown in Figure 4. That is, the observations are in most cases well fit by a radiation monopole plus $\cos 2\Phi$ and $\sin 2\Phi$ terms.

RESULTS: ESTIMATION OF ISOTROPIC MOMENT AND TECTONIC RELEASE

The next step is to interpret our quantitative characterization of the radiation pattern in order to obtain source parameters for each explosion. However, even if there is no error in determining values of U_i , and the point source is correctly characterized by an isotropic component plus a shear dislocation, knowledge only of the three quantities (U_1 , U_2 , U_3) is inadequate to determine the desired five source parameters (M_I , M_0 , Φ_S , δ , λ). The inadequacy has separate elements, and we shall develop additional information that results in specific estimates of isotropic moment M_I and strike Φ_S , plus two constraints on the remaining parameters (M_0 , δ , λ) of the shear dislocation.

The first element of inadequacy in working with radiation patterns alone is that our empirical method requires an overall scale factor (the same for all sources) to relate the values of (U_1 , U_2 , U_3) listed in Table 1 to absolute moment units. Let K be the constant needed, to multiply the tabulated values and thus give moment in, say, units of 10^{15} Nm. It is for such scaled values of the U_i , that equations (12) to (19) have meaning in absolute moment units.

The second element of inadequacy is due to the fact that (M_0 , δ , λ) in equations (12) to (19) appear only as linear combinations of $M_0 \sin \delta \cos \lambda$ or $\frac{1}{2} M_0 \sin 2\delta \sin \lambda$. Thus, at best we can hope (from teleseismic surface wave data) to determine only these two combinations. We introduce the notation

$$SS = M_0 \sin \delta \cos \lambda \quad (21)$$

$$DS = \frac{1}{2} M_0 \sin 2\delta \sin \lambda, \quad (22)$$

intended to associate the first combination with strike-slip motion at the source, and the second with dip-slip motion. It follows from Aki & Richards (1980, page 106) that the strike-slip component of the shear dislocation is left-lateral or right-lateral, according as SS is positive or negative; and the dip-slip component is that of a thrust fault or a normal fault according as DS is positive or negative.

With this notation, we can now rewrite equations (12) to (19) in order to address the third element of inadequacy in determining source parameters from measurements of the radiation pattern. We have

$$M_I = \frac{\alpha^2}{2\beta^2} K U_1 + \left(\frac{3\alpha^2}{2\beta^2} - 2 \right) DS \quad (23)$$

$$DS = K(U_2 \cos 2\Phi_S + U_3 \sin 2\Phi_S) \quad (24)$$

$$SS = K(-U_2 \sin 2\Phi_S + U_3 \cos 2\Phi_S) \quad (25)$$

which are three equations for the four unknowns M_I , Φ_S , DS , and SS . It follows that

$$DS^2 + SS^2 = K^2(U_2^2 + U_3^2) \quad (26)$$

$$\Phi_S = \frac{1}{2} \tan^{-1} \left(\frac{DS \times U_3 - SS \times U_2}{DS \times U_2 + SS \times U_3} \right) \quad (27)$$

Figure 5 shows a geometrical relationship between (U_2, U_3) and (DS, SS, Φ_S) . From equations (23) to (27) we can see that knowledge only of (U_1, U_2, U_3) is inadequate even to determine the relative size of the strike-slip and dip-slip components of the shear dislocation. For example, note two extreme cases: we can always find a solution with $SS = 0$ (associated with purely dip-slip motion); and we can always find a solution with $DS = 0$ (purely strike-slip motion). This type of ambiguity was noted by Murphy, O'Donnell & Barker (1987) who described special cases in which $\delta = 90^\circ$. They showed that radiation patterns can always be fit exactly by a dip-slip solution ($\lambda = 90^\circ$) or a strike-slip solution ($\lambda = 0$). Our presentation has shown how ambiguities extend to values of dip angle and double couple moment in addition to the rake. The fundamental source parameters here are DS , SS , and Φ_S , and even these are undecided by radiation patterns alone. The purely dip-slip solution has a strike given by $\frac{1}{2} \tan^{-1}(U_3/U_2)$, and the purely strike-slip solution has strike $\frac{1}{2} \tan^{-1}(-U_3/U_2)$. These two strike directions differ by 45° .

This paper is principally concerned with tectonic release estimated from surface waves, a subject which is closely related to problems of yield estimation via interpretation of the isotropic component in the surface wave radiation pattern. Equation (23) is the key result for yield estimation, presuming that the isotropic moment is proportional to yield. Introducing the constant L = ratio of isotropic moment to yield, the yield estimate \hat{Y} is

$$\hat{Y} = \left[\frac{1}{2} \frac{\alpha^2}{\beta^2} K U_1 + \left(\frac{3}{2} \frac{\alpha^2}{\beta^2} - 2 \right) DS \right] / L \quad (28)$$

This equation shows explicitly how the yield estimate is affected by the value taken for DS , the strength of the dip-slip component of tectonic release. For typical values of α and β , the coefficient of DS in equation (28) is almost twice as large as the coefficient of KU_1 , so that thrusting is in some sense about twice as effective as an explosion in generating Rayleigh waves with explosion polarity and shape. Given & Mellman (1986) used equation (23) to estimate M_I for explosions at the Nevada Test Site and at Balapan, interpreting Nevada explosions as triggering a tectonic release solely via strike-slip motion, and the Balapan explosions solely via dip-slip motion. They used their estimates of M_I to obtain a relationship between P wave magnitude m_b and M_I , for each test site, in the form

$$m_b = 0.9 \log M_I - a \quad (29)$$

where the constant a is different for different test sites. From the different values of their estimates for a at NTS and Balapan they concluded that for a given M_I , an explosion at Balapan has an m_b that is about 0.32 magnitude units higher than an explosion at Balapan. This method for estimating m_b bias, between

the two test sites, may be valid in its use of M_I as a surrogate for yield. But such a bias estimate is too low if either the Balapan explosions include some component of tectonic release via strike-slip motion or the Nevada explosions have some thrusting dip-slip motion. The bias estimate is too high in this type of analysis only if the Nevada explosions trigger some type of normal faulting.

It is first of interest to pursue an interpretation of Balapan radiation patterns based upon the long held assumption of a purely thrusting style of tectonic release. Only a thrust mechanism (as opposed to a strike-slip mechanism) can produce inverted polarities for Rayleigh waves at all azimuths, something we observe for three events in our study. We take $\lambda = 90^\circ$ and $\Phi_S = \frac{1}{2} \tan^{-1}(U_3/U_2)$, which maximizes the estimate of M_I ; and we also choose $\delta = 45^\circ$, which minimizes the estimate of M_0 for the maximized M_I estimate. In order to scale the results in terms of moment release or explosive yield, we need to introduce specific values for the three constants, K , $\frac{\alpha^2}{\beta^2}$, and L . To this end, we shall use the published explosive moment and yield estimates of the Joint Verification Experiment (JVE) performed at the Balapan test site on September 14, 1988, for which we have excellent data, to obtain initial estimates of K and L . The explosive and tectonic moment release for this event were estimated by Walter & Patton (1990) who modeled regional seismic waveforms. We will use the results obtained by these authors for the case where the tectonic release is assumed to be due to a thrust fault mechanism. We note, however, that Walter & Patton (1990) preferred a strike-slip mechanism, since it produced better agreement for a small number of observations with predicted SV/SH-wave amplitude ratios. The explosive moment M_I estimated by Walter & Patton (1990) for a thrust geometry of tectonic moment release is 24×10^{15} Nm.

We also need the ratio of compressional and shear wave speeds at the hypocenter, which determines the relative wave excitation of $M_{xx} + M_{yy}$ as compared with that of M_{zz} . We will use the values suggested by Given and Mellman (1986) for the Balapan test site, $\alpha = 5.0$ km/s and $\beta = 2.7$ km/s, so that $\frac{\alpha^2}{\beta^2} = 3.43$. It follows from the entry in Table 1 for the JVE that K , the scale factor needed to multiply all entries in Table 1 to obtain KU_i in moment units (10^{15} Nm), is estimated as 9.46.

To obtain an estimate of L , the ratio between isotropic moment and yield, we note that the yield of the JVE was carefully measured by the Soviet Union and the U.S. using on site techniques (CORRTEX). The actual measurements are known to the two governments, but remain classified. A bilateral agreement stated that the yield of the JVE explosion was to be between 100 and 150 kt. The New York Times (1988) has stated that American and Soviet measurements gave 115 and 122 kt, and we will here use the average of these two unconfirmed values, 118.5 kt, as the yield calibration point. It follows from these values of yield and isotropic moment for the JVE that $L = 0.203$ in units of 10^{15} Nm/kt.

Table 2 and Figure 6 show our results based upon the assumption of pure thrusting for the 71 events at Balapan for which we measured the surface wave radiation pattern. The Table includes uncertainties in our derived parameters (M_I , M_0 , and Φ_S), calculated by generating a large number of realizations of the source parameters U_1, U_2, U_3 assuming normal distributions of these with the variances listed in Table 1. Figure 6 shows the range of M_I corresponding to the one-sigma distribution. In Figure 6 we have identified events

with large amounts of tectonic release based on value of the F -ratio ($F = M_0/M_I$). By this analysis, a large number of events are similar in size to the JVE, and none has much greater moment or yield. Only one event (030487) is estimated to have a yield greater than 150 kt.

Given & Mellman (1986) analyzed 37 of the 71 Balapan explosions included in this study, using similar data (but fewer stations) and a technique based on cross-correlation with synthetic long-period surface wave seismograms calculated using path structures determined by Stevens (1986), and with allowance for station corrections. The results of that study were presented in terms of absolute estimates of moments and Figure 7 shows a comparison of their isotropic moments with those of our Table 2, both estimates being based on the assumption of a pure thrusting component. The correlation between the two estimates is very good, which indicates that the two methods of calibrating the paths and estimating the parameters U_1, U_2, U_3 of the radiation pattern are robust. A factor of approximately 1.25 describes well the ratio in the absolute values of isotropic seismic moments, and this factor is due to our estimates being scaled directly to the moment determined from regional data by Walter & Patton (1990), while Given & Mellman's (1986) moments were arrived at from comparisons with synthetic teleseismic surface waves. For many events we used about twice as many stations as Given & Mellman (1986), but most of the seismic data are the same in the two studies for events that overlap. The agreement between estimates of M_0 from the two studies is also very good. There are small systematic differences between the two studies in the strike orientation of the assumed thrust component of tectonic release. We believe this is due to a different choice of normal Love wave polarity for one of the stations in Given & Mellman's (1986) study. We found that the addition of the CDSN stations for later events allowed us to constrain the strike of the radiation pattern better for all events. Figure 8 shows our estimates of the strike direction (assuming pure thrusting), plotted on a map of explosion locations obtained from inversion of P wave travel times by Lilwall & Farthing (1990). The trend is seen to be approximately northwest-southeast, nearly all these strikes falling between 130° and 150° .

Unfortunately, however, this self-consistency of strike directions, and agreement with previous studies of isotropic moment, does not mean that Table 2 and Figures 6 and 8 give correct answers. Approaches based upon the assumption of pure thrusting are called into question when we turn to the implications for yield estimation. Yields of Balapan explosions are now known with good precision, using P wave and Lg wave data and calibration via a number of Balapan explosions whose yields have been announced. Figure 9 shows the yield estimates obtained in Table 2, plotted against recent results obtained from short-period P and Lg waves by Ringdal, Marshall & Alewine (1992). The scatter is very large, about 0.2 in units of the logarithm of yield, and we have not been able to find any physical basis for selecting a subset of these explosions that gives significantly better results, that is better consistency between yields determined from surface waves (interpreted via the assumption of pure thrusting) and yields determined with high confidence from short-period seismic waves.

Fortunately, when the assumption of pure thrusting is abandoned, the apparent poor correlation shown in Figure 9 can be turned to an advantage: the information contained in yield estimates based on short-period

waves can be used to provide a constraint, separate from the surface wave radiation pattern, on the isotropic moment for each explosion. In this approach we need to estimate the overall scaling constant L relating yield and isotropic moment for Balapan explosions. Then M_I can be estimated for each event from yields as published by Ringdal *et al.* (1992). The value of the dip-slip component DS follows from equation (23), and the strike-slip component from equation (26). There are two interpretation (left-lateral, right-lateral), having strikes Φ , as determined from equation (27) and from the geometrical relationships shown in Figure 5.

We started such an approach with the values $K = 9.46$ and $L = 0.203$ as used above, but immediately found that for 50 of the 71 explosions the outcome was a value of DS from equation (23) that exceeded $K\sqrt{U_2^2 + U_3^2}$. Such high values of DS must be incorrect (see equation (26) and the geometrical relations in Figure 5), and alternative ways are needed to obtain the unknown scaling factors K and L . Fortunately, it is only the ratio $\frac{L}{K}$ that is needed, to interpret radiation pattern parameters (U_1, U_2, U_3) in terms of a strike direction Φ , and a ratio of dip-slip to strike-slip strengths, DS/SS . In effect, this means that we are using only the relative isotropic moments estimated from P and Lg waves. Two very different ways are suggested, to revise our estimates of the ratio $\frac{L}{K}$ (which equalled about 0.0215 in the pure thrusting approach above).

First, we can select those explosions for which $U_1 \gg \sqrt{U_2^2 + U_3^2}$, and assume in these cases that there is negligible tectonic release. Then $U_1 = \frac{2\theta^2}{\alpha^2} \frac{L}{K} Y$ for these events, and $\frac{L}{K}$ can be obtained from the slope of U_1 against a good yield estimate \hat{Y} such as that of Ringdal *et al.* (1992). There are 6 events for which $U_1 > 4.8\sqrt{U_2^2 + U_3^2}$ and the surface wave observations are of high quality. Figure 10 shows U_1 versus \hat{Y} for these events: the fit to a straight line is quite good, and the resulting value of $\frac{L}{K}$ is 0.0132.

A second way to estimate $\frac{L}{K}$ is to impose the requirement that $-1 \leq \cos[2(\Phi_S - \Phi_U)] \leq 1$, or, in Figure 5, that the origin must lie outside a circle with radius DS centered on (KU_2, KU_3) . (Two tangents can then be drawn from the origin to the circle. They have the same length, $|SS|$, and correspond to left-lateral and right-lateral solutions.) In terms of $\frac{L}{K}$ this requires that

$$-1 \leq \cos[2(\Phi_S - \Phi_U)] = \frac{(\frac{L}{K})\hat{Y} - \frac{\alpha^2}{2\beta^2}U_1}{(\frac{2\alpha^2}{\beta^2} - 2)\sqrt{U_2^2 + U_3^2}} \leq 1 \quad (30)$$

which should be valid for all 71 explosions.

Note that

$$\frac{DS}{SS} = \cos \delta \tan \lambda = \cot[2(\Phi_U - \Phi_S)]$$

which we can estimate from (U_1, U_2, U_3, \hat{Y}) once we have settled on a value for $\frac{L}{K}$. To the extent that we find DS/SS is large, then, since $|\cos \delta| \leq 1$, λ must be near 90° and pure thrusting would be inferred from the data.

Figure 11 shows examples of the set of cosine values determined from equation (30) that result from a few different choices of the $\frac{L}{K}$. Fortunately, the sets of cosine values (and associated estimates of strike direction) are not very sensitive to choices in the range $0.0125 \leq \frac{L}{K} \leq 0.0175$, which includes the value 0.0132 we obtained via the analysis of Figure 10. There is, however, reason to exclude values around 0.0215 and above (associated with interpretations such as that of Given & Mellman (1986), based on a pure thrusting

assumption). Note from Figure 11f that for smaller values of $\frac{L}{K}$ there are several negative cosine values. For the associated explosions, such values would indicate normal faulting rather than a thrusting component. To the extent that normal faulting at Balapan is unlikely, we thus have an additional constraint on the plausible range of values of $\frac{L}{K}$. In subsequent analysis we choose to work with the value $\frac{L}{K} = 0.015$, noting where necessary how dependent (or not) our conclusions are on this particular choice.

Thus, Figure 12 shows the strike directions plotted as a map for the 34 explosions with solutions based on high quality surface wave data, corresponding to Figure 11. We show here the left-lateral solutions, and note that these strike directions are significantly different from those of Figure 8. For these 34 explosions, Table 3 gives numerical values for both left- and right-lateral solutions, and values also for the ratio $DS/|SS|$ of dip-slip to strike-slip components. The right-lateral solutions generally show strikes in the North-South direction, and we believe the left-lateral solutions are to be preferred, because the resulting strike directions (Figure 12) conform far better with the orientations of mapped faults at Balapan. Such faults are indicated in part in Figure 13, which also shows the radiation pattern of SH waves observed from the nuclear explosion of 1987 August 2, as determined from SH body waves observed over a local network of three-component stations operated on and near the Balapan test site. Figure 13 also shows the trace of the Kalba-Chingiz deep regional fault, striking at 115° very near the 1987 explosion, for which our analysis (Table 3) is in good agreement, indicating a tectonic release with inferred left-lateral motion in an oblique thrust, on a fault striking at 110° .

Figure 14 shows the left- and right-lateral strike directions and the ratio $DS/|SS|$ of dip-slip to strike-slip components, corresponding to three values of the ratio of scaling constants $\frac{L}{K}$ (compare with Figure 11g, f, and e). It may be seen that the strike directions are insensitive to the ratio of scaling constants in the range 0.0125 to 0.0175, but that $DS/|SS|$ is quite sensitive. This latter ratio is large and positive for only a few events, the set of such events being different for different values of $\frac{L}{K}$. We may conclude that pure thrusting is rare, as the mode of tectonic release at Balapan. For a few cases the ratio $DS/|SS|$ is large and negative, apparently indicating normal faulting and extension. However, such cases are spurious in that they arise when surface wave radiation is almost isotropic, so that DS and $|SS|$ are very small, and the value of $\frac{L}{K}$ is slightly greater than that suggested by the study of isotropic events. (The four most negative values of $DS/|SS|$ in Table 3 correspond to events used, because of their isotropic nature, in Figure 10.)

COMMENTS ON SURFACE WAVES AS A BASIS FOR YIELD ESTIMATION

Having determined that strikes in the range $90^\circ - 120^\circ$ are preferred over the $130^\circ - 150^\circ$ directions of previous studies (e.g. Given & Mellman 1986, and our Figure 8), it is of interest to see whether the assumption of a fixed strike direction can be made the basis of an improved set of yield estimates based upon surface waves. The yield estimate, from equations (24) and (28), is

$$\hat{Y} = \left(\frac{L}{K}\right)^{-1} \left[\frac{\alpha^2}{2\beta^2} U_1 + \left(\frac{3\alpha^2}{\beta^2} - 2\right) (U_2 \cos 2\Phi_S + U_3 \sin 2\Phi_S) \right] \quad (31)$$

which depends on scaling constants only via the ratio $\frac{L}{K}$.

Taking Φ_S fixed as 110° , for the 38 explosions for which surface wave quality is high, Figure 15 compares the yield estimate of equation (31) with the yield estimate of Ringdahl *et al.* (1992) based on P and Lg . The scatter is very high – as bad as Figure 9. One point in Figure 15, with yield (from P and Lg) of 79 kt, has \hat{Y} less than 3 kt, according to equation (31) with strike fixed at 110 degrees. For this event, 120284, U_1 is small and the strike (from Table 3) is 28 degrees greater than the fixed direction assumed for Figure 15.

The conclusion to be drawn from this analysis is that the orientation of tectonic moment release at Balapan is so variable that without additional information about individual explosions, we are not in a position to provide a high precision yield estimate based only on the teleseismic surface wave observations.

In addition, there are certain events for which even allowing for variability in the orientation of tectonic release does not reconcile the surface wave observations (U_1, U_2, U_3) with estimates of yield based on P and Lg waves. If we compare the events 122884 and 111587, which have very similar $m_b(Lg)$ (5.98 and 5.97) and $m_b(P)$ (6.00 and 5.98), we find that they produced surface waves with very different amplitudes. Both events have very small Love waves and correspondingly small F -ratios (0.13 and 0.16). Figure 16 shows the results from cross correlating the Rayleigh and Love waves for these two events at all stations that are in common for the two events. This shows that the surface waves for 122884 indeed are about half as large as those for 111587 for most stations, and that this factor is directly evident in the data and not introduced artificially by our analysis. Different double couple geometries for the tectonic release for these events cannot reconcile these observations, since the non-axisymmetric part of the radiation pattern is small. We suggest that it is possible that our assumption that the tectonic release has a single double couple mechanism is incorrect for at least some events. There is no clear reason why slip on just one single fault should be triggered by the explosion (Aki *et al.*, 1969; Aki & Tsai, 1972; Wallace *et al.*, 1983), and if two faults of different orientations experience slip, the summed moment tensor will in general not be a double couple, even though the trace of the tensor will be zero. Similarly, the shattering model for tectonic release (Archambeau, 1972; Stevens, 1980; Day *et al.*, 1987) contains no physical requirement for the strain release to have double couple geometry. In fact, Day *et al.* (1987) present the result

$$M_{ij} = \sigma_{ij} R^3 \frac{20\pi\alpha^2}{9\alpha^2 - 4\beta^2}$$

for the deviatoric moment tensor due to stress relaxation in a rock with prestress σ_{ij} in a shattered zone of radius R . In a medium in which the shear modulus μ suddenly is decreased, while the bulk modulus remains more or less unchanged, there is little reason to believe that the isotropic part of the tectonic release would be as significant as the deviatoric part.

Under the condition of axisymmetric prestress, Day *et al.* (1987) show that teleseismic Rayleigh waves are reversed (the tectonic moment release is greater than that due to the explosion) if the tectonic stress exceeds about 100 bars. This is a plausible deviatoric stress level at several hundred meters depth in the crust. Smaller, non-axisymmetric stresses (but in general not with double couple geometry) could also be responsible for the tectonic release in some Balapan explosions.

CONCLUSION

Using a new empirical approach, we have determined relative source parameters for 71 explosions at the Balapan test site. The parameters, three for each event, describe and quantify the long-period Love and Rayleigh wave radiation from the explosions. Simultaneously we have determined parameters that calibrate the propagation paths from the test site to 29 seismic stations outside the former Soviet Union. Together, the source and path parameters provide good fits to the measurements of surface wave amplitudes for the events.

By initially interpreting the radiation patterns in terms of an explosive and a double couple source with thrust mechanism, and by calibrating the results with an independently estimated explosive moment and an unofficial yield estimate for the Joint Verification Experiment, we have obtained moments and yields for each explosion. An analysis based on these traditional assumptions of the geometry of tectonic release does not result in a good correlation between our estimated yields and isotropic moments with $m_b(Lg)$ or $m_b(P)$, which are both known to correlate well with explosive yield.

We have found a partial solution to this inconsistency by relaxing the assumption that all events share the same double couple dip and rake. By allowing for variability in the dip-slip/strike-slip excitation ratio, as well as in the strike, we can reconcile the surface wave data with P and Lg data for most events. More importantly, this analysis leads to significantly different estimates of fault strike than have been previously presented for the Balapan test site, but which appear to be in better agreement with geological observations and one locally determined radiation pattern.

The validity of our interpretations may be testable as more of the locally recorded data from the former Soviet Union become available. Further study would be of interest if additional yield and geological information became available. This would allow us to remove the uncertainty involved in using the short-period yield estimates instead of the measured yields. We note that the teleseismic radiation from some events appears to be inconsistent with the double couple model for tectonic release. Local seismic and geodetic data may help explain what the physical mechanism is that can explain this observation. It would also be of interest to apply the empirical approach to events at the United States nuclear test site in Nevada.

Underground nuclear tests are in many ways ideally suited for analysis using the empirical method presented here. Several simplifying approximations that are valid for very shallow sources are in general not valid for earthquake sources. However, the empirical approach may be applicable to clusters of small earthquakes in, for example, an aftershock zone. A propagation operator which is frequency dependent must be substituted in place of the constant factor determined in the present study, and an additional operator which includes the variability of source excitation with source depth must be added. With a sufficient number of events in a cluster, and with one or several calibration events for which the source parameters are known, this approach may prove useful for source parameter retrieval for small events.

REFERENCES

- Aki, K. & Richards, P. G., 1980. *Quantitative Seismology: Theory and methods*, W. H. Freeman, San Francisco.
- Aki, K., Reasonberg, P., De Fazio, T. & Tsai, Y. B., 1969. Near-field and far-field seismic evidence for triggering of an earthquake by the Benham explosion, *Bull. Seism. Soc. Am.*, 59, 2197-2207.
- Aki, K. & Tsai, Y., 1972. The mechanism of Love wave excitation by explosive sources, *J. Geophys. Res.*, 77, 1452.
- Archambeau, C. B., 1972. The theory of stress wave radiation from explosions in prestressed media, *Geophys. J. R. Astron. Soc.*, 29, 329-366.
- Brune, J. N., & Pomeroy, P., 1962. Surface wave radiation for underground nuclear explosions and small magnitude earthquakes, *J. Geophys. Res.*, 68, 5005-5028.
- Day, S. M., Cherry, T., Rimer, N. & Stevens, J. L., 1987. Nonlinear model of tectonic release from underground explosions, *Bull. Seism. Soc. Am.*, 77, 996-1016.
- Given, J. W. & Mellman, G. R., 1986. Estimating explosions and tectonic source parameters of underground nuclear explosions from Rayleigh and Love wave observations, Final Report-Part 1, AFGL-TR-86-0171(I), 70 pages, ADB110040.
- Goforth, T., Rafipour, B. & Herrin, E., 1982. Anomalous Rayleigh waves from nuclear explosions in the USSR Shagan River test site, in AFOSR Semiannual Technical Report edited by E. Herrin and T. Goforth, Geophysical Laboratory, Southern Methodist University.
- Gutenberg, B., 1945. Amplitudes of surface waves and magnitudes of shallow earthquakes, *Bull. Seism. Soc. Am.*, 35, 3-12.
- Helle, H. B. & Rygg, E., 1984. Determination of tectonic release from surface waves generated by nuclear explosions in Eastern Kazakhstan, *Bull. Seism. Soc. Am.*, 74, 1883-1898.
- Lilwall, R. C. & Farthing, J., 1990. Joint epicentre determination of Soviet underground nuclear explosions 1973-89 at the Semipalatinsk test site, *AWRE Report No. O 12/90*, H. M. Stationery Office, London.
- Marshall, P. D. & Basham, P. W., 1972. Discrimination between earthquakes and underground explosions employing an improved M_S scale, *Geophys. J. R. Astron. Soc.*, 28, 431-458.
- Massé, R. P., 1981. Review of seismic source models for underground nuclear explosions, *Bull. Seism. Soc. Am.*, 71, 1249-1268.
- Murphy, J. R., O'Donnell, A. & Barker, B. W., 1987. An analysis of the effects of tectonic release on the long-period surface waves observed from explosions at NTS (abstract), *Seism. Res. Lett.*, 58, 18.
- Nelder, J. A. & Mead R., 1965. A simplex method for function minimization, *Computer Journal*, 7, 308-313.
- New York Times, article by M. R. Gordon, October 30, 1977, page A15, 1977.
- North, R. G. & Fitch, T. J., 1982. Surface wave generation by underground nuclear explosions, Semiannual Technical Summary, March 31, No. ESD-TR-81-84 (Lincoln Laboratory, MIT, Cambridge, Mass.), 47-55, ADA109184/2.

- Press, F., & Archambeau, C., 1962. Release of tectonic strain by underground nuclear explosions, *J. Geophys. Res.*, 67, 337-343.
- Richards, P. G. & Zavales, J., 1990. Seismic discrimination of nuclear explosions, *Annu. Rev. Earth Planet. Sci.*, 18, 257-86.
- Richter, C. F., 1935. An instrumental earthquake magnitude scale, *Bull. Seism. Soc. Am.*, 25, 1-32.
- Ringdal, F., Marshall, P. D. & Alewine, R., 1992. Seismic yield determination of Soviet underground nuclear explosions at the Shagan River test site, *Geophys. J. Int.*, 109, 65-77.
- Rygg, E., 1979. Anomalous surface waves from underground explosions, *Bull. Seism. Soc. Am.*, 69, 1995-2000.
- Stevens, J. L., 1980. Seismic radiation from the sudden creation of a spherical cavity in an arbitrarily prestressed elastic medium, *Geophys. J. R. Astron. Soc.*, 61, 303-328.
- Stevens, J. L., 1986. Estimation of scalar moments from explosion-generated surface waves, *Bull. Seism. Soc. Am.*, 76, 123-151.
- Stevens, J. L. & Day, S. M., 1985. The physical basis of $m_b:M_S$ and variable frequency magnitude methods for earthquake/explosion discrimination, *J. Geophys. Res.*, 90, 3009-3020.
- Toksöz, M. N., Ben-Menahem, A. & Harkrider, D. G., 1965. Determination of source parameters of explosions and earthquakes by amplitude equalization of seismic surface waves; release of tectonic strain by underground nuclear explosions and mechanisms of earthquakes, *J. Geophys. Res.*, 70, 907-922.
- Wallace, T. C., Helmberger, D. V. & Engen, G. R., 1983. Evidence for tectonic release from underground nuclear explosions in long-period *P*-waves, *Bull. Seism. Soc. Am.*, 73, 593-613.
- Walter, W. R. & Patton, H. J., 1990. Tectonic release from the Soviet Joint Verification Experiment, *Geophys. Res. Lett.*, 17, 1517-1520.

TABLE 1. Basic Source Parameters

Event	U_1	σ_1	U_2	σ_2	U_3	σ_3	N	Q
052977								
062977								
090577	-0.211	0.058	-0.052	0.034	-0.175	0.038	5	0.4137
102977	-0.217	0.062	0.072	0.037	-0.207	0.031	5	0.3643
113077	0.189	0.097	0.051	0.027	-0.189	0.036	5	0.7224
061178	0.750	0.071	0.000	0.053	-0.203	0.052	5	0.6068
070578	0.074	0.057	-0.124	0.062	-0.198	0.030	6	0.9799
082978	0.033	0.046	0.058	0.032	-0.314	0.031	9	0.6318
091578	0.489	0.050	0.030	0.046	-0.237	0.032	10	0.9605
110478	0.060	0.038	0.058	0.020	-0.349	0.027	16	0.9611
112978	0.477	0.040	0.109	0.019	-0.226	0.023	13	0.2906
020179	-0.025	0.016	0.021	0.006	-0.064	0.011	7	0.8259
062379	0.435	0.050	0.096	0.027	-0.583	0.037	15	0.0174
070779	-0.841	0.089	0.178	0.037	-0.893	0.070	12	0.8623
080479	0.757	0.053	-0.016	0.024	-0.484	0.034	15	0.9992
081879	-0.185	0.043	0.081	0.018	-0.448	0.030	14	0.3996
102879	0.683	0.057	0.267	0.035	-0.336	0.037	12	0.9902
120279	0.862	0.070	-0.014	0.022	-0.181	0.041	13	0.6222
122379	0.376	0.044	-0.007	0.011	-0.216	0.025	16	0.9869
042580								
061280	0.123	0.025	0.028	0.009	-0.055	0.026	9	0.9412
062980	0.156	0.022	0.050	0.009	-0.096	0.017	12	0.9611
091480	0.125	0.067	0.120	0.028	-0.877	0.050	16	0.5689
101280	0.706	0.052	0.073	0.018	-0.304	0.033	16	0.9846
121480	0.443	0.035	-0.058	0.016	-0.375	0.026	15	0.9998
122780	-0.305	0.044	0.064	0.023	-0.274	0.031	12	0.3838
032981	0.029	0.033	0.083	0.012	-0.214	0.020	12	0.9855
042281	0.678	0.064	-0.005	0.021	-0.255	0.033	13	0.9503
052781	0.045	0.021	-0.014	0.022	-0.035	0.014	8	0.6340
091381	0.852	0.087	0.004	0.033	-0.424	0.053	10	0.9527
101881	0.693	0.088	0.104	0.023	-0.271	0.078	11	0.9992
112981	0.372	0.059	0.044	0.029	-0.112	0.051	12	0.9829
122781	0.668	0.067	0.134	0.015	-0.367	0.043	15	0.9995
042582	0.585	0.065	0.061	0.016	-0.323	0.040	16	0.9990
070482								
083182	0.186	0.059	0.018	0.051	-0.033	0.065	7	0.9794
120582	0.540	0.053	0.045	0.017	-0.455	0.044	17	0.5336
122682	-0.077	0.073	0.016	0.028	-0.218	0.039	5	0.3681
061283	1.063	0.082	0.120	0.027	-0.282	0.055	25	0.9999
100683	0.858	0.068	-0.189	0.038	-0.165	0.088	16	0.8694
102683	0.743	0.071	0.054	0.034	-0.591	0.076	17	0.9995
112083								
021984	0.654	0.075	-0.105	0.057	-0.085	0.075	15	0.9756
030784	0.143	0.028	-0.002	0.013	-0.183	0.021	14	0.9782
032984	0.479	0.052	-0.034	0.022	-0.271	0.050	15	0.9995
042584	0.921	0.098	0.138	0.042	-0.027	0.062	15	0.9800
052684								
071484	0.933	0.074	0.114	0.021	-0.307	0.055	26	0.9995
091584								
102784	0.616	0.049	0.119	0.016	-0.352	0.042	23	0.0002
120284	-0.071	0.048	0.264	0.028	-0.394	0.040	19	0.9944
121684	0.932	0.061	0.145	0.022	-0.436	0.045	21	0.9998
122884	0.547	0.041	-0.059	0.016	-0.050	0.024	19	0.0380
021085	0.832	0.062	0.036	0.026	-0.296	0.043	17	0.9961
042585	0.505	0.052	0.057	0.029	-0.152	0.038	15	0.6535
061585	0.369	0.037	-0.022	0.017	-0.257	0.041	20	0.8770
063085	0.508	0.042	0.108	0.014	-0.207	0.057	19	0.9999
072085	0.362	0.035	0.069	0.013	-0.297	0.040	23	1.0000
031287	0.307	0.036	0.017	0.009	-0.057	0.026	17	0.9994
040387	1.363	0.090	0.088	0.021	-0.445	0.063	26	0.9983
041787	0.362	0.069	0.022	0.024	-0.419	0.050	18	0.9999
062087	0.444	0.032	-0.023	0.011	-0.189	0.020	21	0.7475
080287	0.076	0.048	-0.067	0.015	-0.385	0.034	19	0.9365
111587	1.189	0.064	0.044	0.026	-0.217	0.028	21	0.9994
121387	0.761	0.050	0.070	0.013	-0.379	0.029	24	0.9995
122787	0.446	0.041	0.018	0.018	-0.318	0.030	20	1.0000
021388	0.800	0.043	0.149	0.012	-0.206	0.018	29	0.9288
040388	0.782	0.050	0.016	0.013	-0.359	0.028	29	1.0000
050488	0.775	0.122	0.104	0.037	-0.432	0.127	10	0.8669
061488	0.037	0.010	0.009	0.006	-0.022	0.007	9	0.6461
091488	0.933	0.052	0.099	0.013	-0.281	0.024	29	0.9716
111288	0.031	0.028	-0.018	0.005	-0.096	0.014	11	0.6503
121788	0.635	0.059	0.093	0.020	-0.536	0.043	18	0.9976
012289	0.867	0.056	0.026	0.014	-0.283	0.026	21	0.9924
021289	0.955	0.071	0.075	0.027	0.016	0.060	20	0.7645
070889	0.314	0.028	0.073	0.007	-0.109	0.013	27	0.9974
090289	0.124	0.013	0.011	0.005	-0.057	0.011	14	0.9874
101989	1.119	0.062	0.105	0.019	-0.014	0.038	24	0.8153

TABLE 2. Derived Source Parameters

Event	M_I	$\sigma(M_I)$	M_0	$\sigma(M_0)$	Φ_S	$\sigma(\Phi_S)$	F	\hat{Y}	$m_b(Lg)$	$m_b(P)$
052977										5.75
062977										5.20
090577	2.0	1.5	3.4	0.7	126.7	5.4	1.73	10	5.879	5.73
102977	3.0	1.4	4.2	0.6	144.6	4.9	1.38	15	5.757	5.56
113077	8.9	1.9	3.7	0.7	142.5	4.1	0.42	44	5.753	5.89
061178	18.2	1.9	3.8	1.0	135.0	7.9	0.21	90	5.755	5.83
070578	8.1	1.5	4.4	0.8	119.0	6.7	0.54	40	5.794	5.77
082978	10.0	1.2	6.0	0.6	140.2	2.8	0.60	50	6.010	5.90
091578	15.0	1.2	4.5	0.6	138.7	5.4	0.30	74	5.908	5.89
110478	11.5	1.0	6.7	0.5	139.7	1.7	0.58	57	5.690	5.56
112978	15.2	0.9	4.7	0.4	147.8	2.3	0.31	75	5.971	5.96
020179	1.6	0.4	1.3	0.2	144.0	3.0	0.80	8		5.29
062379	24.6	1.4	11.2	0.7	139.7	1.3	0.45	122	6.064	6.16
070779	13.4	2.4	17.2	1.3	140.6	1.2	1.28	66	5.966	5.84
080479	26.7	1.4	9.2	0.6	134.1	1.4	0.34	132	6.100	6.13
081879	10.5	1.1	8.6	0.5	140.1	1.2	0.82	52	6.126	6.13
102879	23.8	1.4	8.1	0.7	154.2	2.4	0.34	118	6.051	5.98
120279	19.4	1.6	3.4	0.8	132.8	3.8	0.18	96	5.929	5.99
122379	12.5	1.0	4.1	0.5	134.0	1.5	0.33	62	6.039	6.13
042580										5.45
061280	3.8	0.8	1.2	0.4	149.7	8.9	0.30	19	5.627	5.52
062980	5.7	0.6	2.0	0.3	148.9	3.3	0.36	28	5.706	5.69
091480	28.3	1.8	16.7	0.9	138.9	0.9	0.59	140		6.21
101280	20.8	1.2	5.9	0.6	141.7	1.9	0.29	103	5.927	5.88
121480	18.4	1.0	7.2	0.5	130.6	1.3	0.39	91	5.936	5.93
122780	3.4	1.1	5.3	0.6	141.5	2.3	1.56	17	5.933	5.87
032981	7.3	0.8	4.3	0.4	145.6	1.7	0.59	36	5.548	5.49
042281	18.6	1.4	4.8	0.6	134.4	2.5	0.26	92	5.929	5.94
052781	1.9	0.6	0.7	0.3	124.0	19.2	0.39	9	5.456	5.30
091381	26.4	2.1	8.0	1.0	135.3	2.3	0.30	131	6.108	6.06
101881	19.9	2.6	5.5	1.4	145.5	4.4	0.28	98	5.981	6.00
112981	9.6	1.7	2.3	0.9	145.8	11.6	0.24	47	5.580	5.62
122781	22.4	1.6	7.4	0.8	145.0	1.5	0.33	111	6.075	6.16
042582	19.3	1.6	6.2	0.7	140.4	1.6	0.32	95	6.072	6.03
070482										6.08
083182	4.1	1.5	0.7	0.8	149.4	40.9	0.17	20		5.20
120582	22.3	1.6	8.6	0.8	137.8	1.2	0.39	110	5.996	6.08
122682	5.2	1.6	4.1	0.7	137.1	3.9	0.79	26	5.665	5.58
061283	26.3	2.0	5.8	1.0	146.6	3.3	0.22	130	6.072	6.02
100683	21.4	2.2	4.7	1.2	110.6	26.4	0.22	106	5.868	5.95
102683	29.7	2.6	11.2	1.4	137.6	1.7	0.38	147	6.016	6.04
112083										5.33
021984	14.6	2.1	2.6	1.1	109.5	51.0	0.17	72	5.725	5.77
030784	7.8	0.8	3.5	0.4	134.6	2.0	0.45	38	5.680	5.56
032984	15.9	1.7	5.2	0.9	131.4	2.5	0.33	79	5.902	5.86
042584	19.1	2.0	2.7	0.4	174.6	11.9	0.14	94	5.867	5.90
052684										6.01
071484	24.8	1.9	6.2	1.0	145.2	2.6	0.25	123	6.054	6.10
091584										5.04
102784	21.0	1.4	7.0	0.7	144.4	1.6	0.33	104	6.098	6.19
120284	12.9	1.4	9.0	0.7	151.9	1.9	0.69	64	5.880	5.77
121684	28.8	1.7	8.7	0.8	144.2	1.6	0.30	142	6.043	6.12
122884	11.2	0.9	1.5	0.4	110.2	27.2	0.13	55	5.980	6.00
021085	22.3	1.6	5.6	0.8	138.5	2.4	0.25	110	5.806	5.83
042585	13.0	1.4	3.1	0.7	145.3	5.8	0.24	64	5.859	5.84
061585	13.6	1.4	4.9	0.8	132.6	2.0	0.36	67	5.987	6.05
063085	15.2	1.6	4.4	0.9	148.8	4.3	0.29	75		5.92
072085	14.9	1.3	5.8	0.7	141.5	1.5	0.39	74	5.865	5.89
031287	6.7	0.9	1.1	0.5	143.5	9.7	0.17	33	5.218	5.31
040387	35.6	2.4	8.6	1.2	140.6	1.6	0.24	176	6.063	6.12
041787	18.3	1.9	7.9	0.9	136.5	1.7	0.43	91	5.910	5.92
062087	12.9	0.8	3.6	0.4	131.6	1.6	0.28	63	5.971	6.03
080287	12.9	1.2	7.4	0.6	130.1	1.2	0.58	64	5.871	5.83
111587	25.9	1.3	4.2	0.5	140.7	3.4	0.16	128	5.975	5.98
121387	23.8	1.1	7.3	0.5	140.2	1.0	0.31	117	6.082	6.06
122787	16.7	1.1	6.0	0.6	136.6	1.7	0.36	83	6.042	6.00
021388	20.5	0.9	4.8	0.3	153.0	1.7	0.23	101	6.042	5.97
040388	23.4	1.2	6.8	0.5	136.3	1.0	0.29	115	6.063	5.99
050488	25.8	4.0	8.4	2.3	141.7	3.6	0.33	127	6.046	6.09
061488	1.3	0.3	0.5	0.1	145.4	8.0	0.35	7		4.80
091488	24.0	1.1	5.6	0.4	144.7	1.4	0.24	119	5.969	6.03
111288	3.4	0.6	1.8	0.2	129.8	1.6	0.54	17		5.20
121788	26.5	1.6	10.3	0.8	139.9	1.2	0.39	131	5.801	5.80
012289	22.5	1.2	5.4	0.5	137.7	1.3	0.24	111	5.960	6.10
021289	17.8	1.5	1.5	0.6	6.1	18.0	0.08	88	5.791	5.86
070889	9.0	0.6	2.5	0.2	151.8	2.2	0.28	45	5.418	5.55
090289	3.7	0.4	1.1	0.2	140.6	2.9	0.29	18		4.94
101989	21.3	1.1	2.0	0.4	176.2	9.7	0.09	105	5.789	5.86

TABLE 3. Inferred strike directions

Event	left-lateral (degrees)	right-lateral (degrees)	$DS/ SS $
110478	109.73	169.74	0.58
080479	109.54	158.59	0.87
102879	130.57	177.92	0.92
101280	106.21	177.27	0.34
121480	105.30	155.94	0.82
032981	117.42	173.77	0.67
042281	97.29	171.55	0.28
112981	87.16	204.43	-0.52
122781	138.32	151.70	4.20
061283	109.00	184.11	0.27
102683	99.37	175.87	0.24
021984	31.66	187.40	-2.22
030784	110.66	158.64	0.90
032984	101.13	161.63	0.57
042584	88.54	80.62	-7.19
071484	112.40	177.93	0.46
120284	137.51	166.26	1.82
121684	108.38	179.97	0.33
021085	77.44	199.49	-0.63
063085	121.18	176.33	0.70
072085	111.83	171.19	0.59
040387	90.80	190.39	-0.17
041787	106.73	166.23	0.59
080287	110.39	149.78	1.22
111587	73.06	208.29	-1.01
121387	114.38	166.08	0.79
122787	132.26	140.94	6.55
021388	127.47	178.47	0.81
040388	109.92	162.69	0.76
091488	100.33	189.12	0.02
121788	93.78	186.07	-0.04
012289	101.90	173.44	0.33
070889	91.65	212.01	-0.59
090289	74.31	206.81	-0.92

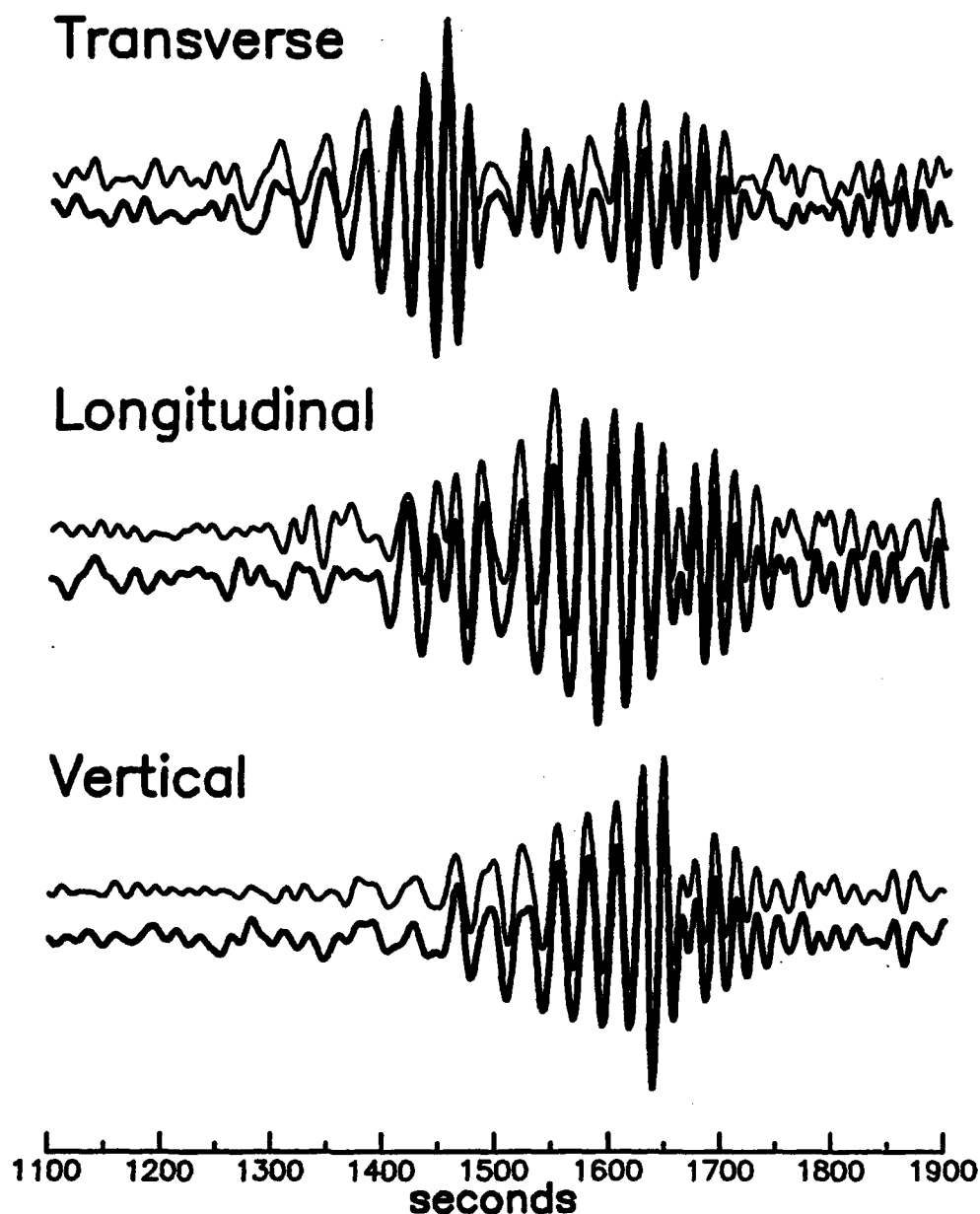


Figure 1. Surface waves from two explosions at the Balapan nuclear test site recorded at Matsushiro (MAJO) in Japan at a distance of 44° . In each pair, the bottom (thicker) seismogram corresponds to the August 4, 1979 explosion. The top trace corresponds to the April 3, 1988 explosion. The traces have been scaled by arbitrary factors in order to maximize the correlation in each trace pair.



Figure 2. Azimuthal equidistant projection centered on the Kazakhstan test site, showing the geographical distribution of 29 stations used in the analysis.

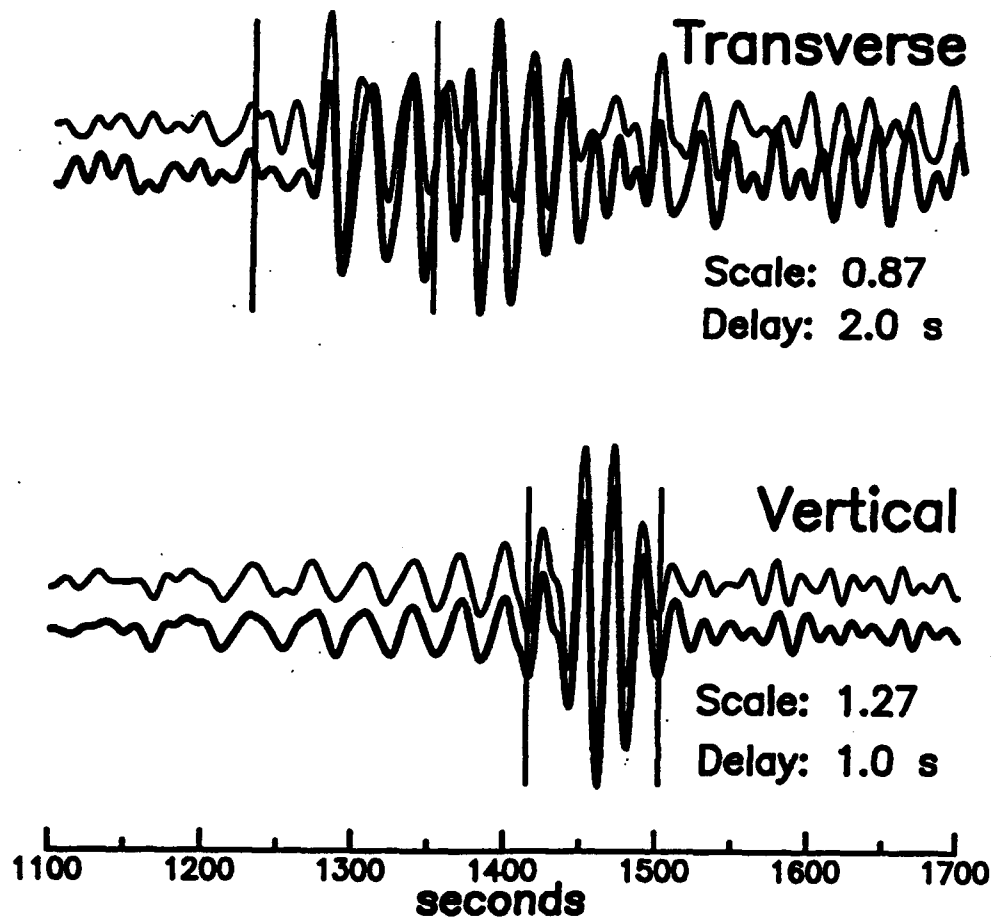
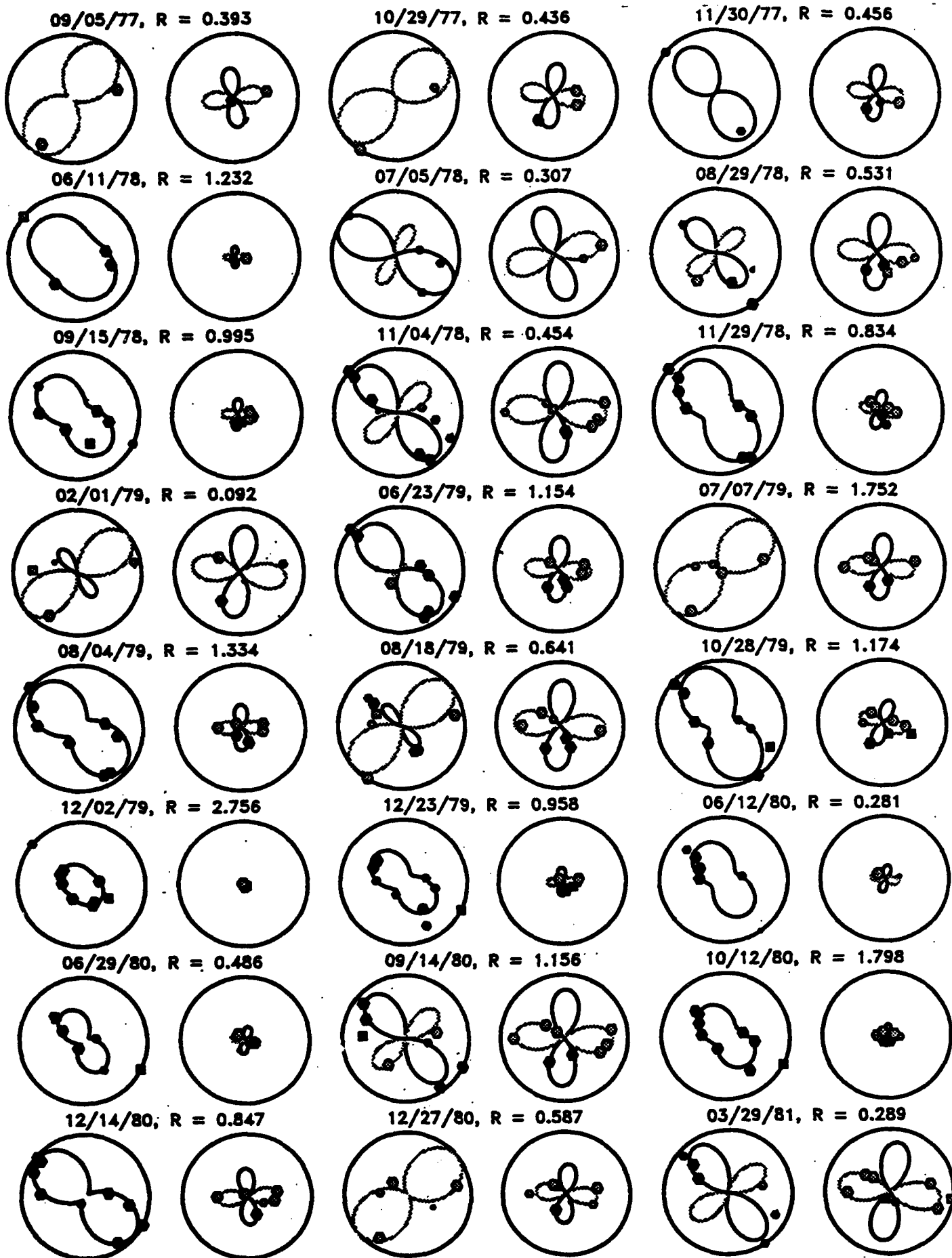
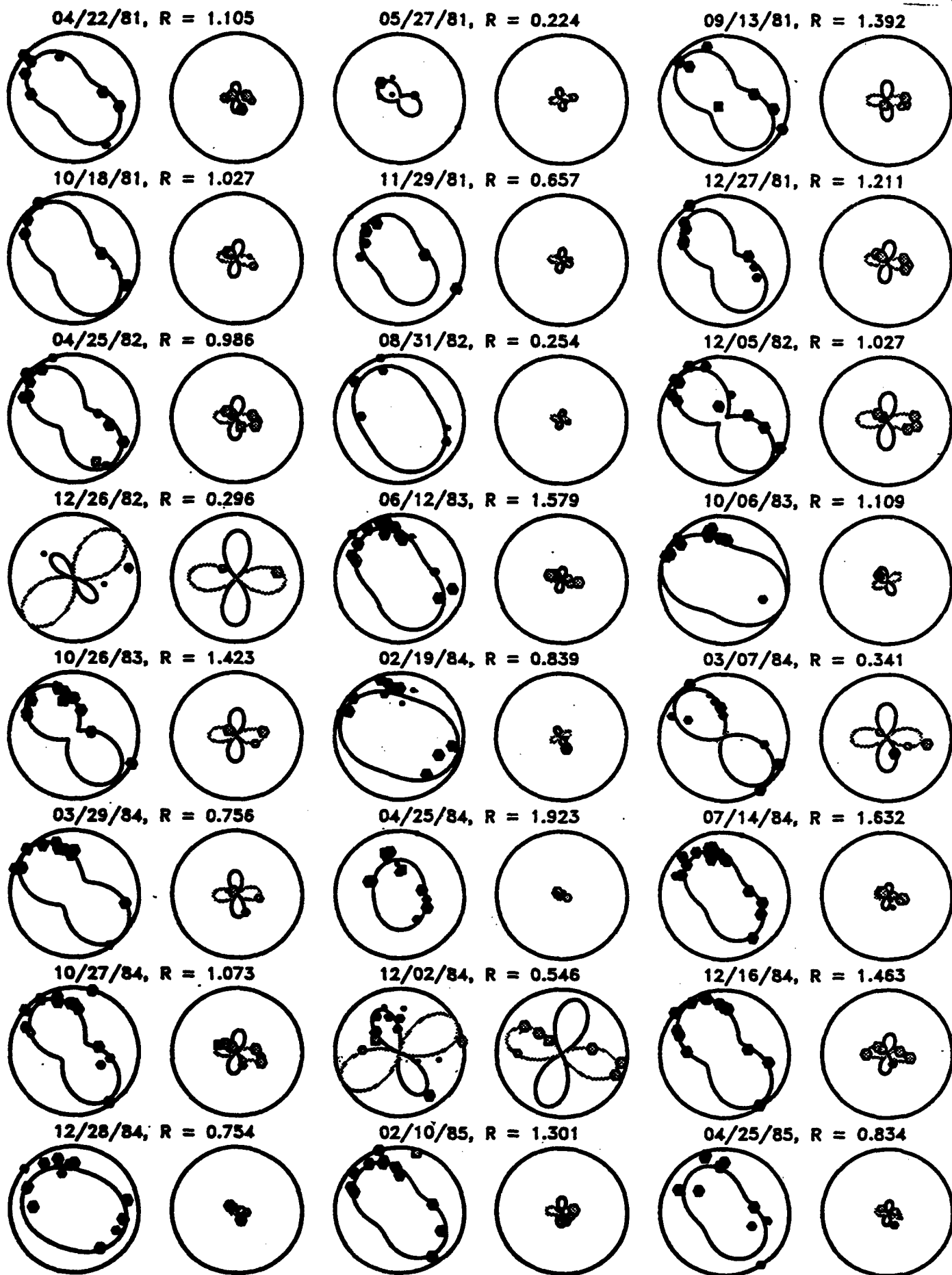
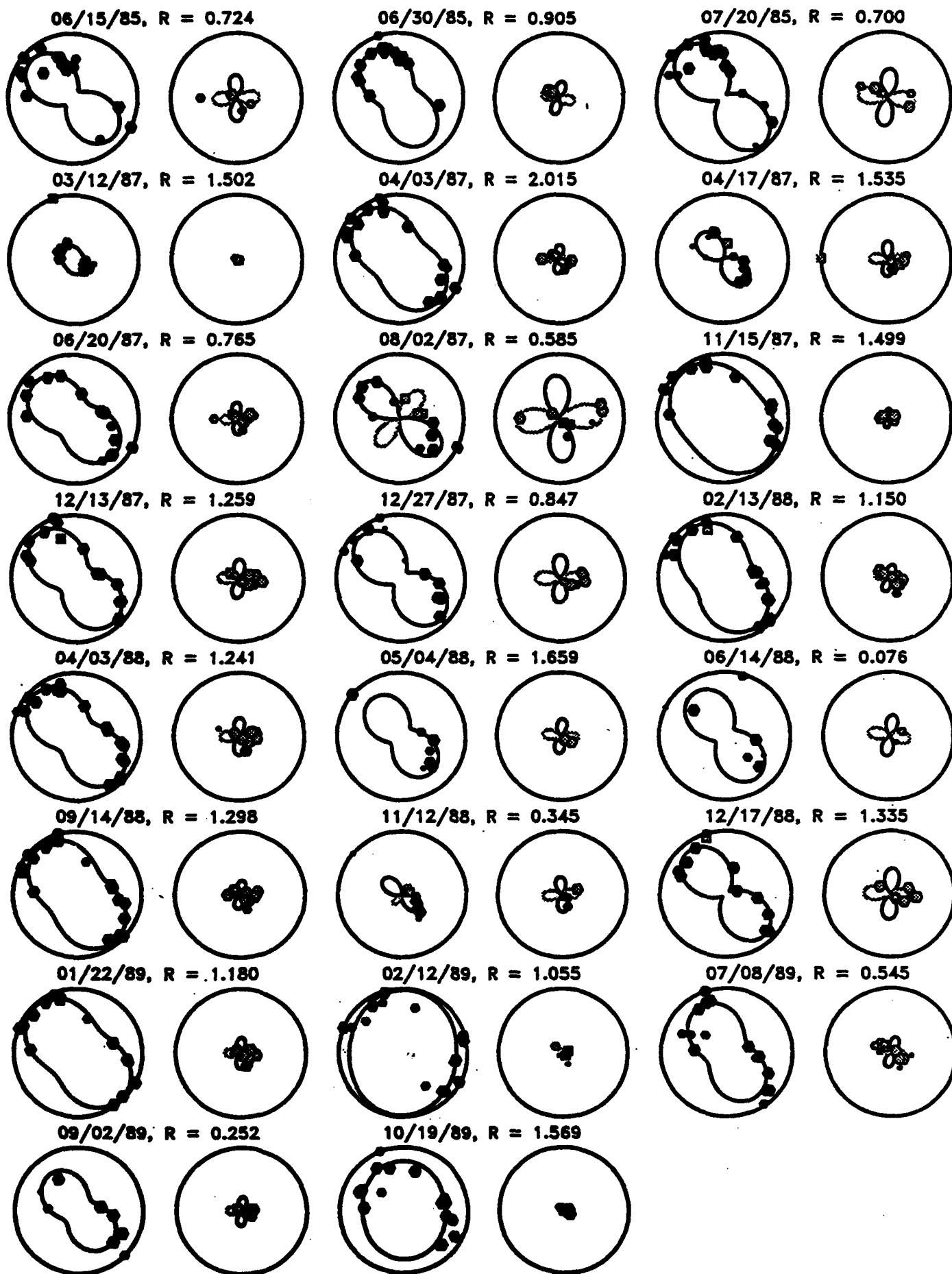


Figure 3. Correlation of vertical and transverse seismograms for the Balapan Joint Verification Experiment (September 14, 1988) with the reference seismograms for KONO. In each pair, the bottom (thicker) seismogram corresponds to the JVE. The upper (thinner) seismogram, is the reference seismogram, which for KONO corresponds to the event of September 14, 1980. The correlation windows are shown with vertical bars, and the time delay and scaling factor that have been applied to the reference seismograms to achieve maximum correlation are given.

Figure 4. Comparison of observed and predicted radiation amplitudes for Rayleigh (left circle) and Love (right circle) waves for the 71 events for which we obtained results. The solid lines and symbols correspond to positive amplitudes, and the radial distance is proportional to the absolute value of the radiation amplitude. The radial scale is different for each event, and the dimension of each radiation pattern should be multiplied by the factor R to obtain the proper scaling between events. The hexagon size reflects the quality of the observation: 'A' quality is biggest, followed by 'B' and 'C'. Suspect observations ('S' quality) are plotted as squares. Tails (barely visible) on the symbols indicate the small correction in take-off azimuth ($\delta\Phi$) obtained in the inversion. Each symbol is plotted at the azimuthally adjusted location.







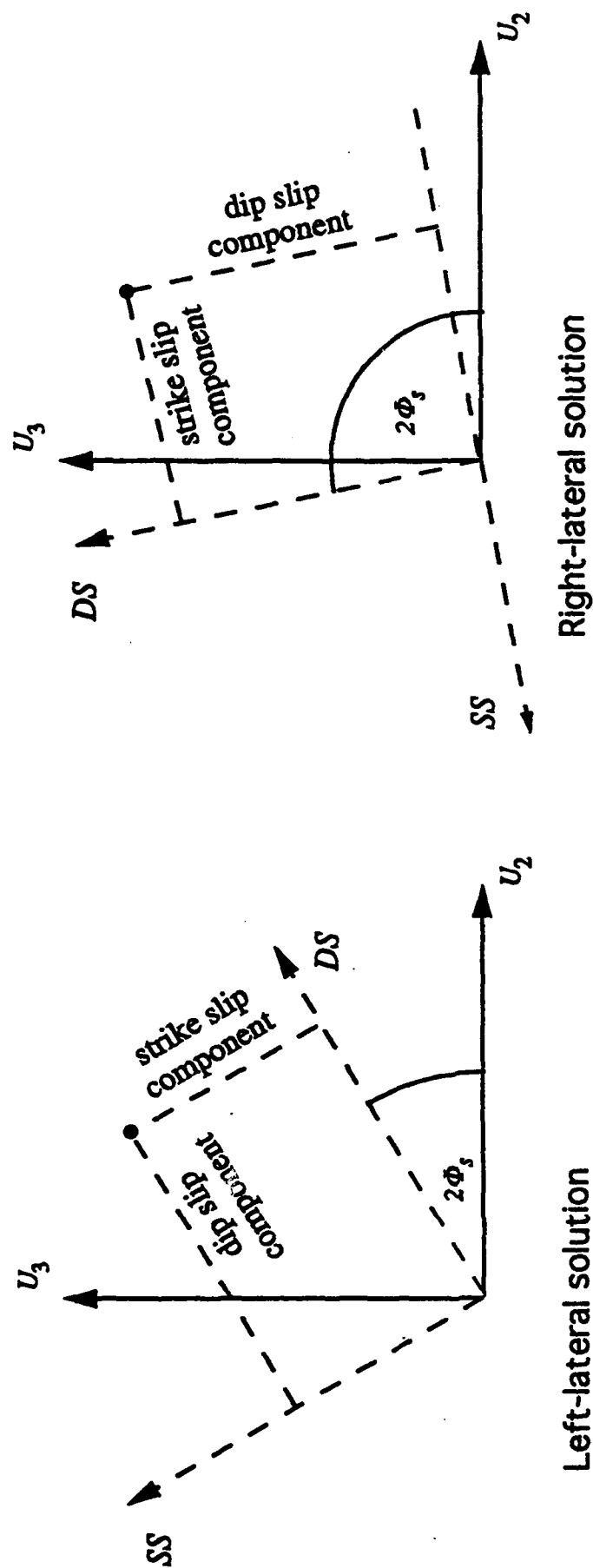


Figure 5. A geometrical relationship is shown, in which a point may be specified either by values of (KU_2, KU_3) or of (DS, SS) , where the second axes are rotated with respect to the first by an angle $2\phi_s$. Note that for each value of DS , determined from equation (23), there are two values of SS , determined from taking the square root of SS^2 in equation (26). Both left-lateral and right-lateral solutions are shown. Note that $2\phi_s$ is not affected by changes in the scaling factor K .

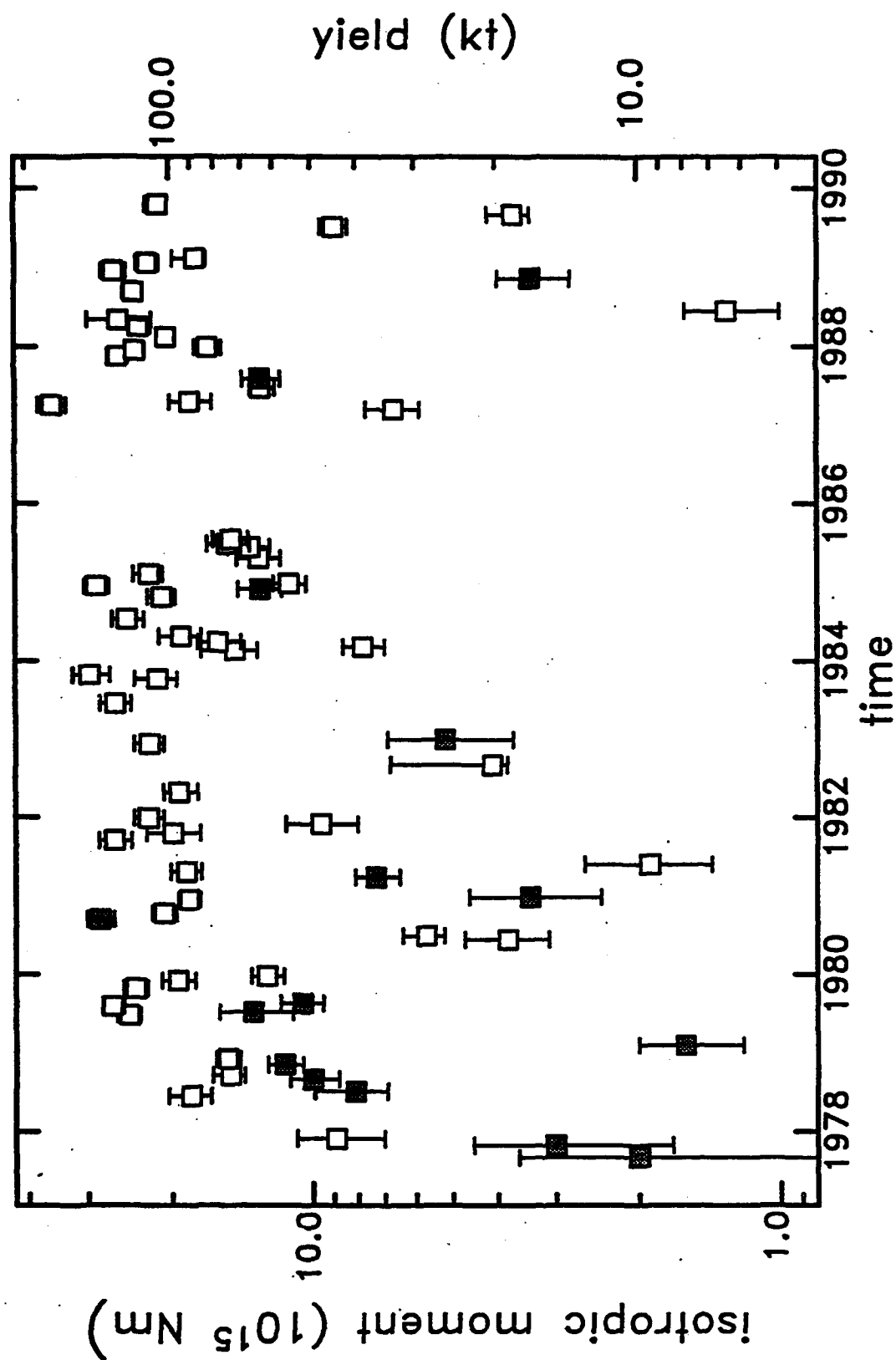


Figure 6. Isotropic moments and yields estimated for 71 events in our analysis, under the assumption of pure dip-slip geometry for the tectonic release. The error bars show the one sigma range of the estimate. Filled symbols indicate an F -ratio ($F = M_0/M_I$) greater than 0.5.

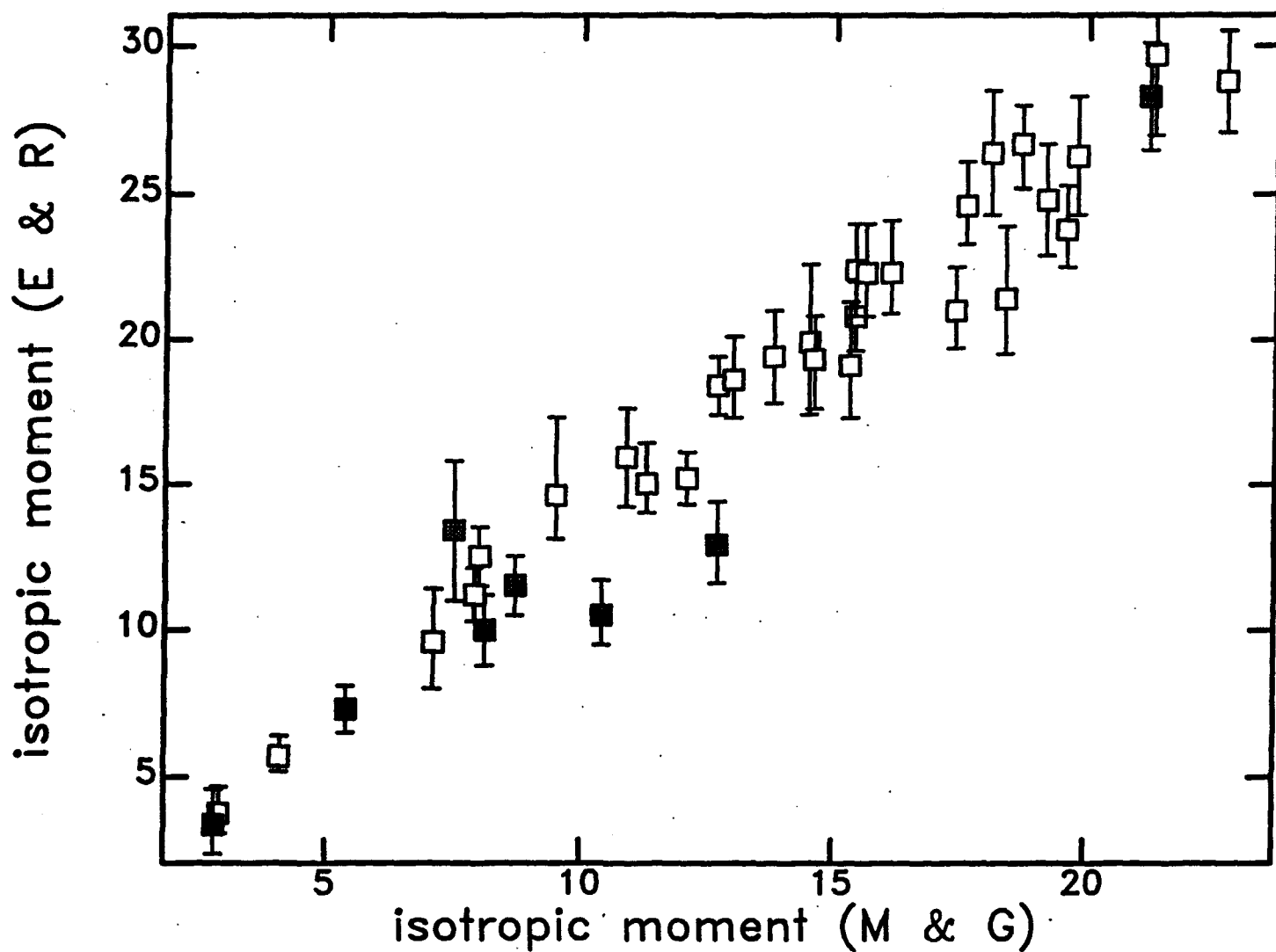


Figure 7. Comparison of the isotropic moment release estimated in this study (E & R) with that estimated by Given & Mellman (1986) for events analyzed in both studies, and making the assumption of pure thrusting. The units are 10^{15} Nm. Symbol shading as in Figure 6.

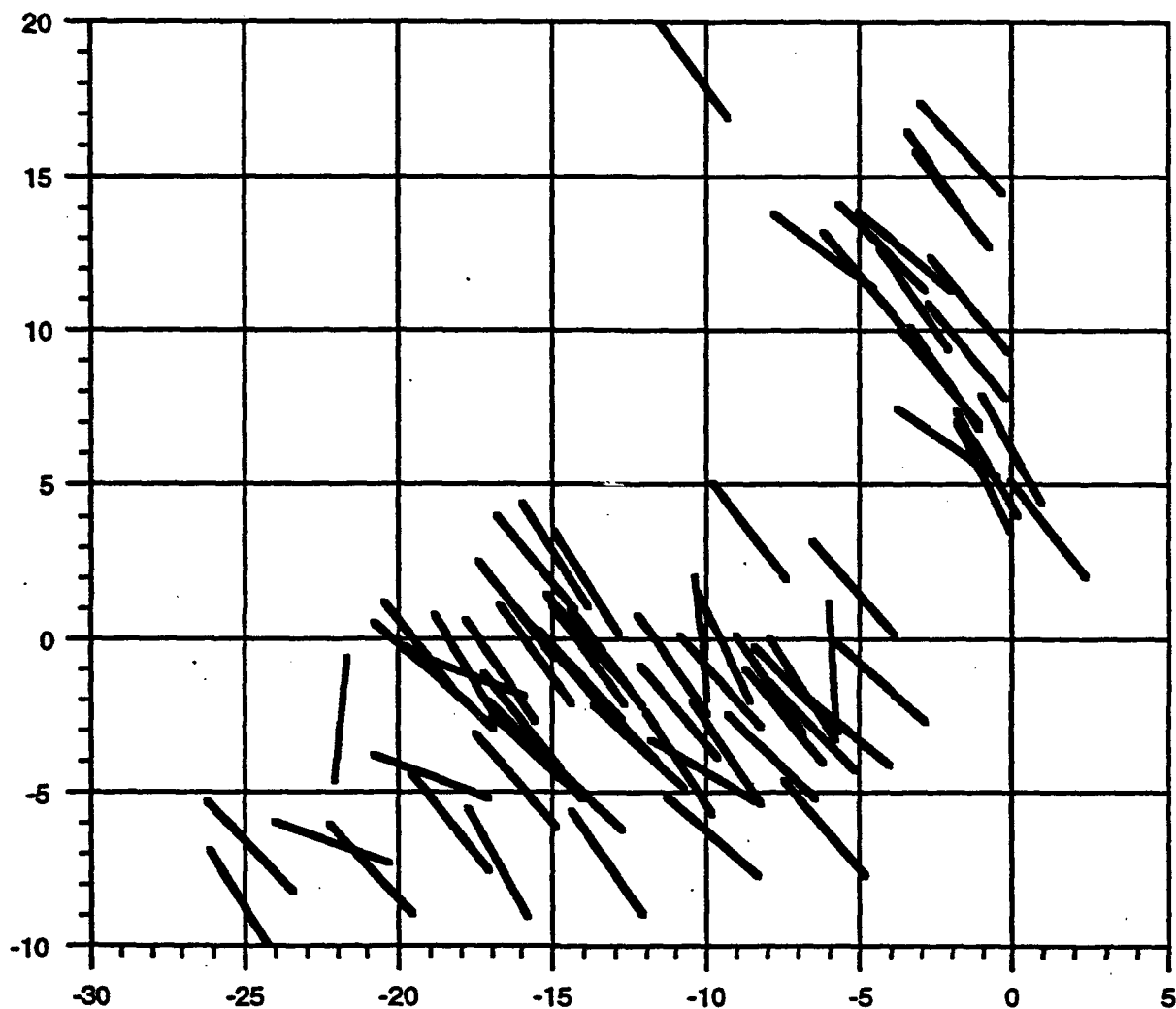


Figure 8. Direction of strike, for faulting inferred for 71 nuclear explosions at Balapan, if pure thrusting is assumed. Locations (from Lilwall & Farthing, 1990) are in km East and North of the cratering explosion of 1965 Jan 15. The average strike is 140° .

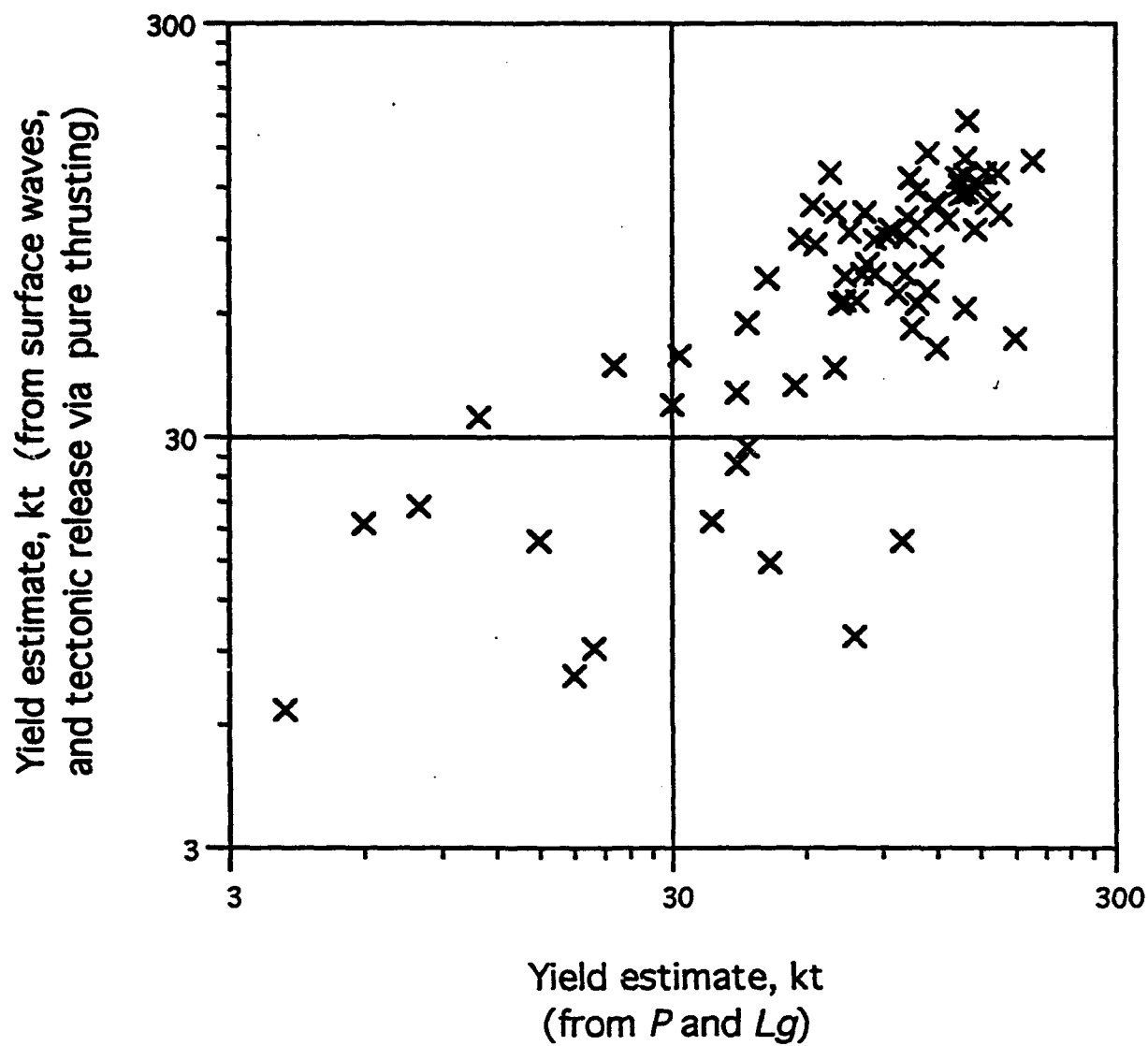


Figure 9. Yield estimates from surface waves, assuming tectonic release via pure thrusting, are compared with the yield estimates of Ringdal *et al.* (1992), based upon *P* and *Lg*.

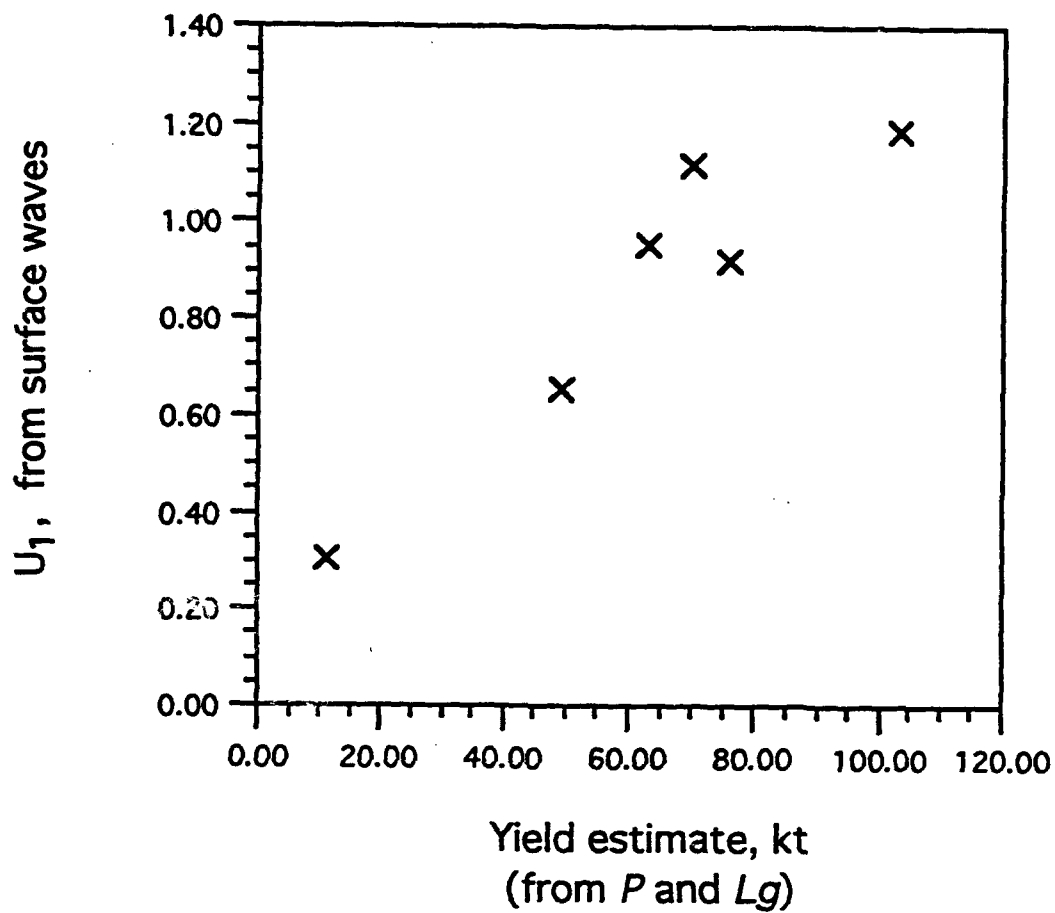


Figure 10. The isotropic source strength U_1 is compared with the yield estimate of Ringdal *et al.* (1992), for six Balapan explosions with Love waves that are very weak relative to Rayleigh waves. From the slope of a best-fitting line through the origin, we estimate the ratio $\frac{L}{K}$ as 0.0132.

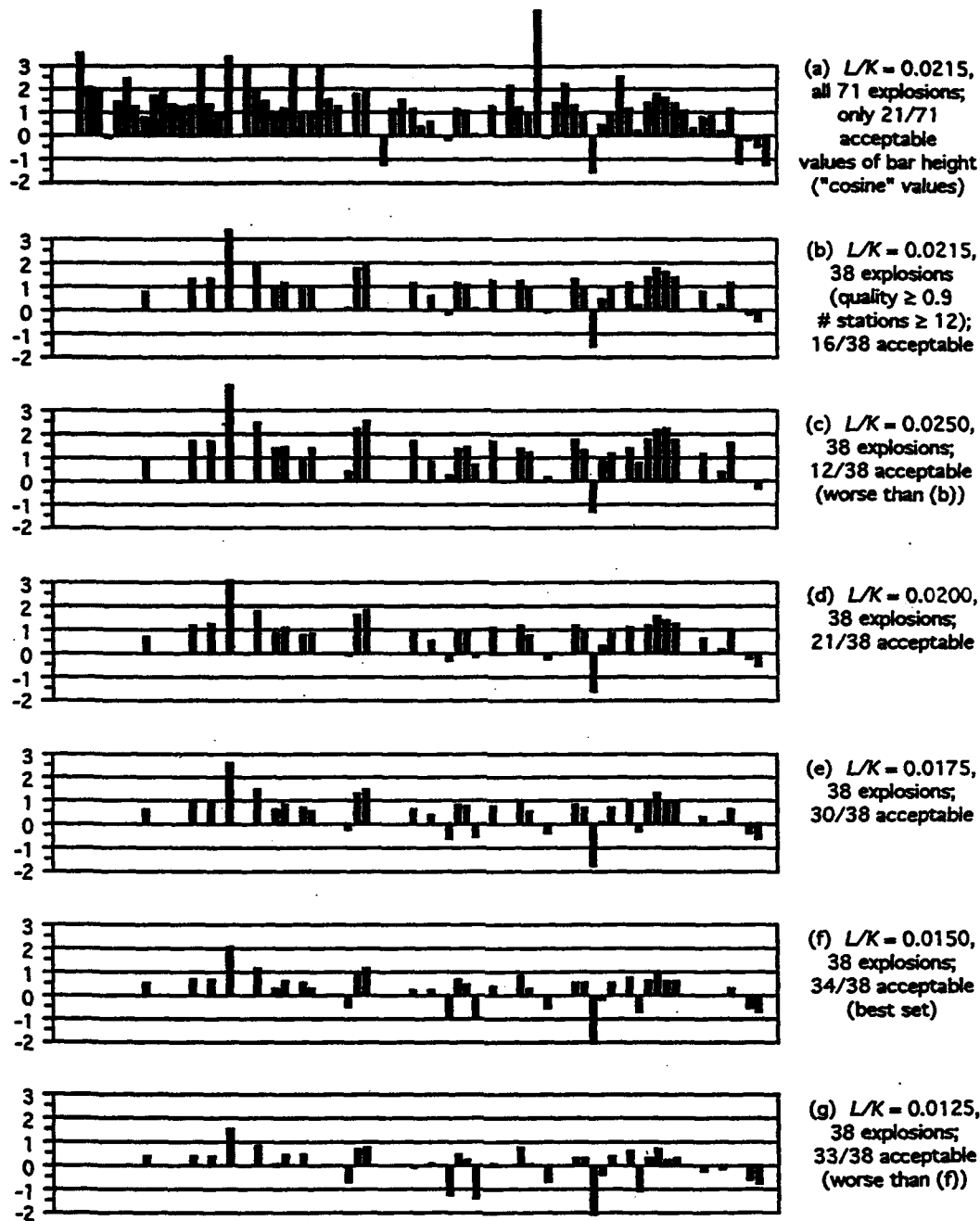


Figure 11. A display of the dependence of $\cos[2(\Phi_U - \Phi_S)]$ on the ratio $\frac{L}{K}$. In each bar graph the bar represents a particular explosion and the bar height is given by the expression for the cosine in equation (30). The goal here is to identify values of $\frac{L}{K}$ such that bar height lies in the range $[-1, +1]$, for as many explosions as possible that also have high quality determinations of surface wave radiation patterns. (a) $\frac{L}{K} = 0.0215$, and values of the "cosine" are shown in chronological order for all 71 explosions for which the values of U_1 , U_2 , and U_3 were estimated. 50 values lie outside $[-1, +1]$. (b) again $\frac{L}{K} = 0.0215$, but for this and the rest of the Figure there is a restriction to the 38 explosions with high quality solutions for the surface wave radiation patterns. Only 16 values lie inside $[-1, +1]$, indicating that this value of $\frac{L}{K}$ is unacceptable. (c) $\frac{L}{K} = 0.025$, and now only 12 of 38 bar heights ("cosines") lie within $[-1, +1]$, worse than for the previous value of $\frac{L}{K}$. (d) $\frac{L}{K} = 0.02$, and 21 suitable "cosines". (e) $\frac{L}{K} = 0.0175$, and 30 suitable bar heights. (f) $\frac{L}{K} = 0.015$, 34 suitable values. (g) $\frac{L}{K} = 0.0125$, 33 suitable values. The best overall set is (f).

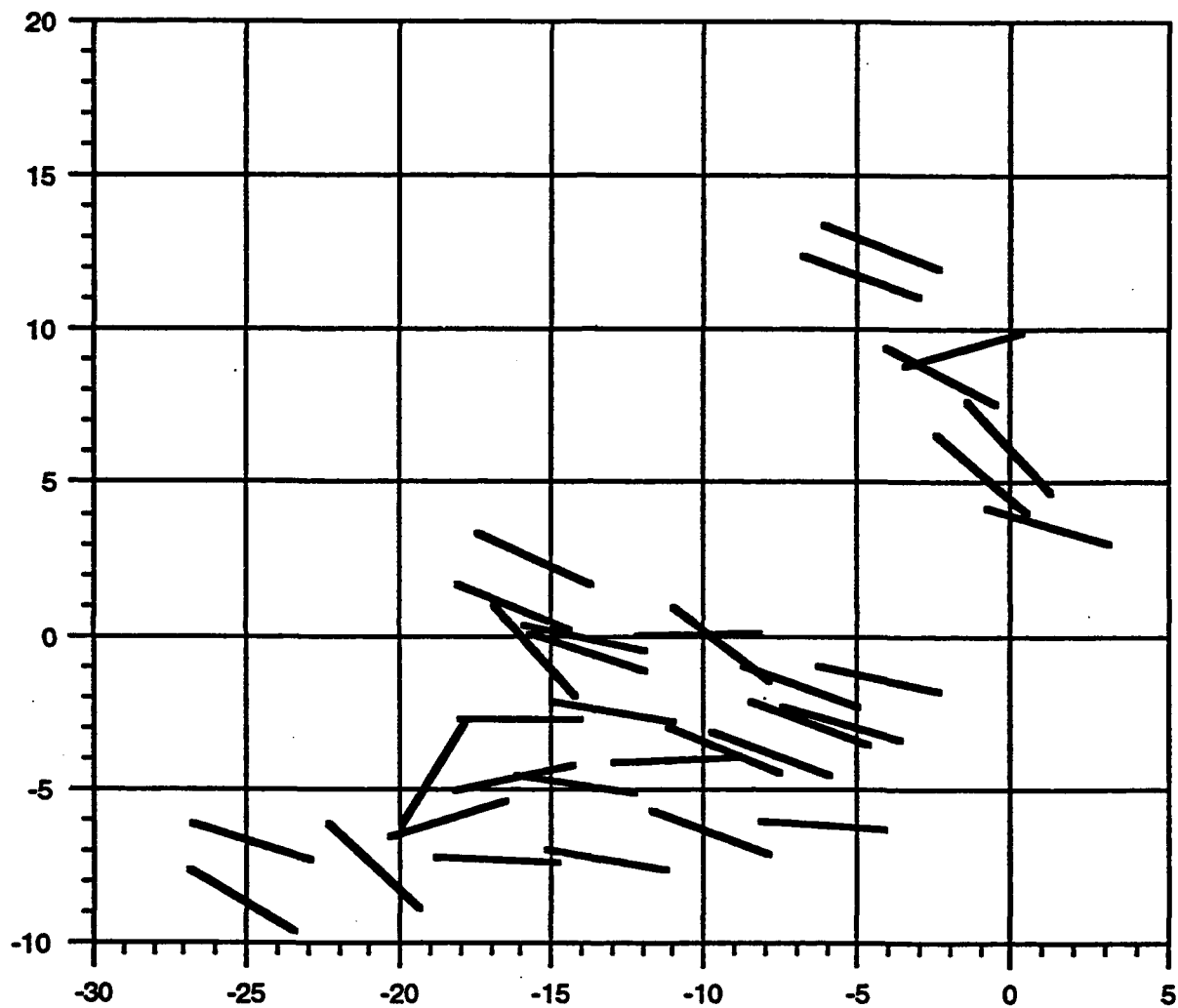


Figure 12. Directions of the strike of inferred left-lateral faulting associated with 34 nuclear explosions at the Balapan test site. $\frac{K}{L} = 0.015$. The average strike is 104° .

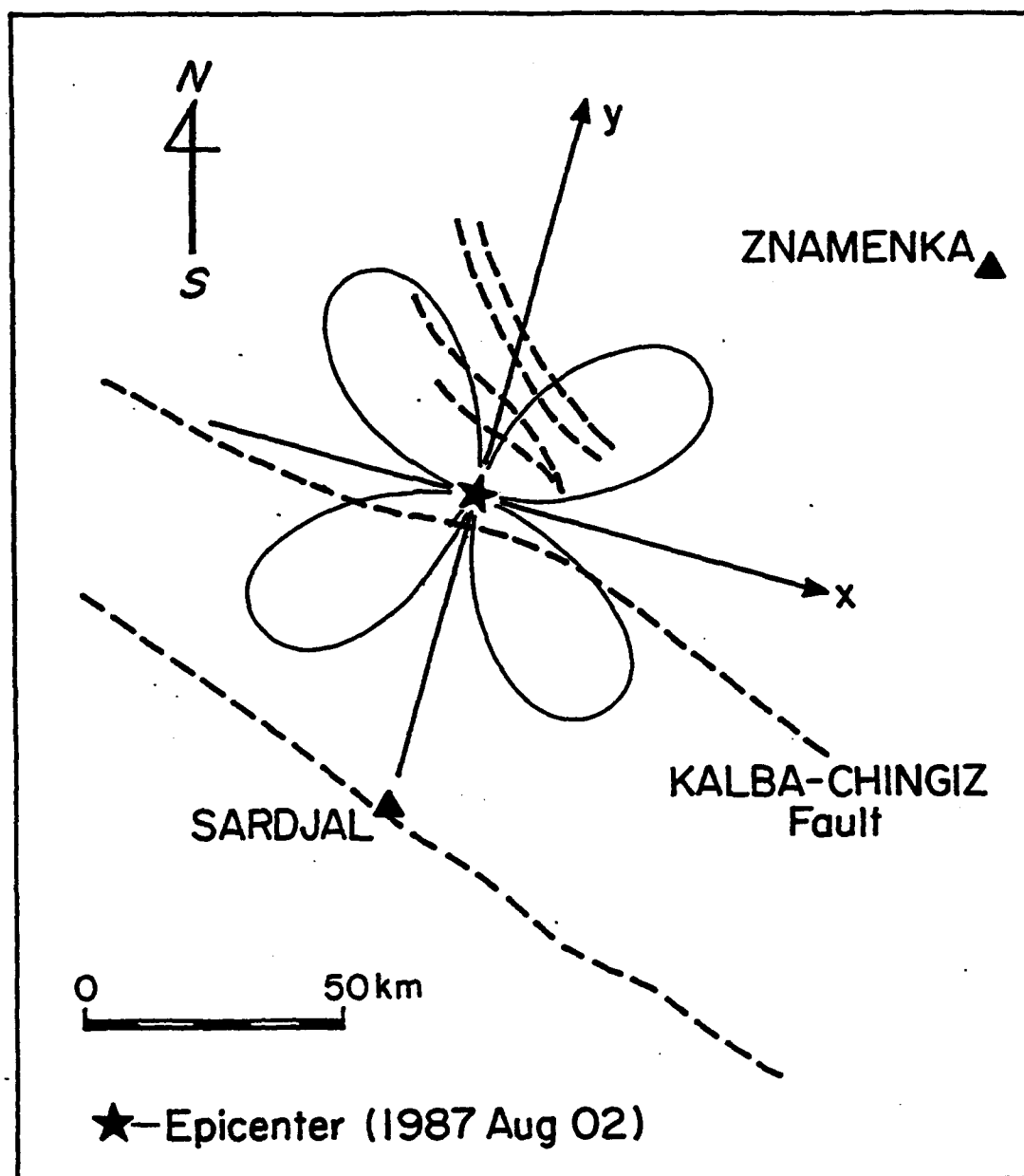


Figure 13. A map of faults (dashed lines) on part of the Balapan test site, and the radiation pattern of *SH* waves as measured for the nuclear explosion of 1987 Aug 2 by seismic stations on and near the test site. At the station Sardjal, *SH* waves had a node; Znamenka was near an antinode. The strike of the Kalba-Chingiz fault, at the point nearest ground zero, is about 115° . (From Adushkin, paper presented at the May 1992 meeting of the Seismological Society of America in Santa Fé, New Mexico.)

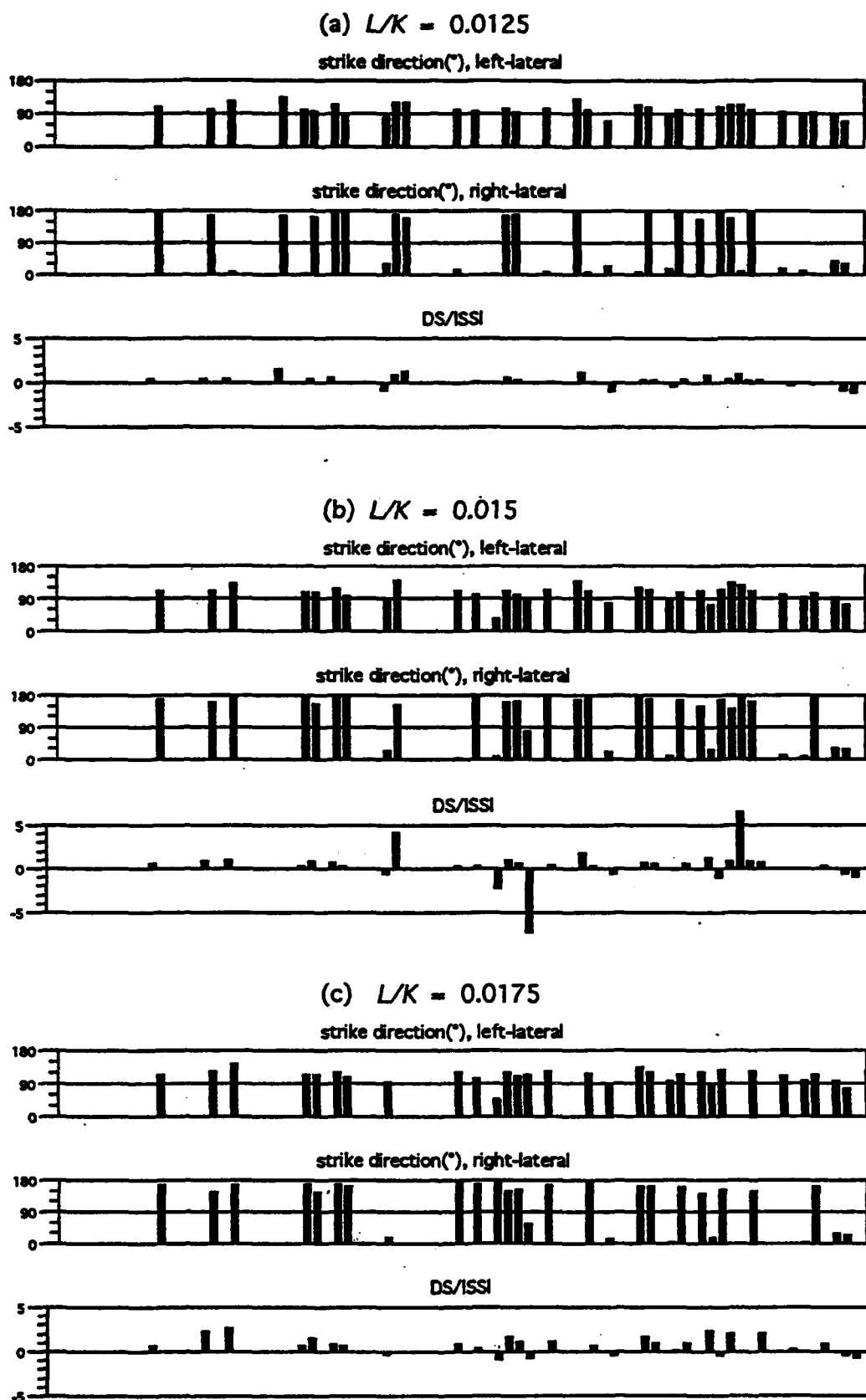


Figure 14.. Display of Φ_S (left-lateral), Φ_S (right-lateral), and $DS/|SSI|$, for L/K values of 0.0125, 0.015, 0.0175.

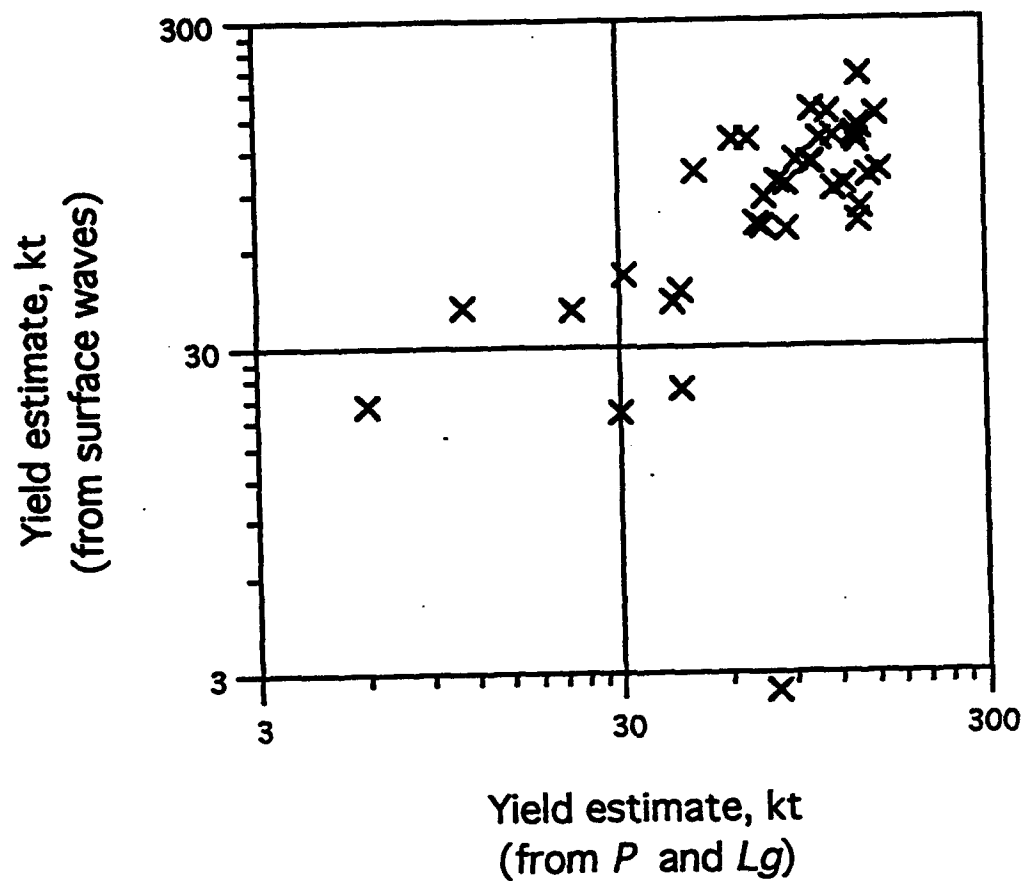


Figure 15. Yield estimates from surface waves, assuming tectonic release via slip on a fault striking at 110 degrees, are compared (for 38 explosions with excellent determinations of U_1 , U_2 , and U_3 with the yield estimates of Ringdahl *et al.* (1992), based upon P and Lg . The scatter is very high, indicating the need to allow for variable strike directions.

12/28/84 relative to 11/15/87

Rayleigh waves

Love waves

COL
1.9

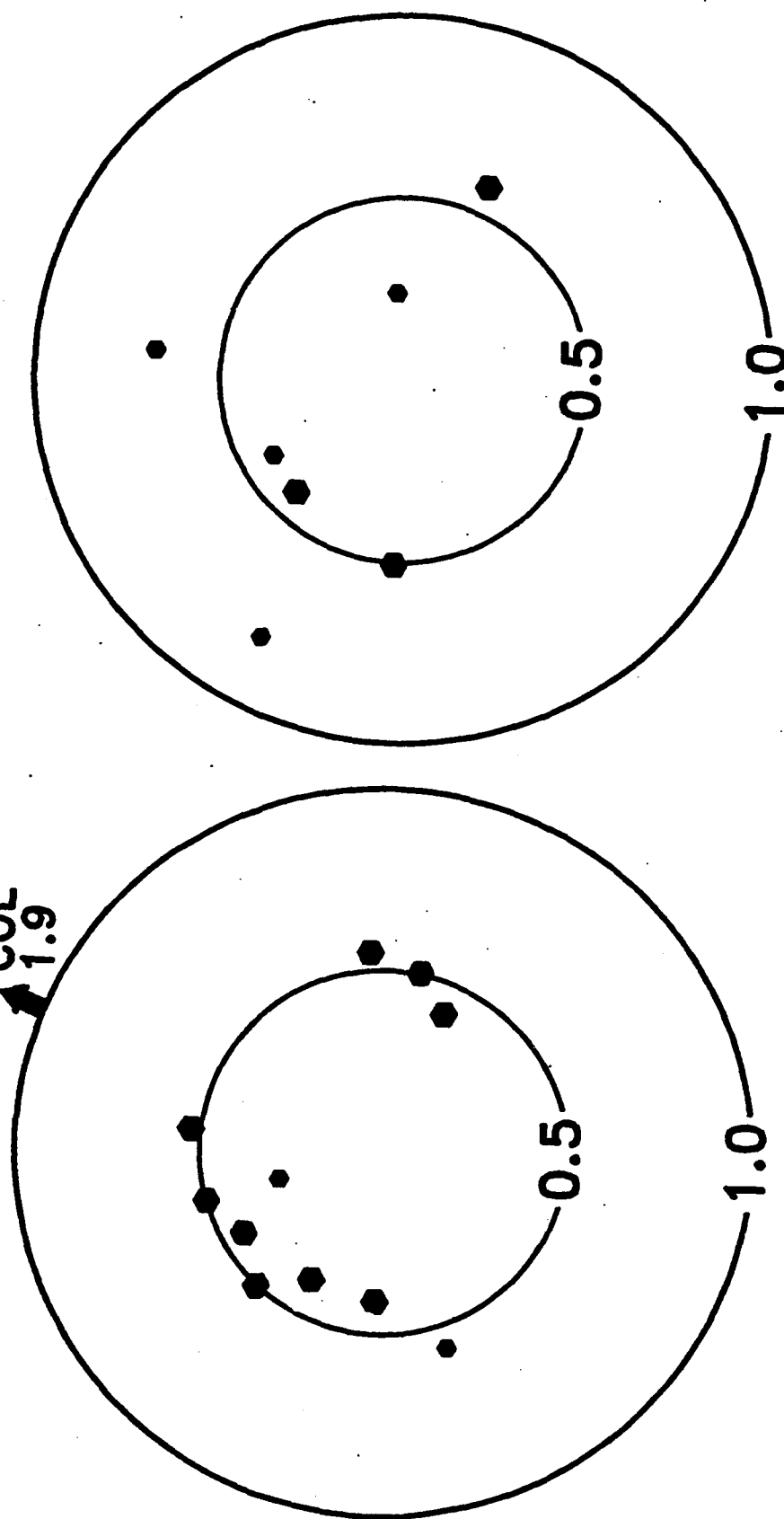


Figure 16. Azimuthal plot of the cross-correlations of seismograms for two explosions. The radial distance is proportional to the cross-correlation of the Rayleigh and Love waves for the event 122884 with respect to 111587. Except for one large Rayleigh wave measurement for the station COL, which probably is due to erroneous gain information for this station, the Rayleigh and Love wave amplitudes from the two events are different by approximately a factor of 0.5.

Appendix to "Empirical measurements of tectonic moment release in nuclear explosions from teleseismic surface waves and body waves".

This appendix contains some of the details of the methods and tables of intermediate results omitted from the main text of the previous paper.

MEASUREMENTS

The seismograms used in this study were read from Network Day Tapes of the Global Digital Seismograph Network prepared by the USGS (1980-1989) and for earlier data, from similarly arranged, concatenated SRO/ASRO Station Day tapes borrowed from the Earth Resources Laboratory at MIT (1977-1979). Instrument response information was obtained from the GDSN Network Day Tapes directly, or from subroutines provided by NEIC/USGS.

After the data had been read from the tapes, the three-component seismograms were deconvolved to displacement, and reconvolved with a bandpass filter consisting of an 8-pole Butterworth lowpass filter with a corner at 18 s period and a 4-pole highpass filter with a corner at 60 s. The filtering is done in the frequency domain. As indicated in the main portion of the previous paper, the primary data set consists of cross correlation measurements of surface wave amplitudes (equation (6)). In practice these were obtained by the following procedure:

1. After initial viewing of all Rayleigh and Love waves recorded at a certain station, a selection is made of a 'master seismogram' for both Rayleigh and Love waves.
2. A window is selected corresponding to the arrival of the main energy in the passband of the filtered seismograms.
3. All other seismograms are correlated against the 'master seismogram'. The correlation is calculated for several different discrete time shifts, from 5 seconds before the expected arrival to 5 s after the expected arrival in increments of one second. The correlation scale factor is calculated at the shift that provides the smallest least squares difference between the two seismograms.
4. A quality factor 'A', 'B', or 'C' is assigned to the measurement, based on the fit and a subjective assessment of the reliability of the measurement. Measurements which are in doubt can be flagged as 'S', or special.
5. The correlation window, the correlation factor, the predicted and measured time shifts, and the quality factor are stored for processing in the next step of analysis.
6. The previous steps are repeated for Love and Rayleigh arrivals for all events and all stations.

The result of this analysis is a set of 1100 relative amplitude measurements (c_{im}^n in equation (7)), which are given in Table A1. In these tables, the columns represent, from left to right: the name of the event being measured, vertical Rayleigh (1) or transverse Love (3) measurement, start time of correlation window in seconds after the event, end time of correlation window, observed delay of arrival with respect to master event (ignoring difference in location), predicted difference in arrival time (based on difference in location), correlation factor, residual normalized variance between the waveforms, and the quality assessment. For each station, the master events for Rayleigh and Love wave measurements are also given. We have so far made no effort to interpret the observed delay times.

Table A1. Observed Correlation Coefficients at 29 Stations

GUN (Rayleigh - 061283; Love - 061283)

061178	1	2240.0	2400.0	2.0	3.4	0.569	0.084	A	070578	1	2156.4	2407.6	1.0	0.7	0.168	0.362	B
091578	1	2240.0	2400.0	1.0	0.7	0.408	0.077	A	110478	1	2245.2	2341.6	0.0	0.5	0.209	0.213	B
112978	1	2240.0	2400.0	2.0	4.3	0.334	0.208	A	062379	1	2143.0	2386.6	0.0	1.0	0.407	0.169	A
080479	1	2240.0	2400.0	1.0	0.4	0.621	0.094	A	102879	1	2209.3	2429.4	-2.0	-1.9	0.416	0.203	B
122379	1	2296.2	2391.2	2.0	3.9	0.368	0.138	B	091480	1	2276.3	2365.4	2.0	2.6	0.315	0.152	B
101280	1	2240.0	2400.0	-2.0	-2.7	0.631	0.049	A	121480	1	2240.0	2400.0	-1.0	-0.2	0.454	0.140	A
042281	1	2240.0	2400.0	1.0	1.3	0.609	0.111	A	091381	1	2240.0	2400.0	0.0	-0.3	0.824	0.128	A
101881	1	2264.7	2400.7	2.0	1.6	0.498	0.429	C	122781	1	2240.0	2400.0	2.0	2.4	0.448	0.137	B
042582	1	2240.0	2400.0	1.0	0.9	0.426	0.120	A	083182	1	2285.7	2411.4	5.0	4.0	0.148	0.554	C
120582	1	2240.0	2400.0	2.0	2.3	0.503	0.059	A	122682	1	2268.1	2384.4	0.0	-0.9	0.107	0.554	C
061283	1	2240.0	2400.0	0.0	0.0	1.000	0.000	A	021984	1	2157.1	2410.4	3.0	3.3	0.539	0.132	A
030784	1	2194.5	2402.6	-2.0	0.1	0.167	0.414	B	032984	1	2240.0	2400.0	-1.0	-0.5	0.460	0.115	A
042584	1	2234.0	2362.6	2.0	1.3	0.621	0.259	B	071484	1	2240.0	2400.0	0.0	0.8	0.744	0.042	A
102784	1	2240.0	2400.0	2.0	3.2	0.464	0.133	B	120284	1	2237.5	2381.2	-2.0	-1.1	-0.256	0.463	C
121684	1	2240.0	2400.0	2.0	3.1	0.770	0.056	A	122884	1	2240.0	2400.0	3.0	5.3	0.442	0.197	A
042585	1	2240.0	2400.0	-2.0	0.0	0.423	0.129	B	061585	1	2240.0	2400.0	1.0	1.9	0.401	0.121	A
063085	1	2284.2	2384.0	5.0	5.8	0.441	0.107	A	072085	1	2240.0	2400.0	2.0	3.8	0.342	0.128	B
031287	1	2240.0	2400.0	1.0	3.0	0.383	0.401	C	040387	1	2240.0	2400.0	2.0	3.3	1.157	0.113	B
062087	1	2185.5	2391.0	2.0	5.2	0.348	0.422	B	080287	1	2240.0	2400.0	0.0	1.0	0.230	0.425	C
111587	1	2240.0	2400.0	3.0	3.8	0.958	0.065	A	021388	1	2201.9	2387.0	1.0	1.6	0.480	0.336	B
040388	1	2240.0	2400.0	0.0	0.5	0.705	0.045	A	050488	1	2240.0	2400.0	2.0	4.5	0.637	0.177	B
091488	1	2240.0	2400.0	2.0	3.1	0.744	0.067	A	121788	1	2240.0	2400.0	0.0	0.8	0.491	0.173	B
012289	1	2240.0	2400.0	2.0	3.2	0.725	0.125	B	021289	1	2240.0	2400.0	4.0	5.2	0.642	0.272	B
070889	1	2166.9	2382.9	3.0	3.7	0.187	0.291	B	101989	1	2240.0	2400.0	1.0	0.2	0.911	0.105	A
061178	3	1970.0	2070.0	2.0	3.4	0.519	0.106	A	070578	3	1988.3	2063.1	3.0	0.7	0.340	0.203	B
082978	3	1996.0	2057.1	0.0	-0.7	0.762	0.311	B	091578	3	1970.0	2070.0	2.0	0.7	0.572	0.118	A
110478	3	1998.7	2064.5	1.0	0.5	0.704	0.311	B	112978	3	1996.0	2067.9	3.0	4.3	0.547	0.168	A
062379	3	1970.0	2070.0	1.0	1.0	1.031	0.225	A	080479	3	1970.0	2070.0	1.0	0.4	1.065	0.159	A
061879	3	1994.8	2076.0	1.0	-0.1	0.983	0.198	A	102879	3	1978.2	2074.6	-1.0	-1.9	1.012	0.163	A
122379	3	2020.2	2069.3	2.0	3.9	0.626	0.249	C	062980	3	1995.5	2072.4	2.0	2.4	0.190	0.378	B
091480	3	1997.3	2075.4	2.0	2.6	1.867	0.137	A	101280	3	1977.2	2066.1	-2.0	-2.7	0.865	0.237	B
121480	3	1990.6	2073.3	2.0	-0.2	0.858	0.185	A	032981	3	1994.4	2061.9	-2.0	-0.7	0.663	0.142	S
042281	3	1989.1	2057.1	2.0	1.3	0.630	0.305	B	091381	3	1988.5	2069.6	0.0	-0.3	0.945	0.196	A
122781	3	1988.3	2075.4	4.0	2.4	0.926	0.166	A	042582	3	1977.2	2076.8	0.0	0.9	0.739	0.303	A
120582	3	1985.1	2069.5	2.0	2.3	1.127	0.136	A	061283	3	1970.0	2070.0	0.0	0.0	1.000	0.000	A
030784	3	1981.7	2064.4	0.0	0.1	0.509	0.164	A	032984	3	1994.6	2075.7	1.0	-0.5	0.629	0.102	B
071484	3	1969.5	2098.1	0.0	0.8	0.986	0.131	A	102784	3	1983.8	2073.0	2.0	3.2	0.948	0.308	B
120284	3	1977.5	2057.0	-2.0	-1.1	1.190	0.291	A	121684	3	1970.0	2070.0	2.0	3.1	1.217	0.133	A
122884	3	2022.9	2072.0	7.0	5.3	0.284	0.548	B	121788	3	1991.5	2064.9	-1.0	0.8	-1.003	0.255	S
070889	3	1990.6	2055.0	3.0	3.7	0.401	0.388	C									

ZOB0 (Rayleigh - 091488)

113077	1	4570.0	4700.0	-2.0	-0.8	0.395	0.187	B	061178	1	4479.8	4698.2	-5.0	-1.1	-1.067	0.172	S
070578	1	4570.0	4700.0	-2.0	1.7	0.255	0.236	B	082978	1	4570.0	4700.0	-2.0	0.3	0.310	0.291	B

110478	1	4570.0	4700.0	0.0	-1.6	0.393	0.132	A
062379	1	4570.0	4700.0	-2.0	0.6	0.999	0.050	A
061879	1	4570.0	4700.0	-3.0	0.7	0.378	0.231	B
120279	1	4561.0	4648.3	1.0	-0.6	2.387	0.158	B
061280	1	4570.0	4700.0	0.0	1.6	0.182	0.382	B
091480	1	4570.0	4700.0	-2.0	-1.6	0.863	0.070	A
121480	1	4570.0	4700.0	1.0	1.9	0.713	0.117	A
032981	1	4570.0	4700.0	0.0	0.3	0.227	0.195	B
112981	1	4570.0	4700.0	1.0	0.2	0.569	0.337	C
061283	1	4570.0	4700.0	2.0	1.0	1.152	0.067	A
102683	1	4570.0	4700.0	-1.0	0.2	1.141	0.393	C
061585	1	4570.0	4700.0	-4.0	0.6	0.371	0.075	A
040387	1	4570.0	4700.0	-2.0	-0.9	1.453	0.018	A
040388	1	4570.0	4700.0	0.0	0.4	0.885	0.034	A
091488	1	4570.0	4700.0	0.0	0.0	1.000	0.000	A
121788	1	4570.0	4700.0	1.0	0.7	0.889	0.024	A
021289	1	4570.0	4700.0	-3.0	-3.4	0.691	0.196	B

112978	1	4570.0	4700.0	-3.0	-2.7	0.722	0.038	A
080479	1	4570.0	4700.0	1.0	1.6	1.155	0.048	A
102879	1	4570.0	4700.0	1.0	1.6	0.972	0.104	A
122379	1	4570.0	4700.0	-2.0	-2.4	0.445	0.214	A
062980	1	4570.0	4700.0	-2.0	-0.9	0.257	0.354	B
101280	1	4570.0	4700.0	2.0	2.6	0.963	0.086	A
122780	1	4514.2	4752.0	3.0	-0.2	-0.129	0.795	C
042281	1	4570.0	4700.0	0.0	0.7	0.957	0.052	A
120582	1	4570.0	4700.0	1.0	-0.5	0.813	0.070	A
100683	1	4570.0	4700.0	0.0	-1.4	0.884	0.032	A
042585	1	4570.0	4700.0	-3.0	1.5	0.375	0.145	A
072085	1	4570.0	4700.0	-5.0	-2.2	0.406	0.078	A
021388	1	4570.0	4700.0	-2.0	-0.9	0.996	0.087	B
050488	1	4570.0	4700.0	-2.0	-2.9	1.437	0.077	A
111288	1	4570.0	4700.0	-3.0	-2.5	0.299	0.470	C
012289	1	4570.0	4700.0	-2.0	-1.6	0.918	0.025	A

CNT0 (Rayleigh - 091480; Love 091480)

113077	1	1301.4	1395.7	1.0	-0.7	0.301	0.126	B
082978	1	1342.2	1392.4	-1.0	-0.9	0.488	0.033	A
112978	1	1260.0	1380.0	1.0	0.7	0.692	0.052	A
080479	1	1260.0	1380.0	-2.0	-3.3	1.044	0.064	A
102879	1	1305.2	1403.6	0.0	-2.1	1.079	0.134	A
122379	1	1281.5	1385.9	0.0	0.5	0.467	0.211	A
062980	1	1276.0	1414.5	1.0	-0.9	0.250	0.351	B
101280	1	1231.8	1381.6	-2.0	-3.0	1.095	0.096	A
032981	1	1231.1	1385.4	1.0	-0.9	0.266	0.258	B
042582	1	1260.0	1380.0	0.0	-2.8	0.810	0.211	B
030784	1	1260.0	1380.0	3.0	0.1	0.313	0.186	A
042584	1	1260.0	1380.0	0.0	-1.5	0.844	0.145	B
102784	1	1260.0	1380.0	0.0	-0.2	0.947	0.108	A
121684	1	1260.0	1380.0	1.0	-1.2	1.312	0.050	A
021085	1	1226.8	1433.6	1.0	-1.7	1.055	0.130	A
061585	1	1344.3	1420.9	0.0	-2.7	0.507	0.213	B
040387	1	1196.6	1391.7	1.0	-1.4	1.520	0.112	A
062087	1	1135.5	1391.7	1.0	0.2	0.551	0.388	B
021388	1	1203.0	1389.1	-1.0	-0.4	0.997	0.153	A
050488	1	1213.5	1422.9	3.0	0.9	0.930	0.388	C
111288	1	1229.0	1426.5	0.0	2.4	0.150	0.545	C
021289	1	1324.9	1404.3	1.0	1.2	0.608	0.203	B
090577	3	1180.0	1250.0	1.0	2.3	0.454	0.367	C
062978	3	1180.0	1250.0	1.0	-0.9	0.366	0.230	A
112978	3	1213.5	1255.2	3.0	0.7	0.638	0.223	B
080479	3	1180.0	1250.0	-1.0	-3.3	0.975	0.041	A
102879	3	1174.4	1291.2	1.0	-2.1	0.670	0.707	S
122379	3	1180.0	1250.0	1.0	0.5	0.430	0.067	A
091480	3	1180.0	1250.0	0.0	0.0	1.000	0.000	A
121480	3	1182.0	1232.7	-1.0	-3.4	0.772	0.076	A
032981	3	1163.6	1235.1	-1.0	-0.9	0.159	0.426	B
021984	3	1180.0	1250.0	3.0	-1.6	0.506	0.041	A
032984	3	1180.0	1250.0	0.0	-3.5	0.687	0.122	B
102784	3	1180.0	1250.0	1.0	-0.2	0.701	0.214	B
122884	3	1180.0	1250.0	1.0	-1.2	0.353	0.133	A
042585	3	1210.5	1253.0	2.0	-3.0	0.510	0.325	B
040387	3	1190.7	1288.2	2.0	-1.4	1.111	0.208	B
062087	3	1180.0	1250.0	2.0	0.2	0.442	0.277	B
021388	3	1206.4	1269.0	2.0	-0.4	0.897	0.367	B
091488	3	1207.0	1273.0	0.0	-2.5	0.969	0.237	B
012289	3	1180.0	1250.0	2.0	-0.2	0.728	0.065	A
070889	3	1217.2	1272.3	1.0	-0.7	0.426	0.425	C

070578	1	1295.6	1377.3	-2.0	-3.6	0.206	0.231	B
110478	1	1276.9	1402.9	2.0	1.1	0.373	0.159	A
062379	1	1256.7	1410.8	-1.0	-2.2	0.855	0.081	A
061879	1	1324.6	1394.6	-3.0	-1.8	0.272	0.105	A
120279	1	1260.0	1380.0	0.0	-1.5	0.872	0.069	A
061280	1	1151.6	1411.6	-1.0	-2.3	0.258	0.809	C
091480	1	1260.0	1380.0	0.0	0.0	1.000	0.000	A
121480	1	1228.6	1410.9	-1.0	-3.4	0.698	0.097	A
042281	1	1165.4	1424.7	0.0	-2.5	0.899	0.152	B
021984	1	1260.0	1380.0	1.0	-1.6	0.576	0.068	A
032984	1	1124.9	1453.6	0.0	-3.5	0.678	0.377	B
071484	1	1232.8	1396.1	0.0	-3.3	1.205	0.083	A
120284	1	1260.0	1380.0	-2.0	-1.9	0.414	0.355	A
122884	1	1260.0	1380.0	0.0	-1.2	0.504	0.122	A
042585	1	1223.1	1341.2	0.0	-3.0	0.766	0.210	B
072085	1	1222.2	1408.6	1.0	0.2	0.575	0.371	C
041787	1	1244.8	1388.4	1.0	-0.7	0.628	0.169	A
080287	1	1292.4	1407.9	-2.0	-3.2	0.304	0.327	B
040388	1	1260.0	1380.0	-2.0	-1.7	1.040	0.084	A
091488	1	1221.3	1419.6	-1.0	-2.5	1.047	0.143	A
012289	1	1260.0	1380.0	2.0	-0.2	1.067	0.077	A
070889	1	1205.6	1396.7	-1.0	-0.7	0.489	0.152	B
113077	3	1180.0	1250.0	3.0	-0.7	0.220	0.310	B
110478	3	1180.0	1250.0	3.0	1.1	0.451	0.109	A
062379	3	1209.1	1255.8	-1.0	-2.2	1.047	0.083	A
081879	3	1180.0	1250.0	-1.0	-1.8	0.436	0.145	A
120279	3	1180.0	1250.0	2.0	-1.5	0.513	0.360	B
062980	3	1180.0	1250.0	1.0	-0.9	0.092	0.836	C
101280	3	1180.0	1250.0	-1.0	-3.0	0.659	0.518	B
122780	3	1180.0	1250.0	-1.0	-0.2	0.245	0.402	C
042281	3	1180.0	1250.0	1.0	-2.5	0.640	0.063	A
030784	3	1180.0	1250.0	5.0	0.1	0.284	0.068	A
071484	3	1186.3	1257.9	1.0	-3.3	0.907	0.283	C
121684	3	1180.0	1250.0	2.0	-1.2	0.744	0.381	B
021085	3	1155.1	1231.9	1.0	-1.7	0.553	0.063	A
061585	3	1185.9	1262.6	0.0	-2.7	0.448	0.462	B
041787	3	1180.0	1250.0	0.0	-0.7	0.800	0.048	A
080287	3	1180.0	1250.0	-2.0	-3.2	0.522	0.291	B
040388	3	1180.0	1250.0	-1.0	-1.7	0.881	0.052	A
111288	3	1163.0	1256.6	3.0	2.4	0.216	0.501	B
021289	3	1166.2	1261.6	4.0	1.2	0.577	0.471	C

TATU (Rayleigh - 091480; Love - 091480)

082978	1	1562.3	1615.4	-4.0	-2.8	0.292	0.593	C
110478	1	1446.8	1608.8	-2.0	-1.4	0.360	0.530	B
102879	1	1435.5	1635.7	-2.0	-4.1	0.865	0.605	S
122379	1	1525.0	1625.0	1.0	1.1	0.829	0.795	S
091480	1	1525.0	1625.0	0.0	0.0	1.000	0.000	A
121480	1	1464.0	1598.4	-3.0	-3.2	0.733	0.231	A
032981	1	1547.8	1594.1	-1.0	-2.8	0.205	0.369	B
091381	1	1379.4	1619.5	-1.0	-3.1	1.204	0.254	A
112981	1	1525.0	1625.0	-1.0	-0.9	0.562	0.193	A
042582	1	1478.8	1624.1	-1.0	-2.1	0.726	0.267	A
120582	1	1458.5	1629.6	0.0	-0.6	0.859	0.185	A
100683	1	1557.8	1597.1	2.0	0.3	0.647	0.177	B
112083	1	1448.3	1617.2	-3.0	-1.8	1.096	0.737	C
030784	1	1471.1	1606.6	-1.0	-2.0	0.282	0.450	A
071484	1	1441.6	1587.6	-1.0	-2.4	0.906	0.296	A
120284	1	1528.2	1652.8	-2.0	-3.4	0.153	0.870	C
021085	1	1462.5	1599.9	-1.0	-0.5	0.802	0.328	A
061585	1	1465.7	1601.2	-1.0	-1.3	0.626	0.278	A
031287	1	1468.3	1603.0	-1.0	0.1	0.214	0.646	B
041787	1	1467.0	1607.8	3.0	2.6	0.462	0.429	B
080287	1	1525.0	1625.0	-2.0	-2.2	0.506	0.127	A
121387	1	1463.4	1610.2	0.0	1.0	0.875	0.258	A
021388	1	1456.2	1608.7	-2.0	-0.9	0.724	0.329	A
102977	3	1318.1	1431.2	-3.0	1.3	0.254	0.236	A
082978	3	1300.0	1390.0	-2.0	-2.8	0.319	0.149	A
110478	3	1300.0	1390.0	-1.0	-1.4	0.394	0.057	A
120279	3	1300.0	1390.0	2.0	-0.3	-0.196	0.421	S
062980	3	1324.2	1401.0	1.0	-0.4	-0.094	0.156	S
101280	3	1300.0	1390.0	-2.0	-5.0	0.408	0.533	C
122780	3	1300.0	1390.0	-2.0	-2.7	0.384	0.088	B
052781	3	1300.0	1390.0	-1.0	-3.1	0.023	0.916	C
101881	3	1300.0	1390.0	1.0	-1.4	0.418	0.093	B
122781	3	1300.0	1390.0	1.0	-0.5	0.523	0.052	A
083182	3	1300.0	1390.0	6.0	1.1	0.040	0.634	C
061283	3	1300.0	1390.0	0.0	-2.7	0.344	0.300	B
112083	3	1300.0	1390.0	-6.0	-1.8	0.057	0.947	C
030784	3	1300.0	1390.0	-1.0	-2.0	0.173	0.477	B
071484	3	1300.0	1390.0	0.0	-2.4	0.490	0.085	B
120284	3	1300.0	1390.0	-3.0	-3.4	0.692	0.057	A
042585	3	1300.0	1390.0	-2.0	-2.8	0.237	0.302	C
072085	3	1300.0	1390.0	1.0	1.0	0.369	0.079	A
040387	3	1300.0	1390.0	1.0	0.2	0.389	0.148	B
062087	3	1300.0	1390.0	3.0	2.1	0.135	0.278	A
121387	3	1300.0	1390.0	1.0	1.0	0.468	0.076	B
021388	3	1300.0	1390.0	-1.0	-0.9	0.261	0.464	C

091578	1	1487.6	1634.9	-1.0	-2.0	0.861	0.380	B
062379	1	1468.4	1639.3	-2.0	-1.9	0.958	0.253	A
120279	1	1525.0	1625.0	1.0	-0.3	1.108	0.544	S
062980	1	1544.6	1614.4	0.0	-0.4	0.420	0.180	S
101280	1	1525.0	1625.0	-2.0	-5.0	1.555	0.219	S
122780	1	1515.4	1618.3	-3.0	-2.7	0.227	0.511	C
052781	1	1510.8	1567.6	-4.0	-3.1	0.194	0.193	C
101881	1	1537.4	1615.1	-1.0	-1.4	0.821	0.147	A
122781	1	1498.3	1636.9	0.0	-0.5	0.598	0.351	B
083182	1	1463.1	1627.3	2.0	1.1	0.179	0.669	B
061283	1	1463.2	1620.2	-1.0	-2.7	0.927	0.352	A
102683	1	1460.7	1627.6	0.0	-1.5	1.231	0.161	A
021984	1	1489.7	1613.7	1.0	0.0	0.502	0.450	A
042584	1	1497.2	1643.5	0.0	-1.4	0.785	0.278	A
102784	1	1444.9	1618.8	1.0	0.4	0.438	0.740	B
122884	1	1449.5	1629.8	0.0	1.8	0.472	0.467	B
042585	1	1476.8	1604.5	-2.0	-2.8	0.341	0.577	B
072085	1	1545.6	1629.2	0.0	1.0	0.516	0.202	A
040387	1	1452.8	1601.2	0.0	0.2	1.260	0.312	A
062087	1	1448.4	1615.9	1.0	2.1	0.662	0.200	A
111587	1	1463.1	1602.6	1.0	0.6	1.032	0.378	A
122787	1	1479.2	1597.4	1.0	1.1	0.519	0.424	A
040388	1	1455.8	1613.9	-2.0	-2.1	0.855	0.286	A
113077	3	1300.0	1390.0	-2.0	-0.7	0.256	0.101	A
091578	3	1300.0	1390.0	0.0	-2.0	0.269	0.155	A
102879	3	1300.0	1390.0	-3.0	-4.1	-0.813	0.043	S
122379	3	1300.0	1390.0	2.0	1.1	-0.268	0.279	S
091480	3	1300.0	1390.0	0.0	0.0	1.000	0.000	A
121480	3	1300.0	1390.0	0.0	-3.2	0.316	0.131	B
032981	3	1300.0	1390.0	-2.0	-2.8	0.330	0.030	A
091381	3	1300.0	1390.0	0.0	-3.1	0.472	0.101	B
112981	3	1300.0	1390.0	1.0	-0.9	0.116	0.439	B
042582	3	1300.0	1390.0	0.0	-2.1	0.443	0.085	A
120582	3	1300.0	1390.0	1.0	-0.6	0.503	0.060	A
102683	3	1300.0	1390.0	1.0	-1.5	0.656	0.102	B
021984	3	1300.0	1390.0	-2.0	0.0	-0.094	0.553	C
042584	3	1300.0	1390.0	1.0	-1.4	0.259	0.507	B
102784	3	1300.0	1390.0	1.0	0.4	0.623	0.116	A
021085	3	1300.0	1390.0	2.0	-0.5	0.291	0.265	B
061585	3	1300.0	1390.0	0.0	-1.3	0.250	0.189	B
031287	3	1300.0	1390.0	3.0	0.1	0.071	0.671	C
041787	3	1300.0	1390.0	3.0	2.6	0.458	0.042	A
111587	3	1319.5	1384.2	3.0	0.6	0.212	0.336	C
122787	3	1300.0	1390.0	2.0	1.1	0.320	0.064	B
040388	3	1300.0	1390.0	0.0	-2.1	0.331	0.157	A

KAA0 (Rayleigh - 091480; Love - 091480)

090577	1	645.0	695.0	4.0	4.1	0.578	0.024	A
081178	1	645.0	695.0	-3.0	-2.4	-1.064	0.038	A
091578	1	645.0	695.0	-3.0	-0.1	-0.458	0.024	A
062379	1	568.4	726.8	4.0	-0.9	0.509	0.082	A
080479	1	645.0	695.0	-4.0	-1.6	-0.635	0.017	A
102879	1	552.8	717.0	1.0	2.9	-0.770	0.157	A
122379	1	559.0	743.8	-6.0	-1.0	-0.384	0.143	B
062980	1	645.0	695.0	-4.0	-0.9	-0.123	0.050	A
101280	1	645.0	695.0	0.0	2.6	-0.733	0.121	A
122780	1	645.0	695.0	4.0	4.0	0.854	0.002	A
090577	3	550.0	600.0	5.0	4.1	0.035	0.351	A
113077	3	550.0	600.0	2.0	0.0	0.250	0.011	A
082978	3	550.0	600.0	3.0	2.9	0.346	0.023	A
020179	3	550.0	600.0	5.0	4.5	0.097	0.135	A

102977	1	645.0	695.0	5.0	3.8	0.751	0.037	A
082978	1	645.0	695.0	5.0	2.9	0.492	0.013	A
020179	1	645.0	695.0	4.0	4.5	0.130	0.018	A
070779	1	645.0	695.0	4.0	5.5	2.510	0.003	A
081879	1	645.0	695.0	2.0	1.0	1.105	0.002	A
120279	1	645.0	695.0	-3.0	-2.1	-1.249	0.002	A
042580	1	575.6	732.9	2.0	-1.1	0.052	0.522	B
091480	1	645.0	695.0	0.0	0.0	1.000	0.000	A
121480	1	545.7	717.6	-5.0	-0.9	-0.181	0.274	B
091381	1	645.0	695.0	-3.0	-0.2	-0.324	0.003	S
102977	3	550.0	600.0	5.0	3.8	0.381	0.129	A
061178	3	550.0	600.0	0.0	-2.4	0.132	0.254	B
091578	3	550.0	600.0	-1.0	-0.1	0.269	0.138	C
062379	3	550.0	600.0	-2.0	-0.9	0.736	0.023	A

070779	3	550.0	600.0	4.0	5.5	1.219	0.020	A
081879	3	550.0	600.0	2.0	1.0	0.535	0.007	A
120279	3	550.0	600.0	-1.0	-2.1	0.060	0.797	A
062980	3	550.0	600.0	1.0	-0.9	0.175	0.442	C
101280	3	550.0	600.0	2.0	2.6	0.378	0.013	A
032981	3	550.0	600.0	1.0	3.0	0.074	0.401	S

080479	3	550.0	600.0	0.0	-1.6	0.376	0.023	A
102879	3	550.0	600.0	4.0	2.9	0.877	0.001	A
122379	3	550.0	600.0	-1.0	-1.0	0.088	0.068	B
091480	3	550.0	600.0	0.0	0.0	1.000	0.000	A
122780	3	550.0	600.0	3.0	4.0	0.352	0.064	A
091381	3	550.0	600.0	-3.0	-0.2	-0.240	0.109	S

HAJO (Rayleigh - 040388; Love - 040388)

090577	1	1441.7	1647.6	2.0	0.0	-0.456	0.175	A
061178	1	1605.0	1665.0	5.0	3.3	1.032	0.006	A
091578	1	1605.0	1665.0	2.0	0.3	0.555	0.007	A
112978	1	1605.0	1665.0	1.0	3.8	0.434	0.022	A
062379	1	1489.8	1652.9	-2.0	0.8	0.614	0.081	A
080479	1	1605.0	1665.0	1.0	0.4	0.880	0.004	A
102879	1	1578.3	1673.7	-3.0	-2.8	0.499	0.227	B
122379	1	1605.0	1665.0	2.0	3.3	0.538	0.046	B
061280	1	1605.0	1665.0	-3.0	-2.6	0.129	0.181	B
091480	1	1566.9	1668.0	6.0	1.9	-0.919	0.094	A
121480	1	1571.8	1655.8	-1.0	-0.3	0.498	0.041	A
032981	1	1543.0	1659.7	1.0	-1.8	-0.252	0.176	B
052781	1	1590.6	1657.8	-1.0	-1.4	0.087	0.284	B
101881	1	1605.0	1665.0	2.0	1.5	0.724	0.008	A
122781	1	1568.2	1668.9	2.0	2.1	0.745	0.054	A
120582	1	1493.2	1648.0	2.0	2.1	0.624	0.041	A
061283	1	1409.7	1529.5	0.0	-0.4	1.407	0.168	B
042584	1	1605.0	1665.0	3.0	0.9	1.090	0.011	A
102784	1	1605.0	1665.0	2.0	2.7	0.665	0.031	A
121684	1	1605.0	1665.0	2.0	3.0	0.885	0.029	A
021085	1	1605.0	1665.0	4.0	2.6	1.085	0.013	A
072085	1	1605.0	1665.0	1.0	3.4	0.338	0.085	B
062087	1	1605.0	1665.0	3.0	5.0	0.594	0.022	A
111587	1	1605.0	1665.0	5.0	3.8	1.756	0.012	A
122787	1	1542.8	1662.9	2.0	4.5	0.520	0.045	A
040388	1	1605.0	1665.0	0.0	0.0	1.000	0.000	A
091488	1	1544.4	1661.2	3.0	3.4	1.162	0.045	A
090289	1	1605.0	1665.0	-1.0	-2.0	0.131	0.107	B
090577	3	1400.0	1460.0	0.0	0.0	0.611	0.039	A
070578	3	1400.0	1460.0	3.0	0.9	0.699	0.073	A
110478	3	1400.0	1460.0	-1.0	-1.0	1.048	0.117	A
020179	3	1400.0	1460.0	0.0	1.0	0.192	0.393	B
070779	3	1400.0	1460.0	0.0	-2.9	2.827	0.105	A
102879	3	1400.0	1460.0	-2.0	-2.8	0.579	0.209	A
122379	3	1400.0	1460.0	4.0	3.3	0.756	0.051	A
062980	3	1400.0	1460.0	0.0	2.0	0.208	0.416	C
101280	3	1400.0	1460.0	-2.0	-3.4	0.622	0.097	A
122780	3	1400.0	1460.0	-1.0	-2.1	0.867	0.153	A
042281	3	1400.0	1460.0	3.0	1.3	0.575	0.084	A
091381	3	1400.0	1460.0	2.0	-0.6	1.201	0.067	A
112981	3	1400.0	1460.0	2.0	2.5	0.274	0.341	C
042582	3	1400.0	1460.0	2.0	0.8	0.763	0.064	A
122682	3	1400.0	1460.0	-2.0	-2.7	0.562	0.109	A
102683	3	1423.4	1471.6	2.0	1.2	1.803	0.036	A
071484	3	1400.0	1460.0	1.0	0.9	0.475	0.111	B
120284	3	1354.0	1450.5	-2.0	-1.9	0.773	0.097	A
122884	3	1419.6	1462.9	6.0	5.7	0.157	0.480	B
042585	3	1421.0	1465.2	-1.0	-0.1	0.276	0.212	B
041787	3	1400.4	1460.9	5.0	6.6	1.362	0.049	B
080287	3	1400.0	1460.0	1.0	1.1	1.199	0.095	A
121387	3	1400.0	1460.0	3.0	2.2	1.052	0.028	A
021388	3	1400.0	1460.0	0.0	0.8	0.469	0.105	A
091488	3	1400.0	1460.0	0.0	3.4	1.090	0.104	A
090289	3	1400.0	1460.0	-1.0	-2.0	0.136	0.592	A

102977	1	1446.2	1671.4	-1.0	1.3	-0.448	0.400	B
070578	1	1497.3	1673.8	-1.0	0.9	0.190	0.339	B
110478	1	1551.1	1662.4	4.0	-1.0	-0.281	0.209	B
020179	1	1565.5	1663.1	3.0	1.0	-0.132	0.368	B
070779	1	1505.5	1643.9	0.0	-2.9	-1.933	0.041	A
081879	1	1566.9	1664.8	3.0	-0.7	-0.874	0.046	A
120279	1	1605.0	1665.0	4.0	2.6	1.248	0.008	A
042580	1	1474.4	1687.1	8.0	3.1	-0.075	0.662	C
062980	1	1605.0	1665.0	1.0	2.0	0.156	0.099	B
101280	1	1605.0	1665.0	-2.0	-3.4	0.794	0.021	A
122780	1	1538.3	1654.6	0.0	-2.1	-0.730	0.064	A
042281	1	1605.0	1665.0	4.0	1.3	0.838	0.015	A
091381	1	1605.0	1665.0	2.0	-0.6	1.059	0.028	A
112981	1	1605.0	1665.0	3.0	2.5	0.415	0.008	A
042582	1	1605.0	1665.0	1.0	0.8	0.614	0.036	B
122682	1	1525.2	1662.8	-2.0	-2.7	-0.404	0.512	B
102683	1	1605.0	1665.0	1.0	1.2	0.640	0.028	A
071484	1	1605.0	1665.0	1.0	0.9	1.028	0.018	A
120284	1	1571.1	1649.8	0.0	-1.9	-0.866	0.037	A
122884	1	1605.0	1665.0	6.0	5.7	1.005	0.015	A
042585	1	1605.0	1665.0	1.0	-0.1	0.624	0.016	A
041787	1	1500.6	1649.5	2.0	6.6	0.392	0.112	B
080287	1	1559.6	1655.4	6.0	1.1	-0.353	0.071	S
121387	1	1605.0	1665.0	2.0	2.2	0.815	0.024	A
021388	1	1605.0	1665.0	1.0	0.8	0.840	0.005	A
050488	1	1540.4	1674.3	2.0	4.0	0.852	0.210	B
021289	1	1605.0	1665.0	6.0	4.7	1.627	0.013	A
101989	1	1605.0	1665.0	2.0	-0.5	1.498	0.029	A
102977	3	1400.0	1460.0	-1.0	1.3	0.483	0.117	A
091578	3	1400.0	1460.0	2.0	0.3	0.572	0.113	A
112978	3	1400.0	1460.0	2.0	3.8	0.376	0.112	A
062379	3	1406.9	1455.4	1.0	0.8	1.445	0.064	A
080479	3	1400.0	1460.0	3.0	0.4	1.380	0.049	A
120279	3	1415.5	1447.0	1.0	2.6	0.359	0.646	C
061280	3	1400.0	1460.0	-1.0	-2.6	0.189	0.496	C
091480	3	1400.0	1460.0	3.0	1.9	2.624	0.069	A
121480	3	1400.0	1460.0	2.0	-0.3	1.189	0.063	A
032981	3	1400.0	1460.0	-1.0	-1.8	0.556	0.144	A
052781	3	1400.0	1460.0	1.0	-1.4	0.128	0.277	B
101881	3	1400.0	1460.0	2.0	1.5	0.648	0.409	C
122781	3	1400.0	1460.0	4.0	2.1	0.966	0.067	A
120582	3	1400.0	1460.0	3.0	2.1	1.334	0.123	A
061283	3	1400.0	1460.0	-1.0	-0.4	0.530	0.169	B
042584	3	1400.0	1460.0	5.0	0.9	-0.137	0.803	C
102784	3	1400.0	1460.0	3.0	2.7	0.962	0.035	A
121684	3	1400.0	1460.0	1.0	3.0	0.846	0.045	A
021085	3	1400.0	1460.0	2.0	2.6	0.746	0.049	A
072085	3	1412.3	1466.0	3.0	3.4	0.784	0.327	B
062087	3	1400.0	1460.0	4.0	5.0	0.608	0.204	B
111587	3	1400.0	1460.0	2.0	3.8	0.505	0.217	A
122787	3	1400.0	1460.0	4.0	4.5	0.913	0.063	A
040388	3	1400.0	1460.0	0.0	0.0	1.000	0.000	A
021289	3	1350.5	1461.3	4.0	4.7	-0.315	0.718	C
101989	3	1385.9	1488.6	-4.0	-0.5	0.183	0.839	C

SMIO (Rayleigh - 080479; Love - 080479)

082978	1	1030.0	1090.0	1.0	2.9	0.258	0.033	A	091578	1	1033.1	1107.6	7.0	1.5	-0.444	0.111	S
110478	1	1030.0	1090.0	3.0	4.9	0.300	0.013	A	112978	1	1030.0	1090.0	3.0	3.8	0.631	0.010	A
062379	1	1030.0	1090.0	-1.0	1.1	0.883	0.013	A	070779	1	1030.0	1090.0	10.0	4.7	-0.128	0.230	A
080479	1	1030.0	1090.0	0.0	0.0	1.000	0.000	A	081879	1	1030.0	1090.0	-1.0	1.8	0.258	0.076	A
120279	1	1030.0	1090.0	2.0	1.6	0.910	0.003	A	122379	1	1030.0	1090.0	3.0	3.6	0.675	0.436	B
042582	1	953.8	1092.1	-2.0	0.5	-0.671	0.262	S	082978	3	895.0	955.0	2.0	2.9	-0.547	0.011	S
091578	3	895.0	955.0	-3.0	1.5	0.391	0.468	S	110478	3	895.0	955.0	2.0	4.9	0.478	0.010	A
112978	3	895.0	955.0	5.0	3.8	0.231	0.229	A	020179	3	895.0	955.0	7.0	7.4	0.041	0.844	C
062379	3	895.0	955.0	0.0	1.1	0.610	0.054	A	070779	3	895.0	955.0	3.0	4.7	1.162	0.011	A
080479	3	895.0	955.0	0.0	0.0	1.000	0.000	A	081879	3	895.0	955.0	1.0	1.8	0.697	0.005	A
120279	3	895.0	955.0	4.0	1.6	0.364	0.043	A	122379	3	895.0	955.0	3.0	3.6	0.377	0.093	A
042582	3	895.0	955.0	-1.0	0.5	-0.426	0.336	S									

ANTO (Rayleigh - 091480; Love - 091480)

091578	1	1260.0	1400.0	1.0	2.5	0.626	0.108	A	110478	1	1340.0	1423.7	4.0	3.4	0.161	0.552	C
112978	1	1260.0	1400.0	-1.0	-1.1	0.476	0.072	A	020179	1	1336.5	1383.8	1.0	1.1	-0.073	0.372	S
062379	1	1276.8	1421.5	3.0	2.1	0.481	0.612	C	070779	1	1060.6	1239.5	6.0	5.2	-0.756	0.440	B
080479	1	1260.0	1400.0	1.0	2.6	0.986	0.039	A	081879	1	1280.9	1424.8	6.0	3.4	-0.344	0.597	B
102879	1	1260.0	1400.0	2.0	5.4	0.563	0.180	A	120279	1	1260.0	1400.0	0.0	0.3	0.944	0.050	A
122379	1	1355.8	1495.3	-2.0	-0.6	0.477	0.095	B	061280	1	1260.0	1400.0	3.0	5.6	0.123	0.341	A
091480	1	1425.1	1457.7	-2.0	1.1	0.894	0.028	S	101280	1	1260.0	1400.0	4.0	6.5	0.767	0.108	A
121480	1	1260.0	1400.0	2.0	3.6	0.677	0.066	A	122780	1	1260.0	1400.0	6.0	4.9	-0.295	0.403	B
042281	1	1260.0	1400.0	0.0	2.0	0.818	0.024	A	052781	1	1260.0	1400.0	2.0	4.5	0.075	0.476	C
112981	1	1260.0	1400.0	2.0	0.9	0.453	0.288	B	083182	1	1260.0	1400.0	-1.0	-0.5	0.171	0.520	B
120284	1	1242.0	1407.0	7.0	4.9	-0.360	0.630	B	121684	1	1260.0	1400.0	0.0	0.2	0.976	0.033	A
122884	1	1260.0	1400.0	-3.0	-2.2	0.544	0.110	A	061585	1	1260.0	1400.0	0.0	1.3	0.586	0.066	A
063085	1	1260.0	1400.0	-3.0	-2.7	0.461	0.077	A	031287	1	1260.0	1400.0	0.0	0.4	0.349	0.143	A
040387	1	1260.0	1400.0	-1.0	0.0	1.566	0.023	A	041787	1	1348.9	1463.2	-3.0	-3.1	0.453	0.744	C
062087	1	1260.0	1400.0	-2.0	-1.8	0.638	0.042	A	080287	1	1356.6	1467.5	1.0	2.2	0.274	0.331	B
111587	1	1260.0	1400.0	-2.0	-0.5	1.390	0.047	A	091488	1	1260.0	1400.0	0.0	0.0	1.000	0.000	A
012289	1	1260.0	1400.0	-1.0	0.4	0.989	0.025	A	070889	1	1260.0	1400.0	0.0	-0.2	0.304	0.090	A
090289	1	1260.0	1400.0	4.0	4.6	0.136	0.629	B	101989	1	1260.0	1400.0	2.0	3.6	1.104	0.063	A
110478	3	998.7	1139.5	3.0	2.3	0.401	0.329	B	070779	3	979.3	1075.9	5.0	4.1	1.092	0.063	A
080479	3	1100.0	1250.0	2.0	1.5	0.529	0.118	A	081879	3	973.0	1075.1	4.0	2.3	0.419	0.132	A
102879	3	1265.8	1324.6	5.0	4.4	0.399	0.071	B	091480	3	1100.0	1250.0	0.0	0.0	1.000	0.000	A
101280	3	986.4	1080.0	3.0	5.4	0.300	0.242	A	121480	3	1100.0	1250.0	3.0	2.5	0.437	0.138	A
122780	3	985.7	1116.1	3.0	3.8	0.372	0.332	B	032981	3	1100.0	1250.0	2.0	3.6	0.208	0.335	A
042281	3	985.7	1119.1	2.0	0.9	0.206	0.356	B	120284	3	996.2	1106.6	5.0	3.8	0.405	0.217	B
121684	3	1100.0	1250.0	-1.0	-0.9	0.528	0.125	A	061585	3	1100.0	1250.0	2.0	0.3	0.432	0.162	B
040387	3	985.9	1073.3	-2.0	-1.1	0.583	0.152	A	041787	3	1003.4	1094.5	-9.0	-4.2	1.678	0.211	S
062087	3	1100.0	1250.0	-2.0	-2.9	0.295	0.200	B	080287	3	1003.0	1109.8	0.0	1.2	0.388	0.273	A
111587	3	1004.6	1111.9	-4.0	-1.5	0.183	0.460	A	091488	3	976.6	1098.6	-1.0	-1.1	0.264	0.318	A
012289	3	993.0	1082.8	-6.0	-0.7	0.159	0.252	C	070889	3	1100.0	1250.0	-3.0	-1.3	0.116	0.553	C

KOED (Rayleigh - 091480; Love - 091480)

091578	1	1295.6	1415.7	2.0	2.0	0.718	0.351	B	110478	1	1370.0	1490.0	2.0	0.0	0.401	0.089	A
112978	1	1370.0	1490.0	0.0	-1.1	0.669	0.010	A	062379	1	1370.0	1490.0	0.0	2.2	0.992	0.033	A
070779	1	1330.0	1435.1	3.0	0.8	-0.158	0.487	B	081879	1	1370.0	1490.0	0.0	2.3	0.358	0.058	A
102879	1	1370.0	1490.0	2.0	3.1	0.890	0.020	A	120279	1	1370.0	1490.0	1.0	1.0	1.011	0.022	A
122379	1	1370.0	1490.0	-1.0	-0.8	0.534	0.024	A	042580	1	1433.5	1477.5	-2.0	-0.4	0.051	0.099	B
061280	1	1370.0	1490.0	2.0	3.1	0.158	0.095	A	062980	1	1370.0	1490.0	0.0	0.7	0.272	0.115	A
091480	1	1370.0	1490.0	0.0	0.0	1.000	0.000	A	101280	1	1370.0	1490.0	2.0	4.0	0.985	0.041	A
121480	1	1370.0	1490.0	3.0	3.5	0.762	0.029	A	122780	1	1370.0	1490.0	5.0	1.2	-0.180	0.226	A
032981	1	1370.0	1490.0	2.0	1.8	0.203	0.077	A	042281	1	1370.0	1490.0	1.0	2.3	0.950	0.023	A
052781	1	1370.0	1490.0	1.0	2.5	0.083	0.107	A	091381	1	1370.0	1490.0	3.0	3.2	1.287	0.030	A
101881	1	1370.0	1490.0	2.0	1.9	0.947	0.012	A	112981	1	1370.0	1490.0	3.0	1.9	0.441	0.220	A
122781	1	1370.0	1490.0	0.0	0.9	0.927	0.033	A	042582	1	1370.0	1490.0	2.0	2.6	0.878	0.027	A
083182	1	1370.0	1490.0	1.0	-0.5	0.229	0.176	A	120582	1	1435.2	1482.1	0.0	1.2	1.015	0.006	A
122682	1	1370.0	1490.0	-1.0	0.4	0.174	0.519	C	061283	1	1370.0	1490.0	2.0	2.5	1.324	0.011	A
100683	1	1437.3	1485.3	0.0	0.2	0.962	0.026	A	102683	1	1370.0	1490.0	2.0	1.8	1.206	0.023	A

021984	1	1370.0	1490.0	0.0	1.0	0.783	0.037	A
102784	1	1370.0	1490.0	-1.0	0.0	1.059	0.027	A
121684	1	1370.0	1490.0	1.0	0.7	1.463	0.011	A
021085	1	1370.0	1490.0	1.0	1.3	1.197	0.051	A
063085	1	1370.0	1490.0	0.0	-0.6	0.705	0.050	A
031287	1	1370.0	1490.0	1.0	0.4	0.357	0.052	A
062087	1	1370.0	1490.0	-1.0	-1.0	0.692	0.022	A
111587	1	1370.0	1490.0	1.0	0.4	1.495	0.019	A
122787	1	1370.0	1490.0	2.0	0.2	0.791	0.142	B
040388	1	1370.0	1490.0	2.0	2.0	1.183	0.030	A
091488	1	1416.2	1502.4	1.0	1.7	1.269	0.032	A
101989	1	1425.0	1497.4	0.0	1.8	0.691	0.201	B
112978	3	1230.0	1300.0	0.0	-1.1	0.938	0.193	A
070779	3	1230.0	1300.0	1.0	0.8	1.702	0.210	A
102879	3	1238.9	1293.0	1.0	3.1	1.732	0.263	A
061280	3	1240.1	1310.6	4.0	3.1	0.231	0.102	A
091480	3	1230.0	1300.0	0.0	0.0	1.000	0.000	A
121480	3	1192.0	1300.1	3.0	3.5	-0.408	0.805	S
032981	3	1230.0	1300.0	2.0	1.8	0.617	0.268	A
101881	3	1230.0	1300.0	2.0	1.9	0.774	0.049	A
042582	3	1230.0	1300.0	2.0	2.6	0.488	0.260	A
061283	3	1255.4	1310.5	4.0	2.5	1.065	0.221	A
102683	3	1252.2	1350.6	2.0	1.8	0.815	0.280	B
102784	3	1259.1	1290.1	-2.0	0.0	0.925	0.069	A
121684	3	1257.1	1318.9	1.0	0.7	1.067	0.025	A
072085	3	1230.0	1300.0	-1.0	-0.5	0.587	0.163	A
040387	3	1203.4	1292.9	2.0	0.8	0.870	0.218	A
111587	3	1241.6	1302.3	5.0	0.4	0.538	0.581	B
021388	3	1230.0	1300.0	1.0	0.6	1.302	0.265	A
091488	3	1230.0	1300.0	2.0	1.7	0.662	0.108	A
101989	3	1261.2	1299.9	5.0	1.8	0.533	0.245	C

GRFO (Rayleigh - 091488; Love - 091488)

110478	1	1500.0	1630.0	0.0	0.4	0.165	0.148	A
020179	1	1580.1	1626.5	0.0	-2.4	0.029	0.202	C
080479	1	1500.0	1630.0	0.0	2.3	0.853	0.029	A
120279	1	1500.0	1630.0	-1.0	0.0	0.822	0.021	A
061280	1	1466.4	1606.9	0.0	3.1	0.093	0.122	A
091480	1	1500.0	1630.0	-2.0	-0.7	0.647	0.040	A
121480	1	1500.0	1630.0	1.0	2.6	0.612	0.040	A
042281	1	1500.0	1630.0	0.0	1.2	0.739	0.036	A
101881	1	1500.0	1630.0	0.0	0.8	0.691	0.014	A
122781	1	1500.0	1630.0	-2.0	-0.1	0.673	0.039	A
120582	1	1500.0	1630.0	-1.0	0.1	0.746	0.049	A
100683	1	1500.0	1630.0	-1.0	-0.9	0.826	0.022	A
021984	1	1403.2	1629.9	-1.0	-0.5	0.591	0.085	A
032984	1	1500.0	1630.0	1.0	2.8	0.550	0.015	A
071484	1	1500.0	1630.0	1.0	1.9	0.964	0.008	A
102784	1	1363.3	1634.2	-3.0	-1.0	0.722	0.040	A
121684	1	1500.0	1630.0	-1.0	-0.6	0.972	0.009	A
021085	1	1500.0	1630.0	0.0	0.0	0.881	0.044	A
061585	1	1500.0	1630.0	0.0	0.9	0.525	0.034	A
072087	1	1500.0	1630.0	-2.0	-1.6	0.431	0.102	B
040387	1	1500.0	1630.0	-2.0	-0.6	1.483	0.004	A
080287	1	1439.5	1618.1	1.0	1.7	0.336	0.049	A
121387	1	1500.0	1630.0	-2.0	-1.9	0.846	0.037	A
021388	1	1500.0	1630.0	-1.0	0.1	0.780	0.027	A
061488	1	1554.6	1593.8	3.0	0.6	0.061	0.135	C
121788	1	1500.0	1630.0	3.0	1.5	0.859	0.069	A
021289	1	1315.4	1625.5	-3.0	-3.0	0.751	0.494	B
090289	1	1547.5	1591.9	-2.0	0.9	0.135	0.089	C
110478	3	1267.0	1398.9	-3.0	0.4	0.181	0.778	S
020179	3	1339.6	1403.0	-3.0	-2.4	0.228	0.183	A

071484	1	1370.0	1490.0	3.0	3.1	1.237	0.019	A
120284	1	1370.0	1490.0	2.0	2.6	0.264	0.127	A
122884	1	1422.2	1523.5	-1.0	0.0	0.754	0.148	B
061585	1	1370.0	1490.0	1.0	2.2	0.705	0.020	A
072085	1	1370.0	1490.0	0.0	-0.5	0.700	0.017	A
040387	1	1370.0	1490.0	0.0	0.8	1.954	0.013	A
080287	1	1370.0	1490.0	2.0	2.9	0.446	0.038	A
121387	1	1370.0	1490.0	0.0	-1.5	1.167	0.015	A
021388	1	1370.0	1490.0	1.0	0.6	1.063	0.032	A
061488	1	1370.0	1490.0	2.0	0.0	0.046	0.366	A
070889	1	1332.4	1476.7	-2.0	0.1	0.229	0.159	B
110478	3	1230.0	1300.0	1.0	0.0	0.568	0.182	B
062379	3	1258.5	1304.9	0.0	2.2	1.196	0.072	A
081879	3	1230.0	1300.0	2.0	2.3	0.520	0.253	B
122379	3	1230.0	1300.0	-6.0	-0.8	0.090	0.918	B
062980	3	1248.1	1295.5	1.0	0.7	0.442	0.166	A
101280	3	1230.0	1300.0	1.0	4.0	0.650	0.141	A
122780	3	1221.0	1291.4	0.0	1.2	0.634	0.254	S
091381	3	1224.6	1300.9	6.0	3.2	0.263	0.809	C
122781	3	1230.0	1300.0	0.0	0.9	1.082	0.155	A
120582	3	1241.8	1299.7	0.0	1.2	0.513	0.137	A
100683	3	1222.2	1323.3	5.0	0.2	0.428	0.925	S
071484	3	1235.2	1316.3	4.0	3.1	0.795	0.209	A
120284	3	1248.2	1309.1	2.0	2.6	1.577	0.301	A
063085	3	1251.2	1299.5	1.0	-0.6	0.835	0.135	A
031287	3	1230.0	1300.0	2.0	0.4	0.185	0.621	B
062087	3	1190.5	1286.6	1.0	-1.0	-0.425	0.696	S
121387	3	1230.0	1300.0	3.0	-1.5	0.616	0.555	B
040388	3	1249.4	1320.8	1.0	2.0	0.337	0.828	B
070889	3	1230.0	1300.0	2.0	0.1	0.466	0.153	A

112978	1	1500.0	1630.0	-2.0	-2.0	0.452	0.032	A
070779	1	1325.4	1620.0	5.0	1.7	-0.172	0.729	B
081879	1	1349.2	1533.0	7.0	2.0	-0.225	0.631	S
122379	1	1500.0	1630.0	-3.0	-1.6	0.415	0.042	A
062980	1	1500.0	1630.0	-1.0	-0.3	0.139	0.176	A
101280	1	1500.0	1630.0	2.0	4.1	0.678	0.015	A
032981	1	1537.1	1611.8	0.0	1.9	0.120	0.150	A
052781	1	1400.6	1657.0	2.0	2.3	0.022	0.925	C
112981	1	1406.0	1645.9	1.0	0.5	0.303	0.282	B
042582	1	1500.0	1630.0	0.0	1.6	0.616	0.041	A
061283	1	1336.7	1659.8	1.0	2.0	1.042	0.023	A
102683	1	1349.2	1630.6	-1.0	0.9	0.927	0.029	A
030784	1	1533.4	1612.9	-1.0	0.9	0.168	0.364	B
042584	1	1356.5	1634.8	0.0	0.8	0.737	0.065	A
091584	1	1563.4	1597.6	-2.0	-3.0	0.044	0.159	C
120284	1	1561.6	1606.1	8.0	2.5	-0.182	0.113	S
122884	1	1386.7	1607.0	-2.0	-2.0	0.486	0.049	A
042585	1	1440.0	1642.9	1.0	2.2	0.539	0.177	A
063085	1	1544.7	1612.2	-3.0	-2.6	0.522	0.039	A
031287	1	1500.0	1630.0	-1.0	-0.7	0.330	0.439	B
062087	1	1500.0	1630.0	-3.0	-2.5	0.510	0.013	A
111587	1	1500.0	1630.0	-1.0	-1.0	1.210	0.011	A
122787	1	1336.9	1628.2	-2.0	-1.5	0.665	0.296	B
040388	1	1500.0	1630.0	1.0	1.4	0.892	0.024	A
091488	1	1500.0	1630.0	0.0	0.0	1.000	0.000	A
012289	1	1500.0	1630.0	-1.0	-1.0	0.900	0.057	A
070889	1	1380.5	1632.3	-2.0	-1.1	0.270	0.464	B
101989	1	1291.9	1642.2	-3.0	1.5	0.921	0.118	A
112978	3	1333.3	1395.7	-4.0	-2.0	0.351	0.553	S
070779	3	1330.0	1430.0	-1.0	1.7	2.716	0.076	A

080479	3	1330.0	1430.0	0.0	2.3	0.842	0.028	A
120279	3	1330.0	1430.0	2.0	0.0	0.301	0.246	A
061280	3	1330.0	1430.0	1.0	3.1	0.245	0.154	A
091480	3	1330.0	1430.0	-2.0	-0.7	2.510	0.035	A
121480	3	1330.0	1430.0	4.0	2.6	0.334	0.296	A
032981	3	1330.0	1430.0	0.0	1.9	0.849	0.078	A
101881	3	1330.0	1430.0	0.0	0.8	1.026	0.033	A
042582	3	1330.0	1430.0	0.0	1.6	1.157	0.074	A
122682	3	1330.0	1430.0	-1.0	1.2	0.484	0.270	B
100683	3	1330.0	1430.0	-4.0	-0.9	-1.012	0.171	A
030784	3	1330.0	1430.0	-1.0	0.9	0.280	0.400	B
042584	3	1330.0	1430.0	0.0	0.8	0.841	0.103	A
102784	3	1330.0	1430.0	-3.0	-1.0	1.431	0.039	A
121684	3	1330.0	1430.0	-1.0	-0.6	1.656	0.022	A
021085	3	1364.3	1408.4	-2.0	0.0	0.552	0.164	C
061585	3	1330.0	1430.0	2.0	0.9	0.375	0.081	A
072085	3	1330.0	1430.0	-2.0	-1.6	1.030	0.064	A
040387	3	1330.0	1430.0	-1.0	-0.6	1.348	0.016	A
080287	3	1330.0	1430.0	1.0	1.7	0.430	0.071	A
121387	3	1330.0	1430.0	-1.0	-1.9	1.193	0.062	A
040388	3	1330.0	1430.0	2.0	1.4	0.611	0.069	A
121788	3	1330.0	1430.0	2.0	1.5	1.729	0.071	A
070889	3	1330.0	1430.0	-6.0	-1.1	0.703	0.037	A
101989	3	1337.2	1408.0	-2.0	1.5	0.381	0.594	B

SCP (Rayleigh - 091488)

042281	1	3164.1	3305.6	-2.0	-0.7	0.628	0.257	B
091381	1	3060.0	3200.0	0.0	-0.8	1.032	0.124	A
120582	1	3082.0	3279.9	-2.0	-1.6	0.783	0.251	A
100683	1	3093.4	3264.0	-2.0	-2.5	0.744	0.320	A
021984	1	3103.4	3176.0	-1.0	-1.0	0.676	0.196	A
102784	1	3073.9	3182.2	-3.0	-2.8	0.745	0.195	A
122884	1	3330.6	3413.9	-2.0	-0.7	0.390	0.308	B
061585	1	3358.4	3429.4	-1.0	-0.3	0.333	0.117	B
031287	1	3231.1	3310.0	-6.0	-2.2	1.293	0.403	S
041787	1	3063.6	3186.8	-2.0	-0.9	0.598	0.264	B
121387	1	3394.2	3425.6	-10.0	-5.1	0.718	0.090	S
021388	1	3060.0	3200.0	-2.0	-3.3	-0.792	0.462	S
091488	1	3060.0	3200.0	0.0	0.0	1.000	0.000	A
012289	1	3060.0	3200.0	-3.0	-2.9	-0.871	0.275	S
101989	1	3045.1	3311.7	1.0	-2.6	0.944	0.412	A

BEL (Rayleigh - 122781; Love - 122781)

091381	1	1412.7	1550.2	4.0	2.2	1.010	0.198	A
122781	1	1470.0	1550.0	0.0	0.0	1.000	0.000	A
061283	1	1493.4	1565.0	2.0	1.6	1.527	0.197	B
102683	1	1489.7	1542.8	1.0	0.9	1.259	0.088	B
071484	1	1470.0	1550.0	3.0	2.2	1.399	0.025	A
061283	3	1300.0	1370.0	4.0	1.6	1.205	0.372	C

KEV (Rayleigh - 122781; Love - 122781)

101881	1	1140.0	1240.0	1.0	0.9	0.848	0.050	A
122781	1	1140.0	1240.0	0.0	0.0	1.000	0.000	A
120582	1	1140.0	1240.0	1.0	0.3	0.848	0.051	A
030784	1	1126.7	1243.1	0.0	-1.4	0.277	0.112	A
052684	1	1095.2	1244.1	1.0	1.1	0.768	0.432	C
102784	1	1140.0	1240.0	-1.0	-0.9	0.851	0.050	A
121684	1	1147.7	1217.9	0.0	0.1	1.138	0.058	A
021085	1	1140.0	1240.0	1.0	0.7	0.932	0.086	A
063085	1	1140.0	1240.0	-1.0	-0.2	0.598	0.026	A
040387	1	1106.7	1239.1	0.0	0.3	1.509	0.073	A

081879	3	1330.0	1430.0	0.0	2.0	1.388	0.069	A
122379	3	1330.0	1430.0	-3.0	-1.6	0.382	0.149	A
062980	3	1330.0	1430.0	-1.0	-0.3	0.439	0.175	A
101280	3	1330.0	1430.0	1.0	4.1	0.984	0.030	A
122780	3	1330.0	1430.0	-1.0	1.6	0.905	0.153	A
042281	3	1330.0	1430.0	2.0	1.2	0.462	0.055	A
122781	3	1330.0	1430.0	-3.0	-0.1	1.466	0.072	A
120582	3	1330.0	1430.0	-2.0	0.1	1.151	0.066	A
061283	3	1330.0	1430.0	2.0	2.0	1.025	0.110	A
102683	3	1330.0	1430.0	-1.0	0.9	1.246	0.046	A
032984	3	1330.0	1430.0	2.0	2.8	0.326	0.129	A
071484	3	1330.0	1430.0	1.0	1.9	1.176	0.050	A
120284	3	1330.0	1430.0	0.0	2.5	2.394	0.085	A
122884	3	1330.0	1430.0	-4.0	-2.0	-0.582	0.333	A
042585	3	1330.0	1430.0	-1.0	2.2	0.651	0.368	B
063085	3	1330.0	1430.0	-3.0	-2.6	1.078	0.058	A
031287	3	1330.0	1430.0	2.0	-0.7	0.206	0.342	B
062087	3	1330.0	1430.0	-4.0	-2.5	0.114	0.687	A
111587	3	1280.5	1398.4	4.0	-1.0	0.732	0.136	S
021388	3	1330.0	1430.0	-1.0	0.1	1.298	0.063	A
091488	3	1330.0	1430.0	0.0	0.0	1.000	0.000	A
012289	3	1330.0	1430.0	1.0	-1.0	0.528	0.114	A
090289	3	1243.1	1408.3	-4.0	0.9	0.130	0.669	S

052781	1	3118.6	3197.5	-2.0	-2.3	0.065	0.762	C
042582	1	3355.8	3459.9	-1.0	-0.6	0.845	0.365	B
061283	1	3075.2	3289.7	0.0	-1.6	0.993	0.335	A
102683	1	3078.2	3180.1	-1.0	-1.4	0.943	0.102	A
030784	1	3062.4	3147.6	-1.0	-4.4	0.204	0.415	C
121684	1	3060.0	3200.0	-2.0	-1.6	1.137	0.112	A
021085	1	3087.9	3183.9	-1.0	-1.1	1.120	0.061	A
063085	1	3088.4	3144.9	-2.0	-1.1	0.779	0.183	B
040387	1	3081.8	3273.3	-4.0	-1.3	1.335	0.195	A
111587	1	3060.0	3200.0	-1.0	-1.5	1.067	0.240	A
122787	1	3062.8	3163.1	-2.0	-1.3	0.729	0.322	B
040388	1	3058.6	3179.1	1.0	-2.0	0.789	0.304	A
121788	1	3080.2	3167.7	-1.0	-1.2	-1.074	0.122	S
070889	1	3077.1	3274.9	1.0	-2.1	0.402	0.449	B

112981	1	1501.1	1565.9	2.0	1.0	0.481	0.455	C
042582	1	1470.0	1550.0	2.0	1.7	0.953	0.040	A
100683	1	1494.2	1559.9	0.0	-0.7	1.055	0.165	B
032984	1	1371.5	1541.6	2.0	2.7	0.731	0.148	A
122781	3	1300.0	1370.0	0.0	0.0	1.000	0.000	A
071484	3	1331.9	1384.0	3.0	2.2	0.736	0.688	C

112981	1	1140.0	1240.0	2.0	1.4	0.353	0.082	A
042582	1	1077.1	1227.5	2.0	1.6	0.738	0.082	A
061283	1	1155.0	1248.8	3.0	1.0	1.192	0.071	A
032984	1	1128.6	1241.6	3.0	2.3	0.559	0.135	A
071484	1	1159.1	1231.8	2.0	2.2	1.085	0.087	A
120284	1	1119.3	1251.6	1.0	0.5	0.297	0.188	B
122884	1	1140.0	1240.0	-1.0	0.3	0.534	0.102	A
061585	1	1164.9	1232.3	1.0	1.6	0.539	0.032	A
072085	1	1140.0	1240.0	0.0	-1.3	0.555	0.055	A
041787	1	1166.6	1257.7	0.0	-0.2	0.503	0.382	C

062087	1	1140.0	1240.0	-1.0	-1.2	0.480	0.057	A
111587	1	1132.5	1223.6	1.0	0.1	1.122	0.056	A
122787	1	1140.0	1240.0	0.0	0.0	0.638	0.085	A
040388	1	1098.9	1231.3	2.0	0.5	0.893	0.066	A
121788	1	1162.2	1250.6	3.0	1.1	0.947	0.055	A
021289	1	1097.5	1221.2	0.0	-2.3	0.755	0.119	A
090289	1	1112.5	1242.5	3.0	-2.2	0.121	0.244	A
101881	3	1055.6	1114.9	1.0	0.9	0.952	0.210	B
122781	3	1020.0	1120.0	0.0	0.0	1.000	0.000	A
120582	3	1020.0	1120.0	-1.0	0.3	0.573	0.599	C
071484	3	1024.2	1118.6	2.0	2.2	1.024	0.375	A
120284	3	1020.0	1120.0	0.0	0.5	1.198	0.699	S
122884	3	1020.0	1120.0	-1.0	0.3	0.476	0.603	C
063085	3	1038.8	1101.5	0.0	-0.2	0.811	0.110	A
040387	3	1062.6	1096.3	1.0	0.3	1.206	0.349	B
021388	3	1020.0	1120.0	1.0	-0.9	0.957	0.421	A
021289	3	1060.3	1102.1	0.0	-2.3	1.222	0.283	B
101989	3	1029.0	1099.2	4.0	0.1	0.917	0.412	B

TOL (Rayleigh - 061283; Love - 061283)

112981	1	1910.6	2202.6	0.0	-1.6	0.319	0.731	C
042582	1	1926.3	2224.0	0.0	-0.5	0.712	0.226	A
061283	1	2020.0	2120.0	0.0	0.0	1.000	0.000	A
102683	1	1920.0	2202.9	-1.0	-1.2	0.961	0.138	A
030784	1	1937.9	2165.1	0.0	-0.9	0.257	0.491	B
042584	1	1932.1	2152.7	-1.0	-1.2	0.870	0.094	A
102784	1	2040.4	2186.1	-4.0	-3.0	-0.680	0.413	B
122884	1	2065.6	2198.1	-3.0	-4.2	0.526	0.340	B
061585	1	1937.5	2178.4	-1.0	-1.2	0.529	0.413	B
072085	1	2047.4	2166.4	-1.0	-3.6	0.537	0.255	B
040387	1	1951.1	2148.3	-2.0	-2.7	1.531	0.198	A
121387	1	1928.4	2229.2	-3.0	-3.8	0.822	0.159	A
021388	1	1985.7	2168.2	-5.0	-1.8	0.961	0.468	B
091488	1	1899.1	2178.9	-1.0	-2.1	1.036	0.110	A
012289	1	1901.1	2165.8	-1.0	-3.0	1.011	0.117	A
070889	1	1872.8	2143.1	0.0	-3.2	0.349	0.340	B
061283	3	1830.0	1930.0	0.0	0.0	1.000	0.000	A
032984	3	1830.0	1930.0	-2.0	0.8	0.388	0.367	C
071484	3	1830.0	1930.0	-2.0	-0.2	0.931	0.277	C
063085	3	1839.8	1913.8	-6.0	-4.8	0.523	0.353	C
040388	3	1866.7	1923.5	-5.0	-0.6	1.426	0.194	C

COL (Rayleigh - 021388)

120582	1	2220.0	2320.0	0.0	2.4	0.553	0.400	B
102683	1	2203.0	2395.9	0.0	2.0	0.761	0.354	A
042584	1	2229.1	2289.1	1.0	1.3	2.463	0.131	C
102784	1	2026.6	2345.4	-1.0	1.6	1.374	0.224	A
063085	1	2215.3	2424.3	3.0	5.3	0.632	0.144	A
040387	1	2242.8	2342.7	2.0	3.4	1.353	0.066	A
062087	1	2203.1	2374.6	-1.0	3.4	0.405	0.257	A
111587	1	2220.0	2320.0	3.0	3.6	1.285	0.072	A
122787	1	2220.0	2320.0	1.0	4.1	0.327	0.390	C
040388	1	2179.7	2341.0	0.0	0.7	0.789	0.158	A
091488	1	2220.0	2320.0	2.0	4.7	0.914	0.240	B
012289	1	2220.0	2320.0	1.0	1.6	0.840	0.181	B
101989	1	2220.0	2320.0	2.0	-0.2	1.294	0.052	A

GAC (Rayleigh - 040387)

083182	1	2915.0	3204.8	0.0	-1.5	0.138	0.263	B
061283	1	2900.0	3040.0	1.0	-0.2	0.693	0.060	A
102683	1	3114.5	3250.0	-3.0	0.0	0.431	0.261	S

080287	1	1140.0	1240.0	2.0	2.1	0.321	0.042	A
121387	1	1086.4	1233.9	0.0	-2.9	0.904	0.061	A
021388	1	1085.4	1230.3	2.0	-0.9	0.851	0.074	A
091488	1	1070.5	1220.2	2.0	1.5	0.946	0.082	A
012289	1	1155.1	1226.1	0.0	-0.9	0.893	0.068	A
070889	1	1140.0	1240.0	2.0	-0.4	0.354	0.079	A
101989	1	1140.0	1240.0	3.0	0.1	1.019	0.066	A
112981	3	1020.0	1120.0	2.0	1.4	0.381	0.770	C
042582	3	1020.0	1120.0	2.0	1.6	0.362	0.742	C
061283	3	1042.9	1107.1	3.0	1.0	0.892	0.519	C
102784	3	1045.4	1097.6	-1.0	-0.9	0.804	0.158	A
121684	3	1046.0	1104.4	1.0	0.1	1.209	0.175	B
021085	3	1020.0	1120.0	1.0	0.7	0.480	0.824	C
072085	3	1020.0	1120.0	-1.0	-1.3	0.482	0.299	B
121387	3	1020.0	1120.0	1.0	-2.9	0.796	0.557	B
091488	3	1020.0	1120.0	2.0	1.5	1.229	0.349	B
070889	3	1061.2	1086.7	2.0	-0.4	0.713	0.093	B

122781	1	1955.8	2176.1	-2.0	-2.1	0.714	0.207	A
120582	1	1905.8	2216.8	-2.0	-2.0	0.697	0.268	A
100683	1	1904.7	2157.4	-2.0	-2.9	0.930	0.169	A
021984	1	1921.3	2134.9	-1.0	-2.6	0.729	0.443	C
032984	1	1898.9	2152.1	1.0	0.8	0.648	0.109	A
071484	1	1898.1	2143.1	1.0	-0.2	1.154	0.150	B
121684	1	1931.9	2225.4	-2.0	-2.7	0.961	0.131	A
021085	1	1963.8	2176.1	-1.0	-2.1	0.860	0.301	A
063085	1	1947.7	2185.3	-3.0	-4.8	0.523	0.109	A
031287	1	1922.6	2155.2	-1.0	-2.7	0.306	0.790	B
041787	1	1966.1	2209.3	-3.0	-5.0	0.666	0.774	C
122787	1	1909.9	2216.6	-3.0	-3.6	0.534	0.439	A
040388	1	2020.0	2120.0	-3.0	-0.6	1.078	0.130	B
121788	1	1908.6	2153.7	2.0	-0.5	0.859	0.196	A
021289	1	1909.6	2142.9	-3.0	-5.0	0.917	0.252	A
101989	1	1838.2	2164.3	2.0	-0.4	1.026	0.129	A
100683	3	1841.4	1916.9	2.0	-2.9	0.485	0.533	C
042584	3	1830.0	1930.0	-2.0	-1.2	0.361	0.485	C
102784	3	1861.8	1943.1	-5.0	-3.0	-1.104	0.304	S
072085	3	1836.8	1905.6	-4.0	-3.6	1.063	0.156	B
070889	3	1830.0	1930.0	-2.0	-3.2	0.516	0.306	B

061283	1	2218.8	2427.3	1.0	0.8	1.411	0.454	C
021984	1	2157.6	2355.0	3.0	3.7	0.815	0.597	C
071484	1	2270.8	2465.2	1.0	3.2	2.090	0.548	C
021085	1	2252.5	2438.5	2.0	3.2	-1.582	0.420	S
072085	1	2142.9	2391.3	0.0	1.9	0.366	0.282	A
041787	1	2378.7	2421.6	10.0	5.8	-0.491	0.103	S
080287	1	2235.6	2338.5	4.0	3.2	-0.241	0.193	S
121387	1	2220.0	2320.0	-1.0	-0.7	0.810	0.066	A
021388	1	2220.0	2320.0	0.0	0.0	1.000	0.000	A
061488	1	2215.0	2406.3	-9.0	-4.1	0.094	0.660	B
121788	1	2220.0	2320.0	2.0	1.8	0.737	0.139	A
021289	1	2220.0	2320.0	3.0	2.0	0.979	0.268	B

120582	1	2825.8	3020.0	0.0	-0.3	0.124	0.458	A
100683	1	2900.0	3040.0	0.0	-1.2	0.477	0.031	A
052684	1	2843.6	3053.3	2.0	-0.5	1.023	0.815	C

071484	1	2900.0	3040.0	1.0	1.4	0.688	0.028	A
120284	1	2900.0	3040.0	-3.0	-1.1	0.170	0.220	B
122884	1	2922.5	3212.5	-1.0	0.6	0.340	0.266	A
042585	1	2900.0	3040.0	1.0	0.7	0.425	0.045	A
063085	1	2900.0	3040.0	1.0	0.2	0.393	0.057	A
031287	1	2717.9	3007.8	0.0	-0.9	0.238	0.512	B
041787	1	2900.0	3040.0	-1.0	0.4	0.352	0.225	A
080287	1	2838.1	3037.9	1.0	1.4	0.086	0.584	B
121387	1	2900.0	3040.0	-1.0	-3.8	0.626	0.068	A
021388	1	2900.0	3040.0	0.0	-2.0	0.568	0.074	A
091488	1	2859.2	3249.2	1.0	1.3	0.705	0.030	A
012289	1	2900.0	3040.0	1.0	-1.5	0.573	0.033	A
070889	1	2900.0	3040.0	2.0	-0.7	0.249	0.072	A

GDH (Rayleigh - 042584)

083182	1	2002.5	2162.8	-1.0	-0.9	0.165	0.453	B
032984	1	1999.7	2179.5	1.0	1.8	0.452	0.284	A
071484	1	1863.3	2129.7	1.0	2.1	0.800	0.341	A
120284	1	1993.5	2202.1	-2.0	-0.5	0.332	0.401	C
063085	1	1966.4	2153.6	0.0	0.7	0.517	0.359	B
031287	1	2030.0	2187.9	1.0	-0.2	0.256	0.543	C
041787	1	2038.2	2147.9	1.0	0.9	0.491	0.294	C
121387	1	2070.0	2170.0	-1.0	-3.1	1.027	0.169	A

RSCP (Rayleigh - 061283)

061283	1	3450.0	3580.0	0.0	0.0	1.000	0.000	A
102683	1	3450.0	3580.0	0.0	0.3	0.712	0.057	A
030784	1	3450.0	3580.0	-4.0	-3.0	0.141	0.182	B
042584	1	3450.0	3580.0	0.0	-0.3	0.941	0.160	A
061585	1	3450.0	3580.0	0.0	1.5	0.230	0.040	A
072085	1	3450.0	3580.0	0.0	-1.2	0.334	0.012	A

RSWT (Rayleigh - 061283)

061283	1	2450.0	2570.0	0.0	0.0	1.000	0.000	A
021984	1	2463.5	2532.7	0.0	2.1	0.444	0.233	C
071484	1	2458.9	2655.0	0.0	2.2	0.929	0.108	A
120284	1	2678.3	2734.2	-3.0	-1.5	0.383	0.221	C
061585	1	2459.2	2559.0	1.0	2.3	0.451	0.086	B
072085	1	2408.6	2617.3	1.0	0.1	0.341	0.287	A

RSSD (Rayleigh - 061283)

061283	1	3290.0	3400.0	0.0	0.0	1.000	0.000	A
102683	1	3290.0	3400.0	-1.0	0.8	0.780	0.048	A
030784	1	3175.7	3381.4	-4.0	-3.1	0.112	0.479	B
042584	1	3113.3	3366.7	-2.0	0.1	0.640	0.382	B
102784	1	3290.0	3400.0	-1.0	-0.2	0.736	0.063	A
121684	1	3290.0	3400.0	0.0	1.2	1.002	0.029	A
021085	1	3197.5	3374.1	2.0	1.5	0.685	0.057	A
061585	1	3182.9	3380.6	0.0	2.2	0.327	0.106	A
072085	1	3065.7	3402.8	0.0	-0.2	0.443	0.071	A

RSFY (Rayleigh - 061283)

061283	1	2850.0	2960.0	0.0	0.0	1.000	0.000	A
102683	1	3047.7	3188.3	0.0	0.2	0.827	0.382	C
032984	1	2916.1	3187.6	0.0	1.4	0.433	0.229	A
071484	1	2850.0	2960.0	0.0	1.6	0.770	0.163	A
120284	1	2891.8	3260.5	-1.0	-0.9	0.272	0.367	C
122884	1	2925.9	2985.2	-2.0	0.7	0.377	0.210	B
042585	1	2878.1	2998.9	0.0	0.9	0.514	0.193	A

102784	1	2900.0	3040.0	-1.0	-1.5	0.520	0.026	A
121684	1	2900.0	3040.0	0.0	-0.3	0.709	0.036	A
021085	1	2900.0	3040.0	1.0	0.2	0.579	0.038	A
061585	1	2900.0	3040.0	1.0	1.1	0.255	0.059	A
072085	1	2900.0	3040.0	-1.0	-1.7	0.353	0.025	A
040387	1	2900.0	3040.0	0.0	0.0	1.000	0.000	A
062087	1	2900.0	3040.0	-2.0	-1.2	0.288	0.047	A
111587	1	2900.0	3040.0	1.0	-0.1	0.755	0.019	A
122787	1	2911.0	3189.5	0.0	0.0	0.375	0.269	C
040388	1	2900.0	3040.0	3.0	-0.7	0.569	0.041	A
121788	1	2930.5	3028.3	3.0	0.2	0.725	0.136	B
021289	1	2900.0	3040.0	0.0	-2.5	0.552	0.035	A

100683	1	2022.9	2164.7	0.0	-0.6	0.660	0.346	B
042584	1	2070.0	2170.0	0.0	0.0	1.000	0.000	A
102784	1	2070.0	2170.0	-1.0	-0.9	0.712	0.257	B
042585	1	2000.3	2215.9	0.0	1.3	0.616	0.677	C
072085	1	1979.5	2158.9	-1.0	-1.1	0.463	0.154	A
040387	1	2045.3	2145.7	0.0	0.6	1.644	0.255	B
111587	1	1961.0	2172.5	1.0	0.5	1.047	0.274	A
070889	1	1968.1	2136.7	0.0	-0.1	0.445	0.304	A

100683	1	3450.0	3580.0	-1.0	-0.7	0.642	0.032	A
021984	1	3450.0	3580.0	0.0	0.9	0.502	0.050	A
032984	1	3450.0	3580.0	0.0	1.4	0.380	0.042	A
071484	1	3450.0	3580.0	1.0	1.8	0.906	0.020	A
063085	1	3450.0	3580.0	1.0	1.0	0.489	0.037	A

100683	1	2386.0	2585.2	0.0	0.4	0.714	0.192	A
042584	1	2095.1	2341.3	-1.0	0.2	0.779	0.178	S
102784	1	2387.6	2607.8	0.0	0.0	0.725	0.188	A
121684	1	2450.0	2570.0	0.0	1.4	1.051	0.083	A
063085	1	2458.3	2548.5	4.0	3.2	0.584	0.085	A

100683	1	3290.0	3400.0	-1.0	0.1	0.675	0.041	A
021984	1	3290.0	3400.0	1.0	1.9	0.597	0.061	A
032984	1	3290.0	3400.0	0.0	1.4	0.485	0.056	A
071484	1	3290.0	3400.0	0.0	2.1	0.906	0.027	A
120284	1	3171.6	3366.9	-3.0	-1.4	0.273	0.280	B
122884	1	3139.0	3336.8	0.0	3.0	0.524	0.247	A
042585	1	3186.3	3352.9	1.0	1.1	0.619	0.143	A
063085	1	3161.4	3404.3	1.0	2.7	0.491	0.128	A

100683	1	2785.3	2989.2	-2.0	-1.0	0.539	0.148	A
021984	1	2862.0	2967.1	-1.0	0.5	0.402	0.291	B
042584	1	3108.8	3207.8	-1.0	-0.4	0.904	0.184	S
102784	1	2850.0	2960.0	-2.0	-1.3	0.615	0.047	A
121684	1	2895.0	3210.1	-1.0	-0.1	0.931	0.099	A
021085	1	2921.6	3195.1	0.0	0.4	0.699	0.238	A
061585	1	2916.3	3213.7	0.0	1.3	0.330	0.167	A

063085 1 2850.0 2960.0 0.0 0.3 0.492 0.096 A

072085 1 2889.4 3242.4 -1.0 -1.6 0.358 0.337 A

R50N (Rayleigh - 061283)

061283 1 2780.0 2900.0 0.0 0.0 1.000 0.000 A
 102683 1 2826.9 2939.0 0.0 0.6 0.662 0.085 A
 030784 1 2798.6 3048.4 -4.0 -3.1 0.127 0.219 A
 042584 1 2780.0 2900.0 -1.0 -0.1 0.740 0.461 C
 102784 1 2780.0 2900.0 0.0 -0.6 0.637 0.043 A
 121684 1 2780.0 2900.0 1.0 0.8 0.902 0.010 A
 021085 1 2780.0 2900.0 2.0 1.1 0.709 0.031 A
 061585 1 2780.0 2900.0 0.0 1.9 0.278 0.078 A
 072085 1 2780.0 2900.0 0.0 -0.7 0.398 0.018 A

100683 1 2780.0 2900.0 0.0 -0.3 0.573 0.030 A
 021984 1 2780.0 2900.0 1.0 1.4 0.498 0.060 A
 032984 1 2780.0 2900.0 0.0 1.4 0.365 0.088 A
 071484 1 2780.0 2900.0 0.0 2.0 0.853 0.031 A
 120284 1 2826.9 3056.0 -4.0 -1.3 0.158 0.162 B
 122884 1 2780.0 2900.0 1.0 2.3 0.422 0.181 A
 042585 1 2780.0 2900.0 1.0 1.0 0.479 0.050 A
 063085 1 2780.0 2900.0 2.0 1.9 0.491 0.029 A

RJI (Rayleigh - 091488; Love - 091488)

031287 1 1040.0 1100.0 1.0 -0.2 0.331 0.010 A
 041787 1 1040.0 1100.0 3.0 3.1 0.576 0.031 A
 111587 1 1040.0 1100.0 2.0 0.6 1.373 0.019 A
 122787 1 1040.0 1100.0 2.0 1.2 0.600 0.038 A
 040388 1 1040.0 1100.0 -1.0 -2.8 1.018 0.022 A
 061488 1 1040.0 1100.0 -2.0 -3.6 0.042 0.037 A
 111288 1 1040.0 1100.0 -1.0 -3.0 0.092 0.115 B
 012289 1 1040.0 1100.0 1.0 -0.1 1.067 0.003 A
 070889 1 1040.0 1100.0 2.0 0.4 0.313 0.012 A
 101989 1 1040.0 1100.0 -1.0 -3.2 1.214 0.013 A
 040387 3 900.0 960.0 0.0 0.1 1.315 0.012 A
 080287 3 900.0 960.0 -1.0 -2.2 1.002 0.106 C
 121387 3 920.8 958.7 0.0 -0.1 1.557 0.031 A
 021388 3 900.0 960.0 -1.0 -1.8 0.832 0.022 A
 091488 3 900.0 960.0 0.0 0.0 1.000 0.000 A
 012289 3 900.0 960.0 0.0 -0.1 0.946 0.034 A

040387 1 1040.0 1100.0 1.0 0.1 1.646 0.005 A
 080287 1 1040.0 1100.0 -2.0 -2.2 0.365 0.038 A
 121387 1 1040.0 1100.0 2.0 -0.1 0.967 0.012 A
 021388 1 1040.0 1100.0 0.0 -1.8 0.800 0.023 A
 050488 1 1040.0 1100.0 2.0 1.3 0.993 0.005 A
 091488 1 1040.0 1100.0 0.0 0.0 1.000 0.000 A
 121788 1 1040.0 1100.0 -1.0 -2.5 0.758 0.028 A
 021289 1 1040.0 1100.0 3.0 1.9 1.027 0.029 A
 090289 1 1040.0 1100.0 -1.0 -3.9 0.160 0.038 A
 031287 3 900.0 960.0 0.0 -0.2 0.208 0.122 B
 041787 3 900.0 960.0 3.0 3.1 1.303 0.023 A
 111587 3 905.5 958.7 1.0 0.6 0.521 0.227 B
 122787 3 900.0 960.0 2.0 1.2 1.090 0.043 A
 040388 3 900.0 960.0 -1.0 -2.8 1.134 0.034 A
 121788 3 900.0 960.0 -2.0 -2.5 1.830 0.031 A

LZN (Rayleigh - 091488; Love - 091488)

031287 1 800.0 900.0 1.0 0.7 0.370 0.064 A
 062087 1 800.0 900.0 2.0 2.6 0.505 0.030 A
 111587 1 800.0 900.0 2.0 1.0 1.247 0.030 A
 122787 1 800.0 900.0 2.0 1.5 0.513 0.048 A
 040388 1 800.0 900.0 -1.0 -1.3 0.965 0.022 A
 061488 1 843.9 902.6 2.0 -0.4 0.046 0.612 C
 111288 1 843.4 898.9 0.0 0.5 0.071 0.173 B
 012289 1 800.0 900.0 2.0 1.1 1.088 0.017 A
 070889 1 800.0 900.0 2.0 1.2 0.352 0.045 A
 101989 1 800.0 900.0 0.0 -1.4 1.279 0.013 A
 040387 3 700.0 800.0 2.0 0.6 -1.300 0.070 S
 062087 3 700.0 800.0 3.0 2.6 -0.363 0.390 S
 111587 3 734.4 810.4 2.0 1.0 0.846 0.427 B
 122787 3 700.0 800.0 2.0 1.5 0.724 0.159 A
 040388 3 700.0 800.0 -1.0 -1.3 0.919 0.052 A
 091488 3 700.0 800.0 0.0 0.0 1.000 0.000 A
 121788 3 700.0 800.0 -2.0 -1.4 1.480 0.110 A
 021289 3 700.0 800.0 8.0 3.0 0.382 0.819 C
 090289 3 700.0 800.0 -2.0 -0.7 0.208 0.449 B

040387 1 800.0 900.0 1.0 0.6 1.825 0.015 A
 080287 1 800.0 900.0 -1.0 -1.7 0.309 0.036 A
 121387 1 800.0 900.0 2.0 2.0 0.908 0.030 A
 021388 1 800.0 900.0 1.0 0.0 0.814 0.024 A
 050488 1 800.0 900.0 2.0 2.4 0.770 0.120 B
 091488 1 800.0 900.0 0.0 0.0 1.000 0.000 A
 121788 1 800.0 900.0 -1.0 -1.4 0.893 0.014 A
 021289 1 800.0 900.0 3.0 3.0 0.948 0.039 A
 090289 1 300.0 900.0 0.0 -0.7 0.179 0.060 A
 031287 3 700.0 800.0 1.0 0.7 -0.203 0.397 S
 041787 3 700.0 800.0 3.0 2.8 -0.405 0.897 S
 080287 3 700.0 800.0 -2.0 -1.7 -0.525 0.145 S
 121387 3 700.0 800.0 2.0 2.0 1.087 0.038 A
 021388 3 700.0 800.0 0.0 0.0 1.011 0.037 A
 050488 3 700.0 800.0 1.0 2.4 1.467 0.142 A
 111288 3 700.0 800.0 -1.0 0.5 0.171 0.575 B
 012289 3 700.0 800.0 1.0 1.1 0.824 0.124 A
 070889 3 700.0 800.0 1.0 1.2 0.516 0.083 A
 101989 3 700.0 800.0 0.0 -1.4 0.826 0.195 A

RNI (Rayleigh - 091488; Love - 091488)

031287 1 1170.0 1240.0 2.0 1.4 0.290 0.023 A
 041787 1 1170.0 1240.0 2.0 2.3 0.604 0.010 A
 080287 1 1170.0 1240.0 -1.0 -1.1 0.352 0.005 A
 122787 1 1170.0 1240.0 2.0 1.5 0.604 0.007 A
 040388 1 1170.0 1240.0 -1.0 -0.1 0.968 0.006 A
 061488 1 1170.0 1240.0 2.0 2.2 0.030 0.363 B
 111288 1 1170.0 1240.0 2.0 3.2 0.114 0.062 A

040387 1 1170.0 1240.0 2.0 1.0 1.461 0.021 A
 062087 1 1170.0 1240.0 2.0 2.7 0.509 0.007 A
 121387 1 1170.0 1240.0 3.0 3.4 0.975 0.005 A
 021388 1 1170.0 1240.0 1.0 1.3 0.913 0.009 A
 050488 1 1170.0 1240.0 2.0 3.1 0.921 0.029 A
 091488 1 1170.0 1240.0 0.0 0.0 1.000 0.000 A
 121788 1 1170.0 1240.0 -1.0 -0.5 0.927 0.020 A

012289	1	1170.0	1240.0	2.0	1.9	0.941	0.007	A
070889	1	1170.0	1240.0	1.0	1.6	0.377	0.003	A
101989	1	1170.0	1240.0	1.0	0.1	1.013	0.007	A
041787	3	1040.0	1100.0	3.0	2.3	0.349	0.186	C
121387	3	1040.0	1100.0	3.0	3.4	0.633	0.097	A
021388	3	1040.0	1100.0	0.0	1.3	1.341	0.158	A
050488	3	1040.0	1100.0	8.0	3.1	1.026	0.230	A
091488	3	1040.0	1100.0	0.0	0.0	1.000	0.000	A
121788	3	1040.0	1100.0	-1.0	-0.5	1.079	0.041	A
021289	3	1040.0	1100.0	9.0	3.6	0.392	0.599	C
090289	3	1040.0	1100.0	7.0	1.8	0.070	0.944	C

021289	1	1170.0	1240.0	3.0	3.6	0.749	0.017	A
090289	1	1170.0	1240.0	3.0	1.8	0.207	0.131	B
040387	3	1013.7	1116.9	3.0	1.0	0.779	0.262	B
080287	3	1040.0	1100.0	-3.0	-1.1	-0.408	0.430	B
122787	3	1040.0	1100.0	4.0	1.5	0.379	0.426	C
040388	3	1040.0	1100.0	4.0	-0.1	0.396	0.408	B
061488	3	1040.0	1100.0	1.0	2.2	0.087	0.835	C
111288	3	1040.0	1100.0	3.0	3.2	-0.029	0.984	C
012289	3	1040.0	1100.0	6.0	1.9	0.504	0.272	A
070889	3	1040.0	1100.0	0.0	1.6	0.554	0.116	A
101989	3	1040.0	1100.0	1.0	0.1	0.797	0.268	C

WNQ (Rayleigh - 091488; Love - 091488)

031287	1	330.0	390.0	2.0	1.3	0.268	0.022	A
041787	1	330.0	390.0	3.0	2.4	0.562	0.015	A
080287	1	330.0	390.0	-1.0	-1.2	0.331	0.012	A
021388	1	330.0	390.0	0.0	1.1	0.851	0.005	A
050488	1	330.0	390.0	3.0	3.0	0.799	0.012	A
091488	1	330.0	390.0	0.0	0.0	1.000	0.000	A
121788	1	330.0	390.0	-1.0	-0.6	0.941	0.009	A
070889	1	330.0	390.0	1.0	1.5	0.372	0.007	A
101989	1	350.4	384.8	0.0	-0.1	0.992	0.009	A
040387	3	280.0	340.0	3.0	0.9	0.949	0.063	B
062087	3	305.1	366.5	8.0	2.7	0.508	0.271	B
121387	3	280.0	340.0	2.0	3.2	0.669	0.089	B
021388	3	280.0	340.0	-1.0	1.1	1.240	0.020	A
091488	3	280.0	340.0	0.0	0.0	1.000	0.000	A
121788	3	280.0	340.0	-2.0	-0.6	0.899	0.085	B
070889	3	280.0	340.0	-1.0	1.5	0.615	0.037	A
101989	3	280.0	340.0	1.0	-0.1	0.763	0.085	B

040387	1	330.0	390.0	1.0	0.9	1.392	0.008	A
062087	1	330.0	390.0	3.0	2.7	0.490	0.019	A
121387	1	330.0	390.0	3.0	3.2	0.923	0.005	A
040388	1	330.0	390.0	-1.0	-0.3	0.912	0.007	A
061488	1	330.0	390.0	2.0	1.8	0.042	0.040	A
111288	1	294.4	390.0	1.0	2.9	0.092	0.069	A
021289	1	330.0	390.0	3.0	3.5	0.733	0.012	A
090289	1	330.0	390.0	1.0	1.4	0.145	0.018	A
031287	3	311.8	361.1	6.0	1.3	0.147	0.208	B
041787	3	280.0	340.0	2.0	2.4	0.743	0.409	B
080287	3	270.7	355.6	-5.0	-1.2	-0.397	0.097	S
122787	3	280.0	340.0	2.0	1.5	0.476	0.302	B
040388	3	280.0	340.0	2.0	-0.3	0.567	0.217	A
111288	3	290.7	351.6	-2.0	2.9	-0.135	0.496	B
021289	3	257.3	337.4	-2.0	3.5	-0.441	0.711	S
090289	3	280.0	340.0	2.0	1.4	0.179	0.243	B

MIA (Rayleigh - 091488; Love - 091488)

062087	1	960.0	1030.0	0.0	1.2	0.475	0.024	A
111587	1	960.0	1030.0	2.0	0.1	1.582	0.011	A
021388	1	960.0	1030.0	-2.0	-3.2	0.725	0.009	A
091488	1	960.0	1030.0	0.0	0.0	1.000	0.000	A
121788	1	960.0	1030.0	-2.0	-3.1	0.324	0.033	A
021289	1	960.0	1030.0	3.0	0.6	1.424	0.006	A
101989	1	960.0	1030.0	-1.0	-4.4	1.424	0.019	A
080287	3	856.4	895.3	0.0	-2.4	3.020	0.077	A
121387	3	850.0	920.0	0.0	-2.0	1.738	0.127	A
040388	3	852.6	900.7	-1.0	-3.8	2.023	0.041	A
091488	3	850.0	920.0	0.0	0.0	1.000	0.000	A
121788	3	855.5	900.6	-1.0	-3.1	2.946	0.056	A
021289	3	780.8	910.3	4.0	0.6	-0.754	0.498	S
101989	3	790.5	903.2	1.0	-4.4	-0.781	0.321	S

080287	1	832.7	996.2	3.0	-2.4	-0.245	0.297	S
121387	1	960.0	1030.0	-1.0	-2.0	0.622	0.017	A
040388	1	960.0	1030.0	-2.0	-3.8	0.850	0.010	A
111288	1	856.6	1035.8	-2.0	-6.1	-0.060	0.479	S
012289	1	960.0	1030.0	0.0	-1.2	0.935	0.011	A
070889	1	960.0	1030.0	2.0	-0.3	0.255	0.010	A
062087	3	850.0	920.0	2.0	1.2	1.252	0.095	A
111587	3	850.0	920.0	1.0	0.1	1.297	0.102	A
021388	3	850.0	920.0	-3.0	-3.2	0.483	0.224	A
061488	3	850.0	920.0	-1.0	-6.3	0.118	0.185	B
111288	3	850.0	920.0	-4.0	-6.1	0.663	0.262	A
012289	3	850.0	920.0	0.0	-1.2	1.470	0.087	A
070889	3	850.0	920.0	2.0	-0.3	0.285	0.117	A

NDJ (Rayleigh - 122787; Love - 122787)

122787	1	1270.0	1360.0	0.0	0.0	1.000	0.000	A
090289	1	1270.0	1360.0	-3.0	-6.9	0.275	0.094	A
122787	3	1110.0	1180.0	0.0	0.0	1.000	0.000	A
090289	3	1110.0	1180.0	-8.0	-6.9	0.126	0.612	C

021388	1	1270.0	1360.0	-2.0	-3.9	1.776	0.055	A
101989	1	1223.6	1326.4	-1.0	-5.2	3.120	0.127	A
021388	3	1058.5	1178.6	-5.0	-3.9	0.188	0.597	B
101989	3	1110.0	1180.0	-1.0	-5.2	-0.452	0.421	A

HRV (Rayleigh - 040388)

040388	1	2970.0	3110.0	0.0	0.0	1.000	0.000	A
012289	1	2970.0	3110.0	0.0	-1.0	1.155	0.072	A
070889	1	2830.4	3090.0	1.0	-0.3	0.464	0.256	A

091488	1	2970.0	3110.0	0.0	1.8	1.231	0.058	A
021289	1	2959.3	3083.3	-1.0	-2.1	0.905	0.454	B
101989	1	2907.5	3060.8	1.0	-0.5	1.614	0.500	B

INVERSION

The inversion for source and path parameters is described in the previous paper and follows equations (7), (11), and (20). Only events for which ten or more observations are available are included in the total misfit function (for path corrections), but source parameters are calculated for all events with five or more observations. The final values for the path coefficients F_{lm} are given in Table A2, as are the perturbations $\delta\Phi_{lm}$ to the great circle path. The entries in this table are, from left to right, station code, F_{1m} (Rayleigh), F_{1m} (Love), clockwise perturbation $\delta\Phi_{1m}$ in takeoff angle (Rayleigh), $\delta\Phi_{1m}$ (Love), total number of Rayleigh wave observations, and total number of Love wave observations. One F_{1m} coefficient, corresponding to KONO Rayleigh waves, was held constant in the inversions.

TABLE A2. Station Path Parameters

Station	F_{1m}	F_{2m}	$\delta\Phi_{1m}$	$\delta\Phi_{2m}$	N_1	N_2
GUMO	0.759	-2.380	0.920	-0.605	48	29
ZOBO	0.866		0.902		36	0
CHTO	0.919	2.907	0.082	8.681	44	38
TATO	0.865	-1.425	5.078	1.001	40	39
KAAO	-1.740	1.951	4.239	2.256	18	18
MAJO	1.587	-2.998	-5.375	-4.190	54	52
SHIO	0.897	2.786	0.243	1.259	9	9
ANTO	1.141	-1.093	3.509	-0.445	34	21
KONO	1.0	-6.193	-1.326	0.988	52	34
GRFO	0.807	-6.224	-0.225	9.548	53	47
SCP	0.861		-0.543		24	0
BER	0.967	-6.531	0.010	-0.158	9	3
KEV	0.826	-7.881	-0.354	-12.880	33	20
TOL	0.869	-3.464	-1.187	-1.626	32	9
COL	1.281		-4.572		22	0
GAC	0.543		1.169		29	0
GDH	0.816		0.088		16	0
RSCP	0.713		0.818		11	0
RSNT	1.020		-1.135		10	0
RSSD	0.938		-1.263		17	0
RSNY	0.682		0.034		15	0
RSO	0.789		0.398		17	0
BJI	1.168	-3.321	0.966	0.220	19	12
LZH	0.922	-4.628	-0.796	1.707	19	14
KMI	0.822	-7.603	-0.021	-1.909	19	17
WMQ	0.787	-7.114	0.065	-1.754	17	14
HIA	1.380	-7.664	-1.189	-4.887	11	12
MDJ	3.027	-3.412	0.152	-3.540	4	4
HRV	1.029			-0.030	6	0

DISCRIMINATION OF EARTHQUAKES AND EXPLOSIONS IN THE EASTERN UNITED STATES USING REGIONAL HIGH-FREQUENCY DATA

Won-Young Kim, D. W. Simpson¹ and P. G. Richards²

Lamont-Doherty Earth Observatory
of Columbia University, Palisades, NY 10964

Abstract

High-frequency regional records from small earthquakes ($1.3 < \text{magnitude} < 4$), and comparable magnitude explosions, are analyzed to find a reliable seismic discriminant in the eastern United States. Over 500 digital, vertical-component seismograms recorded by the New York State Seismic Network in the distance ranges 10 to 610 km are used. Mean P/Lg spectral ratios in the band 1 – 25 Hz are about 0.5 and 1.25 for earthquakes and explosions, respectively, in the eastern U. S. We find that the high-frequency P/Lg spectral amplitude ratio in the frequency band 5 – 25 Hz is an adequate discriminant for classifying these events. A linear discriminant function analysis indicates that the P/Lg spectral amplitude ratio method provides discrimination power with a total misclassification probability of about 1%. The P/Lg spectral amplitude ratio method we propose is sufficiently reliable and robust that it can be used in discriminating chemical explosions (especially numerous quarry blasts) from small regional earthquakes in the routine analysis of regional earthquake monitoring networks. Single-hole instantaneous explosions and ripple-fired quarry blasts have somewhat different P/Lg spectral ratios, but as a group are distinctly different from earthquakes.

Introduction

The discrimination of small earthquakes from large chemical explosions (from mines and quarries) based on seismic signals recorded at regional distances (10 – 1000 km) is an important issue facing numerous regional seismic networks. The seismic discrimination problem becomes especially severe in an area with low seismicity such as the eastern United States. For instance, in New York and adjacent states covered by the New York State Seismic Network (NYSSN) run by the Lamont-Doherty Earth Observatory (Fig. 1), a few small earthquakes (magnitude < 4) occur per month, but about 20 chemical explosions per day may be recorded during weekdays [Richards et al., 1992]. It would be extremely useful to have a reliable and robust criterion that could be used to discriminate earthquakes from explosions in the day-to-day operation of these networks.

¹ now at Incorporated Research Institutions for Seismology, Arlington, VA 22209

² also at Department of Geological Sciences, Columbia University

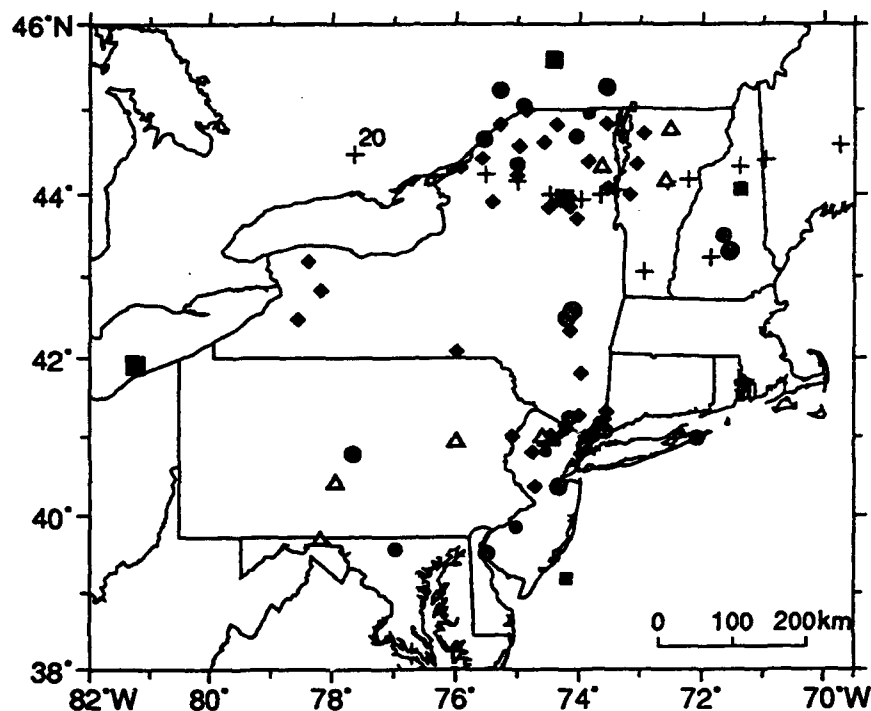


Fig. 1. Locations of earthquakes (*shaded circles*), NYNEX explosions (*pluses*), quarry blasts (*open triangles*) and NYSSN stations (*diamonds*). Note the location of NYNEX explosion #20. Size of the circles are proportional to the magnitude of the earthquakes. Earthquakes used for testing the discriminant function are plotted with *shaded squares*.

Much previous work on seismic discrimination has focused on separating underground nuclear explosions from earthquakes in the context of a future comprehensive test ban (e.g., Pomeroy et al., 1982; Evernden et al., 1986; Taylor et al., 1989). In most earlier studies, data available for discrimination analyses were limited to frequencies below 10 Hz, and previous work on regional signals from earthquakes and explosions in the western U.S. suggested that *P* and *S* waves from earthquakes have higher frequency content than signals from explosions (e.g., Murphy & Bennett, 1982; Bennett & Murphy, 1986; Taylor et al., 1988; Chael, 1988). These western U.S. results are contrary to our observations and to the claim by Evernden et al. (1986) that regional signals from explosions should show higher frequency content than those from earthquakes. Regional discriminants must be evaluated on a regional basis, however we presume the method reported here would work to discriminate small nuclear explosions from small earthquakes, in regions that support high-frequency signals.

Our typical observations of high-frequency (1-35 Hz) regional signals from earthquakes and explosions in the eastern United States may be summarized as: 1) *P* waves from single-hole explosions have much higher frequency content than *S* waves; 2) *S* waves from earthquakes have

higher frequency content than *P* waves, as much as by a factor of about two; 3) *P* and *S* waves from ripple-fired quarry blasts have similar frequency content and show frequency banding due to spectral modulation; 4) records from explosions often show a strong *Rg* phase out to about 100 km. [We use *P* and *Pg* interchangeably to indicate *P* waves with a group velocity around 6 km/s; and likewise *S* and *Lg* are used to indicate shear waves with group velocity about 3.5 km/s, without further classification.]

Typical vertical-component digital seismograms from an earthquake and a single-hole explosion are shown in Fig. 2. Unfiltered seismograms (top traces) support the differences 1) and 2) stated above. When the seismograms are filtered to show the conventional low-frequency band (1-10 Hz, middle traces), the spectral characteristics appear similar to the unfiltered signals. But bandpass filtered, 10-25 Hz, high-frequency seismograms (bottom traces) accentuate the differences and show that there are distinctively different patterns in the spectral content of the *P* and *S* signals between the earthquake and the explosion. Such high-frequency seismograms suggest that the *Pg/Lg* spectral amplitude ratio can be made the basis of a useful discriminant. In the following sections, we report our measurements of the *Pg/Lg* spectral amplitude ratio, using high-frequency, vertical-component digital seismograms from earthquakes and chemical explosions recorded by the NYSSN (Fig. 1); and we evaluate its discrimination capability.

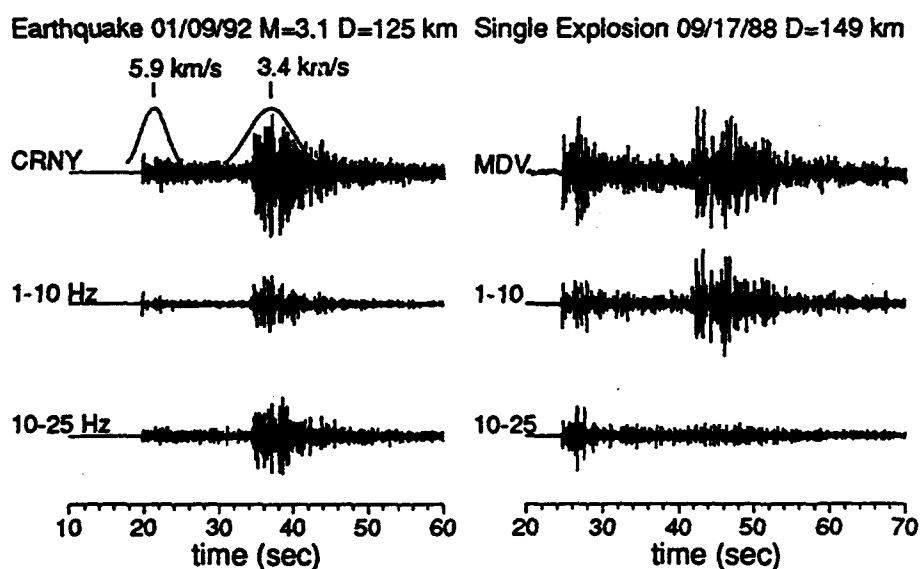


Fig. 2. Typical vertical-component records from an earthquake and an explosion. Unfiltered (top), low-frequency bandpass filtered (middle) and high-frequency bandpass filtered (bottom) traces are plotted. Example Gaussian time windows used for *Pg* and *Lg* spectral amplitude measurements are shown on the unfiltered earthquake trace.

Data

We first present the analysis of digital seismograms from 30 explosions (16 quarry blasts and 14 single-hole explosions) and 30 earthquakes to obtain a specific discriminant, which later is applied to other events. Most of the earthquakes are felt events in the magnitude range 1.3 to 3.5 and are reported by organizations such as the Geological Survey of Canada, Weston Observatory and the U.S. Geological Survey. Events are selected to sample a wide range of propagation paths within the eastern U. S. (Fig. 1). All quarry blasts are from eight known quarry sites. Only blasts for which quarry personnel have provided us with pertinent information (delay times, number of shot holes, maximum charge/delay period etc.) are included. The maximum charge-weight per delay period (within 8 milliseconds) of the ripple-fired blasts ranged from 0.1 to 27 tons. All single-hole explosions are from the NYNEX experiment and had 1 – 2 ton charge weights (Mangino & Cipar, 1990). Distance ranges of the data are 5 to 610 km with means of 149 (± 135) km and 129 (± 107) km for earthquakes and explosions, respectively.

P_g and L_g signals are windowed with a Gaussian weighting function centered at group velocities around 5.9 km/s and 3.4 km/s, respectively (see Fig. 2). A standard deviation, σ , of $\sigma_{\text{ref}} = 2.5$ s is used for the L_g Gaussian window at a reference distance of $\Delta_{\text{ref}} = 100$ km. It includes the L_g arrivals with group velocities between 3.72 and 3.13 km/s in its $\pm\sigma$ width and the Gaussian window is truncated at $\pm 1.96 \sigma$ ($\approx 95\%$). The window lengths at different distances are scaled by $\sigma = \sigma_{\text{ref}} * \Delta / \Delta_{\text{ref}}$. Thus, the time window used for L_g has the same group velocity window regardless of distance. The P_g window length is scaled to the L_g window using an average propagation velocity ratio V_s/V_p ($\approx 1/\sqrt{3}$) \times L_g window length, so that P_g crustal paths similar to the paths making up L_g are included.

Digital seismograms from the NYSSN are sampled at 100 samples/sec and instrument responses of the stations are nearly flat to ground velocity in the frequency band 1 – 25 Hz. The P_g and L_g signals, weighted by the Gaussian functions, are fast Fourier transformed. The resulting amplitude spectra are smoothed with another Gaussian function having $\sigma = 2.5$ Hz and are re-sampled at every 5 Hz interval from 5 to 35 Hz. Spectral amplitudes for the frequency band 1 to 10 Hz, with 1 Hz interval, are obtained using $\sigma = 0.5$ Hz. Noise analyses indicate that the signal-to-noise (S/N) ratios are quite high in most of the records, but in some cases the signals fall to the background noise level above about 35 Hz. The S/N ratio becomes less than 2 at about 25 Hz for records from distant events ($\Delta > 300$ km). The $\log_{10} (P_g/L_g)$ spectral ratios at discrete frequency points are obtained for each record. Network averaged $\log_{10} (P_g/L_g)$ ratios are then obtained for each event by averaging the discrete frequency values from all stations (Fig. 3). Earthquake and explosion populations are well separated in the frequency band 10 to 25 Hz. At 5 Hz and at frequencies higher than 30 Hz, there is some overlap. Thus, the frequency band 5 – 25 Hz is the most reliable and a sampled version will be used in the following discrimination analysis.

The Linear Discriminant Function

To test the discriminant power of the high-frequency P_g/L_g spectral ratio, we performed multivariate discriminant analysis on $\log_{10} (P_g/L_g)$ spectral ratios for the data set of earthquakes and explosions. Each training group of 30 events (i.e. 30 explosions, 30 earthquakes) is described

by a matrix of 5 rows [$\log_{10}(Pg/Lg)$ at 5 Hz frequency intervals from 5 to 25 Hz] and 30 columns. Preliminary analysis suggested somewhat higher Pg/Lg ratios from NYNEX single-hole shots than for quarry blasts, but we merged both data sets into one explosion group because the differences between them was much less than their differences from earthquakes.

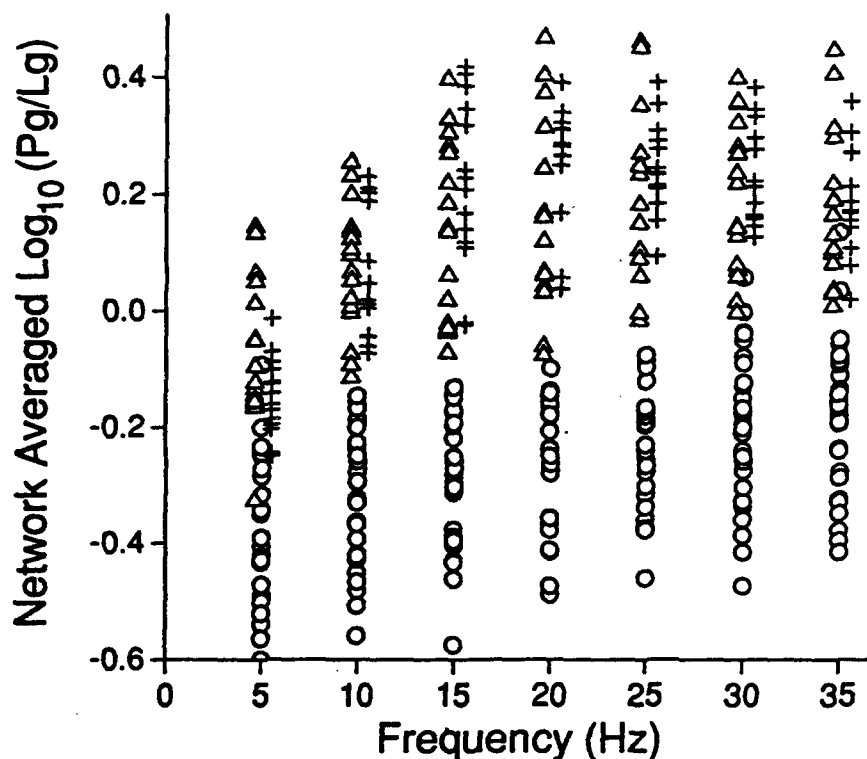


Fig. 3. Network averaged $\log_{10}(Pg/Lg)$ spectral amplitude ratios at seven discrete frequency points used in discrimination analysis are plotted for earthquakes (*circles*), NYNEX explosions (*pluses*) and quarry blasts (*triangles*).

We introduce $f_{Ex}(\mathbf{r})$ and $f_{Eq}(\mathbf{r})$ as the probability densities of the two types of events, with \mathbf{r} as a column vector representing the log spectral ratios sampled at 5 values. And we take π_{Ex} and π_{Eq} as the *a priori* probability of the two types of events, so $\pi_{Ex} + \pi_{Eq} = 1$. We follow standard practice by assigning an event to the earthquake class if

$$f_{Eq}(\mathbf{r}) / f_{Ex}(\mathbf{r}) > \pi_{Ex} / \pi_{Eq} \quad (1)$$

and to the explosion class otherwise (see e.g., Seber, 1984 for multivariate discrimination methods). This rule is optimum, in that it minimizes the total probability of misclassification. Our knowledge of $f_{Ex}(\mathbf{r})$ and $f_{Eq}(\mathbf{r})$ comes from the training groups, and we introduce and evaluate a linear discriminant function $D(\mathbf{r})$ under the assumptions that: a) the sample distributions are normal; b) the dispersion (variance-covariance) matrices of the two groups are the same; and c) the training observations are correctly classified. The linear function is

$$D(r) = \lambda^T [r - (\mu_{Eq} + \mu_{Ex})/2] \quad (2)$$

where μ_{Eq} is the mean of the earthquake training values r_{Eq}^i ($i = 1, \dots, 30$), and similarly for μ_{Ex} ; $\lambda = S^{-1}(\mu_{Eq} - \mu_{Ex})$, and S is the average of the dispersion matrices S_{Eq} and S_{Ex} , with (for example) $S_{Eq} = \frac{1}{29} \sum_{i=1}^{30} (r_{Eq}^i - \mu_{Eq})(r_{Eq}^i - \mu_{Eq})^T$; and T denotes a transpose.

In terms of these easily calculated quantities, the discrimination analysis is very simple. The rule (1) becomes: assign an event r to the earthquake population if $D(r) > \ln(\pi_{Eq}/\pi_{Ex})$. If $\pi_{Eq} = \pi_{Ex} = \frac{1}{2}$ the rule is even simpler: the event is labelled an earthquake or an explosion according as $D(r) > 0$ or $D(r) < 0$. In this case, we have

$$P(\text{misclassification}) = \frac{1}{\sqrt{2\pi}} \int_{-\infty}^{-\Delta^2} \exp(-x^2/2) dx \quad \text{where } \Delta^2 = \lambda^T (\mu_{Eq} - \mu_{Ex}) \quad (3)$$

for the probability of misclassification. Δ^2 is the Mahalanobis D-squared measure of distance between the two means.

This type of multivariate analysis was developed and used by Fisher (1936), and has been used in many seismological applications — for example by Jebe and Willis (1964), and Sandvin and Tjostheim (1978). The equality of the dispersion matrices for the two groups is tested using a χ^2 test (Seber, 1984). If the dispersion matrices of the populations are not same, then a quadratic discriminant function is appropriate (e.g., Seber, 1984; Taylor et al., 1988).

Four Applications of Discriminant Analysis

High-frequency network averaged Pg/Lg ratio: The sample data sets consisting of 30 earthquakes and 30 explosions were analyzed using the linear discriminant function given in (2). For each event, network averaged $\log_{10}(Pg/Lg)$ ratios at frequencies of 5, 10, 15, 20 and 25 Hz correspond to the variables r_1, r_2, r_3, r_4 , and r_5 . The linear discriminant function obtained is

$$D(r) = -1.313 + 15.157 r_1 - 43.894 r_2 + 17.485 r_3 - 0.489 r_4 - 34.707 r_5 \quad (4)$$

and the Mahalanobis D-squared measure is $\Delta^2 = 20.768$. Assuming equal prior probabilities for the two groups, we assign event r to the earthquake class if $D(r) > 0$. Applying this rule to the earthquake and explosion data, we find that all events are classified correctly and the misclassification probability is 0.0113. Values of $D(r)$ may be called the discriminant score and are plotted in Fig. 4 with respect to the mean $\log_{10}(Pg/Lg)$ spectral amplitude ratio of each event. Vertical lines in the figure denoted as Eq and Ex are the projection of the multivariate mean of the earthquake and explosion populations, respectively. The vertical line, D_0 , is the line $D(r) = 0$, which serves to classify the events when the *a priori* probability of the two populations is the same. The distance between Eq and Ex is the Mahalanobis D-squared measure of distance between two populations, since, from (2), $D(\mu_{Eq}) - D(\mu_{Ex}) = \Delta^2$. It is shown in Fig. 4 that all the earthquake records from various paths in the eastern U. S. have a mean Pg/Lg spectral ratio of about 0.5, while the explosion records show a mean of about 1.25.

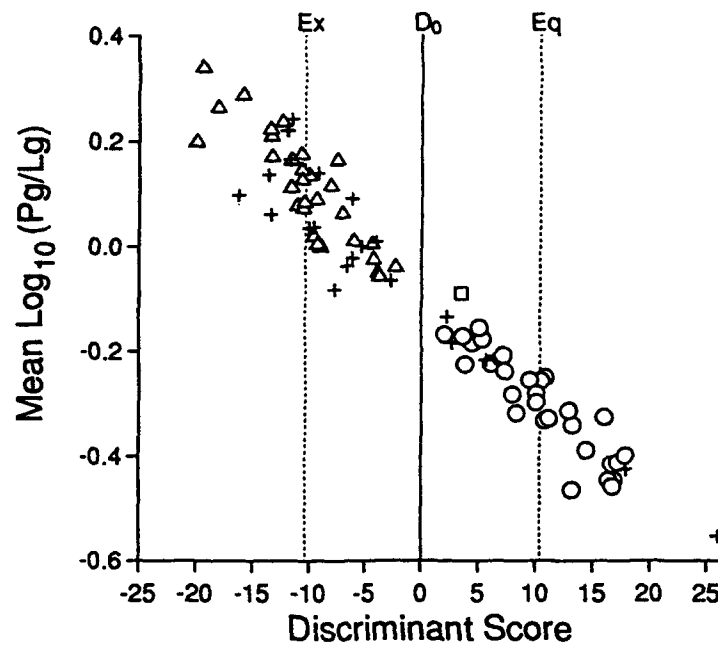


Fig. 4. Discriminant scores of earthquakes (*circles*) and explosions (*triangles*) of the sample data are plotted with their mean network-averaged $\log_{10} (Pg/Lg)$ ratios. The two populations are also well separated by mean $\log_{10} (Pg/Lg)$ ratio = -0.1. Events used to test the discriminant function are plotted with *pluses* and the explosion misclassified as an earthquake is plotted with a *square*.

The equality of the dispersion matrices for the two groups is tested using a χ^2 test. The χ^2 statistic for this analysis is 10.89 with 15 degrees of freedom. Since the critical value of χ^2 for 15 degrees of freedom and 5 % level of significance is approximately 25, our 10.89 value suggests that the dispersion matrices of the parent populations are the same. To test the null hypothesis of equality of means of two groups, we obtained an F statistic using the Mahalanobis D-squared distance measure (Seber, 1984; Davis, 1986). The F statistic for this analysis is 58.0 with 5 and 54 degrees of freedom. The critical value of F for 5 and 54 degrees of freedom at the 5 % level of significance is about 2.38. Our F statistic exceeds this critical value, so we reject the null hypothesis and conclude that our samples do indicate a difference in the means of the two populations. That is, there is a statistically significant difference in Pg/Lg spectral ratios of signals from the two groups of events.

Single record Pg/Lg ratio: When single-record $\log_{10} (Pg/Lg)$ ratios of 230 explosions records and 255 earthquakes records are analyzed as the previous case, we find that about 14.9 % of earthquakes records and about 14.8 % of explosions records are classified incorrectly. The Mahalanobis D-squared measure of distance between two samples is 4.10 and the misclassification probability is 0.156 according to (3). This substantially higher misclassification probability of the single-record Pg/Lg ratio over the network-averaged Pg/Lg ratio indicates that the frequency content of regional Pg and Lg are strongly influenced by propagation paths as well as by local receiver site responses.

Low-frequency network Pg/Lg ratio: To compare the high frequency results with the more conventional lower frequency observations, we repeated the analysis using network averaged $\log_{10}(Pg/Lg)$ ratios in the frequency band 1 – 10 Hz with 1 Hz intervals, so r had 10 elements. Discriminant function analyses for this low-frequency band suggest that most of the discriminant power is carried by frequencies higher than 5 Hz. The Mahalanobis D-squared measure is $\Delta^2 = 10.426$. The discriminant function analysis indicates that one event in each group in the training data is misclassified and the misclassification probability is 0.0532, suggesting that the low-frequency band performs more poorly than the high-frequency band. Using the low-frequency band, many ripple-fired explosions as well as several distant earthquakes had discriminant scores close to zero, i.e. clustered close to the classification line.

Discrimination test for another set of known events: We tested the performance of the above high-frequency discriminant function, eq. (4), by applying it to another set of five known earthquakes and 18 known explosions. Since these events were not used in the sample data set they can be used to evaluate the discriminant. We found that all events except one were correctly classified. The one exception, an explosion misclassified as an earthquake, is NYNEX shot #20 (Fig. 1), which was fired in a water-filled quarry site (water depth about 200 m; see Kim et al., 1991). The shot excited very strong Pg and Lg waves in the range 1–10 Hz due to the effects of bubble pulse and reverberations in the water column, but Pg waves in the range 10–25 Hz were not comparably high and therefore the spectral shape differed from other explosions fired in hard rock. This is an abnormal explosion, to be recognized as not an earthquake by the dominance of P over S , at distances up to 200 km. This single misclassification by our Pg/Lg spectral ratio method is instructive but does not undercut the general utility of the method.

Discussion and Conclusions

We find that Pg waves from explosions (single-hole and multiple-hole ripple-fired explosions) have stronger high frequency content than Lg waves over the broad high-frequency band 5 – 25 Hz at regional distances in the eastern U. S.: the mean ratio for 230 explosion records is about 1.25. The opposite is true for signals from earthquakes with magnitudes 1.3 – 3.5: the mean Pg/Lg ratio for 255 earthquake records in the frequency band 5 – 25 Hz is about 0.5.

In a lower frequency band, 1-10 Hz, Pg/Lg ratios show similar results but the separation between explosions and earthquakes is less clear. We note that observations in the western U. S. have been reported as having Pg/Lg higher for earthquakes than explosions (e.g., Bennett & Murphy, 1986). More basically, the western U.S. results are different from ours because they were made from time-domain observations at dominant frequencies near 1 Hz. The key to our method and conclusions is the observability of frequencies up to about 20 Hz at regional distances in the eastern U.S.

One basis for the empirical success of our proposed high-frequency Pg/Lg ratio method is that, if selected spectral amplitude reinforcement occurs at the source (as is the case for ripple-fired blasts), it will affect both early P phases as well as later-arriving Lg phases. Such spectral

scalloping will largely cancel in the ratio we have used. The ratio is robust as a discriminant to the extent that there is cancellation of other characteristics, such as event size, corner frequency, some effects of focal depth, and instrument response. However, the Pg/Lg ratio discriminant shows some dependence on near source conditions which may excite Pg and Lg signals with different efficiency (e.g., explosion source in low velocity rocks; explosion in a water-filled quarry site).

Strong Pg excitation but weak Lg excitation from a near vertical strike-slip earthquake (see e.g., Bouchon, 1981; Kim, 1987) may diminish the discrimination power of the Pg/Lg ratio method at some station azimuths, as indicated by Lilwall (1988). The dependence of frequency content of P and S waves on specific propagation paths and local structure at the receiver may also explain why the Pg/Lg ratio method applied to single station records had mixed results in several previous studies (e.g., Taylor, 1989). We believe the key to avoidance of such problems of source and path is use of a network averaged Pg/Lg ratio.

We have shown that the Pg/Lg spectral amplitude ratio is an adequate discriminant for explosions from earthquakes (magnitude smaller than 4) in the eastern U. S. The stability of the Pg/Lg ratio in discriminating multiple-hole, ripple-fired explosions from small regional earthquakes is significant for earthquake monitoring in the eastern U. S., since the region is characterized by low seismicity with frequent occurrences of such explosions. Our results demonstrate the importance of data at frequencies up to at least 20 Hz, with implications for the design of networks in regions that have observable high-frequency signals.

Acknowledgments

D. Johnson, D. Lentricchia, and R. Such of the Lamont-Doherty Earth Observatory have put considerable effort into maintaining the NYSSN and assisted in collecting the data used in this study. Mr. R. McCormic at RAMAC Explosive, Mr. M. Green of Green Mountain Explosive and Ms. D. Wiedman at Atlas Northeast Inc. kindly provided us with copies of blaster's reports for the quarry blasts used in this study. This project was supported by the USGS under Grant No. 1434-92-A-069, and by the Air Force Phillips Laboratory under F19628-90-K-0048. Lamont-Doherty Earth Observatory contribution number 5083.

References

- Bennett, T. J. and J. R. Murphy (1986). Analysis of seismic discrimination capabilities using regional data from western United States events, *Bull. Seism. Soc. Am.*, **76**, 1069-1086.
- Bouchon, M. (1981). A simple method to calculate Green's functions for elastic layered media, *Bull. Seism. Soc. Am.*, **71**, 959-971.
- Chael, E. P. (1988). Spectral discrimination of NTS explosions and earthquakes in the southwestern United States using high-frequency regional data, *Geophys. Res. Lett.*, **15**, 625-628.
- Davis, J. C. (1986). *Statistics and Data Analysis in Geology*, 2nd ed., John Wiley & Sons, Inc., New York, 646pp.
- Evernden, J. F., C. B. Archambeau and E. Cranswick (1986). An evaluation of seismic decoupling and underground nuclear test monitoring using high-frequency seismic data, *Review Geophys.*, **24**, 143-215.

- Fisher, R. A. (1936). The use of multiple measurement in taxonomic problems, *Ann. Eugen.*, 7, 179-188.
- Jebe, E. H. and D. E. Willis (1964). An application of the discriminant function technique to seismic records, *Earthquake Notes*, 35, No. 3-4, 28-49.
- Kim, W. Y. (1987). Modelling short-period crustal phases at regional distances for seismic source parameter inversion, *Phys. Earth Planet. Inter.*, 47, 159-178.
- Kim, W. Y., D. W. Simpson and P. G. Richards (1991). High-frequency spectra of regional phases from earthquakes and chemical explosions, Scientific Report PL-TR-91-2285, Phillips Lab., Hanscom AFB, MA., 43-96, ADA251594.
- Lilwall, R. C. (1988). Regional mb:Ms, Pg/Lg amplitude ratios and Lg spectral ratios as criteria for distinguishing between earthquakes and explosions: a theoretical study, *Geophys. J.*, 93, 137-147.
- Mangino, S. and Cipar, J. (1990). Data report for the 1988 Ontario-New York-New England Seismic Refraction Experiment: Three-Component Profiles, GL-TR-90-0039, Geophysics Laboratory, Hanscom AFB, MA., 143pp, ADA221898.
- Murphy, J. R. and T. J. Bennett (1982). A discrimination analysis of short-period regional data at Tonto Forest Observatory, *Bull. Seism. Soc. Am.*, 72, 1351-1366.
- Pomeroy, P. W., W. J. Best, and T. V. McEvelly (1982). Test ban treaty verification with regional data - A review, *Bull. Seism. Soc. Am.*, 72, S89-S129.
- Richards, P. G., D. A. Anderson and D. W. Simpson (1992). A survey of blasting activity in the United States, *Bull. Seism. Soc. Am.*, 82, 1416-1433.
- Seber, G. A. F. (1984). *Multivariate Observations*, John Wiley & Sons, Inc., New York, 686pp.
- Sandvin, O. and D. Tjostheim (1978). Multivariate autoregressive representation of seismic P-wave signals with application to short-period discrimination, *Bull. Seism. Soc. Am.*, 68, 735-756.
- Taylor, S. R., N. W. Sherman and M. D. Denny (1988). Spectral discrimination between NTS explosions and western United States earthquakes at regional distances, *Bull. Seism. Soc. Am.*, 78, 1563-1579.
- Taylor, S. R., M. D. Denny, E. S. Vergino and R. E. Glaser (1989). Regional discrimination between NTS explosions and western U.S. earthquakes, *Bull. Seism. Soc. Am.*, 79, 1142-1176.

SPOT picks of nuclear explosion locations on the Balapan test site, near Semipalatinsk, Kazakhstan

Paul G. Richards
Lamont-Doherty Earth Observatory,
and Dept. of Geological Sciences, Columbia University

Locations of 83 nuclear explosions from 1965 to 1989 at the Balapan test site, near Semipalatinsk, Kazakhstan, are derived from SPOT photographs.

The procedure is essentially the same as that reported for a smaller set of explosions by Thurber et al (1993). That is, by comparing SPOT picks of ground disturbances with locations of specific explosions determined seismically in a joint epicenter study such as that by Lilwall and Farthing (1990), it is often possible to associate the ground disturbance with a particular event.

The precision of correctly associated SPOT picks (approx. 100 m) is about an order magnitude better than the precision claimed by Lilwall and Farthing for seismically determined locations (a little more than 1 km for large Balapan explosions). But, of course, the error of locations picked from a satellite photo will be substantial for misassociated events. In this regard, it is of interest to compare the locations in the Table below, with those listed by Thurber and Quin (1992). For the period prior to 1986, Thurber and Quin based their picks on Landsat data. For events number 7, 10, 40, 46, 65, and 70, the Landsat-picked locations of Thurber and Quin differ from my SPOT-picked locations by more than 1 km. For 18 events, I have not listed a SPOT pick. For the remaining 57 events prior to 1986, our locations differ by less than 1 km. [Locations post-1986 are the same in the two studies, because we cooperated closely for this period, though analysing the SPOT photos at different institutions.]

COMMENTS ON THE FOLLOWING TABLE:

The first column (h, l, or blank) characterizes the quality of the SPOT pick:

h means very high quality,

l means lesser quality - but still high - and

a blank means that no SPOT pick is listed, usually because of ambiguities in association. Note that "quality" here refers to the degree of certainty of the association of a notable ground disturbance, visible in SPOT photographs, with a particular nuclear event. The center of the ground disturbance is determined to within about 100 m, which may be taken as the precision of location of the nuclear event, to the extent that the association is correct.

The second column is the event number, as used by Ringdal et al (1992).

After the date, is my SPOT pick of latitude and longitude (degrees, minutes, second).

Next is the Lilwall and Farthing (1990) latitude and longitude (degrees and decimal), which is an excellent listing based upon *P*-wave arrival times and a joint epicentral determination relative to locations published by Bocharov et al (1989) for some events. These are given for all 101 events in the list. (#72 is a chemical explosion.)

Last, is the difference, in kilometers, between my SPOT pick and the seismically determined location of Lilwall and Farthing (1990). This last column has a value often greater than 1 km. As noted by Thurber et al (1993), SPOT-picked locations often fall outside the 95% confidence ellipses associated with formal error analysis of seismic locations.

TABLE OF SPOT-PICKED LOCATIONS FOR 83 BALAPAN EXPLOSIONS

			latitude			longitude			seismic	lat/long	
h	1	15-Jan-65	49	56	6	79	0	33	49.935	79.009	0.01
h	2	19-Jun-68	49	58	52	78	59	7	49.980	78.986	0.10
h	3	30-Nov-69	49	55	28	78	57	20	49.924	78.956	0.02
h	4	30-Jun-71	49	56	47	78	58	50	49.946	78.980	0.04
h	5	10-Feb-72	50	1	30	78	52	39	50.024	78.878	0.09
h	6	2-Nov-72	49	55	37	78	48	58	49.927	78.817	0.08
l	7	10-Dec-72	50	1	40	78	59	42	50.027	78.996	0.10
	8	23-Jul-73							49.966	78.810	
l	9	14-Dec-73	50	2	54	78	59	9	50.054	78.987	0.64
h	10	16-Apr-74	50	1	49	78	55	29	50.039	78.946	1.80
	11	31-May-74							49.953	78.846	
	12	16-Oct-74							49.985	78.896	
l	13	27-Dec-74	49	58	5	79	0	16	49.949	79.011	2.17
h	14	27-Apr-75	49	56	23	78	54	23	49.955	78.926	2.20
	15	30-Jun-75							50.001	78.996	
	16	29-Oct-75							49.955	78.877	
h	17	25-Dec-75	50	2	56	78	49	4	50.051	78.813	0.41
l	18	21-Apr-76	49	54	5	78	49	43	49.906	78.827	0.53
l	19	9-Jun-76	49	59	41	79	1	21	50.002	79.025	0.83
h	20	4-Jul-76	49	54	12	78	53	53	49.912	78.908	1.20
h	21	28-Aug-76	49	58	33	78	55	35	49.979	78.928	0.37
h	22	23-Nov-76	50	1	5	78	56	35	50.013	78.962	1.47
	23	7-Dec-76							49.927	78.847	
l	24	29-May-77	49	56	48	78	46	28	49.932	78.774	1.63
	25	29-Jun-77							50.033	78.861	
	26	5-Sep-77							50.048	78.923	
h	27	29-Oct-77	50	3	28	78	58	44	50.068	78.977	1.14
h	28	30-Nov-77	49	58	7	78	52	24	49.966	78.890	1.23
h	29	11-Jun-78	49	54	49	78	48	2	49.903	78.791	1.36

h	30	5-Jul-78	49	54	11	78	52	0	49.896	78.868	0.79
h	31	29-Aug-78	50	0	35	78	57	58	50.011	78.976	0.72
h	32	15-Sep-78	49	55	45	78	51	40	49.922	78.876	1.33
	33	4-Nov-78							50.040	78.941	
	34	29-Nov-78							49.959	78.801	
h	35	1-Feb-79	50	5	10	78	51	2	50.101	78.863	1.88
l	36	23-Jun-79	49	54	57	78	50	39	49.913	78.857	0.97
h	37	7-Jul-79	50	2	23	78	59	18	50.032	78.989	0.86
	38	4-Aug-79							49.900	78.900	
h	39	18-Aug-79	49	56	54	78	55	6	49.949	78.937	1.34
h	40	28-Oct-79	49	59	49	78	59	43	49.982	78.996	1.66
h	41	2-Dec-79	49	54	35	78	47	3	49.900	78.793	1.25
	42	23-Dec-79							49.920	78.753	
l	43	25-Apr-80	49	58	50	78	45	12	49.981	78.756	0.20
h	44	12-Jun-80	49	59	24	78	59	26	49.986	78.998	0.69
	45	29-Jun-80							49.951	78.815	
l	46	14-Sep-80	49	55	52	78	47	9	49.930	78.801	1.09
h	47	12-Oct-80	49	58	9	79	1	19	49.967	79.026	0.38
h	48	14-Dec-80	49	54	33	78	55	6	49.909	78.932	0.98
h	49	27-Dec-80	50	4	5	78	58	27	50.063	78.982	0.79
h	50	29-Mar-81	50	1	22	78	58	43	50.011	78.978	1.31
h	51	22-Apr-81	49	53	58	78	48	21	49.891	78.811	1.01
h	52	27-May-81	49	59	19	78	58	8	49.992	78.979	0.82
h	53	13-Sep-81	49	54	50	78	53	42	49.920	78.911	1.33
h	54	18-Oct-81	49	55	44	78	50	36	49.927	78.854	0.79
h	55	29-Nov-81	49	54	8	78	50	50	49.898	78.857	0.84
h	56	27-Dec-81	49	55	59	78	46	43	49.930	78.792	1.02
h	57	25-Apr-82	49	55	4	78	53	12	49.912	78.906	1.53
h	58	4-Jul-82	49	57	34	78	48	27	49.958	78.800	0.56
h	59	31-Aug-82	49	54	52	78	45	39	49.926	78.760	1.29
	60	5-Dec-82							49.924	78.812	
h	61	26-Dec-82	50	4	8	78	59	32	50.078	78.986	1.11
h	62	12-Jun-83	49	55	28	78	53	46	49.920	78.914	1.37
l	63	6-Oct-83	49	55	30	78	45	23	49.924	78.761	0.35
h	64	26-Oct-83	49	54	48	78	49	24	49.912	78.828	0.37
h	65	20-Nov-83	50	3	25	78	59	47	50.055	78.997	0.22
h	66	19-Feb-84	49	54	1	78	44	39	49.894	78.745	0.70
h	67	7-Mar-84	50	3	19	78	57	12	50.049	78.950	0.74
	68	29-Mar-84							49.922	78.949	
h	69	25-Apr-84	49	56	14	78	51	5	49.935	78.867	1.14
h	70	26-May-84	49	58	46	79	0	21	49.973	79.000	0.83
h	71	14-Jul-84	49	54	33	78	52	39	49.901	78.879	0.91
	72	15-Sep-84							49.992	78.881	
	73	27-Oct-84							49.925	78.776	
l	74	2-Dec-84	50	0	35	79	0	29	49.990	79.009	2.19
l	75	16-Dec-84	49	56	49	78	48	56	49.930	78.816	1.88
l	76	28-Dec-84	49	52	51	78	41	32	49.875	78.700	0.86

h	77	10-Feb-85	49	53	56	78	46	43	49.893	78.783	0.73
h	78	25-Apr-85	49	55	35	78	52	49	49.921	78.899	1.47
	79	15-Jun-85							49.903	78.839	
h	80	30-Jun-85	49	51	52	78	40	0	49.857	78.659	0.99
l	81	20-Jul-85	49	56	44	78	47	5	49.943	78.783	0.31
h	82	12-Mar-87	49	56	9	78	49	34	49.929	78.824	0.77
h	83	3-Apr-87	49	55	7	78	46	46	49.910	78.786	1.07
h	84	17-Apr-87	49	53	0	78	40	12	49.874	78.663	1.15
h	85	20-Jun-87	49	56	12	78	44	47	49.927	78.740	1.17
h	86	2-Aug-87	49	52	50	78	52	29	49.877	78.873	0.41
h	87	15-Nov-87	49	53	55	78	45	20	49.881	78.753	1.97
h	88	13-Dec-87	49	57	42	78	47	34	49.957	78.792	0.52
h	89	27-Dec-87	49	52	45	78	43	27	49.867	78.718	1.42
h	90	13-Feb-88	49	55	58	78	52	3	49.932	78.878	0.76
l	91	3-Apr-88	49	54	25	78	54	23	49.909	78.918	0.86
h	92	4-May-88	49	57	0	78	44	58	49.931	78.741	2.20
h	93	14-Jun-88	50	1	26	78	57	30	50.034	78.964	1.19
h	94	14-Sep-88	49	52	42	78	49	24	49.869	78.825	1.04
h	95	12-Nov-88	50	2	50	78	58	4	50.048	78.960	0.56
h	96	17-Dec-88	49	52	50	78	55	24	49.879	78.924	0.18
h	97	22-Jan-89	49	56	25	78	48	59	49.934	78.815	0.71
h	98	12-Feb-89	49	55	0	78	42	51	49.911	78.704	0.96
h	99	8-Jul-89	49	52	5	78	46	45	49.869	78.775	0.32
h	100	2-Sep-89	50	0	35	78	59	6	50.019	78.988	1.05
h	101	19-Oct-89	49	55	19	78	54	32	49.927	78.927	1.41

REFERENCES

- Bocharov, V.S., S.A. Zelentsov, and V.I. Mikhailov, Characteristics of 96 underground nuclear explosions at the Semipalatinsk test site (in Russian), *Atomnaya Energiya*, 67, 210-214, 1989.
- Lilwall, R.C., and J. Farthing, Joint epicentre determination of Soviet underground nuclear explosions 1973-89 at the Semipalatinsk test site, *AWE Report No. O 12/90*, 13 p, Atomic Weapons Establishment, MOD(PE), August 1990.
- Ringdal, F., P.D. Marshall, and R.W. Alewine, Seismic yield determination of Soviet underground nuclear explosions, *Geophysical Journal Int.*, 109, 65-77, 1992.
- Thurber, C.H., and H.R. Quin, Seismic event location at regional and teleseismic distances, Final report PL-TR-92-2304, 31 December 1992, ADA266873.
- Thurber, C.H., H.R. Quin, and P.G. Richards, Accurate locations of nuclear explosions in Balapan, Kazakhstan, 1987 to 1989, *Geoph. Res. Letters*, 20, 399-402, 1993.
- Vergino, E.S., Soviet test yields, *EOS (Trans. AGU)*, 70, p1511 and 1524 and 1569, 1989.

SEISMICITY INDUCED BY NUCLEAR EXPLOSIONS

Paul G. Richards

Lamont-Doherty Earth Observatory and
Department of Geological Sciences, Columbia University

INTRODUCTION

The objective of this small project was to investigate shallow seismicity following an underground nuclear explosion, thus helping to understand what might be achieved by on-site inspection of a region in which a suspicious event had occurred.

I began the project knowing that a substantial number of papers had been written on seismic activity following the 1.1 megaton underground nuclear explosion BENHAM, conducted on 1968 December 19 at the Nevada Test Site (NTS). I was aware of anecdotal information on post-shot seismicity, but initially found considerable difficulty in obtaining documentation other than for a small number of explosions such as the megaton BENHAM and BOXCAR events, that had aroused public interest because of concern over induced earthquakes that could be damaging.

The plan was twofold: (1) to find papers and reports that had already addressed the subject of post-shot seismicity; and (2) to see if the Southern Great Basin Seismographic Network, Nevada (SGBSN), operated on and around the NTS with funding from the Department of Energy, supplied adequate data for purposes of characterizing post-shot seismicity in Nevada.

The project to find documentation of previous studies met with several successes for the main U.S. and Soviet test sites, and one conspicuous failure. Three technical reports of post-shot seismicity were obtained for NTS. Of these, one NTS study by scientists at Los Alamos National Laboratory (Edwards et al, 1983) goes into considerable detail, and two smaller studies of NTS give results consistent with Edwards et al. A series of papers by Adushkin and colleagues (referenced below) that studied post-shot seismicity at the Balapan test site near Semipalatinsk, East Kazakhstan, report broad features similar to studies at NTS. These broad features are the existence of post-shot microearthquakes that die down over a time-scale of weeks; and that consist of two types of events, having signals dominated either by high frequency or low frequency content.

The conspicuous failure, was an effort to find adequate documentation of the CLOUD GAP project carried out principally at NTS during the 1960s and early 1970s. CLOUD GAP included a major VELA-UNIFORM study of a variety of technologies pertinent to on-site inspection of the vicinity of a suspected underground nuclear explosion. Though funded at around the \$100 million level over a period of years, repeated efforts by several individuals during 1989-1992 have failed

to find any useful summary documentation of CLOUD GAP results. Hearings (U.S. Congress, 1963) conducted by the Joint Committee on Atomic energy, in March 1963, describe much of the early work on on-site inspections, but have little to say on explosion-induced seismicity.

The project to assess the utility of the SGBSN to study NTS post-shot seismicity showed (a) that detections of post-shot events, presumably caused by underground nuclear explosions, are abundant for some but not all explosions; and (b) that this network is probably not sufficiently dense for detailed study of the causal physical relationship between underground nuclear explosions and post-shot microearthquakes.

PREVIOUS STUDIES

The AEC/Nevada Operations Office, of what today is the Department of Energy, has published a detailed report (U.S. Atomic Energy Commission, 1971) of early studies of underground nuclear explosions (UNEs) and their associated aftershocks. At the time, the principal concern was that UNEs might trigger damaging earthquakes in the vicinity of test operations in Nevada and the Aleutians, rather than that investigation of post-shot seismicity might be useful in on-site inspections of a suspected UNE.

Two small studies of NTS post-shot seismicity are described by Lynch (1978, and Smith and Geil (1982). Quoting from Lynch:

"From a general overview of the 24-hour Helicorder records showing the seismic activity for 11 events detonated at the Nevada Test Site (NTS), it is concluded that ... [for] events which formed prompt surface craters, a virtually continuous level of seismic activity is present from the time of detonation until the termination of the surface collapse signal as seen at high gain stations within approximately 60 kilometers of the detonation point. [For] two events ... which formed late surface craters ... each event showed one interval of virtually continuous high level activity. ... An example was presented to show the existence of an underground nuclear explosion that did not produce secondary signals. ... With regard to the secondary signals following the main nuclear event, ... [both] low and high frequency signals are generated by both cavity growth and triggered tectonic activity."

Smith and Geil (1980) deployed seismographic equipment with digital recorders at NTS following the COLWICK shot of 1980 April 26. Quoting their conclusions:

"Approximately three months following the explosion, many events were located between the magnitudes of 1.5 to 0. ... The events extend from near the surface to roughly 1 km in depth ... [two] types of events are prominent: One set is very emergent with a gradual rise in amplitude; while the second group is impulsive. ... Fourteen months following the explosion, events were still detected and occurred with a similar spatial and magnitude distribution."

A major study of NTS post-shot seismicity is reported by Edwards et al (1983), who "fielded on-site [usually within two depth-of-burial (DOB) radii] seismic networks on 25 Los Alamos events with yields ranging from < 20 kt to 150 kt." They found that "as many as 10,000 microquake aftershocks may occur in the region of the detonation during the following 3 or 4 days." Other pertinent quotations from their work are as follows:

"The major faults bounding the site of a nuclear test appear to confine the events within the structural block in which the nuclear test was conducted."

"Microquakes sometimes cluster along structural and stratigraphic interfaces when the detonation is near the interface."

"There are two general groups of microquakes in most of the nuclear tests monitored, one group with shallow hypocenters probably associated with the depth of spall, and the second, deeper group associated with the stress cage. Most of the microquakes associated with the stress cage occur between three to five cavity radii from the working point."

Magnitudes were mostly in the range from -1 to +2. Edwards et al (1983) went on to characterize aftershock activity as a function of time for different classes of tests, categorized by the timing and the extent of collapse phenomena. Basically, they found that for tests resulting in large surface craters, microquake activity decreased to near preshot background levels soon after the surface collapse occurred. For such events, if conducted under an attempted clandestine test program, there would presumably be little need for an on-site inspection program to bother with microseismicity! They also found, for explosions which lacked a surface collapse, that there was subsurface activity – such as the slow growth of a chimney, in a process of subsurface collapse that could continue over a period of several days – followed by microquakes at a rate of about one event per day. Such activity was above the pre-shot background, and continued for weeks.

In a series of papers by V.V. Adushkin and colleagues, describing post-shot seismicity on the main Soviet test in East Kazakhstan, all the main features of the NTS experience, described above, are repeated. Thus, Adushkin et al (1990) describe an on-site network with a station spacing of 100 to 1,500 meters, used to study the seismicity induced by eight UNEs with yields ranging from 0.3 to 150 kt. They briefly note a class of post-shot events related to collapse of the cavity. Such events are marked by an emergent onset, a dominant frequency of about 1 - 2 Hz (i.e. low frequency) recorded for about 10 seconds, and hypocenters in the vicinity of the cavity or chimney. They paid more attention to a class of high-frequency events (5 - 16 Hz) associated with relaxation processes of various types, that continued for periods ranging from five days to 2.5 months after different shots.

Adushkin and Spivak (1990ab) point out the utility of post-shot seismicity, as a phenomena that can be exploited in monitoring on-site following a suspicious main event. They find that the radius of the volume of rock within which induced seismicity occurs, is approximately one kilometer times the cube root of the yield in kt; but the presence of large tectonic faults or rock masses with different impedances can distort the pattern of aftershocks. They went on to propose a relationship between the maximum ground velocity recorded for a series of aftershocks, and the yield of the inducing explosion. Adushkin et al (1992) describe how an underground explosion affects the movement of ground water.

In summary, extensive studies of post-shot seismicity, based upon seismic networks deployed on-site with station spacing comparable to the depth of burial of the explosion, demonstrate that small aftershocks are common for periods of weeks.

USES OF THE SOUTHERN GREAT BASIN SEISMIC NETWORK

For purposes of on-site inspection, there are still questions about how near the epicenter of a suspicious event it would be necessary to deploy a portable network, in order to detect such

aftershocks as might occur from a clandestine UNE. Could shot-induced seismicity be seen, at horizontal distances much greater than the depth of burial? (Typical depths of burial are on the order of 0.1 or 0.12 km, times the cube root of the yield in kt.) And is the signal from shot-induced events significantly different from events that occur as part of the background seismicity?

To address these and related questions, I worked with Joan Gomberg and Steve Harmsen of the U.S. Geological Survey (Branch of Geologic Risk Assessment) in the summer of 1990, who at the time were associated with operation of the Southern Great Basin Seismic Network (SGBSN, see Figure 1). We examined the list of preliminary locations of seismic events recorded by SGBSN, and found many small events close to selected nuclear explosions at NTS, occurring days and months following the nuclear event.

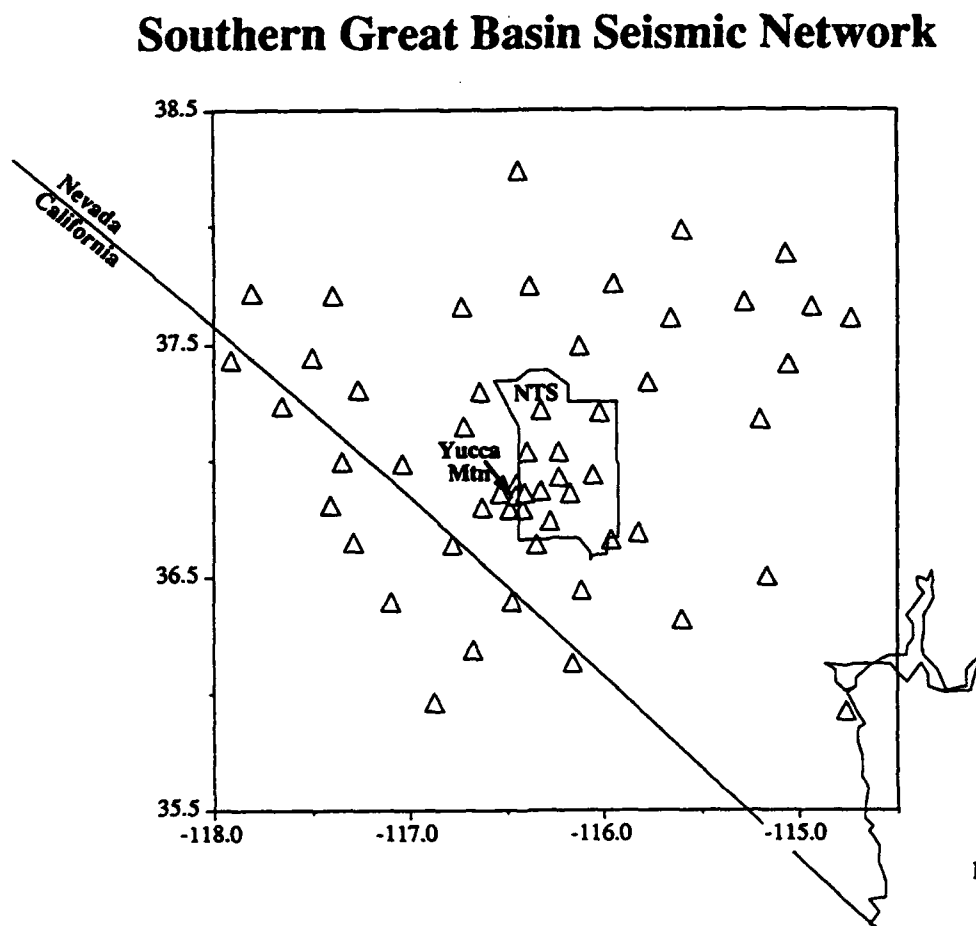


Figure 1. Station map of SGBSN; station locations indicated by triangles. Station EPN (which recorded the earliest arrivals in Figs. 3, 4, 5 below) is the station shown in the northwest section of the Nevada Test Site. [From Gomberg, 1991.]

We concentrated on seismicity in the Silent Canyon Caldera (E. Pahute), following underground nuclear explosions in 1986-89. In particular, following LOCKNEY (magnitude 5.7, 1987 Sept. 24) and up to the time of the next explosion in the region (COMSTOCK, 1988 June 2), we found eleven events occurring within ten km of the LOCKNEY shot point that were routinely located in the preliminary processing of network data.

In the network archive, we also found high quality digital data that had not been routinely processed, but which revealed the occurrence of about an order of magnitude more events. Many of these additional events, whose occurrence rate dropped with time post-LOCKNEY, exhibited a low frequency character that differed from the events routinely located as small earthquakes by the network. Many of the post-LOCKNEY events displayed a dilatational first motion at most of the stations at which first-motion could be determined (S. Harmsen, personal communication). The same pattern, of some small earthquakes and more low frequency events, is observed following the smaller nuclear explosion AMARILLO (magnitude 4.9, 1989 June 27).

Figure 3 shows an example of what is routinely identified as a "small earthquake". For such events, the corner frequency is up around 9 hz (S. Harmsen, personal communication). S-waves are clearly identifiable at many stations, and aid considerably in developing accurate locations. Following identifiable S-arrivals, the level of coda drops significantly after a few seconds.

Figure 4 shows an example of what is called a "low frequency event". Though in this case there are quite easily identifiable P-arrivals at several stations, the onset of S is hard to pick. The corner frequency here is about 4.5 hz (S. Harmsen, personal communication), and coda levels do not drop significantly from their highest levels until some tens of seconds elapse.

Figure 5 shows an example of an event with even lower frequency content. The dominant frequency is now well below 3 hz. S-waves are not identifiable on these vertical-component traces. And the signal reverberates for many tens of seconds.

It appears that low frequency events (LFEs) having the character of Figures 4 and 5 are commonly not selected for processing, at least in the preliminary catalog of events located by SGBSN (see Figure 2 caption).

The reason may well be, that the purpose of the SGBSN is to help assess the suitability of Yucca Mountain to be a repository of high-level radioactive waste. In such a project, the emphasis of seismicity studies based on SGBSN data is on tectonic events, rather than on low frequency activity that may principally be a response to sub-surface collapse or stress-relaxation processes following an underground nuclear explosion.

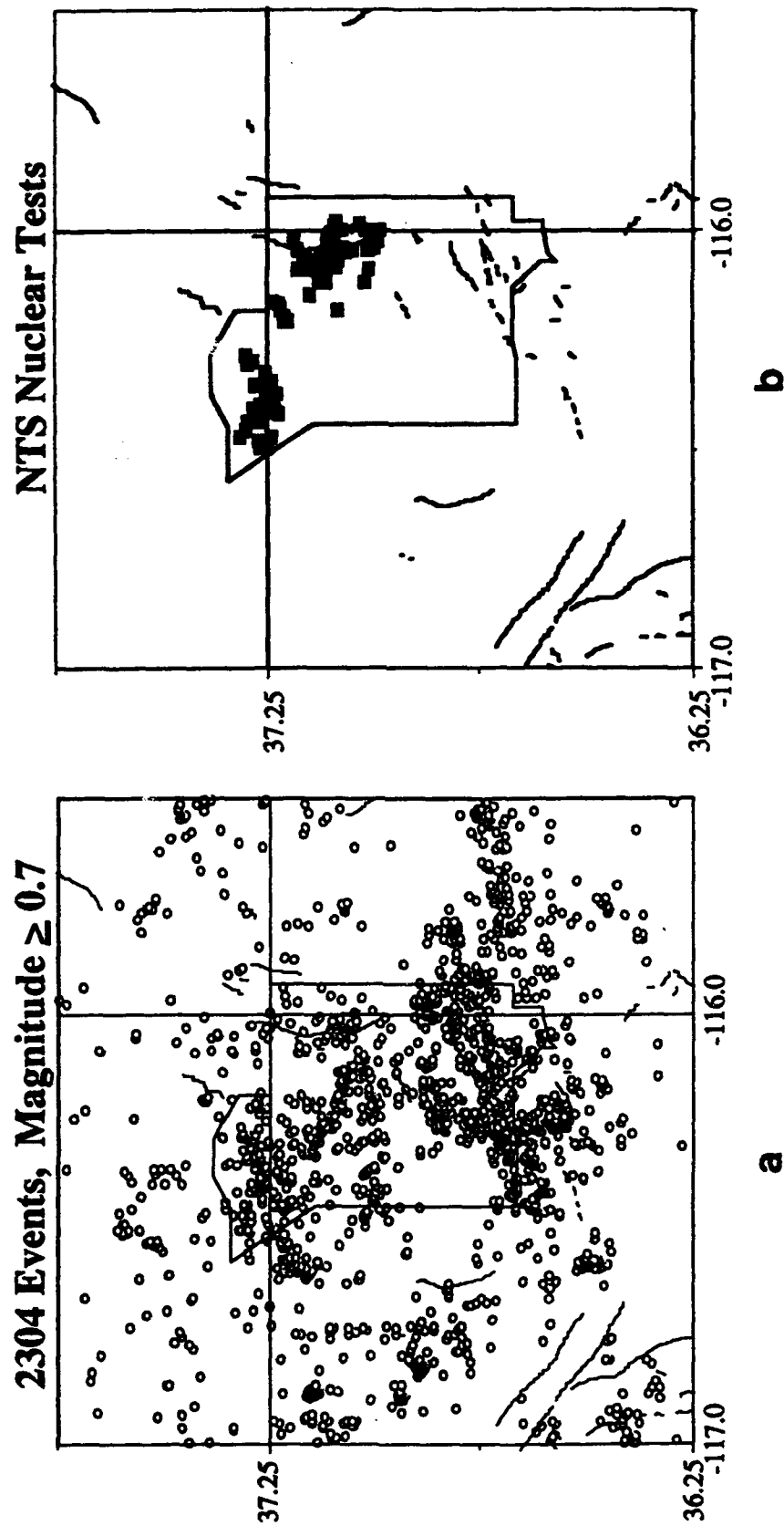


Figure 2. (a) Earthquakes (open ovals) in the NTS region from the SGBSN catalog from 1983-89 with $M_L \geq 0.7$. (b) Underground nuclear explosions (squares) in the same region for the same years. [From Gomberg, 1991.] Low frequency events following explosions are commonly excluded from the procedure used to generate the catalog used in (a).

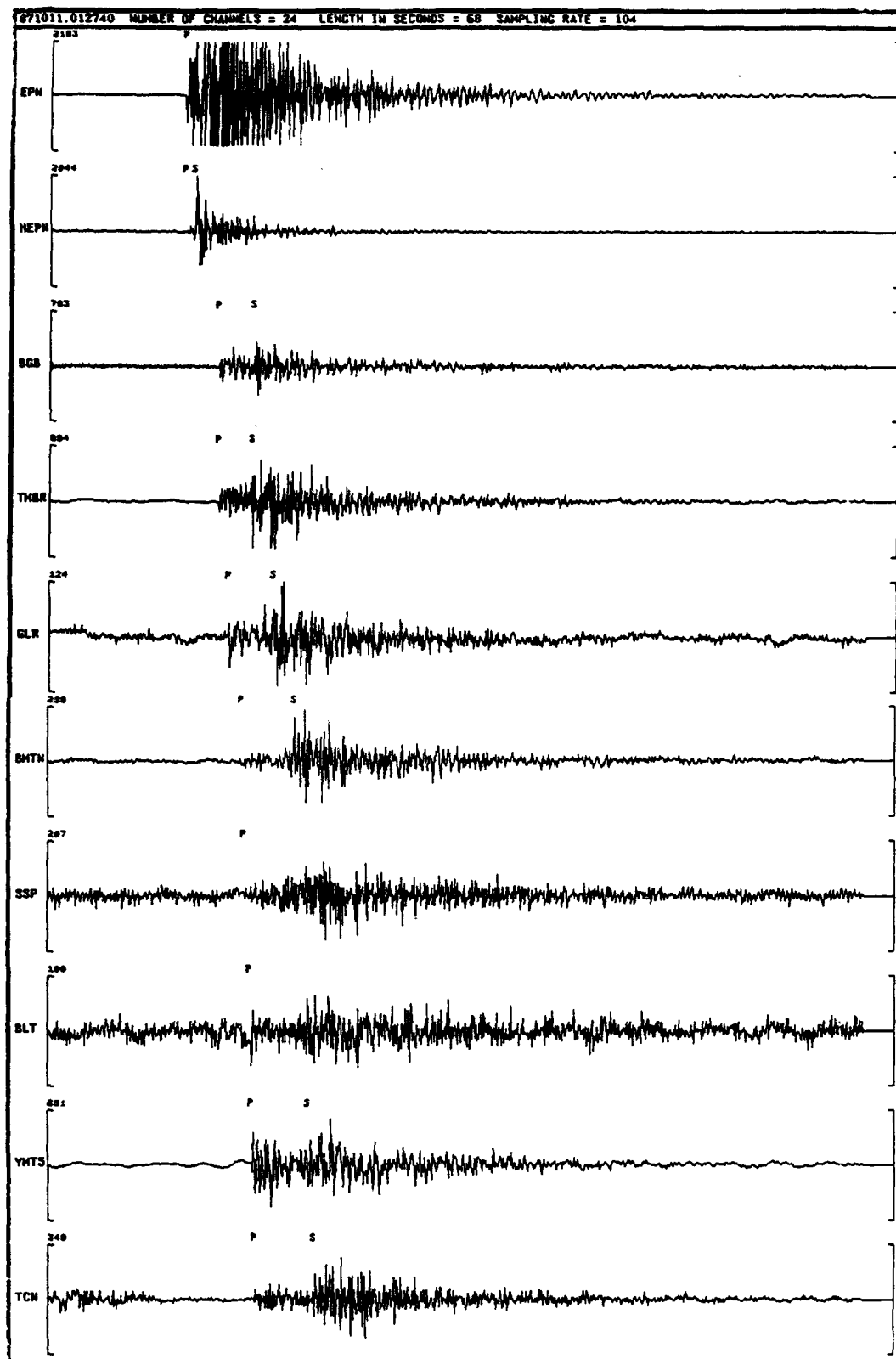


Figure 3. Seismograms of an event classified as a small earthquake, or "normal tectonic event." Traces start at 1987 October 11, 01:27:40 and last for 68 s. It has clear S arrivals, and was located in routine preliminary processing of SGBSN data. The closest station, EPN, is less than 10 km from the LOCKNEY site.

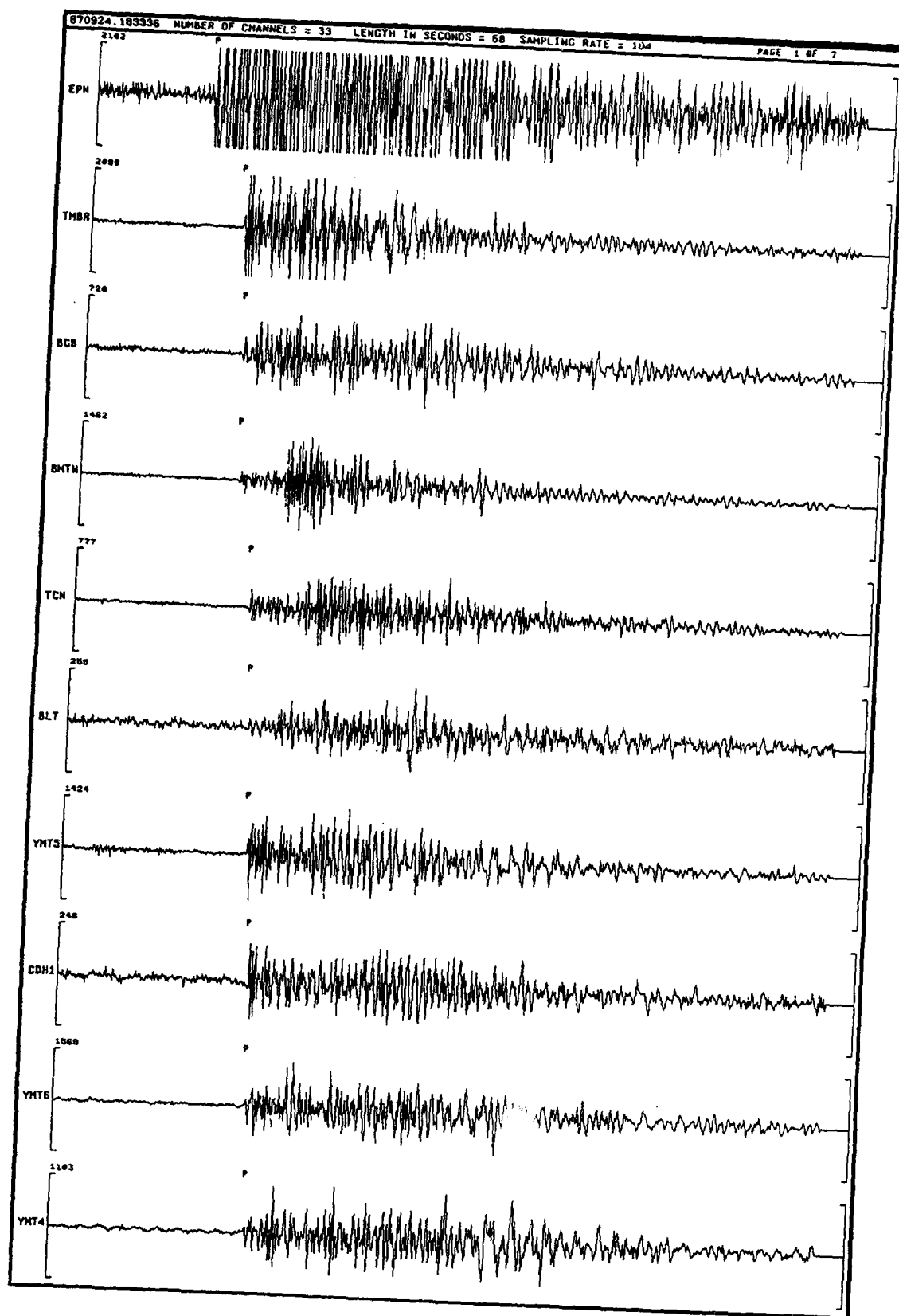


Figure 4. Seismograms for a "low frequency event." Traces start at 1987 Sept. 24, 18:33:36, and last for 68 s. This event is not more than 5 km from (and possibly colocated with) the LOCKNEY site. Such LFEs are usually not routinely located in preliminary processing of SGBSN data.

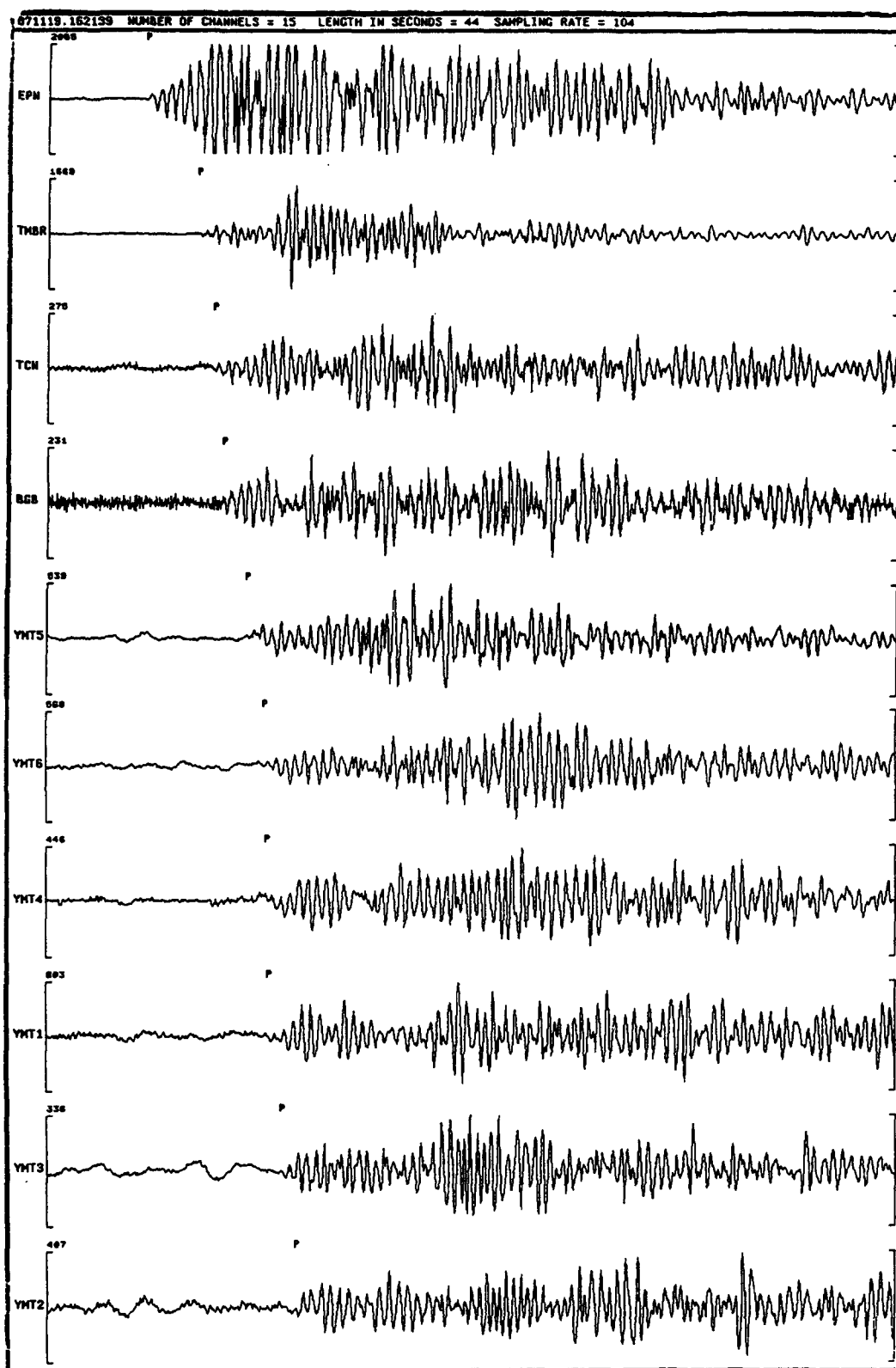


Figure 5. Seismograms for an event with very low frequency character. Traces start at 1987 Nov. 19, 16:21:39, and last for 44 s. This event is also close to the LOCKNEY site, but the emergent arrivals result in lack of depth control.

The low-frequency events in Figures 4 and 5 are particularly interesting, in that they are located close to the LOCKNEY explosion (at 37.228°N, 116.375°W on 1987 Sept. 24). Thus, the event of Figure 4 is given a location at 37.227°N, 116.371°W (S. Harmsen, using station time corrections determined from the LOCKNEY shot). This event is shallow (depth around 2 km, ± 2 km), and occurred just a few hours after LOCKNEY. The next nuclear explosion to occur on NTS

Lockney & Borate Low Frequency Event Hypoinverse Epicenters

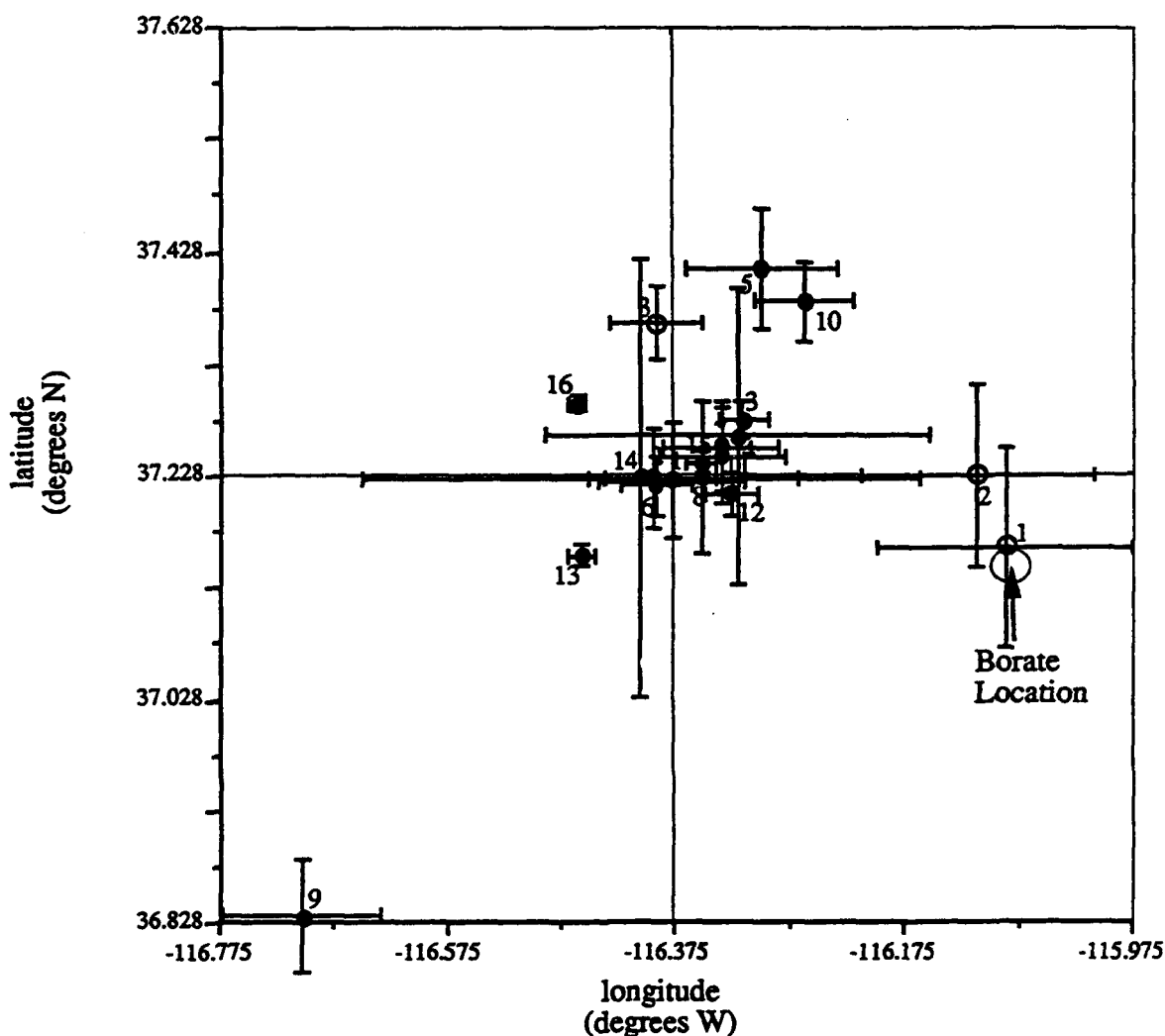


Figure 6. The LOCKNEY site is at the center of this plot, which shows location estimates for nineteen low-frequency events following LOCKNEY. Numbers 1 to 16 (shown with filled circles) occurred between the LOCKNEY (1987 Sept. 24) and BORATE (1987 Oct. 23) shots. Numbers 1 to 3 (shown with open circles) occurred post-BORATE, but within 50 days of LOCKNEY. Event #12 is that of Figure 4. Event #3 (open circle) is that of Figure 5. [Figure, from unpublished work of Joan Gomberg.]

was BORATE (1987 Oct 23 at 37.142°N, 116.079°W), but the subsequent LFE of Figure 5 (1987 Nov. 19) is an example of events occurring back close to the LOCKNEY shot point. That is, the event of Figure 5, 48 days after LOCKNEY, is given a location at 37.314°N, 116.382°W (S. Harmsen). In this case, because of difficulty in picking the onset of emergent P-arrivals (see Fig. 5), the location may have epicentral errors of up to 10 km and there is little depth control. The event could be co-located with LOCKNEY, but definitely not with BORATE.

Out of a set of 21 LFEs in the fifty days following LOCKNEY, data was adequate for 19 events to obtain HYPOINVERSE solutions. Two events appear to be associated with BORATE, and one event lies about 50 km from both explosions. But 16 events appear to be associated with LOCKNEY, clustering in a region about 20 km across that includes the LOCKNEY site (see Figure 6). It is not clear how much of this 20 km is due to location error, but the association of the events taken as a group, with the LOCKNEY site, seems clear.

These examples illustrate the strength and weakness of SGBSN data for studying shot-induced seismicity. The archive was found to be well maintained, and it reveals many events for analysis. (The data is not continuously recorded but is triggered. Again, it should be noted that there are many more events in the archive, than are routinely located.) But if each LFE is to be definitely identified as shot-induced, then locations must be determined with greater precision than SGBSN data alone permits. Possibly, by merging data from SGBSN with that acquired by Los Alamos or Livermore National Laboratories close in for a few shots, the low frequency nature of events such as that shown in Figure 5 could definitely be associated with very shallow depths. However, such an effort goes well beyond that attempted in this preliminary study of SGBSN data.

We can conclude from this project at NTS that shot-induced seismicity as characterized by a group of low-frequency events is often detectable at distances of a few tens of km, and not only at distances comparable to the shot depth.

ACKNOWLEDGEMENT

I thank Joan Gomberg and Steve Harmsen for guidance through the SGBSN archive and associated software, and for assistance with locating events.

REFERENCES

- Adushkin, V.V. and A.A. Spivak, Seismic Monitoring Methods in Relation to Banning of Underground Explosions, *Izvestiya Akademii Nauk SSSR: Fizika Zemli* (in Russian), No. 12, pp 3-5, December, 1990a. [Translated to English by the American Geophysical Union, in *Physics of the Solid Earth*, December, 1990a.]
- Adushkin, V.V. and A.A. Spivak, Possibility of monitoring underground nuclear explosions by analysis of aftershocks, *Izvestiya Akademii Nauk SSSR: Fizika Zemli* (in Russian), No. 12, pp. 15-20, December, 1990b. [Translated to English by the American Geophysical Union, in *Physics of the Solid Earth*, December, 1990b.]
- Adushkin, V.V., A.A. Spivak, M.M. Krekov, M.G. Starshinina, and S.K. Daragan, *Aftershocks of large-scale underground nuclear explosions*, *Izvestiya Akademii Nauk SSSR: Fizika Zemli* (in Russian), No. 9, pp.20-27, September, 1990. [Translated to English by the American Geophysical Union, in *Physics of the Solid Earth*, September, 1990.]
- Adushkin, V.V., A.A. Spivak, E.M. Gorbunova, P.B. Kaazik, and I.N. Nedbayev, Principal regularities in ground water movement resulting from large underground explosions, *Izvestiya Akademii Nauk SSSR: Fizika Zemli* (in Russian), No. 3, pp. 80-93, March, 1992. [Translated to English by the American Geophysical Union, in *Physics of the Solid Earth*, March, 1992.]
- Edwards, C.L., M.D. Harper, T.A. Weaver, D.J. Cash, J.M. Ray, and E.F. Homuth, Microearthquake activity associated with underground nuclear testing at the Nevada Test Site, report LA-8552-MS, Los Alamos Scientific Laboratory, 19 pgs., June, 1983.
- Gomberg, J., Seismicity and Detection/Location Threshold in the Southern Great Basin Seismic Network, *J. Geophys. Res.*, **96**, 16401-16414, September, 1991.
- Lynch, R.D., A preliminary analysis of seismic phenomena associated with the collapse of explosion generated cavities, Interim technical report on contract F08606-76-C-0040, September, 1978.

Smith, A.T., and R.G. Geil, Microseismicity following an explosion, *Earthquake Notes, of the Eastern Section of the Seismological Society of America*, 53, #1, p. 10, 1982.

U.S. Atomic Energy Commission, Seismology, Aftershocks, and Related Phenomena associated with Underground Nuclear Explosions, a bibliography of selected papers with abstracts, compiled and prepared by the Office of Effects Evaluation, Seismology Branch, AEC, Nevada Operations Office, Las Vegas, Nevada, NVO-87 U35 U51, 36 pages, May, 1971.

U.S. Congress, Hearings before the Joint Committee on Atomic Energy, Developments in technical capabilities for detecting and identifying nuclear weapons tests, March 5, 6, 7, 8, 11 and 12, 1963.

LG SIGNALS RECORDED IN CHINA, FOR CERTAIN UNDERGROUND NUCLEAR EXPLOSIONS IN EAST KAZAKHSTAN

Paul G. Richards¹, Won-Young Kim, and Jinghua Shi¹

Lamont-Doherty Earth Observatory of Columbia University, Palisades, NY 10964

(¹also, Department of Geological Sciences, Columbia University)

ABSTRACT

We report our measurements of RMS *Lg* signals for two Balapan explosions for which the usual stations reporting *Lg* had no signal. One of these explosions apparently had the largest *P*-wave signal since the Threshold Test Ban Treaty went into effect, at least according to some sources. But we found the *Lg* signal for this event was not anomalously large; the event appears to be one of a group of events having about the same yield.

INTRODUCTION

Lg signals have long been advocated as providing the best basis for assigning seismic magnitude for events recorded at regional distances. Thus, Baker (1970) used LRSM data at 69 stations for 78 underground explosions (mostly at the Nevada Test Site). He showed that the scatter of station magnitudes about the network average was much smaller for measurements based upon *Lg*, than for *Pn*. A well-known series of papers by Nuttli developed procedures for measuring m_b (*Lg*) from analog records, and Hansen et al (1990) summarized work on the stability of RMS *Lg* measurements on digital recordings of East Kazakhstan nuclear explosions, for purposes of obtaining accurate magnitudes. Once the magnitude scale has been calibrated in terms of yield, such RMS *Lg* values can be used to estimate the yield of Soviet explosions, as discussed by Ringdal et al (1992).

One of the major implications of this work on *Lg*, carried out over more than 20 years, is that a single well-operated station, recording *Lg* with adequate signal-to-noise ratio, potentially can be used to provide yield estimates as accurate as those based on a large global network of stations reporting teleseismic *P*-wave amplitudes. This potential is presumably present for single stations recording *Lg* from explosions at the Balapan test site near Semipalatinsk, Kazakhstan, since Hansen et al (1990) showed for this source region that the single station precision of RMS *Lg* measurement is very low: it is about 0.03 magnitude units.

Unfortunately, prior to 1988 (when efforts by the Natural Resources Defense Council and the Incorporated Research Institutions for Seismology succeeded in installing seismometers on the territory of the U.S.S.R. that were allowed to collect data from Soviet nuclear explosions), western seismologists had only a few stations capable of recording suitable L_g signals for purposes of estimating yields at Balapan – the location of the largest explosions conducted under the restrictions of the 150 kiloton Threshold Test Ban Treaty (TTBT). The capable stations included the NORSAR and Gräfenberg arrays, which produced excellent L_g data for many Balapan explosions. But these stations were not operating at the time of certain Balapan explosions, including the time of one of the largest events, that of 1980 September 14.

Figure 1 shows the P -wave magnitude for 100 Balapan explosions, 1965–1989, as a function of time, as published by Ringdal et al (1992). Many different versions of this Figure have been used, in the context of interpreting the drop in magnitudes of Balapan explosions when the TTBT went into effect after 1976 March 31. Magnitudes of the largest shots subsequently rose for a few years.

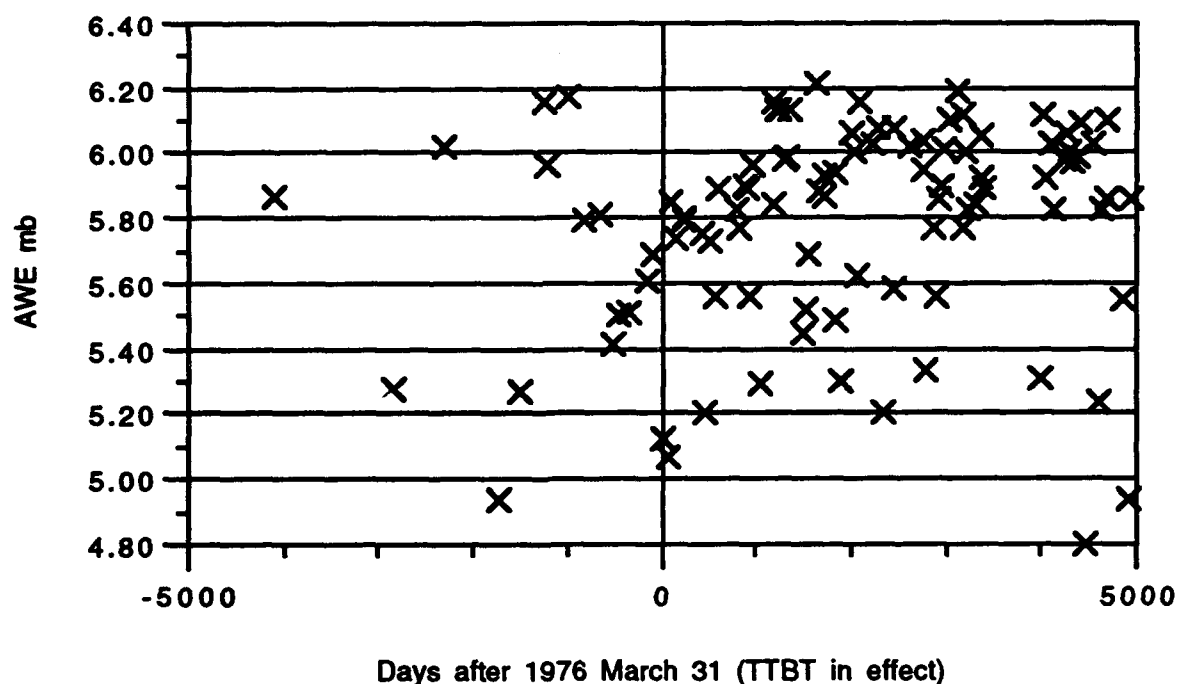


Figure 1. P -wave magnitudes as a function of time, for 100 Balapan underground nuclear explosions, 1965–1989, as a function of time [$m_b(P)$ from Ringdal et al (1992)].

On the basis of the magnitude scale used in Figure 1 (maximum likelihood $m_b(P)$, obtained by the Atomic Weapons Establishment of the British Ministry of Defence using data from stations reporting to the International Seismological Centre), the largest P wave signals came from the event of 1980 September 14, for which $m_b(P) = 6.21$. This event also has the largest value of ψ_{∞} for any Balapan explosion post-1975, according to Ringdal et al (1992). [ψ_{∞} is a measure of the volume change at the source, related to the isotropic moment of a body force equivalent to the explosion. ψ_{∞} is measured from P -waves, and, like $m_b(P)$, is also thought to be a useful indicator of yield.]

It should be noted that P -wave magnitude estimates have been published by other workers for various subsets of explosions at Balapan, and events other than that of 1980 September 14 have in some cases been found to have the largest $m_b(P)$. But the possibility that the 1980 September 14 event had the greatest yield is worth pursuing, in view of fact that the Ringdal et al (1992) study appears to be the most complete publication in the west on Balapan yields, and it lists 196 kt as the yield for this particular event. [While this is the largest yield estimate by Ringdal et al (1992) for a post-1975 shot, a slightly larger yield of 212 kt is given for the shot of 1973 July 23, based on L_g data, and on interpretation of $m_b(P)$ in terms of the particular part of the test site for this shot.]

OUR ANALYSIS

We searched for L_g data from the 1980 September 14 explosion for several stations, but found the signal was either absent because stations were down (such as NORSAR and Gräfenberg) or clipped (Mashad, Iran). However, pursuing a suggestion from Dr. Francis Wu (SUNY, Binghamton), we found high quality analog data from a 3-component Kirnos broad band station that has operated since 1962 September 20 at Urumqi, China (station WMQ) – and that may be presumed to operate to the present day (August 1993). Microfiche film chips from this station have been filed at World Data Center A in Colorado for the years 1980-84, and 1986, and we requested all 23 examples for days that should have given a Balapan explosion record. (Note, there was a moratorium on nuclear explosions in the U.S.S.R. during 1986.) Uses of the fundamental mode surface waves recorded by this analog system at WMQ, for several Balapan explosions, are described by Patton et al (1985). The distance from the 1980 September 14 explosion to station WMQ is 8.62° .

We found that the usual practice at WMQ, on days when a Balapan explosion is recorded, is to change the paper about 20 minutes after the recording commences, to reduce the problem of overlapping traces from the hours following the event. This procedure results in two sets of paper recording for such days, and very often we found that the recording filed at World Data Center A was that begun *after* the explosion signal had died down, resulting in no data. However, for 10 explosions the WMQ data *was* on file, and was of excellent quality. The set included the events of 1980 Sep 14 and 1980 Apr 25, for which Ringdal et (1992) had no *Lg* data. For the other 8 events, *Lg* signals had been obtained and measured at NORSAR. The digitized vertical component signal at WMQ for the event of interest is shown in Figure 2, together with a spectrum for the *Lg* window.

date of Balapan expl.	$m_b(P)$ AWE	$m_b(Lg)$ NOR & GRF	RMS <i>Lg</i> from Kirnos at WMQ:		
			frequency range, window length		
			0.3-3, 90	0.3-3, 120	0.6-3, 120
1980 Apr 25	5.45	none	-4.3141	-4.3502	-4.5799
1980 Jun 12	5.52	5.627	-4.0775	-4.1238	-4.4181
1980 Jun 29	5.69	5.706	-3.9613	-4.0060	-4.2362
1980 Sep 14	6.21	none	-3.4500	-3.4952	-3.8132
1980 Oct 12	5.88	5.927	-3.7068	-3.7242	-4.0000
1980 Dec 14	5.93	5.936	-3.6488	-3.6894	-4.0426
1981 Apr 22	5.94	5.929	-3.6657	-3.6946	-4.0982
1981 May 27	5.30	5.456	-4.3667	-4.4030	-4.7512
1981 Sep 13	6.06	6.108	-3.4954	-3.5370	-3.8706
1984 Jul 14	6.10	6.054	-3.4878	-3.5279	-3.8282
$m_b(Lg)$ predicted at NORSAR, via WMQ measurements, for					
event of 1980 Apr 25			5.470	5.472	5.534
event of 1980 Sep 14			6.099	6.091	6.092

event of 1980 Apr 25, average estimate of $m_b(Lg)$: 5.492.
event of 1980 Sep 14, average estimate of $m_b(Lg)$: 6.094.

Table 1. RMS *Lg* measurements from analog records at WMQ

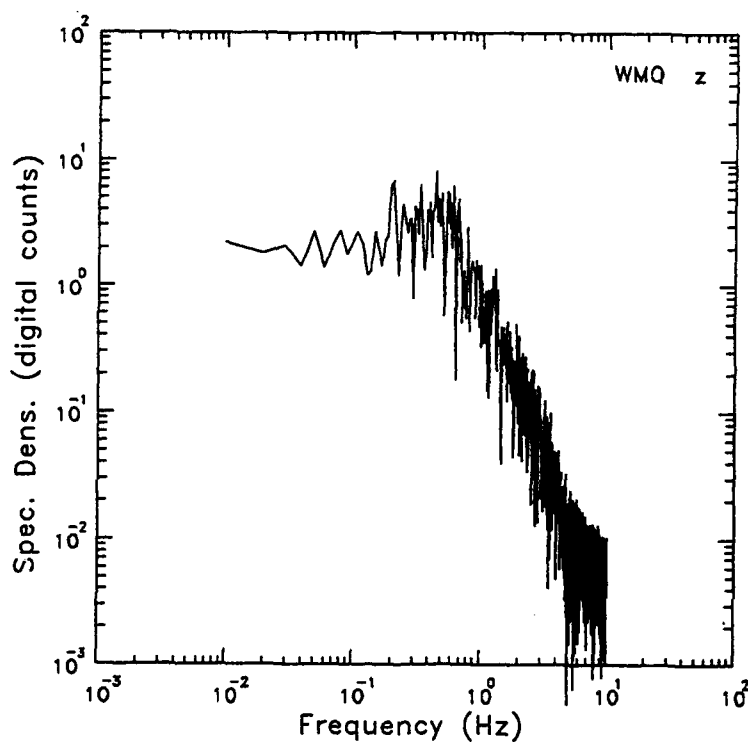
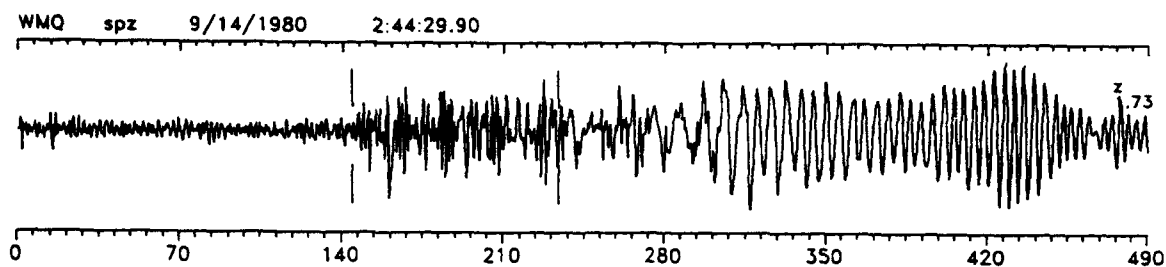


Figure 2. (top) Digitized trace of the WMQ broadband Kirnos vertical component for the Balapan explosion of 1980 Sep 14. A 90 second *Lg* window is indicated.

(bottom) spectrum of the *Lg* window. The high-frequency roll-off indicates no problem with digitizing noise at frequencies below 4hz.

After hand-digitization and measurement of RMS L_g at WMQ for the 10 events, and calibration against NORSAR for the 8 events in common, we conclude that the 1980 Sep 14 event had L_g magnitude corresponding to a value of about 6.094 at NORSAR, and thus was one of a number of events that cluster about this magnitude: it was not unusually large. Our results are shown in Table 1.

A number of choices may be made in the details of digitization window and bandwidth. The NORSAR RMS L_g for Balapan explosions is taken over a 120 second window after filtering the data to pass the band from 0.6 to 3 hz. This was one of our choices, but as shown in Table 1 we also tried the effects of a wider band and a slightly shorter window. The scatter of the eight points about a best-fitting

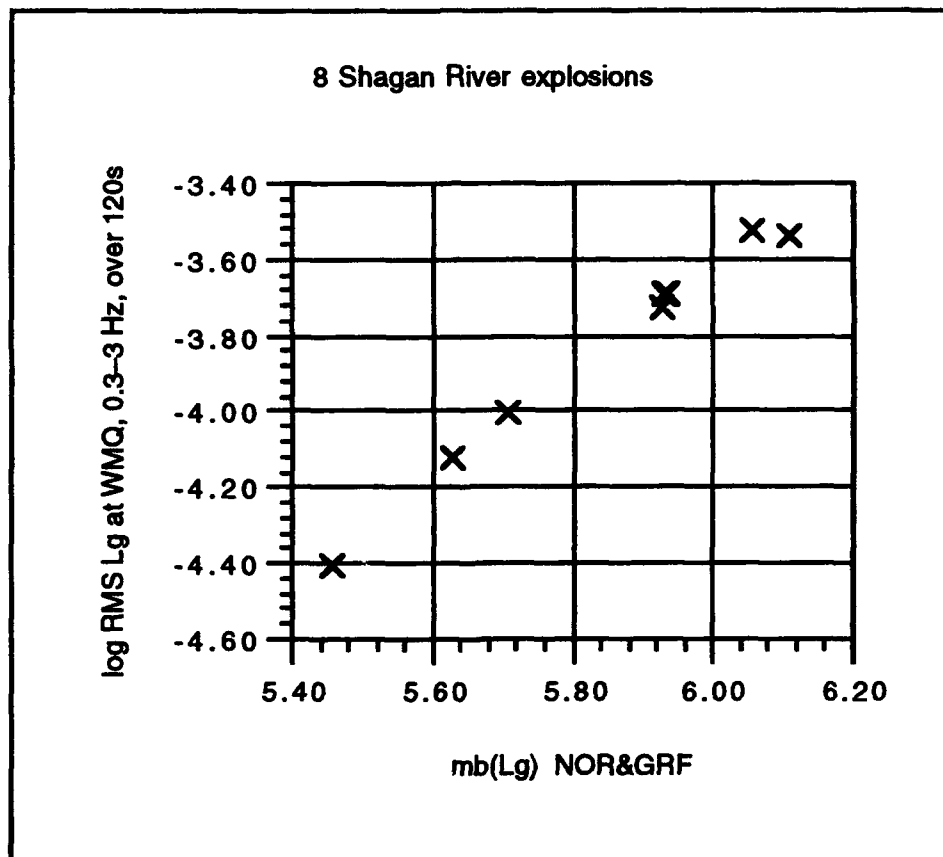


Figure 3. Excellent linear relationship between NORSAR and Gräfenberg $m_b(L_g)$, and RMS L_g measured from digitized WMQ analog data.

straight line (minimizing perpendicular distance) was 0.02, 0.02 and 0.04 logarithmic (i.e. magnitude) units, for the three choices indicated in the last three columns of

Table 1, respectively. For example for the choice {0.3 – 3 hz, 120 s window}, Figure 3 shows the excellence of the correlation between WMQ and the West European array measurements of RMS L_g . The concluding lines of Table 1 give the inferred NOR & GRF value of $m_b(Lg)$ for the two events, 1980 April 25 and September 14.

DISCUSSION

To conclude this study, it is of interest to comment upon the implications for yield estimates of the 1980 September 14 event, if it is assigned a NOR/GRF $m_b(Lg)$ value of 6.094.

Table 2 shows the ranking of 30 Balapan explosions after the 150 kt threshold was intended to go into effect (post-March 1976), using three different measures of event size.

Figure 4 shows the corresponding magnitudes for these three different measures, plotted in a way intended to bring out any tendency of events to cluster about certain magnitudes.

First, it is interesting that only the $m_b(Lg)$ values show a tendency to cluster. The 1980 September 14 explosion is the fifth largest, in this ranking, but no particular significance should be attached to slight differences between the largest 10 $m_b(Lg)$ values. Second, note that the 1980 September 14 explosion has the largest P -wave magnitude (post TTBT), whether or not the magnitude is adjusted using the regional corrections noted in Table 2.

Finally, using the Ringdal et al (1992) formulas¹ for converting between magnitude and yield, an $m_b(Lg)$ value of 6.094 converts to a yield estimate of 156 kt for the 1980 September 14 explosion. When averaged with the estimate based upon adjusted $m_b(P)$, the combined estimate becomes 176 kt. Therefore, the effect of using WMQ analog data in this case is a combined yield estimate 10% lower than the value (196 kt) given by Ringdal et al (1992).

¹ $m_b(Lg) = 4.45 + 0.75 \log Y$, and $m_b'(P) = 4.45 + 0.75 \log Y$

Ranked by $m_b(Lg)$			Ranked by $m_b(P)$			Ranked by adjusted $m_b(P)$, $mb'(P)$			
date	$m_b(Lg)$	$m_b(P)$	date	$m_b(Lg)$	$m_b(P)$	date	$m_b(Lg)$	$mb'(P)$	region
79-Aug-18	6.126	6.13	80-Sep-14	6.094	6.21	80-Sep-14	6.094	6.16	SW
81-Sep-13	6.108	6.06	84-Oct-27	6.098	6.19	79-Aug-18	6.126	6.15	TZ
79-Aug-04	6.100	6.13	79-Jun-23	6.064	6.16	84-Oct-27	6.098	6.14	SW
84-Oct-27	6.098	6.19	81-Dec-27	6.075	6.16	81-Dec-27	6.075	6.11	SW
80-Sep-14	6.094	6.21	79-Aug-18	6.126	6.13	79-Jun-23	6.064	6.11	SW
37-Dec-13	6.082	6.06	79-Aug-04	6.100	6.13	84-May-26	6.079	6.11	NE
84-May-26	6.079	6.01	79-Dec-23	6.039	6.13	81-Sep-13	6.108	6.08	TZ
81-Dec-27	6.075	6.16	87-Apr-03	6.063	6.12	79-Oct-28	6.051	6.08	NE
83-Jun-12	6.072	6.02	84-Dec-16	6.043	6.12	79-Aug-04	6.100	6.08	SW
82-Apr-25	6.072	6.03	84-Jul-14	6.054	6.10	79-Dec-23	6.039	6.08	SW
79-Jun-23	6.064	6.16	89-Jan-22	5.960	6.10	87-Apr-03	6.063	6.07	SW
88-Apr-03	6.063	5.99	88-May-04	6.046	6.09	84-Dec-16	6.043	6.07	SW
87-Apr-03	6.063	6.12	82-Dec-05	5.996	6.08	84-Jul-14	6.054	6.05	SW
84-Jul-14	6.054	6.10	82-Jul-4		6.08	82-Apr-25	6.072	6.05	TZ
79-Oct-28	6.051	5.98	87-Dec-13	6.082	6.06	89-Jan-22	5.960	6.05	SW
88-May-04	6.046	6.09	81-Sep-13	6.108	6.06	83-Jun-12	6.072	6.04	TZ
84-Dec-16	6.043	6.12	85-Jun-15	5.987	6.05	88-May-04	6.046	6.04	SW
87-Dec-27	6.042	6.00	83-Oct-26	6.016	6.04	82-Jul-4		6.03	SW
88-Feb-13	6.042	5.97	88-Sep-14	5.969	6.03	82-Dec-05	5.996	6.03	SW
79-Dec-23	6.039	6.13	82-Apr-25	6.072	6.03	87-Dec-13	6.082	6.01	SW
83-Oct-26	6.016	6.04	87-Jun-20	5.971	6.03	88-Apr-03	6.063	6.01	TZ
78-Aug-29	6.010	5.90	83-Jun-12	6.072	6.02	85-Jun-15	5.987	6.00	SW
82-Dec-05	5.996	6.08	84-May-26	6.079	6.01	78-Aug-29	6.010	6.00	NE
85-Jun-15	5.987	6.05	84-Dec-28	5.980	6.00	83-Oct-26	6.016	5.99	SW
81-Oct-18	5.981	6.00	81-Oct-18	5.981	6.00	88-Feb-13	6.042	5.99	TZ
84-Dec-28	5.980	6.00	87-Dec-27	6.042	6.00	88-Sep-14	5.969	5.98	SW
87-Nov-15	5.975	5.98	79-Dec-02	5.929	5.99	87-Jun-20	5.971	5.98	SW
78-Nov-29	5.971	5.96	88-Apr-03	6.063	5.99	80-Oct-12	5.927	5.98	NE
87-Jun-20	5.971	6.03	87-Nov-15	5.975	5.98	80-Dec-27	5.933	5.97	NE
88-Sep-14	5.969	6.03	79-Oct-28	6.051	5.98	84-Dec-28	5.980	5.95	SW

[to obtain $mb'(P)$

from $mb(P)$:

subtract 0.05 for SW

add 0.02 for TZ

add 0.10 for NE]

Table 2. Thirty Balapan explosions, all post March 1976, are ranked three different ways: (a) by $m_b(Lg)$; (b) by $m_b(P)$; and (c) by adjusted $m_b(P)$. [The adjusted value is intended to account for the fact that explosions in the SW section of the Balapan test site appear to be somewhat more efficient in generated P -wave signals, at a given yield, than do explosions in the NE section. The adjusted value is presumably better suited to yield estimation. For the region of transition (TZ) between SW and NE, the efficiency is intermediate. For details, see Ringdal et al (1992).]

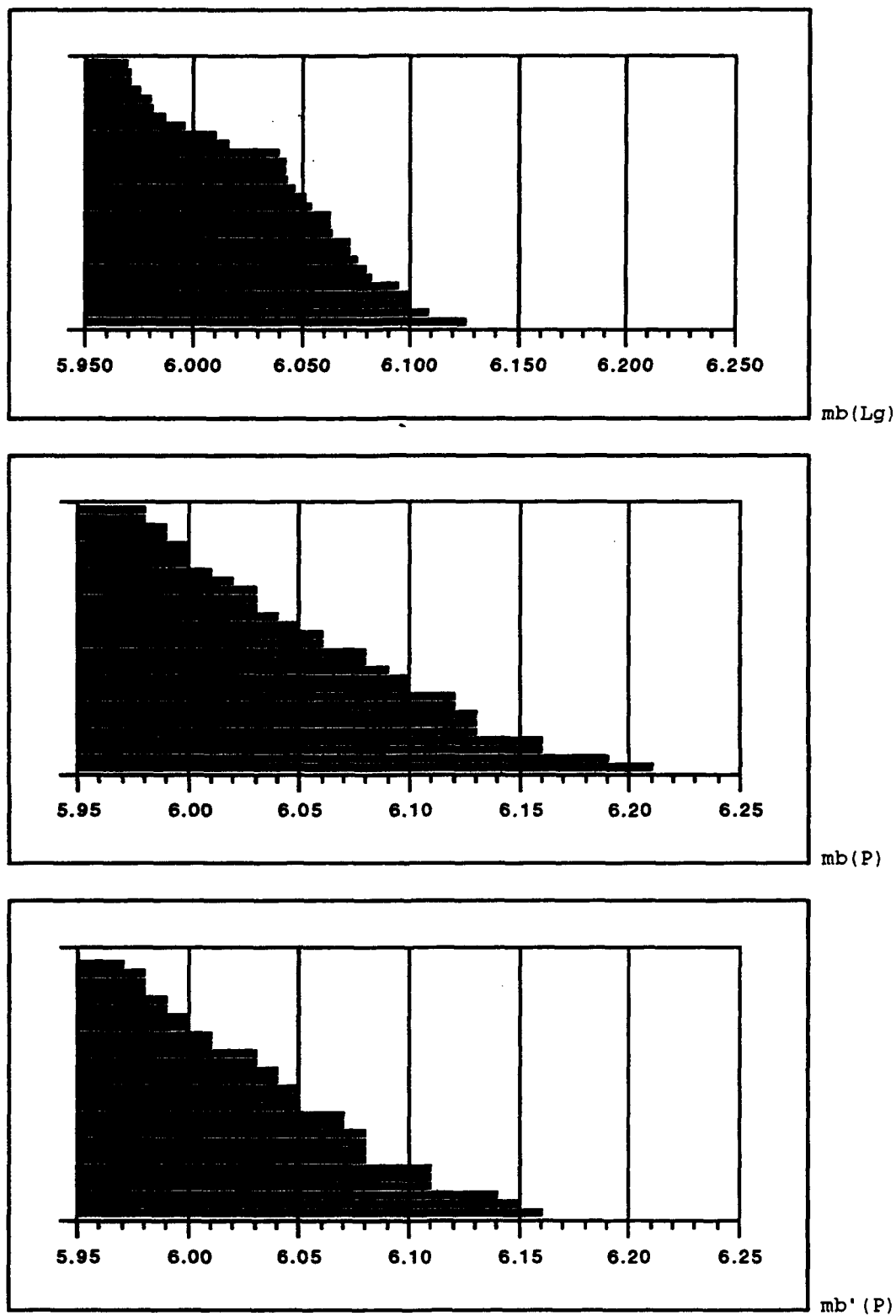


Figure 4. Presentation of explosion sizes, ranked with three different magnitude measures (see Table 2), for 30 large underground nuclear explosions at Balapan since March 1976.

REFERENCES

- Baker, R.G., Determining magnitude from Lg, *Bull. Seism. Soc. Amer.*, **60**, 1907-1919, 1970.
- Hansen, R.A., F. Ringdal and P.G. Richards, The stability of RMS Lg measurements and their potential for accurate estimation of the yields of Soviet underground explosions, *Bull. Seism. Soc. Amer.*, **80**, 2106-2126, 1990.
- Patton, H., S.R. Taylor, D.B. Harris, and J.M. Mills (Jr), The utility of regional Chinese seismograms for source and path studies in central Asia, *Geoph. J. R. Astr. Soc.*, **81**, 469-478, 1985.
- Ringdal, F., P.D. Marshall and R.W. Alewine, Seismic yield determination of Soviet underground nuclear explosions at the Shagan River test site, *Geoph. J. Int.*, **109**, 65-77, 1992.

RMS L_g AMPLITUDE OF BALAPAN EXPLOSIONS USING REGIONAL DATA FROM BOROVOYE, KAZAKHSTAN

Won-Young Kim and Paul G. Richards¹

Lamont-Doherty Earth Observatory, Palisades, NY 10964

(¹ also, Dept. of Geological Sciences, Columbia University)

ABSTRACT

RMS L_g measurements using digital seismograms recorded at the Borovoye Geophysical Observatory, Kazakhstan (station BRVK) from explosions in the Balapan test site ($\Delta \approx 688$ km) show very good correlation with NORSAR ($\Delta \approx 4300$ km) $m_b(L_g)$ which is based on RMS L_g measurements (Ringdal *et al.*, 1992).

Due to very low microseismic noise at BRVK, plus relatively broadband amplitude responses of the seismographs at BRVK, RMS L_g measurement using unfiltered L_g signal in the group velocity window 3.66-3.0 km/s is a good estimator of the strength of the Balapan explosions.

Regression of 12 RMS L_g measurements using BRVK data with NORSAR $m_b(L_g)$ yields a slope of 0.95 and a standard deviation of 0.024 magnitude units. This small scatter for 12 points indicates that one may have confidence in both RMS L_g as a precise measure of source strength, and in BRVK instrument calibrations.

INTRODUCTION

In recent years it has been shown that single-station measurement of L_g -wave amplitude can be as stable, for purpose of estimating the strength of a

seismic source, as the conventional P -wave magnitude measured by averaging several tens of stations in a global network (Hansen *et al.*, 1990; Ringdal *et al.*, 1992). It has been observed by Hansen *et al.* (1990) that the root mean squared (RMS) amplitudes of Lg signal from explosions in Balapan test site in Kazakhstan at pairs of stations are in excellent agreement with a scatter of only 0.03 magnitude units. This observation suggests that RMS Lg is a precise seismic quantity to measure the size of regional events (see e.g., Hansen *et al.*, 1990). In light of this technical result, we evaluate underground nuclear explosions in Balapan test site in Kazakhstan, for which we have found new collections of high quality, digital regional Lg data.

In this study, we evaluate the stability of the RMS Lg using digital seismograms recorded at Borovoye Geophysical Observatory, Kazakhstan (station BRVK) from 13 underground explosions in the Balapan test site in Eastern Kazakhstan ($\Delta = 682 \sim 697$ km). Locations of BRVK and the Balapan test site are shown in Figure 1. BRVK is the nearest digital seismograph station around

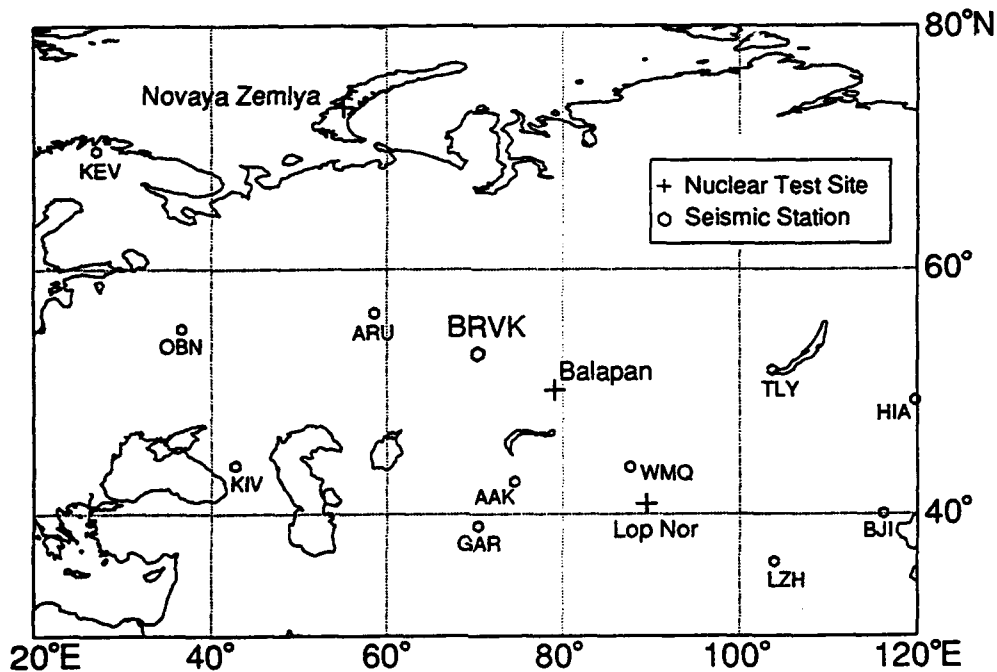


Fig. 1. Map showing locations of nuclear test sites, digital seismograph stations (IRIS/GSN/CDSN) in central Asia and Eastern Europe as well as BRVK station.

the Balapan test site in Kazakhstan and digital data was made available in early 1991 (Richards *et al.*, 1992). The station is known to have extremely low ambient Earth noise and has been operated since 1965 (Adushkin & An, 1990).

DATA

RMS amplitudes of Lg waves are determined using the short-period, vertical-component digital seismograms recorded on a low-gain channel (TSG-KSVM system) at the BRVK station from 13 underground explosions in the Balapan test site ($\Delta = 682 \sim 697$ km). A list of explosions is given in Table 1 and their epicenters are plotted in Figure 2.

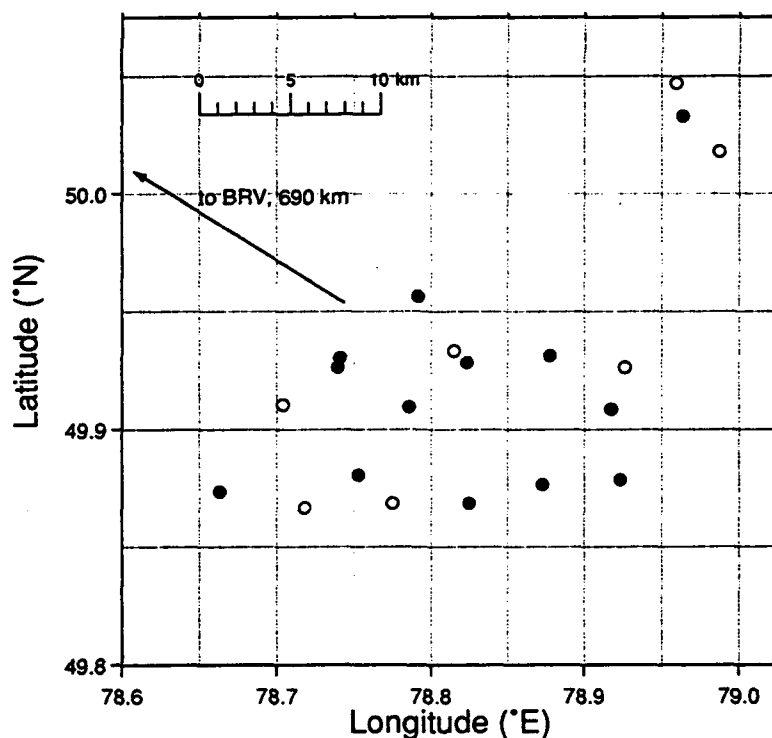


Fig. 2. Locations of known underground explosions since 1987 at Balapan test site in Kazakhstan. Filled circles indicate explosions analyzed in this study.

The TSG-KSVM channel records signal from a Kirnos seismometer with sampling interval of 0.026 s and has low- and high-gain vertical components (Adushkin & An, 1990; Richards *et al.*, 1992). The low-gain channel has been operating with a nominal gain of about 50 and has nearly flat response to the ground displacement in the frequency band 0.7 - 6 Hz (-3 db level; see Figure 3). The seismic signal with frequencies up to about 5 Hz is useful for most of the explosions studied. This channel provides unclipped short-period seismograms for large underground explosions from eastern Kazakhstan test sites. Typical vertical component records analyzed are shown in Figure 4.

Table 1. List of explosions at Balapan test site, Kazakhstan^(a)

Origin time		latitude	longitude	$m_b^{(b)}$	$m_b(Lg)^{(b)}$	RMS Lg
yy mo dd doy hh:mm:sec		(°N)	(°E)		NORSAR	BRVK ^(c)
87 03 12 (071) 01 57 19		49.929	78.824	5.31	5.218	2.6087
87 04 03 (093) 01 17 10		49.910	78.786	6.12	6.063	3.3668
87 04 17 (107) 01 03 07		49.874	78.663	5.92	5.910	3.2800
87 06 20 (171) 00 53 07		49.927	78.740	6.03	5.971	3.3358
87 08 02 (214) 00 58 09		49.877	78.873	5.83	5.871	3.2440
87 11 15 (319) 03 31 09		49.881	78.753	5.98	5.975	3.3797
87 12 13 (347) 03 21 07		49.957	78.792	6.06	6.082	3.4810
88 02 13 (044) 03 05 08		49.932	78.878	5.97	6.042	3.3793
88 04 03 (094) 01 33 08		49.909	78.918	5.99	6.063	3.4287
88 05 04 (125) 00 57 09		49.931	78.741	6.09	6.046	3.3472
88 06 14 (166) 02 27 08		50.034	78.964	4.80	-	2.3742
88 09 14 (258) 03 59 59		49.869	78.825	6.03	5.969	3.3459
88 12 17 (352) 04 18 09		49.879	78.924	5.80	5.801	3.1877

(a) Origin times and locations from Lilwall and Farthing (1990).

(b) from Ringdal, Marshal and Alewine (1992),

(c) Log₁₀ (RMS Lg) is given in nm of ground displacement.

DATA ANALYSIS

To measure the RMS amplitude of Lg , we followed a procedure similar to that of Ringdal & Hokland (1987) and Hansen *et al.* (1990) except that we used a gaussian window with variable width scaled for epicentral distances instead of the usual box-car window of fixed length. The root mean square (RMS) amplitude of Lg waves is obtained by the following procedure: 1) Lg signal is bandpass filtered to improve Lg signal-to-noise ratio (e.g., 0.6 to 3 Hz using 3rd order

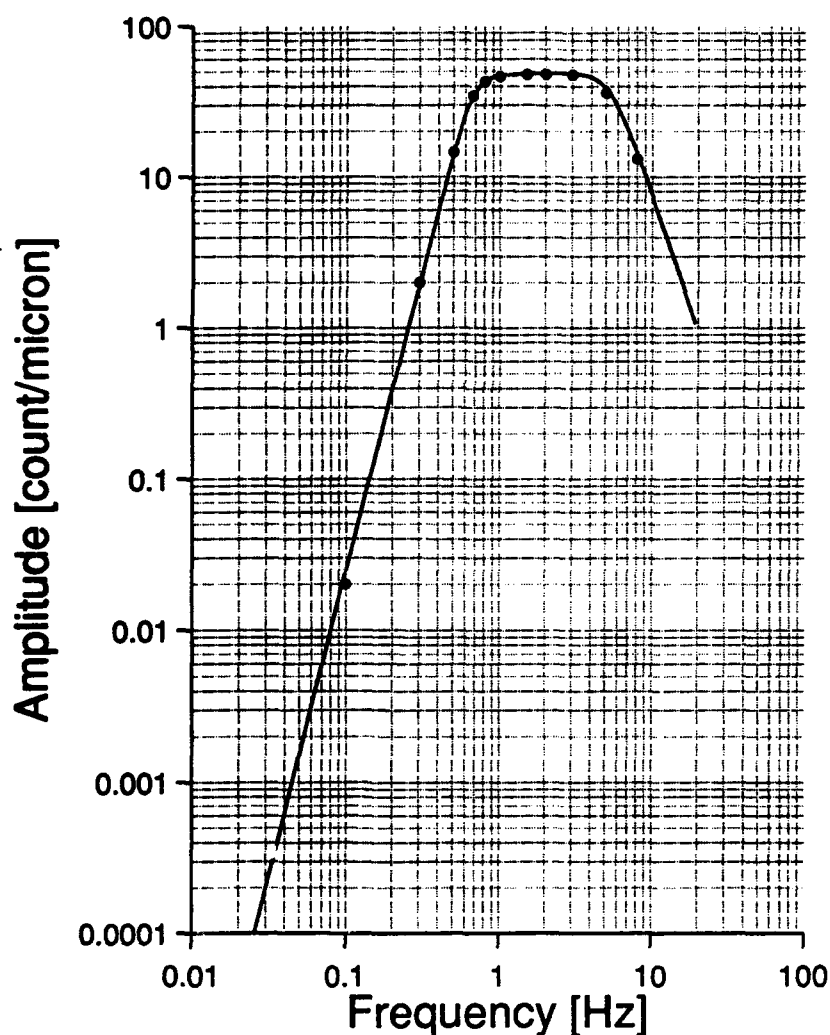


Fig. 3. Amplitude response curve of KSVM channel of the STsR-TSG system. Amplitude response is calculated with the transfer function obtained by inverting the calibration test pulse. Amplitude responses at certain frequencies (*closed circle*) measured independently at BRVK are superposed with the curve.

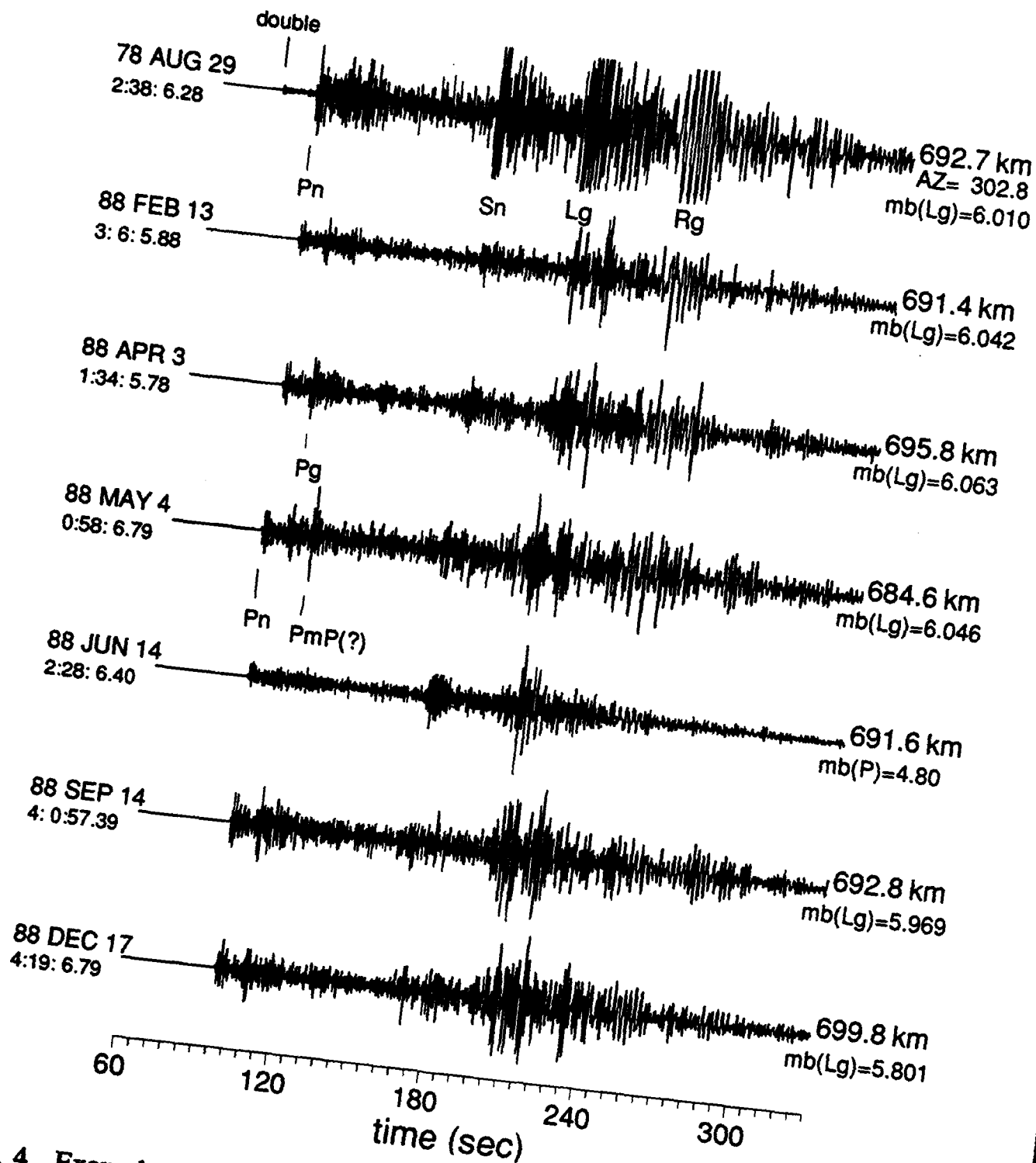


Fig. 4. Example digital records at BRVK from explosions at Balapan test site. Records are from low-gain KSVM channel with sampling interval of 0.026 s. Regional phases are indicated and NORSAR $m_b(Lg)$ is indicated at the end of each record.

Butterworth filter) and weighted with a gaussian window function. 2) mean squared amplitude of Lg waves in the group velocity between 3.66 and 3.0 km/s is obtained. 3) mean squared amplitude of noise is obtained in the noise window (about 30 sec) preceding the first arrival P waves. 4) RMS amplitude of Lg is obtained by correcting for the noise as suggested in Ringdal & Hokland (1987). The method can be written in discrete form as,

$$\text{RMS } Lg = \left[\frac{1}{N} \sum_{i=1}^N x_i^2 - \frac{1}{M} \sum_{j=1}^M x_j^2 \right]^{1/2} \quad (1)$$

where x_i = signal, $x(t)$, in the Lg window, N = number of points in the Lg window, x_j = signal in the noise window and M = number of points in the noise window (Hansen *et al.*, 1990; Ringdal & Hokland, 1987). Noise correction was negligible for all the explosions studied, because Lg signal-to-noise ratio on all seismograms were very high (above 200 and up to few 1000).

It has been a common practice to use a box-car time window with fixed length for RMS Lg measurements. For example, Ringdal & Hokland (1987) used box-car window of 120 s which corresponds to a window including Lg waves arriving with group velocities between 3.67 to 3.33 km/s at NORSAR from explosions in Balapan test site. Hansen *et al.* (1990) also used a fixed 120 s window in calculating RMS Lg amplitude of Balapan explosions for stations at epicentral distance range 950 - 2500 km. A fixed window length of 120 s for various epicentral distance ranges may include phases other than Lg . We used variable window length to include only Lg phases for the RMS Lg amplitude measurements at various distance ranges.

If we set the reference time window length, w_{ref} , of 60 s at a reference distance, Δ_{ref} , of 1000 km, this time window includes Lg wave arrivals in the group velocities between 3.03 and 3.70 km/s, when the window is centered at a group velocity of 3.33 km/s. For a suit of stations at various epicentral distances, the width of the Lg time window, w , at each station can be scaled as,

$$w = w_{\text{ref}} (\Delta/\Delta_{\text{ref}}). \quad (2)$$

RMS L_g Measurements with Gaussian Windowing: L_g arrivals are usually not as sharply defined as the first arrival P waves, but observed as a broad wave train arriving with group velocities between 3.7 and 3.0 km/s. For RMS L_g measurements to be robust, we found it useful to window the L_g signal with a gaussian probability density function centered at the main L_g arrivals. We used a gaussian window function of the form,

$$p(t, \Delta) = \frac{1}{\sigma\sqrt{2\pi}} \exp\left[-(t - \Delta/U_0)^2/2\sigma^2\right] \quad (3)$$

where σ = standard deviation in units of time,
 Δ = epicentral distance in km,
 U_0 = central group velocity in km/s and
 t = time following the event origin time.

The gaussian width, $\pm\sigma$, covers the L_g group velocity window, say 3.7-3.0 km/s. The gaussian window is truncated at $\pm 2\sigma$ which can be considered as 95.5 % probability that the L_g wave energy is distributed within the window.

For a suit of stations at various epicentral distances, the width of the gaussian window at each station can be scaled as (2),

$$\sigma = \sigma_{\text{ref}} (\Delta/\Delta_{\text{ref}}), \quad (4)$$

with $\sigma_{\text{ref}} = \sigma$ at reference distance Δ_{ref} . If we set the $\sigma_{\text{ref}} = 30$ s at a reference distance, $\Delta_{\text{ref}} = 1000$ km, $\pm\sigma$ of the gaussian window covers a group velocity window 3.66 - 3.0 km/s centered at 3.3 km/s. Each gaussian window scaled by distance covers the same range of L_g group velocities for each station.

Maximum Trace RMS L_g Amplitude: Although, the L_g signal shows remarkably stable arrivals in terms of group velocity (global average of about 3.6 km/s), there exist some scatter of L_g arrivals in regional scale. In this case,

maximum RMS L_g amplitude in the preset group velocity range can be used instead of the RMS L_g measured from a single fixed window. The maximum RMS amplitude of L_g is obtained by calculating the RMS values of the L_g signal with moving time window. Mean squared amplitude (MSA) trace is calculated where each point of the trace represents the MSA of signal in time window centered at that time. Each window is offset by 0.1 times the window length from the previous ones to smoothly sample the L_g waves and for computational efficiency. An example of the calculation of RMS L_g is shown in Figure 5.

The group velocities where the maximum of the RMS L_g is measured range from 3.0 to 3.27 km/s with a mean group velocity of 3.17 ± 0.1 km/s for 12 records. The epicentral distances of explosions are nearly identical with a mean of 688.4 ± 5.1 km. Differences between the epicentral distances of these explosions would predict variations of group velocities of about ± 0.05 km/s. The observed variations in the group velocity indicate substantial difference of group velocities between explosions. Considering nearly similar wave propagation paths for the 12 explosions, it is unclear whether this variation represents differences in the depth of burial of the explosions, or variations in the degree of coupling of explosion yields into seismic signal at the source.

RMS L_g Measurements Using Bandpass Filtered Data: If BRVK data are filtered with a 3rd order Butterworth bandpass filter in the pass band 0.6 and 3 Hz as used in Ringdal & Hokland (1987) and Hansen *et al.* (1990), regression of the measured RMS L_g values with NORSAR $m_b(L_g)$ yields a standard deviation of 0.033 magnitude units and a slope of 0.902. The regression of RMS L_g values with NORSAR $m_b(L_g)$ at various pass bands are listed in Table 2.

As the pass band of the filter becomes narrower, the standard deviation of the regression increases, while the slope decreases or increases depending upon the selected pass band (Figure 6; Table 2). RMS L_g measurements with narrower band pass filtered signal yield higher scatter and poorer regression with

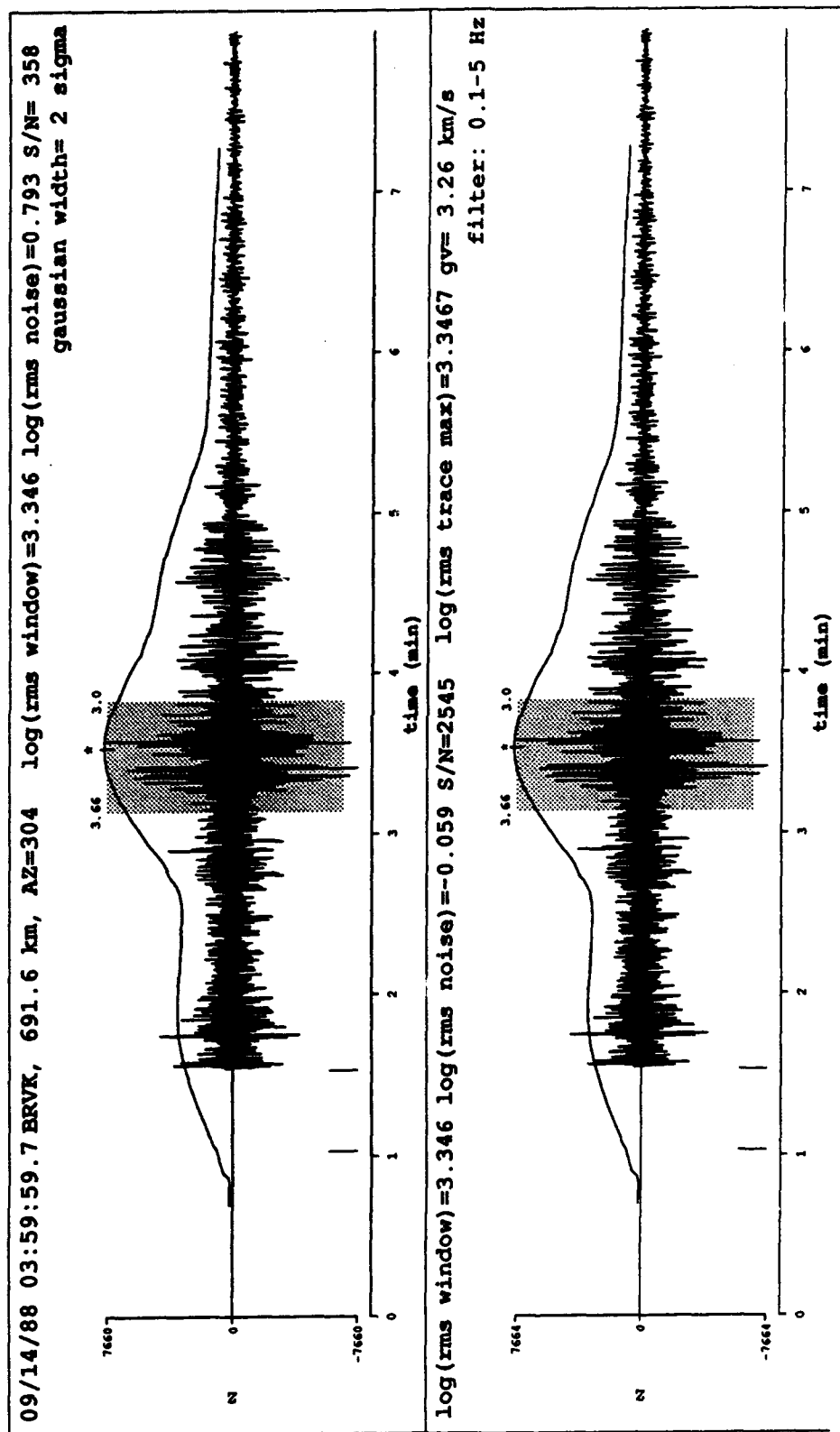


Fig. 5. An example RMS amplitude calculation: a) Mean squared amplitude trace is plotted above the unfiltered raw data (*top trace*) and its maximum is indicated by a star. Shaded area indicates the width of gaussian window with $\pm\sigma = 20$ s centered at the *Lg* group velocity of 3.3 km/s. b) similar to a) but for filtered trace.

NORSAR $m_b(Lg)$. Spectral analyses indicate that there is substantial Lg energy at frequencies below 0.6 Hz for Lg signals at BRVK generated by the explosions at the Balapan test site.

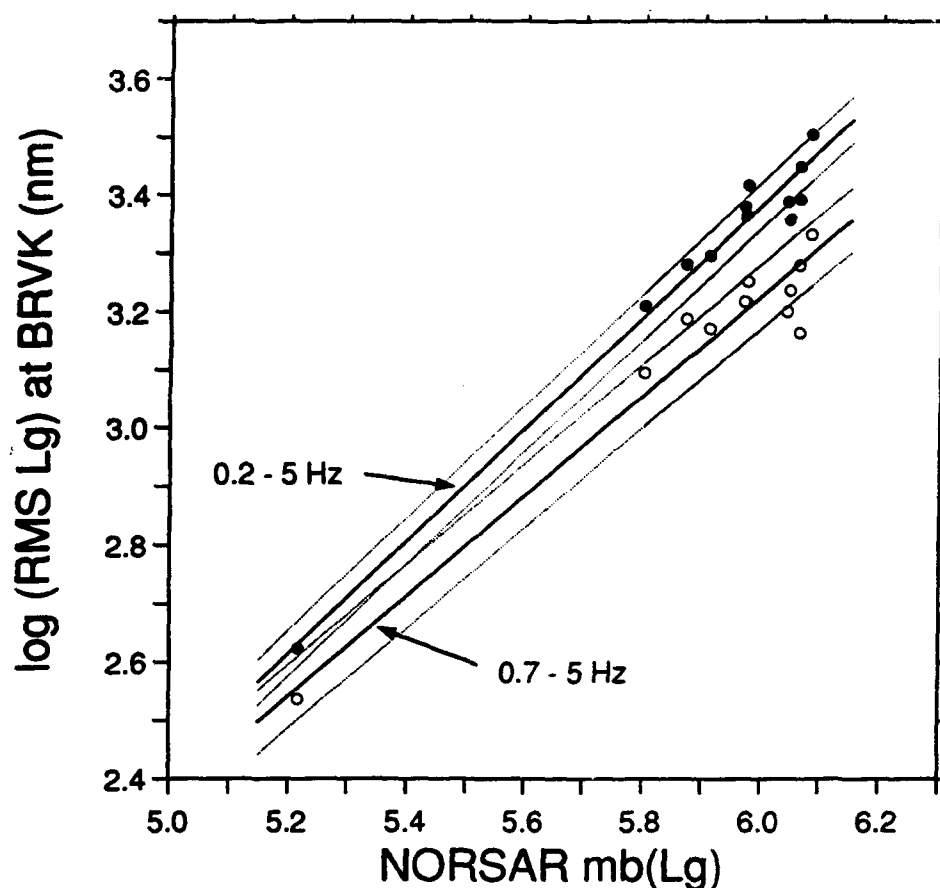


Fig. 6. Comparison of RMS Lg measurements at BRVK with data for two pass bands filtering. $\log_{10}(RMS Lg)$ measurements are plotted with NORSAR $m_b(Lg)$. Solid lines are fitted slopes of 0.964 and 0.860 for wider filter passband (0.2-5 Hz) and narrower (0.7-5 Hz) passband, respectively. Orthogonal rms misfits are 0.028 and 0.042 magnitude units for wider filter passband and narrower passband, respectively. The dotted lines correspond to ± 2 S.D.

RMS L_g measurements obtained from the L_g signal which were high pass filtered with higher cutoff frequency tend to underestimate the size of the larger explosions. This causes the regression slope to become less than 1, and decreases with increasing cutoff frequency of the high pass filter. On the other hand, lowering the low pass cutoff frequency increases the slope of the regression, indicating that the RMS L_g amplitude of smaller explosions tends to underestimate the source strength: smaller explosion source tend to contain more energy at higher frequencies than the larger explosions. Hence, the low pass filter affects smaller explosions more strongly than the larger explosions.

Since the RMS L_g is proportional to the square root of the energy density per unit time, L_g signal in a wider frequency band is required to estimate the stable RMS L_g amplitude (true size of the source). A slope of close to 1 in a regression of RMS L_g from a pair of stations, or against other scales such as, $m_b(L_g)$ ensures the stability of the measurements. Details of the discussion are given in Appendix 1.

Table 2. Regression of RMS L_g for various pass band with NORSAR $m_b(L_g)$

Passband (Hz)	σ (S.D.)	Slope	Passband (Hz)	σ (S.D.)	Slope
unfiltered	0.0222	0.963			
0.1 - 5	0.0222	0.965 [†]	0.1 - 0.3	0.09777	1.167
0.2 - 5	0.0264	0.964	0.1 - 0.5	0.0739	1.125
0.3 - 5	0.0286	0.961	0.1 - 1	0.0222	1.069
0.4 - 5	0.0300	0.955	0.1 - 2	0.0222	0.977
0.5 - 5	0.0318	0.939	0.1 - 4	0.0222	0.965
0.6 - 5	0.0361	0.908	0.1 - 6	0.0222	0.963
0.7 - 5	0.0418	0.863	0.1 - 8	0.0222	0.963

Very low microseismic noise at BRVK in the frequencies between 0.1 to 1 Hz as well as relatively broad amplitude response of short-period TSG-KSVM system at BRVK (Richards et al., 1992) suggest that unfiltered *Lg* signal in the group velocity window 3.66 - 3.0 km/s is a better estimator of the strength of the Balapan explosions. If filtering the data is needed, for example to increase the *Lg* signal-to-noise ratio, then a band pass filter between 0.1 - 5 Hz provides reasonably stable results for RMS *Lg* measurements at BRVK (Table 2).

RMS Lg Amplitude Measurements Using Gaussian Weighted Single Lg Window: RMS amplitude of unfiltered *Lg* signals at BRVK for 13 explosions at Balapan is obtained using the gaussian window with $\sigma \approx 20$ s centered at a group velocity of 3.3 km/s. This is our preferred procedure for measuring RMS *Lg*. The width of the gaussian, $\pm\sigma$, includes *Lg* wave arrivals in the group velocities between 3.66 and 3.0 km/s at a distance of 690 km.

Figure 7 shows the \log_{10} of RMS *Lg* measurements in nanometer (nm) of ground displacement plotted against NORSAR $m_b(Lg)$. Regression of 12 measurements using BRVK data yields a slope of 0.956 and a standard deviation of 0.024 magnitude units. This small scatter for 12 points indicates that one may have confidence in both RMS *Lg* as a precise measure of signal strength, and in BRVK calibration. Due to very low microseismic noise at BRVK plus relatively broadband amplitude responses of seismographs at BRVK, RMS *Lg* measurement using unfiltered *Lg* signal in the group velocity window 3.66 - 3.0 km/s is a good estimator of the strength of the Balapan explosions.

DISCUSSION AND CONCLUSIONS

Due to very low microseismic noise at BRVK, plus relatively broadband amplitude responses of the seismographs at BRVK, RMS *Lg* measurement using unfiltered *Lg* signal in the group velocity window 3.66-3.0 km/s is a better

estimator of the strength of the Balapan explosions than the measurements obtained from narrow band passed data. Gaussian weighting provides a robust RMS Lg measurement procedure for various Lg paths and epicentral distance ranges.

An evaluation of the stability of RMS Lg indicates that Lg signal in a wider frequency band is required to estimate a stable RMS Lg amplitude, since

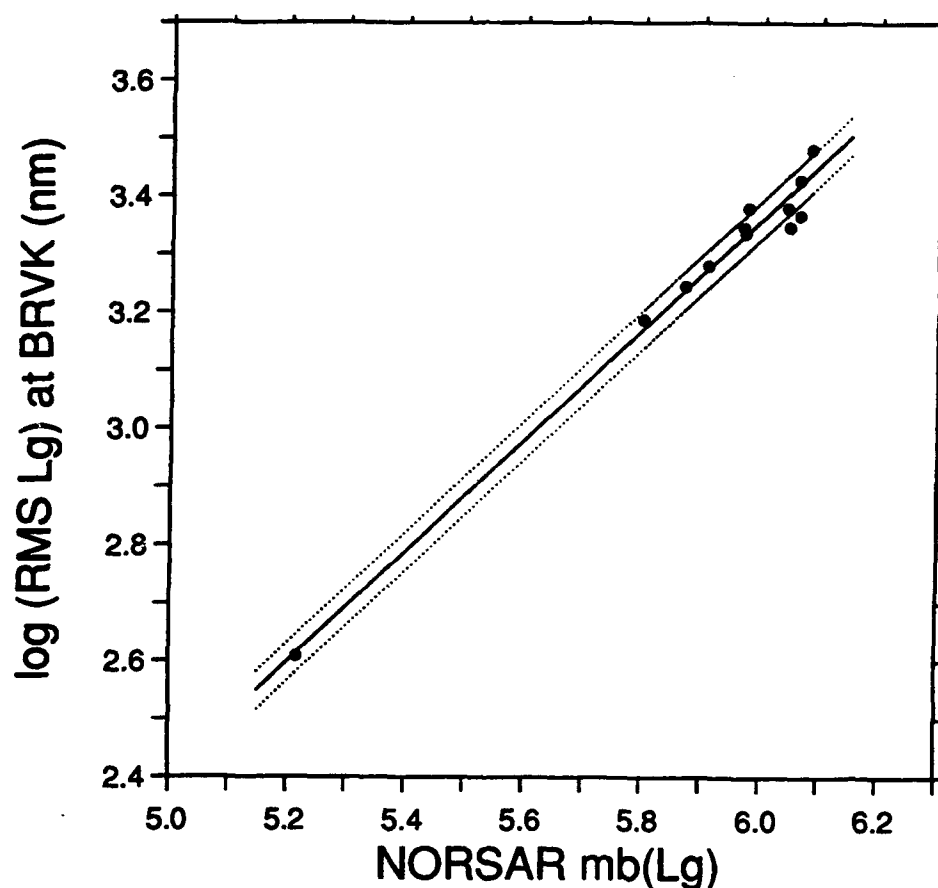


Fig. 7. Comparison of $\log_{10}(\text{RMS } Lg)$ measurements in nm at BRVK with NORSAR $m_b(Lg)$. RMS Lg amplitudes are obtained from unfiltered data with a single gaussian window centered at Lg group velocity about 3.3 km/s. Solid line is a fitted slope of 0.95 and an orthogonal rms misfit of 0.024 magnitude units. The dotted lines correspond to ± 2 S.D.

the RMS amplitude is proportional to the square root of sum of the power spectral density over frequency 0 up to the Nyquist frequency. A significant departure of slope of the regression of RMS L_g amplitude at a pair of station from unity indicates instability of RMS amplitude measurements at that station.

Regression of 12 RMS L_g measurements using BRVK data with NORSAR $m_b(L_g)$ yields a slope of 0.95 and a standard deviation of 0.024 magnitude units. This small scatter for 12 points indicates that one may have confidence in both RMS L_g as a precise measure of source strength, and in BRVK instrument calibrations. The latter result is important for our current plans to work extensively with BRVK data.

REFERENCES

- Aki, K. and P. G. Richards, *Quantitative Seismology*, vol. I, Freeman & Co., 1980.
- Adushkin, V. V. and V. A. An, Seismic observations and monitoring of underground nuclear explosions at Borovoye Geophysical Observatory, *Izvestiya Akademii Nauk SSSR: Fizika Zemeli*, No. 12, 47-59, 1990.
- Butler, R., C. S. McCreery, L. N. Frazer and D. A. Walker, High-frequency seismic attenuation of oceanic P and S waves in the Western Pacific, *J. Geophys. Res.*, 92, 1383-1396, 1987.
- Hansen, R. A., F. Ringdal and P. G. Richards, The stability of RMS L_g measurements and their potential for accurate estimation of the yields of Soviet underground nuclear explosions, *Bull. Seism. Soc. Am.*, 80, 2106-2126, 1990.
- Lilwall, R. C. and J., Farthing, Joint epicenter determination of Soviet underground nuclear explosions 1973-89 at the Semipalatinsk test site, AWE Report No. O 12/90, Atomic Weapons Establishment, UK, 13pp, 1990.
- Richards, P. G., W. Y. Kim and G. Ekström, The Borovoye Geophysical Observatory, Kazakhstan, *EOS*, 73, 201-206, 1992.
- Ringdal, F. and B. Kr. Hokland, Magnitudes of large Semipalatinsk explosions using P coda and L_g measurements at NORSAR, in *Semiannual Technical Summary*, NORSAR Sci. Rept. 1-87/88, NTN/NORSAR, Kjeller, Norway, 1987.

- Ringdal, F. and P. D. Marshall, Yield determination of Soviet underground nuclear explosions at the Shagan River Test Site, in *Semiannual Technical Summary*, NORSAR Sci. Rept. 2-88/89, NTNF/NORSAR, Kjeller, Norway, 1989.
- Ringdal, F., P. D. Marshall and R. W. Alewine, Seismic yield determination of Soviet underground nuclear explosions at the Balapan test site, *Geophys. J. Int.*, **109**, 65-77, 1992.
- Thurber, C. H., H. R. Quin and P. G. Richards, Accurate locations of nuclear explosions in Balapan, Kazakhstan, 1987 to 1989, *Geophys. Res. Lett.*, **20**, 399-402.

Appendix 1

Stability of the RMS Amplitude

RMS amplitude stability can be examined more clearly in the frequency domain. For a discrete time series of finite duration, the mean squared amplitude of digital signal, x_i , (for $i = 1, 2, \dots, N$) is equal to the sum of $N/2+1$ values of power spectral density (PSD) over positive frequencies as,

$$\text{Mean squared amplitude} = \frac{1}{N} \sum_{i=1}^N |x_i|^2 = \frac{1}{N^2} \sum_{j=1}^M |X_j \times X_j^*| \quad (\text{A1})$$

where X_j = discrete Fourier transform of the signal, $M = N/2+1$ (Nyquist frequency point) and * denotes complex conjugate. $\frac{1}{N^2}$ is used for normalization to represent PSD per unit time. This is the result of Parseval's theorem, in which total power, P , in a signal, is given by

$$P = \int_{-\infty}^{\infty} |x(t)|^2 dt = \frac{1}{2\pi} \int_{-\infty}^{\infty} |X(\omega)|^2 d\omega \quad (\text{A2})$$

where $X(\omega)$ = discrete Fourier transform of the signal $x(t)$. Hence, RMS amplitude is proportional to the square root of the sum of the power spectral density over the frequency 0 up to the cutoff frequency, ω_c . The maximum cutoff frequency is the Nyquist frequency, but in practice, it may be the frequency at which the signal falls to the noise level.

When a broadband signal is used for the RMS amplitude measurements, it include signal power spectral densities from long-period spectral level ($\omega \rightarrow 0$) up to a cutoff frequency. Hence, measured RMS amplitude values represent a mean of the source strength (from the long-period spectral level) and the high frequency radiation of the source (from the spectrum above the corner frequency). Thus, it is clear that the stability of the RMS amplitude measurements depend upon frequency content available in observed data. If the cutoff frequency of the signal is close to the corner frequency of a small

earthquake, RMS value will severely underestimate the strength of the earthquake. On the other hand, if there is band limit at low frequencies, measured RMS value will underestimate the strength of larger earthquakes relative to smaller events. A relatively stable RMS measurements can be obtained if observed data covers a frequency band around the source corner frequency with high signal-to-noise ratio, since the PSD of the source spectrum is peaked at the corner frequency.

The energy flux (radiated seismic energy density per unit area) in a plane wave from a seismic source can be represented as (e.g., Aki & Richards, 1980),

$$I_{Es} = \rho v \int_0^t \dot{u}^2 dt \quad (A3)$$

where ρ = density of the medium, v = wave speed in the medium, \dot{u} = ground velocity amplitude and the integration extends over the duration of the wave.

Therefore, when the observed ground motion is proportional to the velocity, the RMS amplitude value is directly proportional to the square root of the energy flux, I_{Es} , per unit time, that is,

$$\text{RMS amplitude} \propto \sqrt{I_{Es}}. \quad (A4)$$

A calculation of energy flux may be more complex for Lg waves in an inhomogeneous Earth, because the typical Lg signal consists of family of rays leaving the focal sphere with different take-off angles, subsequently undergoing multiple reflections within crustal wave guides along the propagation path. However, due to the averaging effects of the Earth, Lg is less dependent upon the radiation pattern of the source and shows remarkable stability as reported in numerous studies of Lg .

Nuttli's $m_b(Lg)$ as well as $m_b(P)$ corresponds to the square root of the maximum energy flux rate (per unit time), since

$$m_b(Lg) = \log_{10} \dot{u}_{\max} + \text{constant} \quad (A5)$$

Comparing eq. (A3) and (A5), it can be seen that a factor in the stability of RMS Lg over $m_b(Lg)$ is provided by the integral over Lg window.

Scalar seismic moment, M_0 , is obtained from the long-period limit of the source spectrum by using, for example,

$$M_0 = 4\pi\rho\beta^3 R \frac{1}{R(\theta, \varphi)} \Omega_0$$

where β = shear wave speed, R = geometrical spreading ($R \approx \Delta^{5/6}$ for Lg), $R(\theta, \varphi)$ = source radiation pattern and Ω_0 = long period spectral level ($\omega \rightarrow 0$). While the total radiated energy, Es , is obtained from the energy flux given in (A3) integrated over the focal sphere. Hence, power spectral density at the high frequency portion of the source spectrum is proportional to the *apparent stress*, τ_a .

$$\tau_a = \mu \frac{Es}{M_0} \quad (A6)$$

where μ = shear modulus (Aki & Richards, 1980).

Prof. Thomas Ahrens
Seismological Lab, 252-21
Division of Geological & Planetary Sciences
California Institute of Technology
Pasadena, CA 91125

Prof. Keiiti Aki
Center for Earth Sciences
University of Southern California
University Park
Los Angeles, CA 90089-0741

Prof. Shelton Alexander
Geosciences Department
403 Deike Building
The Pennsylvania State University
University Park, PA 16802

Prof. Charles B. Archambeau
CIRES
University of Colorado
Boulder, CO 80309

Dr. Thomas C. Bache, Jr.
Science Applications Int'l Corp.
10260 Campus Point Drive
San Diego, CA 92121 (2 copies)

Prof. Muawia Barazangi
Institute for the Study of the Continent
Cornell University
Ithaca, NY 14853

Dr. Jeff Barker
Department of Geological Sciences
State University of New York
at Binghamton
Vestal, NY 13901

Dr. Douglas R. Baumgardt
ENSCO, Inc
5400 Port Royal Road
Springfield, VA 22151-2388

Dr. Susan Beck
Department of Geosciences
Building #77
University of Arizona
Tucson, AZ 85721

Dr. T.J. Bennett
S-CUBED
A Division of Maxwell Laboratories
11800 Sunrise Valley Drive, Suite 1212
Reston, VA 22091

Dr. Robert Blandford
AFTAC/TT, Center for Seismic Studies
1300 North 17th Street
Suite 1450
Arlington, VA 22209-2308

Dr. Stephen Bratt
ARPA/NMRO
3701 North Fairfax Drive
Arlington, VA 22203-1714

Dr. Lawrence Burdick
IGPP, A-025
Scripps Institute of Oceanography
University of California, San Diego
La Jolla, CA 92093

Dr. Robert Burridge
Schlumberger-Doll Research Center
Old Quarry Road
Ridgefield, CT 06877

Dr. Jerry Carter
Center for Seismic Studies
1300 North 17th Street
Suite 1450
Arlington, VA 22209-2308

Dr. Eric Chael
Division ~~MS~~ MS 0655
Sandia Laboratory
Albuquerque, NM 87185 -0655

Dr. Martin Chapman
Department of Geological Sciences
Virginia Polytechnical Institute
21044 Derring Hall
Blacksburg, VA 24061

Mr Robert Cockerham
Arms Control & Disarmament Agency
320 21st Street North West
Room 5741
Washington, DC 20451,

Prof. Vernon F. Cormier
Department of Geology & Geophysics
U-45, Room 207
University of Connecticut
Storrs, CT 06268

Prof. Steven Day
Department of Geological Sciences
San Diego State University
San Diego, CA 92182

US Dept of Energy
Recipient, IS-20, GA-033
Office of Rsch & Development
1000 Independence Ave
Washington, DC 20585

Dr. Cliff Frolich
Institute of Geophysics
8701 North Mopac
Austin, TX 78759

Dr. Zoltan Der
ENSCO, Inc.
5400 Port Royal Road
Springfield, VA 22151-2388

Dr. Holly Given
IGPP, A-025
Scripps Institute of Oceanography
University of California, San Diego
La Jolla, CA 92093

Prof. Adam Dziewonski
Hoffman Laboratory, Harvard University
Dept. of Earth Atmos. & Planetary Sciences
20 Oxford Street
Cambridge, MA 02138

Dr. Jeffrey W. Given
SAIC
10260 Campus Point Drive
San Diego, CA 92121

Prof. John Ebel
Department of Geology & Geophysics
Boston College
Chestnut Hill, MA 02167

Dr. Dale Glover
Defense Intelligence Agency
ATTN: ODT-1B
Washington, DC 20301

Eric Fielding
SNEE Hall
INSTOC
Cornell University
Ithaca, NY 14853

Dan N. Hagedorn
Pacific Northwest Laboratories
Battelle Boulevard
Richland, WA 99352

Dr. Petr Firbas
Institute of Physics of the Earth
Masaryk University Brno
Jecna 29a
612 46 Brno, Czech Republic

Dr. James Hannon
Lawrence Livermore National Laboratory
P.O. Box 808
L-205
Livermore, CA 94550

Dr. Mark D. Fisk
Mission Research Corporation
735 State Street
P.O. Drawer 719
Santa Barbara, CA 93102

Prof. David G. Harkrider
Seismological Laboratory
Division of Geological & Planetary Sciences
California Institute of Technology
Pasadena, CA 91125

Prof Stanley Flatte
Applied Sciences Building
University of California, Santa Cruz
Santa Cruz, CA 95064

Prof. Danny Harvey
CIRES
University of Colorado
Boulder, CO 80309

Prof. Donald Forsyth
Department of Geological Sciences
Brown University
Providence, RI 02912

Prof. Donald V. Helmberger
Seismological Laboratory
Division of Geological & Planetary Sciences
California Institute of Technology
Pasadena, CA 91125

Dr. Art Frankel
U.S. Geological Survey
922 National Center
Reston, VA 22092

Prof. Eugene Herrin
Institute for the Study of Earth and Man
Geophysical Laboratory
Southern Methodist University
Dallas, TX 75275

Prof. Robert B. Herrmann
Department of Earth & Atmospheric Sciences
St. Louis University
St. Louis, MO 63156

Prof. Lane R. Johnson
Seismographic Station
University of California
Berkeley, CA 94720

Prof. Thomas H. Jordan
Department of Earth, Atmospheric &
Planetary Sciences
Massachusetts Institute of Technology
Cambridge, MA 02139

Prof. Alan Kafka
Department of Geology & Geophysics
Boston College
Chestnut Hill, MA 02167

Robert C. Kemerait
ENSCO, Inc.
445 Pineda Court
Melbourne, FL 32940

Dr. Karl Koch
Institute for the Study of Earth and Man
Geophysical Laboratory
Southern Methodist University
Dallas, Tx 75275

US Dept of Energy
Attn: Max Koontz, NN-20, GA-033
Office of Rsch & Development
1000 Independence Ave, SW
Washington, DC 20585

Dr. Richard LaCoss
MIT Lincoln Laboratory, M-200B
P.O. Box 73
Lexington, MA 02173-0073

Dr. Fred K. Lamb
University of Illinois at Urbana-Champaign
Department of Physics
1110 West Green Street
Urbana, IL 61801

Prof. Charles A. Langston
Geosciences Department
403 Deike Building
The Pennsylvania State University
University Park, PA 16802

Jim Lawson, Chief Geophysicist
Oklahoma Geological Survey
Oklahoma Geophysical Observatory
P.O. Box 8
Leonard, OK 74043-0008

Prof. Thorne Lay
Institute of Tectonics
Earth Science Board
University of California, Santa Cruz
Santa Cruz, CA 95064

Dr. William Leith
U.S. Geological Survey
Mail Stop 928
Reston, VA 22092

Mr. James F. Lewkowicz
Phillips Laboratory/GPEH
29 Randolph Road
Hanscom AFB, MA 01731-3010(2 copies)

Mr. Alfred Lieberman
ACDA/VI-OA State Department Building
Room 5726
320-21st Street, NW
Washington, DC 20451

Prof. L. Timothy Long
School of Geophysical Sciences
Georgia Institute of Technology
Atlanta, GA 30332

Dr. Randolph Martin, III
New England Research, Inc.
76 Olcott Drive
White River Junction, VT 05001

Dr. Robert Masse
Denver Federal Building
Box 25046, Mail Stop 967
Denver, CO 80225

Dr. Gary McCartor
Department of Physics
Southern Methodist University
Dallas, TX 75275

Prof. Thomas V. McEvilly
Seismographic Station
University of California
Berkeley, CA 94720

Dr. Art McGarr
U.S. Geological Survey
Mail Stop 977
U.S. Geological Survey
Menlo Park, CA 94025

Dr. Keith L. McLaughlin
S-CUBED
A Division of Maxwell Laboratory
P.O. Box 1620
La Jolla, CA 92038-1620

Stephen Miller & Dr. Alexander Florence
SRI International
333 Ravenswood Avenue
Box AF 116
Menlo Park, CA 94025-3493

Prof. Bernard Minster
IGPP, A-025
Scripps Institute of Oceanography
University of California, San Diego
La Jolla, CA 92093

Prof. Brian J. Mitchell
Department of Earth & Atmospheric Sciences
St. Louis University
St. Louis, MO 63156

Mr. Jack Murphy
S-CUBED
A Division of Maxwell Laboratory
11800 Sunrise Valley Drive, Suite 1212
Reston, VA 22091 (2 Copies)

Dr. Keith K. Nakanishi
Lawrence Livermore National Laboratory
L-025
P.O. Box 808
Livermore, CA 94550

Prof. John A. Orcutt
IGPP, A-025
Scripps Institute of Oceanography
University of California, San Diego
La Jolla, CA 92093

Prof. Jeffrey Park
Kline Geology Laboratory
P.O. Box 6666
New Haven, CT 06511-8130

Dr. Howard Patton
Lawrence Livermore National Laboratory
L-025
P.O. Box 808
Livermore, CA 94550

Dr. Frank Pilotte
HQ AFTAC/TT
1030 South Highway A1A
Patrick AFB, FL 32925-3002

Dr. Jay J. Pulli
Radix Systems, Inc.
201 Perry Parkway
Gaithersburg, MD 20877

Dr. Robert Reinke
ATTN: FCTVTD
Field Command
Defense Nuclear Agency
Kirtland AFB, NM 87115

Prof. Paul G. Richards
Lamont-Doherty Geological Observatory
of Columbia University
Palisades, NY 10964

Mr. Wilmer Rivers
Teledyne Geotech
314 Montgomery Street
Alexandria, VA 22314

Dr. Alan S. Ryall, Jr.
ARPA/NMRO
3701 North Fairfax Drive
Arlington, VA 22203-1714

Dr. Richard Sailor
TASC, Inc.
55 Walkers Brook Drive
Reading, MA 01867

Prof. Charles G. Sammis
Center for Earth Sciences
University of Southern California
University Park
Los Angeles, CA 90089-0741

Prof. Christopher H. Scholz
Lamont-Doherty Geological Observatory
of Columbia University
Palisades, NY 10964

Dr. Susan Schwartz
Institute of Tectonics
1156 High Street
Santa Cruz, CA 95064

Secretary of the Air Force
(SAFRD)
Washington, DC 20330

Office of the Secretary of Defense
DDR&E
Washington, DC 20330

Thomas J. Sereno, Jr.
Science Application Int'l Corp.
10260 Campus Point Drive
San Diego, CA 92121

Dr. Michael Shore
Defense Nuclear Agency/SPSS
6801 Telegraph Road
Alexandria, VA 22310

Dr. Robert Shumway
University of California Davis
Division of Statistics
Davis, CA 95616

Dr. Matthew Sibol
Virginia Tech
Seismological Observatory
4044 Derring Hall
Blacksburg, VA 24061-0420

Prof. David G. Simpson
IRIS, Inc.
1616 North Fort Myer Drive
Suite 1050
Arlington, VA 22209

Donald L. Springer
Lawrence Livermore National Laboratory
L-025
P.O. Box 808
Livermore, CA 94550

Dr. Jeffrey Stevens
S-CUBED
A Division of Maxwell Laboratory
P.O. Box 1620
La Jolla, CA 92038-1620

Lt. Col. Jim Stobie
ATTN: AFOSR/NL
110 Duncan Avenue
Bolling AFB
Washington, DC 20332-0001

Brian Stump
Los Alamos National Laboratory
EES-3, Mail Stop C335
Los Alamos, NM 87545

Prof. Jeremiah Sullivan
University of Illinois at Urbana-Champaign
Department of Physics
1110 West Green Street
Urbana, IL 61801

Prof. L. Sykes
Lamont-Doherty Geological Observatory
of Columbia University
Palisades, NY 10964

Dr. David Taylor
ENSCO, Inc.
445 Pineda Court
Melbourne, FL 32940

Dr. Steven R. Taylor
Los Alamos National Laboratory
P.O. Box 1663
Mail Stop C335
Los Alamos, NM 87545

Prof. Clifford Thurber
University of Wisconsin-Madison
Department of Geology & Geophysics
1215 West Dayton Street
Madison, WI 53706

Prof. M. Nafi Toksoz
Earth Resources Lab
Massachusetts Institute of Technology
42 Carleton Street
Cambridge, MA 02142

Dr. Larry Turnbull
CIA-OSWR/NED
Washington, DC 20505

Dr. Gregory van der Vink
IRIS, Inc.
1616 North Fort Myer Drive
Suite 1050
Arlington, VA 22209

Dr. Karl Veith
EG&G
5211 Auth Road
Suite 240
Suitland, MD 20746

Prof. Terry C. Wallace
Department of Geosciences
Building #77
University of Arizona
Tuscon, AZ 85721

Dr. Thomas Weaver
Los Alamos National Laboratory
P.O. Box 1663
Mail Stop C335
Los Alamos, NM 87545

Dr. William Wortman
Mission Research Corporation
8560 Cinderbed Road
Suite 700
Newington, VA 22122

Prof. Francis T. Wu
Department of Geological Sciences
State University of New York
at Binghamton
Vestal, NY 13901

Prof Ru-Shan Wu
University of California, Santa Cruz
Earth Sciences Department
Santa Cruz
, CA 95064

ARPA, OASB/Library
3701 North Fairfax Drive
Arlington, VA 22203-1714

HQ DNA
ATTN: Technical Library
Washington, DC 20305

Defense Intelligence Agency
Directorate for Scientific & Technical Intelligence
ATTN: DTIB
Washington, DC 20340-6158

Defense Technical Information Center
Cameron Station
Alexandria, VA 22314 (2 Copies)

TACTEC
Batelle Memorial Institute
505 King Avenue
Columbus, OH 43201 (Final Report)

Phillips Laboratory
ATTN: XPG
29 Randolph Road
Hanscom AFB, MA 01731-3010

Phillips Laboratory
ATTN: GPE
29 Randolph Road
Hanscom AFB, MA 01731-3010

Phillips Laboratory
ATTN: TSML
5 Wright Street
Hanscom AFB, MA 01731-3004

Phillips Laboratory
ATTN: PL/SUL
3550 Aberdeen Ave SE
Kirtland, NM 87117-5776 (2 copies)

Dr. Michel Bouchon
I.R.I.G.M.-B.P. 68
38402 St. Martin D'Herès
Cedex, FRANCE

Dr. Michel Campillo
Observatoire de Grenoble
I.R.I.G.M.-B.P. 53
38041 Grenoble, FRANCE

Dr. Kin Yip Chun
Geophysics Division
Physics Department
University of Toronto
Ontario, CANADA

Prof. Hans-Peter Harjes
Institute for Geophysics
Ruhr University/Bochum
P.O. Box 102148
4630 Bochum 1, GERMANY

Prof. Eystein Husebye
NTNF/NORSAR
P.O. Box 51
N-2007 Kjeller, NORWAY

David Jepsen
Acting Head, Nuclear Monitoring Section
Bureau of Mineral Resources
Geology and Geophysics
G.P.O. Box 378, Canberra, AUSTRALIA

Ms. Eva Johannisson
Senior Research Officer
FOA
S-172 90 Sundbyberg, SWEDEN

Dr. Peter Marshall
Procurement Executive
Ministry of Defense
Blacknest, Brimpton
Reading FG7-FRS, UNITED KINGDOM

Dr. Bernard Massinon, Dr. Pierre Mechler
Societe Radiomana
27 rue Claude Bernard
75005 Paris, FRANCE (2 Copies)

Dr. Svein Mykkeltveit
NTNT/NORSAR
P.O. Box 51
N-2007 Kjeller, NORWAY (3 Copies)

Prof. Keith Priestley
University of Cambridge
Bullard Labs, Dept. of Earth Sciences
Madingley Rise, Madingley Road
Cambridge CB3 0EZ, ENGLAND

Dr. Jorg Schlittenhardt
Federal Institute for Geosciences & Nat'l Res.
Postfach 510153
D-30631 Hannover , GERMANY

Dr. Johannes Schweitzer
Institute of Geophysics
Ruhr University/Bochum
P.O. Box 1102148
4360 Bochum 1, GERMANY

Trust & Verify
VERTIC
Carrara House
20 Embankment Place
London WC2N 6NN, ENGLAND